IEKP-KA/2011-4

Nachweis von Top-Quarks und erste Messung des $t\bar{t}$-Wirkungsquerschnitts bei einer Schwerpunktsenergie von 7 TeV mit dem CMS-Experiment am LHC

Jasmin Gruschke

Zur Erlangung des akademischen Grades eines
DOKTORS DER NATURWISSENSCHAFTEN
von der Fakultät für Physik des
Karlsruher Institut für Technologie (KIT)

genehmigte

Dissertation

von

Dipl.-Phys. Jasmin Gruschke
aus Schönau im Schwarzwald

Tag der mündlichen Prüfung: 04.02.2011

Referent: Prof. Dr. Th. Müller, Institut für Experimentelle Kernphysik,
Karlsruher Institut für Technologie (KIT)

Korreferent: Prof. Dr. G. Quast, Institut für Experimentelle Kernphysik,
Karlsruher Institut für Technologie (KIT)

“Dass ich nicht mehr, mit sauerm Schweiß,
Zu sagen brauche was ich nicht weiß;
Dass ich erkenne was die Welt
Im Innersten zusammenhält,”

[Faust, Der Tragödie Erster Teil,
J. W. Goethe, 1808]

Zusammenfassung

Dem fiktiven Doktor Faustus gleich, widmen sich Teilchenphysiker der Erforschung der Bausteine unserer Materie und der Eigenschaften der Kräfte, die zwischen diesen fundamentalen Einheiten wirken. Das Standardmodell der Teilchenphysik fasst das gesammelte Wissen über die elementaren Teilchen und deren Wechselwirkungen zusammen. Es wurde in den frühen siebziger Jahren des 20. Jahrhunderts entwickelt und gilt bislang als vollständigste und erfolgreichste Theorie zur Beschreibung der beobachteten Phänomene. Insgesamt beinhaltet das Standardmodell zwölf fundamentale Fermionen, zu denen jeweils ein Antiteilchen mit entgegengesetzten Ladungen existiert. Die Wechselwirkungen zwischen den Fermionen werden beschrieben durch den Austausch von Eichbosonen, die an die Teilchen mit entsprechender Ladung koppeln. Gemäß dieser Ladungen können die zwölf Fermionen weiter in sechs Quarks und sechs Leptonen unterteilt werden. Dabei nehmen Quarks an allen drei Standardmodellwechselwirkungen teil, d. h. an der elektromagnetischen, der schwachen und der starken Wechselwirkung. Leptonen andererseits nehmen nur an der schwachen Wechselwirkung teil, beziehungsweise die elektrisch geladenen Leptonen zudem an der elektromagnetischen. Als Austauschteilchen stehen im Standardmodell Photonen, W- und Z-Bosonen sowie Gluonen zur Verfügung. Darüber hinaus sagt das Standardmodell ein skalares Boson vorher, das Higgs-Boson, was jedoch bislang nicht experimentell beobachtet werden konnte.

Das schwerste unter den fundamentalen Fermionen ist das Top-Quark, das erstmals im Jahr 1995 von den Experimenten CDF und DØ am Tevatron-Ringbeschleuniger des Fermilab in der Nähe von Chicago nachgewiesen werden konnte [1, 2]. Mit einer Masse von $m_t = 173.3 \pm 1.1\ \mathrm{GeV}/c^2$ [3] ist es etwa so schwer wie der Kern eines Goldatoms und rund 40 mal schwerer als das nächst leichtere Fermion, das Bottom-Quark. Aufgrund dieser großen Ruhemasse treten im Bereich der Top-Quark Physik Phänomene auf, die in dieser Art bei leichteren Quarks nicht beobachtbar sind. So treten alle leichteren Quarks in gebundenen Systemen aus Quark-Antiquark-Paaren oder in Kombinationen aus drei Quarks auf. Top-Quarks dagegen zerfallen mit einer mittleren Lebensdauer von $\tau_t = 4.2 \cdot 10^{-25}$ s [4] bevor sich derartige gebundene Systemen ausbilden können.

Die uns umgebende gewöhnliche Materie besteht ausschließlich aus den zwei leichtesten Quarks, dem Up- und dem Down-Quark. Top-Quarks hingegen können lediglich durch die Kollision hochenergetischer Teilchen erzeugt werden, z. B. bei der Kollision von Teilchen aus der kosmischen Strahlung mit Molekülen in der Atmosphäre, oder unter Laborbedingungen in Kollisionsexperimenten. Für die Erzeugung von Top-Quarks sagt das Standardmodell zwei Mechanismen vorher, zum einen die Produktion von Top-Antitop-Quark-Paaren über die starke Wechselwirkung, zum anderen die elektroschwache Produktion einzelner Top-Quarks. Während die Paarproduktion 1995 zur Entdeckung des

Top-Quarks führte, gelang der Nachweis der elektroschwachen Top-Quark-Erzeugung erst 2009 [5–7], wiederum durch die Experimente CDF und DØ. Top-Quarks zerfallen dann, mit einem Verzweigungsverhältnis von fast 100%, über die elektroschwache Wechselwirkung in ein Bottom-Quark und ein W-Boson. Die $t\bar{t}$-Ereignisse lassen sich entsprechend dem Zerfall der W-Bosonen kategorisieren. Zerfallen beide W-Bosonen hadronisch in ein Quark-Antiquark-Paar bzw. leptonisch in ein geladenes Lepton und das zugehörige Neutrino, so spricht man vom vollhadronischen bzw. vom dileptonischen Kanal. In Prozessen mit einem leptonischen und einem hadronischen W-Boson-Zerfall hingegen spricht man vom semileptonischen Zerfallskanal. Die hier vorgestellte Analyse konzentriert sich auf den semileptonischen Myonkanal, in dem das eine W-Boson in ein Quark-Antiquark-Paar, das andere in ein Myon und ein Myonneutrino zerfällt.

Bis Anfang letzten Jahres war es allein dem Tevatron-Ringbeschleuniger des Fermilab vorbehalten Top-Quarks unter Laborbedingungen zu erzeugen. Hierfür stehen Proton-Antiproton-Kollisionen bei einer Schwerpunktsenergie von $\sqrt{s} = 1.96\,\text{TeV}$ zur Verfügung. Mit Inbetriebnahme des Large Hadron Collider (LHC) des CERN in der Nähe von Genf, ist es nun auch in Europa möglich, Top-Quarks zu erzeugen. Der LHC ist ein Proton-Proton-Ringbeschleuniger, der 2010 bei einer Schwerpunktsenergie von 7 TeV betrieben wurde. Theoretische Berechnungen für diese Schwerpunktsenergie ergeben einen Wirkungsquerschnitt von $\sigma_{t\bar{t}}^{\text{theo}} = 164.6^{+11.4}_{-15.7}$ pb [8–10] für die Erzeugung von Top-Antitop-Quark-Paaren.

Mit dem Compact Muon Solenoid (CMS) Detektor, der sich in einer Untergrundkaverne etwa 100 Meter unter der Erdoberfläche in Cessy, Frankreich, befindet, lassen sich die Proton-Proton-Kollisionen des LHC beobachten und analysieren. Das CMS-Experiment weist den hierfür üblichen zwiebelschalenförmigen Aufbau eines Kolliderdetektors auf, der schematisch in Abbildung I dargestellt ist. Dabei sind zunächst radialsymmetrisch um den Wechselwirkungspunkt Spurdetektoren aufgebaut, die zur Rekonstruktion der Spuren geladener Teilchen dienen. Die Spurrekonstruktionsdetektoren werden hermetisch eingeschlossen von den elektromagnetischen und hadronischen Kalorimetern, die der Energiemessung von elektromagnetisch und stark wechselwirkenden Teilchen dienen, wobei letztere als Hadronen bezeichnet werden. Wie bereits der Name suggeriert, handelt es sich beim CMS-Detektor um ein sehr kompaktes Instrument, d. h. alle bisher beschriebenen Detektorkomponenten befinden sich innerhalb einer supraleitenden Solenoidspule, die ein Magnetfeld von etwa 3.8 T zur Verfügung stellt, und somit die Impulsmessung geladener Teilchen im Spurrekonstruktionsdetektor ermöglicht. Die einzigen experimentell direkt beobachtbaren Teilchen, die diesen inneren Detektorteil verlassen können, sind minimalionisierende Myonen. Zu deren Nachweis sind außerhalb der Solenoidspule weitere Spurrekonstruktionsdetektoren angebracht, die zusammengefasst als Myonsystem bezeichnet werden. Insgesamt weist der CMS-Detektor einen Durchmesser von etwa 15 m, eine Länge von etwa 22 m und ein Gesamtgewicht von rund 12.500 t auf. Im Jahr 2010 konnten mit dem CMS-Detektor Proton-Proton-Kollisionsereignisse aufgezeichnet werden, die einer Datenmenge von $L = (36.1 \pm 4.0)\ \text{pb}^{-1}$ [11] entsprechen, und nun den Physikanalysen zur Verfügung stehen. Ziel dieser Arbeit war es, die Erzeugung von Top-Quarks in den Daten des CMS-Experiments nachzuweisen und eine erste Messung des Wirkungsquerschnitts für die $t\bar{t}$-Produktion vorzunehmen.

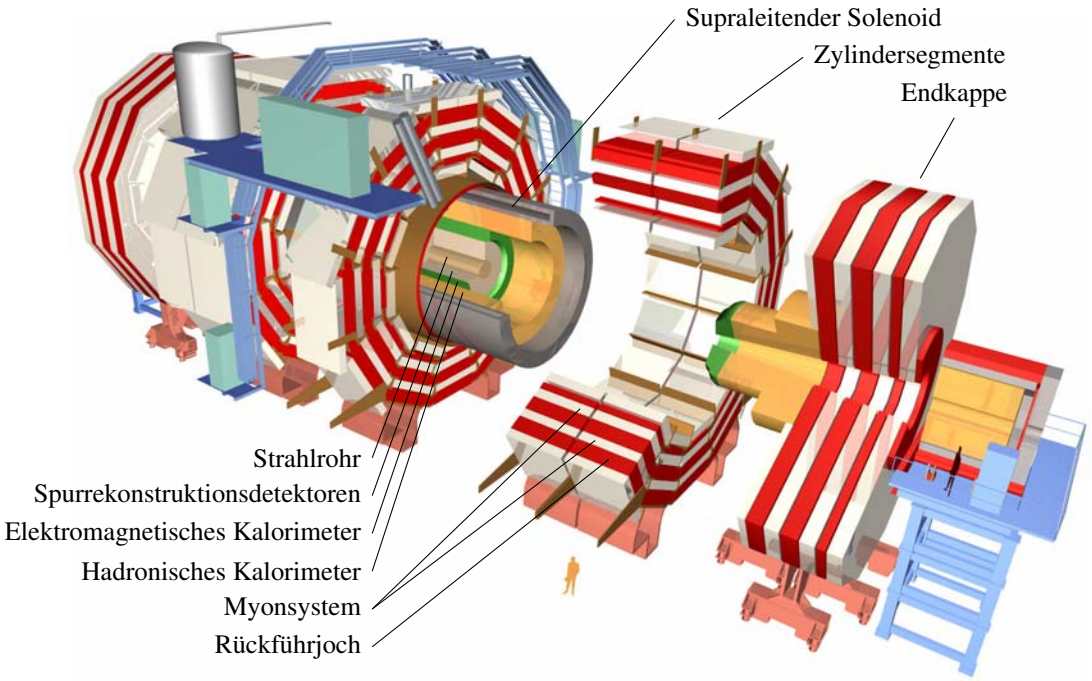

Abbildung I: Schematische Darstellung des Compact Muon Solenoid Detektors mit dem für Kolliderexperimente typischen zwiebelschalenförmigen Aufbau und der Zylinder- und Endkappenstruktur zur maximalen räumlichen Abdeckung [12].

Der Wirkungsquerschnitt der Top-Antitop-Quark-Paarerzeugung liegt etwa neun Größenordnungen unter dem inelastischen pp-Wirkungsquerschnitt. Zudem ist die experimentelle Signatur eines hochenergetischen Myons, fehlender Transversalenergie, die auf das nicht direkt experimentell beobachtbare Neutrino hinweist, und vier Jets nicht allein $t\bar{t}$-Myon+Jets-Ereignissen vorbehalten. Verschiedene andere Standardmodellprozesse weisen eine ähnliche Signatur auf und können dadurch irrtümlicherweise als Signalereignisse klassifiziert werden. Man verwendet daher Monte-Carlo-Methoden um $t\bar{t}$-Signal- und Untergrundprozesse zu simulieren. Basierend auf diesen simulierten Kollisionsereignissen wurde im Rahmen dieser Arbeit eine Ereignisselektion entwickelt, um ein gutes Verhältnis zwischen Signal- und Untergrundbeiträgen zu erhalten. Hierbei wurden Selektionskriterien auf genau ein wohlidentifiziertes und isoliertes Myon, die Abwesenheit weiterer Lepton-Kandidaten und das Auftreten von exakt drei beziehungsweise mindestens vier Jets pro Ereignis angewendet. Auf ein dediziertes Selektionskriterium die fehlende Transversalenergie betreffend wurde verzichtet, um dieser Observablen eine andere, zentralere Rolle in der Analyse zuzuweisen.

Basierend auf der Simulation von $t\bar{t}$-Signal- und den erwarteten Untergrundprozessen, konnten zunächst die Akzeptanz des CMS-Detektors sowie die Effizienz der Ereignisselektion abgeschätzt werden. Um die Abhängigkeit von diesen simulationsbasierten Erwartungen zu minimieren, wurden datenbasierte Techniken verwendet, die eine Korrektur der Trigger- und Lepton-Selektionseffizienzen ermöglicht. Hierfür bedient man sich der sogenannten Tag-And-Probe (T&P) Methode, die unter Verwendung von $Z \to \mu\mu$ Ereignissen die Bestimmung dieser Effizienzen erlaubt. Vergleicht man nun die Effizienzen, die mittels T&P-Methode in Daten und in simulierten Z+Jets Ereignissen bestimmt wurden, so

kann eine Korrektur der rein simulationsbasierten Effizienzen vorgenommen werden. Unter Berücksichtigung dieser Korrekturen erwartet man für die verwendete Ereignisselektion von mindestens vier (genau drei) Jets pro Ereignis rund 220 (204) $t\bar{t}$-Signalereignisse und etwa 146 (388) Untergrundereignisse in einem Datensatz von 36.1 pb^{-1}. Das erwartet Verhältnis von Signal- und Untergrundbeiträgen ergibt sich somit zu $S/B = 1.5$ (0.3) in Ereignissen mit mindestens vier (genau drei) Jets. Der Vergleich von beobachteten und erwarteten Ereigniszahlen jedoch weist eine Abweichung von bis zu 20% auf, die aufgrund eines Vergleichs kinematischer Verteilungen durch eine Unterschätzung von Untergrundbeiträgen begründet wurde.

Zur Bestimmung des $t\bar{t}$-Signalanteils in den aufgezeichneten Kollisionsereignissen, wurde eine Maximum-Likelihood-Methode verwendet. Dieses statistische Verfahren wurde auch von den Experimenten am Tevatron eingesetzt und ermöglichte so die Entdeckung des Top-Quarks 1995. Um die Maximum-Likelihood-Methode anwenden zu können, benötigt man geeignete Observablen, die eine Trennung von Signal- und Untergrundbeiträgen erlauben, sowie Modelle um die Verteilungen dieser Observablen adäquat zu beschreiben. Zum einen wurde hierfür die fehlende Transversalenergie ($\not{E}_{\mathrm{T}}$) ausgewählt, deren Verteilung für Ereignisse mit genau drei Jets in Abbildung II (a) dargestellt ist. Aufgrund des Neutrinos im Endzustand der $t\bar{t}$-Paarerzeugung erwartet man einen signifikanten Beitrag zur fehlenden Transversalenergie. In Prozessen ohne leptonische W-Boson-Zerfälle im Endzustand hingegen erwartet man im Mittel weniger fehlende Transversalenergie, beispielsweise in der Produktion von Z-Bosonen in Assoziation mit Jets, oder auch in QCD-Multijet-Ereignissen. Als zweite Observable wurde M3 definiert als invariante Masse der drei Jets, die vektoriell addiert den höchsten Transversalimpuls aufweisen. Aus einfachen geometrischen Überlegungen erkennt man, dass die Jets aus dem hadronisch zerfallenden Top-Quark typischerweise räumlich sehr dicht beieinander liegen, was einen Zusammenhang zwischen der Masse des hadronisch-zerfallenden Top-Quarks und M3 nahe legt. Die Sensitivität von M3 auf die $t\bar{t}$-Erzeugung wird in Abbildung II (b) für Ereignisse mit mindestens vier Jets deutlich. Während sich die $t\bar{t}$-Signalereignisse bevorzugt im Bereich der Top-Quark-Masse anhäufen, weisen die erwarteten Untergrundprozesse eher breitere Verteilungen auf. Zur Beschreibung der beobachteten $\not{E}_{\mathrm{T}}$- und M3-Verteilungen dienen Modelle, die größtenteils auf Monte-Carlo-Simulationen basieren, sowie ein datenbasiertes Modell zur Beschreibung der Verteilungen von QCD-Multijet-Ereignissen. Letzteres wurde entwickelt, da die Simulation dieser Untergrundprozesse als besonders unzuverlässig gilt. Verwendet man modifizierte Selektionskriterien, so erhält man Kollisionsereignisse in einem QCD-angereicherten Seitenband und somit eine Modellierung der $\not{E}_{\mathrm{T}}$- und M3-Verteilungen für QCD-Multijet-Ereignisse in der Signalregion. Aus der Anpassung der Modelle an die beobachteten $\not{E}_{\mathrm{T}}$- und M3-Verteilungen in pp-Kollisionsereignissen kann nun der Anteil der $t\bar{t}$-Signal- und der Untergrundereignisse ermittelt werden. Dabei gilt es systematische Unsicherheiten zu berücksichtigen, welche die erwarteten Ereigniszahlen und die Form der $\not{E}_{\mathrm{T}}$- und M3-Verteilungen beeinflussen können. Mögliche Quellen systematischer Unsicherheiten stellen dabei einerseits die zur Ereignissimulation verwendeten theoretischen Modelle dar, andererseits können experimentelle Unsicherheiten, wie beispielsweise die Unsicherheit auf die Jet-Energieskala, zu systematischen Unsicherheiten führen. Um den Einfluss dieser systematischen Unsicherheiten zu evaluieren, wurden sogenannte prior-predictive Ensembles verwendet.

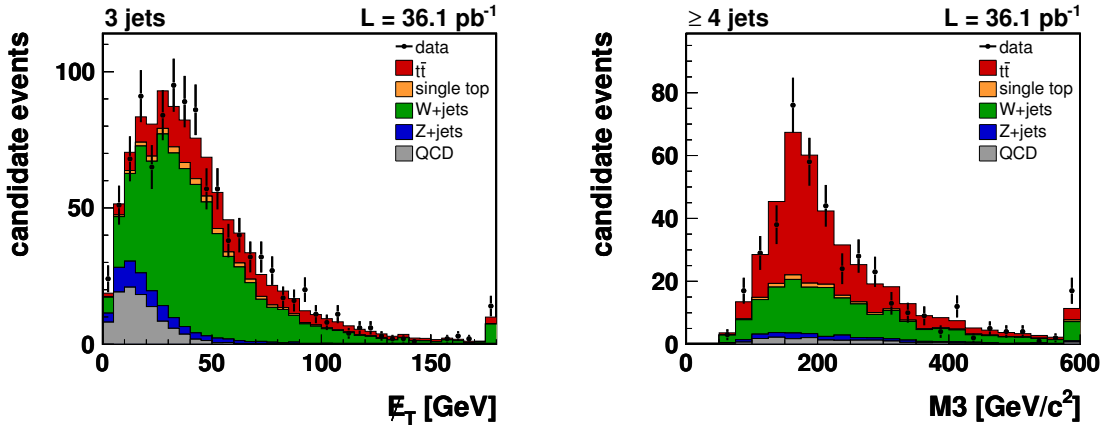

(a) (b)

Abbildung II: Vergleich der beobachteten und erwarteten Verteilungen der fehlenden Transversalenergie (a) und M3 (b), normiert auf die Signal- und Untergrundbeiträge, die auf einer Anpassung der Modelle an die beobachteten $\not\!\!E_{\mathrm{T}}$- und M3-Verteilungen beruhen. Man erkennt eine sehr gute Übereinstimmung der beobachteten und erwarteten Verteilungen.

Der formale Nachweis für die Erzeugung von Top-Quarks über die starke Wechselwirkung wird durch einen Hypothesentest erbracht, in dem die Wahrscheinlichkeit für eine möglicherweise irrtümliche Beobachtung der Top-Antitop-Quark-Paarerzeugung ermittelt wird, die lediglich auf einer Fluktuation von Untergrundbeiträgen beruhen würde. Hierzu bedient man sich der Hypothesen H_0 und H_1, wobei die Hypothese H_0 besagt, dass es ausschließlich Untergrundbeiträge gibt, die Hypothese H_1 hingegen berücksichtigt sowohl Signal- als auch Untergrundbeiträge. Zur Unterscheidung dieser zwei Hypothesen definiert man ein Likelihood-Verhältnis Q, dass nach dem Neyman-Pearson Lemma [13] als sensitivste Observable zur Trennung zweier Hypothesen gilt. Um nun die Signifikanz für die Beobachtung der Top-Antitop-Quark-Paarerzeugung zu bestimmen, generiert man Pseudodaten-Verteilungen für $\not\!\!E_{\mathrm{T}}$ und M3 gemäß einer Datenmenge von 36.1 pb^{-1} unter der Hypothese H_0, und erhält so die in Abbildung III blau dargestellte Verteilung. Der Vergleich des experimentell beobachteten Wert $\widehat{Q}_{\mathrm{obs}}$ mit dieser generierten Q-Wert-Verteilung, ermöglicht nun die Bestimmung der Signifikanz. Eine kleiner Wert, z. B. $\widehat{Q} = 0$, entspricht dabei eher der Untergrund-Hypothese H_0, ein hoher Wert andererseits favorisiert eher die Hypothese H_1. Zudem führt man Pseudoexperimente unter der Hypothese H_1 durch, um über den Median $\widehat{Q}_{\mathrm{exp}}$ der entsprechenden Q-Wert-Verteilung eine erwartete Signifikanz zu bestimmen. Vom Nachweis eines erwarteten Prozesses spricht man, wenn der beobachtete Q-Wert mindestens fünf Standardabweichungen von der reinen Untergrund-Hypothese entfernt liegt. Dieser Q-Wert ist in Abbildung III durch eine vertikale gelbe Linie angedeutet. Der experimentell beobachtete Wert $\widehat{Q}_{\mathrm{obs}}$ in pp-Kollisionsereignissen, sowie der erwartete Wert $\widehat{Q}_{\mathrm{exp}}$, liegen weit oberhalb dieser unteren Grenze. Mit einer Signifikanz von mehr als 6.13σ konnte somit, für eine Datenmenge von $L = (36.1 \pm 4.0)$ pb^{-1}, der Nachweis für die Top-Quark-Paarerzeugung am CMS-Experiment durch die hier vorgestellte Analyse erbracht werden.

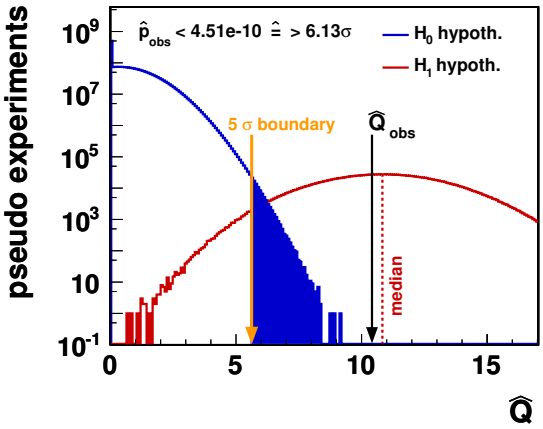

Abbildung III: Experimentell beobachteter Wert $\widehat{Q}_{\text{obs}}$ und erwartete Q-Wert-Verteilungen unter der Hypothese H_0 (blau) und unter der Hypothese H_1 (rot), für die jeweils statistische sowie systematische Unsicherheiten berücksichtigt wurden. Die untere Grenze für den Nachweis der Top-Quark-Paarerzeugung, d. h. ein Signifikanzniveau von 5σ, ist durch die vertikale gelbe Linie angedeutet. Für den beobachteten Wert $\widehat{Q}_{\text{obs}} = 10.45$, berechnet sich eine Signifikanz von mehr als 6.13σ. Somit konnte die Top-Antitop-Quark-Paarerzeugung in einer Datenmenge von $L = (36.1 \pm 4.0)\ \text{pb}^{-1}$ nachgewiesen werden.

Der erfolgreiche Nachweis der Top-Quark-Paarerzeugung erlaubt nun die Messung des $t\bar{t}$-Produktionswirkungsquerschnitts, der wiederum die Bestimmung des $t\bar{t}$-Signalbeitrags mittels Maximum-Likelihood-Methode zugrunde liegt. Um zudem statistische sowie systematische Unsicherheiten zu ermitteln, verwendet man eine Neyman-Konstruktion zur Bestimmung zentraler Konfidenzintervalle mit der Maximum-Likelihood-Abschätzung des Signalparameters als Teststatistik. Zum einfacheren Vergleich mit der theoretischen Vorhersage wurde der Parameter $\beta_{t\bar{t}}$ definiert als Verhältnis der beobachteten und erwarteten $t\bar{t}$-Signalanzahlen, welches gerade dem Verhältnis des beobachteten und theoretisch vorhergesagten Wirkungsquerschnitts, $\beta_{t\bar{t}} = \sigma_{t\bar{t}}^{\text{obs}} / \sigma_{t\bar{t}}^{\text{theo}}$, für die Top-Antitop-Quark-Paarerzeugung entspricht. Generiert man nun unter der Annahme verschiedener $t\bar{t}$-Erzeugungswirkungsquerschnitte Pseudodaten-Verteilungen für die fehlende Transversalenergie und M3 und ermittelt für jedes dieser Pseudoexperimente einen Wert für den Signalparameter $\beta_{t\bar{t}}$, so erhält man die in Abbildung IV dargestellte Neyman-Konstruktion. Der gemessene Wert $\hat{\beta}_{t\bar{t}}^{\text{obs}} = 1.03$ des Signalparameters, kann nun verwendet werden, um den Wirkungsquerschnitt nebst experimentellen Unsicherheiten zu bestimmen. Dies ist in Abbildung IV durch die Schnittpunkte der horizontale rote Linie mit den Zentralwerten und den Grenzen des 68% Konfidenzgürtels angedeutet und ergibt einen zugehörigen wahren Wert für den Parameter von $\hat{\beta}_{t\bar{t}}^{\text{true}} = 1.03$ und eine experimentelle Unsicherheit von etwa $(20 - 25)\%$. Daraus ergibt sich für den Wirkungsquerschnitt der Top-Antitop-Quark-Paarerzeugung bei einer Schwerpunktsenergie von 7 TeV und einer angenommenen Top-Quark-Masse von $172.5\ \text{GeV}/c^2$ ein Wert von

$$\sigma_{t\bar{t}}^{\text{obs}} = 169^{+42}_{-33}\,(\text{stat.+syst.}) \pm 19\,(\text{lumi.})\ \ \text{pb},$$

der sehr gut mit der theoretischen Vorhersage von $\sigma_{t\bar{t}}^{\text{theo}} = 164.6^{+11.4}_{-15.7}$ pb übereinstimmt.

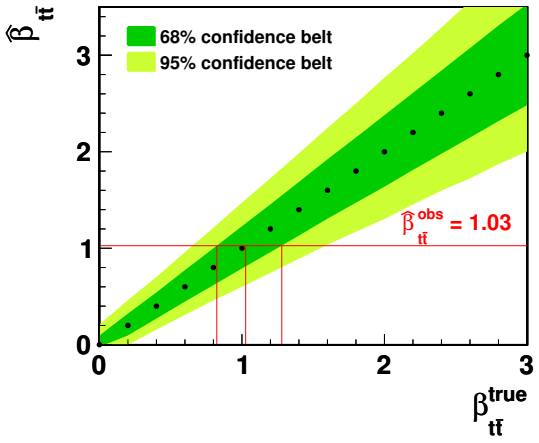

Abbildung IV: Neyman-Konstruktion zur Bestimmung des $t\bar{t}$-Produktionswirkungsquerschnitts. Durch Auswertung der Neyman-Konstruktion bei $\hat{\beta}^{\text{obs}}_{t\bar{t}} = 1.03$ kann der Zentralwert sowie die kombinierte statistische und systematische Unsicherheit ermittelt werden. Dies liefert einen zugehörigen wahren Wert von $\beta^{\text{true}}_{t\bar{t}} = 1.03$ und Unsicherheiten von -19.7% und $+24.7\%$, die zur Berechnung des Produktionswirkungsquerschnitts verwendet werden.

Basierend auf Pseudoexperimenten konnte zudem eine Abschätzung für die rein statistische Unsicherheit auf den beobachteten Wirkungsquerschnitt von etwa 11% bestimmt werden. Somit ist die Messung des Wirkungsquerschnitts bereits nach einem Jahr der Datennahme mit dem CMS-Experiment durch systematische Unsicherheiten dominiert, wobei der Hauptbeitrag auf die Unsicherheiten in der Bestimmung der Jet-Energieskala zurückzuführen ist. Um die Präzision dieser Wirkungsquerschnittsmessung zu erhöhen, könnte man nun einerseits versuchen die Quelle dieser systematischen Unsicherheit zu verringern. Andererseits könnte man eine alternative Analysemethode verwenden, z. B. eine simultane Messung von $\sigma_{t\bar{t}}$ und der Jet-Energieskala durchführen.

Die hier vorgestellte Messung des $t\bar{t}$-Produktionswirkungsquerschnitts im $t\bar{t}$-Myon+Jets-Kanal kann zudem mit den entsprechenden Ergebnissen für den dileptonischen Kanal [14], den Elektron+Jets-Kanal [15], und der simultanen Messung im Lepton+Jets-Kanal [15] verglichen werden, wobei sich der Terminus Lepton auf Elektronen und Myonen bezieht. Diese drei Messungen ergeben für den $t\bar{t}$-Produktionswirkungsquerschnitt

$$\begin{aligned}
\sigma^{\text{dilepton}}_{t\bar{t}} &= 194 \pm 76\,(\text{stat.+syst.}) \pm 21\,(\text{lumi.})\ \text{pb},\\
\sigma^{e+\text{jets}}_{t\bar{t}} &= 178^{+45}_{-37}\,(\text{stat.+syst.}) \pm 20\,(\text{lumi.})\ \text{pb},\\
\sigma^{l+\text{jets}}_{t\bar{t}} &= 172^{+39}_{-32}\,(\text{stat.+syst.}) \pm 19\,(\text{lumi.})\ \text{pb},
\end{aligned}$$

wobei das Ergebnis im dileptonischen Kanal auf einer Datenmenge von 3.1 pb^{-1} beruht, während die Messungen in den Lepton+Jets-Kanälen auf der gesamten Datenmenge von 36.1 pb^{-1} durchgeführt wurden. Aufgrund einer etwas konservativeren Abschätzung der Unsicherheit für die Jet-Energieskala ist die Unsicherheit auf $\sigma_{t\bar{t}}$ in den Lepton+Jets-Kanälen geringfügig größer als das Ergebnis, das im Rahmen der hier vorgestellten Analyse erarbeitet wurde. Darüber hinaus wurde kürzlich von der ATLAS Kollaboration eine Messung des Wirkungsquerschnitts von $\sigma^{\text{ATLAS}}_{t\bar{t}} = 145 \pm 31\,(\text{stat.})\,^{+42}_{-27}\,(\text{syst.})$ pb [16]

veröffentlicht, die auf einer Kombination der Resultate des Elektron+Jets-, Myon+Jets- und des dileptonischen Kanals beruht und der eine Datenmenge von $L = 2.9\ \text{pb}^{-1}$ zugrunde liegt. Im Gegensatz zu den oben genannten Ergebnissen beinhaltet die hier gezeigte systematische Unsicherheit auch die Unsicherheit von 11% auf die integrierte Luminosität. Insgesamt stimmen somit die Ergebnisse in den verschiedenen Kanälen, das Ergebnis der ATLAS Kollaboration, und das in dieser Arbeit gewonnene Resultat innerhalb der Unsicherheiten gut miteinander überein.

Bereits ein Jahr nach der Inbetriebnahme des Large Hadron Collider bei einer Schwerpunktsenergie von 7 TeV konnte die Erzeugung von Top-Quarks nachgewiesen und eine erste Messung des $t\bar{t}$-Produktionswirkungsquerschnitts durchgeführt werden. Diese grundlegende Analyse ermöglicht nun weiterführende Untersuchungen, beispielsweise die Messung der Top-Quark-Masse [17], darüber hinaus ist die Suche nach Physik jenseits des Standardmodells [18] denkbar. Somit läßt dieser erste Schritt auf dem Gebiet der Top-Quark-Physik hoffen auf viele neue Erkenntnisse über die Eigenschaften und Wechselwirkungen des schwersten Fermions im Standardmodell der Teilchenphysik.

Observation of Top Quarks and First Measurement of the $t\bar{t}$ Production Cross Section at a Centre-Of-Mass Energy of 7 TeV with the CMS Experiment at the LHC

Zur Erlangung des akademischen Grades eines
DOKTORS DER NATURWISSENSCHAFTEN
von der Fakultät für Physik des
Karlsruher Institut für Technologie (KIT)

genehmigte

Dissertation

von

Dipl.-Phys. Jasmin Gruschke
aus Schönau im Schwarzwald

Tag der mündlichen Prüfung: 04.02.2011

Referent: Prof. Dr. Th. Müller, Institut für Experimentelle Kernphysik,
Karlsruher Institut für Technologie (KIT)

Korreferent: Prof. Dr. G. Quast, Institut für Experimentelle Kernphysik,
Karlsruher Institut für Technologie (KIT)

“Dass ich nicht mehr, mit sauerm Schweiß,
Zu sagen brauche was ich nicht weiß;
Dass ich erkenne was die Welt
Im Innersten zusammenhält,”

[Faust, Der Tragödie Erster Teil,
J. W. Goethe, 1808]

Introduction

Like the fictional Doctor Faustus, particle physicists devote themselves to the understanding of the elementary building blocks of matter and the nature of the forces acting between them. Over the last six decades, great success has been made on this field as a result of a fruitful interplay between improved experimental techniques and ingenious theoretical insights which enabled a comprehensive description of the observed phenomena. In the early seventies, the Standard Model (SM) of elementary particle physics was derived, summing up our current understanding of the particles composing all matter and their interactions. According to this theory, the fundamental fermions, namely six flavours of quarks and leptons, respectively, interact via the exchange of force-mediating bosons which couple to the charges of the fermions. Since its formulation, the Standard Model has been subject to a large number of experimental tests and highest-precision data which collectively confirmed its predictions.

One major success for the predictive power of the Standard Model was the experimental observation of the top quark in 1995 [1, 2]. With an exceptionally large mass of $m_t = (173.3 \pm 1.1)\,\mathrm{GeV}/c^2$ [3], the top quark is nearly as massive as a gold nucleus and outweighs the next-heaviest fermion, the b quark, by about a factor of 40. This characteristic property implies that top quarks on average decay before top-flavoured hadrons can be formed, offering a unique possibility to study quasi-free quarks. The Standard Model predicts two mechanisms for the production of top quarks, either in pairs of top and anti-top quarks via the strong interaction or singly in charged-current weak interactions. While the pairwise production led to its discovery in 1995, the second production mechanism was experimentally observed only about two years ago [5–7]. Once produced, top quarks almost exclusively decay via the weak interaction into a b quark and a W boson.

While all ordinary matter is composed of the two lightest quarks, the up and down quarks, the four heavier quark flavours only appear in collisions of high-energy particles. Therefore, their production under laboratory conditions requires modern particle-accelerator and collider facilities. Until last year, only the Fermilab Tevatron collider near Chicago, USA, provided sufficient centre-of-mass energy for the production of top quarks and thus paved the way for its discovery about sixteen years ago. Since the Tevatron was built, substantial technological progress in the intervening years has enabled the design and construction of the Large Hadron Collider (LHC) of the European Organisation for Nuclear Research (CERN) near Geneva, Switzerland. Extensively using superconducting magnets, the LHC provides hitherto unachievable centre-of-mass energies for the production of heavy particles in proton-proton collisions. After long design and construction

phases, the first pp collisions at a centre-of-mass energy of $\sqrt{s} = 7$ TeV were achieved on March 30$^{\text{th}}$ 2010, turning the LHC to the most powerful collider ever operated. Given this huge centre-of-mass energy and instantaneous luminosity, the LHC can be considered a top quark factory and will thus facilitate scrutiny of top quark properties and interactions.

The two general-purpose detectors ATLAS and CMS have been built to detect and analyse pp collisions provided by the Large Hadron Collider. Driven by the intention to exploit the full discovery potential of the LHC, the designs of ATLAS and CMS concentrated on the discovery of the as yet unobserved Higgs boson, which constitutes the last particle predicted by the Standard Model, and on the search for experimental evidences of phenomena predicted by extensions of the Standard Model. The CMS apparatus is located near Cessy, France, in an underground cavern about 100 m below surface. Since the first pp collision event recorded by the CMS apparatus, a data set corresponding to an integrated luminosity of $L = (36.1 \pm 4.0)$ pb^{-1} [11] was acquired with a fully-operational detector until November 2010.

Due to the extremely short lifetime of top quarks, only its decay products can be experimentally observed. Therefore, electronic signals recorded by the CMS apparatus are subjected to reconstruction algorithms which aim for the detailed extraction of information available on the interactions occurred in pp collision events. Simulations further serve for the comparison of these reconstructed events with expectations based on theoretical and phenomenological models. Given these simulated samples of signal and background events, criteria for the selection of candidate events can be chosen, driven by the requirement for a good signal-to-background ratio while maintaining high signal selection efficiency. Moreover, analysis strategies can be developed and their expected performance tested, prior to their application to observed pp collision data.

Based on the early data set provided by the CMS collaboration, and employing all the techniques mentioned above, the analysis presented in this thesis is dedicated to the search for top quarks at the LHC and to perform a first measurement of the top quark pair production cross section at a centre-of-mass energy of 7 TeV.

Contents

Chapter 1

The Top Quark in the Standard Model

The traditional goal of elementary particle physics has been to identify the structureless units of matter and to understand the nature of the forces acting between them. The most complete model currently known for the description of these smallest constituents and their interactions is the Standard Model (SM) of elementary particle physics. Since its formulation in the 1960s and 1970s, the Standard Model has undergone and successfully passed a large number of experimental tests. Therefore, despite some remaining open questions, it hitherto constitutes the most accurate theory tested with highest precision data. One important proof for the predictive power of this elegant mathematical formalism was the observation of the top quark about sixteen years ago. Being the heaviest elementary particle observed to date, the top quark is of particular interest for scrutinising the Standard Model and serves as a probe for possible new phenomena beyond it.

1.1. The Standard Model of Elementary Particle Physics

1.1.1. Phenomenological Introduction

The Standard Model of elementary particle physics [19–31] predicts point-like and structureless particles to be the building blocks of matter. Quantum numbers like the electric charge Q can be used to categorise these elementary fermions carrying spin $1/2\ \hbar$. Due to their fermionic nature, they obey the Fermi-Dirac statistics and are subject to the Pauli exclusion principle, which states that two fermions cannot share the same quantum state. For each elementary particle exists a corresponding anti-particle, which exhibits the same properties like mass, spin, and lifetime but has opposite quantum numbers. The fundamental fermions can further be classified as quarks and leptons. In total, the SM predicts six types of quarks and leptons, which can be arranged in three generations as shown in table 1.1. Each generation consists of an up-type quark, a down-type quark, a charged lepton and the corresponding neutrino. While the particles of the first generation constitute the building blocks of all ordinary matter, fermions of the second and third generation appear solely in high-energetic interactions like collider experiments or the interaction of cosmic rays with the earth's atmosphere. The kinetic energies of colliding particles thereby facilitate the production of heavier fermions, which subsequently decay into the lighter fermions of the first generation.

Among the six leptons are the three electrically charged leptons, the electron e^-, the muon μ^-, and the tau τ^- and their corresponding electric charge-neutral neutrinos, the electron neutrino ν_e, the muon neutrino ν_μ, and the tau neutrino ν_τ. The Standard Model postulates neutrinos to be strictly massless, however, several observations [32–36]indicate that neutrinos do have non-vanishing masses. To account for these results, possible extensions of the Standard Model are required [37, 38].

Table 1.1: The three Standard Model fermion generations, each comprising an up-type quark, a down-type quark, a charged lepton, and the corresponding neutrino. Electric charges are given in units of the elementary charge $e = 1.602176487(40) \times 10^{-19}$ C [4]. As the fermion masses are not predicted by the Standard Model, the given values are obtained from experimental measurements summarised in [4], except for the mass of the top quark, which is adapted from [3].

	Generation	Flavour	Symbol	Charge [e]	Mass $\left[\mathrm{MeV}/c^2\right]$
Leptons	1	electron	e	-1	0.511
		electron neutrino	ν_e	0	$< 2 \cdot 10^{-6}$
	2	muon	μ	-1	105.658
		muon neutrino	ν_μ	0	< 0.190
	3	tau	τ	-1	1776.82 ± 0.16
		tau neutrino	ν_τ	0	< 18.2
Quarks	1	up	u	$2/3$	$(1.7 - 3.3)$
		down	d	$-1/3$	$(4.1 - 5.8)$
	2	charm	c	$2/3$	$\left(1.27^{+0.07}_{-0.09}\right) \cdot 10^3$
		strange	s	$-1/3$	101^{+29}_{-21}
	3	top	t	$2/3$	$(173.3 \pm 1.1) \cdot 10^3$
		bottom	b	$-1/3$	$\left(4.19^{+0.18}_{-0.06}\right) \cdot 10^3$

Besides the leptons, the Standard Model predicts six different flavours of quarks, up (u), down (d), charm (c), strange (s), top (t), and bottom (b). In contrast to leptons, quarks carry fractional electric charge of either $+2/3$ (up-type quarks: u, c, t) or $-1/3$ (down-type quarks: d, s, b) of the elementary charge $e = 1.602176487(40) \times 10^{-19}$ C [4]. Furthermore, quarks cannot exist as free particles. Rather, they are forced to form bound states collectively referred to as hadrons, which either consist of three quarks (baryons) or of a quark-antiquark pair (mesons). This special feature of the interaction between quarks is called quark confinement. The top quark constitutes an exception in this context. Due to its large mass the relevant time scale for its decay is much smaller compared to the corresponding time scale for the formation of hadrons. The top quark decay therefore offers a unique possibility to study a quasi-free quark. Section 1.2 is dedicated to a detailed discussion about the top quark and its special role in the Standard Model. Accounting for the Pauli exclusion principle, the formation of hadrons necessitates the introduction of an additional quantum number for quarks, the so-called colour [39–41], and each quark exists in one of the three different colour states, i.e. red, blue, or green. As colour is a non-observable quantum number, all hadrons are colour-neutral objects not carrying any net colour charge. Consequently, mesons consist of a quark carrying a certain colour and of an anti-quark carrying the corresponding anti-colour. For baryons consisting of three quarks the only allowed combinations are those leading to a zero net colour charge, e.g. an equal mixture of red, blue, and green.

Four fundamental forces effectuate the interactions between elementary particles, i.e. the electromagnetic, the strong, the weak, and the gravitational force. The former three can

Table 1.2: Properties of the force mediating bosons adapted from [4]. Electric charges are given in units of the positron charge e. Masses are given in units of GeV/c^2, the value for the $W^{\pm}$ boson mass is taken from [44].

Type	Symbol	Force	Electric Charge [e]	Mass $\left[\text{GeV}/c^2\right]$
gluon	g	strong	0	0
photon	γ	electromagnetic	0	0
$W^{\pm}$ boson	$W^{\pm}$	weak	± 1	80.420 ± 0.031
Z^0 boson	Z^0	weak	0	91.188 ± 0.002

be formulated as quantum gauge field theories and have therefore been successfully incorporated in the Standard Model. The gravitational force on the other hand is described by the theory of general relativity [42, 43]. Gravity is important for understanding interactions on large scales, like the formation of galaxies and solar systems, but can be neglected on sub-nuclear scales. At these scales, the interactions between elementary particles are dominated by the electromagnetic, the weak, and the strong force. Due to this extreme separation of scales on which gravity and the three SM forces are relevant, only the Standard Model forces are considered in the following discussion.

Quantised gauge fields serve for the description of the Standard Model forces. An interaction between elementary particles can be ascribed to the exchange of field quanta of the gauge fields, which can thus be interpreted as the force mediators and are called gauge bosons. In contrast to the half-integer spin fermions, gauge bosons carry spin 1 $\hbar$ and obey the Bose-Einstein statistics, which allows several bosons to occupy the same quantum state. A list of the force mediating bosons and some of their properties is given in table 1.2. Fermions carrying the appropriate charge partake in the corresponding interactions. Hence, quarks carrying electric, weak, and colour charges participate in all SM interactions. All leptons experience the weak but not the strong force. In addition to the weak force, electrically charged leptons also interact via the electromagnetic force.

Feynman diagrams like the ones depicted in figure 1.1 serve as intuitive graphical representations of the interaction between elementary particles via emission and re-absorption of gauge bosons. Moreover, these diagrams embody mathematical expressions, whereas the propagation of particles in space-time is represented by lines and couplings are depicted by vertices. Applying the associated Feynman rules, a diagram is translated into the corresponding formula. For a given process, the summation over all possible contributing Feynman graphs can then be used to calculate the transition amplitude $\mathcal{M}$ for this particular process. Finally, the transition amplitude is used to compute the corresponding cross section, which represents a measure for the probability of an interaction to occur. A more detailed discussion is given in section 1.2.1, exemplarily using top-quark production via the strong interaction in hadron-hadron collisions.

The theory of Quantum Electrodynamics (QED) [45–52] describes the interactions of electrically charged particles. The gauge boson mediating the electromagnetic force is the charge-neutral photon γ which represents the excitation of the massless photon field. This zero-mass of the gauge boson leads to an infinite range of the electromagnetic interaction. For an electrically charged fermion, the interaction strength with the force mediating photon is fully determined by the charge Q the fermion carries.

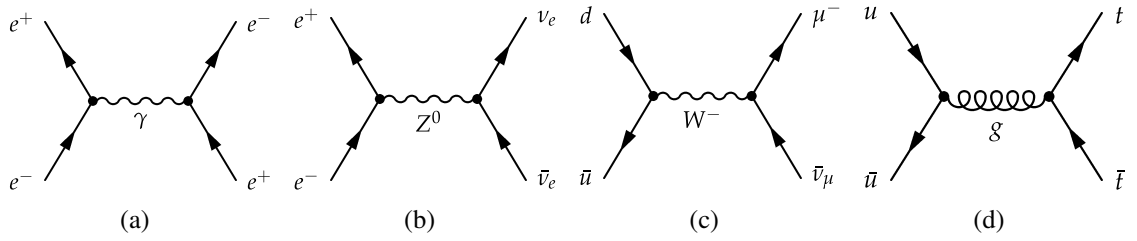

Figure 1.1: An example of leading order Feynman diagrams for typical fundamental interactions. Each diagram illustrates the annihilation of fermions into a virtual gauge boson and subsequent fermion pair-production. Electron-positron annihilation is depicted for the electromagnetic force (a) and for the weak force (b). In (c) the annihilation of quarks via the charged weak force is shown and correspondingly for the strong force in (d). This description uses the convention of time evolving from left to right.

In a similar way, the strong force between colour-charged particles is described by the theory of Quantum Chromodynamics (QCD) [28–31, 41]. Of all fermions, only the colour-charged quarks interact via this force mediated by massless gluons, the gauge bosons of the strong interaction. Similar to the electric charge in QED, the colour charge defines the strength of the interaction between quarks and gluons. As gluons are massless, an infinite range of the strong interaction could naively be expected. However, a completely different behaviour of the strong interaction is observed. For increasing energies and thus decreasing distances the coupling constant decreases, a phenomenon called asymptotic freedom. On the other hand, the strength of the strong interaction increases at large distances. This special feature is referred to as infrared slavery of quarks, forcing quarks to create colourless bound states and limiting the range of the strong interaction to very short length scales of about 10^{-15} m. In contrast to the charge-neutral photons, gluons are colour-charged themselves, each carrying one unit of colour and one unit of anti-colour. Infrared slavery and asymptotic freedom thus constitute two direct consequences of the self-interactions between colour-charged gluons.

Unlike the electromagnetic and the strong forces, the weak force is mediated by massive bosons, i.e. the charge-neutral Z^0 boson and the electrically charged $W^\pm$ bosons. Due to the large mass of the weak gauge bosons given in table 1.2, the range of the weak force is limited to sub-nuclear scales. The charge of the weak interaction to which the gauge bosons couple is called weak isospin I. The weak interaction therefore constitutes the only force in the SM affecting neutrinos, which exhibit a non-zero isospin but carry neither electric nor colour charge. Furthermore, since the eigenstates of the weak interaction are not identical with the mass eigenstates of the quarks, the weak interaction provides the possibility for flavour change via the exchange of charged $W^\pm$ bosons. The unitary transformation of mass eigenstates into flavour eigenstates can be written as a multiplication of the unitary Cabibbo-Kobayashi-Maskawa (CKM) matrix V_{CKM} [53, 54] with the mass eigenstates

$$\begin{pmatrix} d' \\ s' \\ b' \end{pmatrix} = \begin{pmatrix} V_{ud} & V_{us} & V_{ub} \\ V_{cd} & V_{cs} & V_{cb} \\ V_{td} & V_{ts} & V_{tb} \end{pmatrix} \begin{pmatrix} d \\ s \\ b \end{pmatrix} . \tag{1.1}$$

By convention the 3×3 CKM matrix operates on the mass eigenstates of the down-type quarks (d, s, b) resulting in the corresponding weak eigenstates (d', s', b'). For example, the weak partner b' of the top quark results from a linear combination of the mass eigenstates of the three down-type quarks. The coupling of two quarks q and q' to a $W^{\pm}$ boson is proportional to the corresponding CKM matrix element $V_{qq'}$. Assuming unitarity holds, the measured values for the CKM matrix elements are [4]

$$V_{\mathrm{CKM}} = \begin{pmatrix} 0.97428 \pm 0.00015 & 0.2253 \pm 0.0007 & 0.00347^{+0.00016}_{-0.00012} \\ 0.2252 \pm 0.0007 & 0.97345^{+0.00015}_{-0.00016} & 0.0410^{+0.0011}_{-0.0007} \\ 0.00862^{+0.00026}_{-0.00020} & 0.0403^{+0.0011}_{-0.0007} & 0.999152^{+0.000030}_{-0.000045} \end{pmatrix} . \tag{1.2}$$

Diagonal elements exhibit the largest values, as transitions of quarks within one generation are favoured over the transitions into quarks of other generations. For the given example, the top quark decay into a b quark is the most favoured one. Since the values of the diagonal elements are even very close to unity, transitions between two different quark generations are strongly suppressed.

Parity conservation implies the invariance of physical measurements under reversal of all spatial axes. While the electromagnetic and the strong force follow this principle, it is violated in weak interactions mediated by charged $W^{\pm}$ bosons. Particle wave functions can be decomposed into linear combinations of left-handed and right-handed components. The $W^{\pm}$ bosons couple only to the left-handed part of the fermion wave functions and to the right-handed part of anti-particle wave functions. Since the parity transformed object of a left-handed particle is a right-handed particle, this coupling of $W^{\pm}$ bosons constitutes a maximal violation of parity. In contrast, the Z^0 boson couples to both components, but with different strengths depending on the electric charge of the quark-type or lepton involved.

At low energies, there are obvious differences between the weak force with its massive $W^{\pm}$ and Z^0 bosons and the electromagnetic force mediated via massless photons. However, quantum electrodynamics itself is a unified theory of electricity and magnetism. The inclusion of another type of force therefore became conceivable. This has been accomplished in the electroweak theory [19, 20, 22, 24], which explains the electromagnetic and the weak forces as two aspects of a unified theoretical model. Four gauge fields and therewith four strictly massless gauge bosons are predicted to mediate the electroweak force. This seems to be in conflict with the massive $W^{\pm}$ and Z^0 bosons. Consequently, there has to be a mechanism for breaking the electroweak symmetry through which three of the four massless gauge bosons acquire mass while one remains massless.

The most promising description of this symmetry breaking is given by the Higgs mechanism [55–59], wherein the symmetry is broken spontaneously, leading to the occurrence of a massless Goldstone boson [60–63]. Massless gauge bosons can then acquire mass via coupling to one of the broken generators and the Goldstone boson is replaced by the missing longitudinal degree of freedom of the former massless gauge boson. While the gauge bosons of the weak interaction acquire mass, the symmetry of the electromagnetic force is preserved in the Higgs mechanism and consequently the photon remains massless. Furthermore, the masses of the charged SM fermions can be explained via so-called Yukawa interactions. Although the Higgs mechanism provides an explanation for the

fermion masses, a prediction of their values is not implicit since the Yukawa couplings enter the theory as free parameters. One major aim of the Large Hadron Collider (LHC) project is to verify this mechanism for the description of electroweak symmetry breaking. This can be accomplished, since the Higgs mechanism furthermore predicts a massive scalar spin-zero particle, the Higgs boson. As yet unobserved, the Higgs boson is the last particle predicted by the Standard Model. Its discovery would be one further major success for the Standard Model of elementary particle physics.

1.1.2. Mathematical Introduction

Behind the elementary fermions and their interactions via exchange of gauge bosons lies an elegant mathematical framework. The Standard Model is described in terms of a relativistic quantum field theory, incorporating both quantum mechanics and special relativity. The dynamics of a physical system are formulated in functions called Lagrangians. To account for the relativistic nature of the theory, the Lagrangians are required to be invariant under Lorentz transformation. Using the Hamilton principle of least action [64], the equations of motion can be obtained from the Lagrangian density $\mathcal{L}$ through a minimisation of the action S

$$\delta S = \delta \left(\int \mathcal{L} \left(\psi(x), \partial^\mu \psi(x) \right) \, d^4x \right) = 0 \,. \tag{1.3}$$

The Lagrangian density $\mathcal{L}$ depends on the particle's field wave functions $\psi(x)$ and their first derivatives $\partial^\mu \psi(x)$. In the Standard Model, fermion wave functions $\psi(x)$ are represented by Dirac spinors ψ. The Lagrange function for a spin $1/2$ particle[1] of mass m is given by

$$\mathcal{L}_{\text{Dirac}} = i\bar{\psi}\gamma^\mu \partial_\mu \psi - m\bar{\psi}\psi \,, \tag{1.4}$$

with the Dirac matrices γ^μ, the fermionic field ψ, and its adjoint field $\bar{\psi}$. Using the principle of least action leads to the Euler-Lagrange equations, which translates the Lagrangian $\mathcal{L}_{\text{Dirac}}$ into the Dirac equation [65]

$$\left(i\gamma^\mu \partial_\mu - m \right) \psi = 0 \,. \tag{1.5}$$

This equation represents the relativistic quantum mechanical wave equation for the description of an elementary spin $1/2$ particle. The four solutions of equation (1.5) include the two spin states of a fermion and the two spin states of the corresponding anti-fermion.

The Dirac Lagrangian in equation (1.4) describes the motion of an elementary fermion in the absence of any interaction. Since the absolute phase of a complex spinor ψ does not constitute a quantum mechanical observable, local phase transformations are permitted, which leave observables depending on $|\psi|^2$ invariant. An example for such a transformation U is given by

$$\psi \to \psi' = U\psi = e^{ig\epsilon_k(x)\cdot\frac{\tau_k}{2}} \psi \,, \tag{1.6}$$

with a positive real constant g and rotation parameters $\epsilon_k(x)$ in an internal space represented by the generators τ_k of a given Lie group. On the other hand, the Dirac Lagrangian

[1] So-called natural units with $\hbar = c = 1$ are applied if not explicitly stated otherwise.

$\mathcal{L}_{\text{Dirac}}$ is in general not invariant under the transformation given in equation (1.6). However, gauge invariance requires the Lagrangians in gauge theories to be invariant under a certain continuous group of local transformations. These gauge transformations form a Lie group referred to as the symmetry group or gauge group of the theory. According to the Noether theorem [66], gauge invariance of the Lagrangian entails a conserved current to which the charges of the forces correspond. Therefore, to each group generator τ_k an additional vector field called gauge field has to be introduced into the Lagrangian. The effects raised by the transformations can thus be compensated and the invariance of the Lagrangian under local group transformation is ensured. Technically, this can be done by introducing a covariant derivative via a so-called minimal substitution

$$\partial_\mu \rightarrow \mathcal{D}_\mu = \partial_\mu + ig\frac{\tau_k}{2}A_\mu^k\,, \tag{1.7}$$

with the usual space-time derivative ∂_μ and A_μ^k represents the required gauge boson fields. The constant g acquires its physical meaning as the coupling constant, which determines the universal interaction strength associated with the field. Substituting this covariant derivative into the Lagrangian in equation (1.4) leads to

$$\mathcal{L} = i\bar{\psi}\gamma^\mu\partial_\mu\psi - m\bar{\psi}\psi - g\bar{\psi}\gamma^\mu\frac{\tau_k}{2}A_\mu^k\psi\,, \tag{1.8}$$

where the last term characterises the coupling between the fermion field and the gauge fields A_μ^k. Hence, the Lagrangian comprises terms describing fermionic fields in the absence of any interaction as well as those describing the interactions between different fields. The requirement of gauge invariance thus induces the introduction of gauge fields, which imply the existence of the spin 1 $\hbar$ gauge bosons. Since gauge fields per construction interact with the fermion fields, the gauge bosons can be interpreted as the mediator particles of the force emerging from the gauge symmetry. Moreover, gauge fields A_μ^k enter the Lagrangian also through kinematic terms describing the gauge fields in the absence of fermions. These terms are of the form

$$-\frac{1}{4}F_{\mu\nu}^k F_k^{\mu\nu}\,. \tag{1.9}$$

The field strength tensor $F_{\mu\nu}^k$ of the gauge field A_μ^k is defined as

$$F_{\mu\nu}^k = (\partial_\mu A_\nu^k - \partial_\nu A_\mu^k) + g f_{klm} A_\mu^l A_\nu^m\,, \tag{1.10}$$

where g denotes again the coupling constant and f_{klm} are the structure constants specifying the symmetry group. These structure constants define the commutation relations of the generators of the symmetry group through

$$[\tau_k, \tau_l] = i f_{klm}\tau_m\,. \tag{1.11}$$

Requiring the Lagrangian in equation (1.8) to be invariant under the local phase transformation given in equation (1.6) leads to the transformation relation

$$\frac{\tau_k}{2}A_\mu'^k = -\frac{i}{g}(\partial_\mu U)U^{-1} + U\frac{\tau_k}{2}A_\mu^k U^{-1}\,, \tag{1.12}$$

Table 1.3: The fields of the Standard Model and their gauge quantum numbers. There are three generations of quarks and leptons, labelled by the index $i = 1, 2, 3$ and one Higgs field ϕ. I and I_3 are the total weak isospin and its third component. The hypercharge in the last column can be calculated from the charge Q and the third component of the weak isospin via $Y = 2(Q - I_3)$.

				I	I_3	Q	Y
$Q_L^i =$	$\begin{pmatrix} u_L \\ d_L \end{pmatrix}$	$\begin{pmatrix} c_L \\ s_L \end{pmatrix}$	$\begin{pmatrix} t_L \\ b_L \end{pmatrix}$	$1/2$	$+1/2$ $-1/2$	$+2/3$ $-1/3$	$+1/3$ $+1/3$
$u_R^i =$	u_R	c_R	t_R	0	0	$+2/3$	$+4/3$
$d_R^i =$	d_R	s_R	b_R	0	0	$-1/3$	$-2/3$
$L_L^i =$	$\begin{pmatrix} \nu_{e,L} \\ e_L \end{pmatrix}$	$\begin{pmatrix} \nu_{\mu,L} \\ \mu_L \end{pmatrix}$	$\begin{pmatrix} \nu_{\tau,L} \\ \tau_L \end{pmatrix}$	$1/2$	$+1/2$ $-1/2$	0 -1	-1 -1
$\nu_R^i =$	$\nu_{e,R}$	$\nu_{\mu,R}$	$\nu_{\tau,R}$	0	0	0	0
$e_R^i =$	e_R	μ_R	τ_R	0	0	-1	-2
$\phi =$	$\begin{pmatrix} \phi^+ \\ \phi^0 \end{pmatrix}$			$1/2$	$+1/2$ $-1/2$	$+1$ 0	$+1$ $+1$

for the fields A_μ^k, which is valid for any transformation U in some internal space. Choosing for example a $U(1)$ phase transformation $U = e^{i\chi(x)}$ with an arbitrary space-time function $\chi(x)$ and one generator $\tau = 1$, equation (1.10) simplifies to $(\partial_\mu A_\nu - \partial_\nu A_\mu)$. Consequently, the corresponding gauge group is Abelian and equation (1.12) simplifies to $A'_\mu = A_\mu - \partial_\mu \chi(x)/g$. In contrast, a theory with a local non-Abelian phase invariance is called a Yang-Mills theory, wherein self-interactions of gauge bosons arise from the non-commutative structure of the symmetry group.

The Standard Model represents a particular quantum field theory based on the principle of gauge invariance. It is based on the set of fields shown in table 1.3 and the gauge symmetries $SU(3)_C \times SU(2)_L \times U(1)_Y$. The gauge fields introduced by the requirement of gauge invariance under $SU(2)_L \times U(1)_Y$ describe the electroweak force, whereas the gauge bosons of the strong force are linked to the $SU(3)_C$ gauge group. The Standard Model Lagrangian can thus be written as

$$\mathcal{L}_{\text{SM}} = \mathcal{L}_{\text{EW}} + \mathcal{L}_{\text{QCD}} + \mathcal{L}_{\text{Higgs}} + \mathcal{L}_{\text{Yukawa}}\,. \tag{1.13}$$

The first two terms, $\mathcal{L}_{\text{EW}}$ and $\mathcal{L}_{\text{QCD}}$, describe free fermions, free gauge bosons associated with the $SU(2)_L \times U(1)_Y$ and $SU(3)_C$ gauge symmetries, the interaction between fermions and gauge bosons, and the interactions among gauge bosons themselves. The latter terms $\mathcal{L}_{\text{Higgs}}$ and $\mathcal{L}_{\text{Yukawa}}$ introduce the Higgs particle and non-zero gauge boson and fermion masses.

Electroweak phenomena can be described by the $SU(2)_L \times U(1)_Y$ gauge symmetry. The subscript Y denotes the hypercharge and L implies coupling only to left-handed fields. The charges corresponding to the $SU(2)_L$ and $U(1)_Y$ symmetries are the weak

isospin I and the hypercharge Y, respectively. Using the Gell-Mann-Nishijima relation $Q = I_3 - Y/2$, the hypercharge can be calculated from the electric charge Q and the third component of the weak isospin I_3. The electroweak interaction distinguishes between left-handed and right-handed fermion states which can be constructed from an arbitrary spinor ψ via

$$\begin{aligned} \psi_L &= \frac{1}{2}(1-\gamma^5)\psi \text{ and} \\ \psi_R &= \frac{1}{2}(1+\gamma^5)\psi\,. \end{aligned} \tag{1.14}$$

The operator $\gamma^5 = i\gamma^0\gamma^1\gamma^2\gamma^3\gamma^4$ is given as a product of the four Dirac matrices. Left-handed fermions transform as doublets under $SU(2)_L$, whereas right-handed fermion fields are singlets. The analogy in electromagnetism would be that left-handed fermions exhibit a non-zero electric charge, whereas right-handed fermions are charge-neutral. In this way the parity-violating nature of weak interactions is incorporated in the theory. As depicted in table 1.3, left-handed fermions are grouped into weak-isospin doublets called Weyl spinors

$$\Psi_L = \begin{pmatrix} u_L \\ d_L \end{pmatrix}, \quad \begin{pmatrix} c_L \\ s_L \end{pmatrix}, \quad \begin{pmatrix} t_L \\ b_L \end{pmatrix}, \quad \begin{pmatrix} \nu_{e,L} \\ e_L \end{pmatrix}, \quad \begin{pmatrix} \nu_{\mu,L} \\ \mu_L \end{pmatrix}, \quad \begin{pmatrix} \nu_{\tau,L} \\ \tau_L \end{pmatrix}. \tag{1.15}$$

The right-handed states in turn form weak-isospin singlets which remain unchanged under $SU(2)_L$ gauge transformations. A local $SU(2)_L \times U(1)_Y$ phase transformation can be written as

$$\begin{aligned} \Psi_L \to \Psi'_L &= e^{ig\epsilon_k(x)\cdot\frac{\sigma_k}{2}} \cdot e^{ig'\theta(x)\cdot\frac{Y}{2}}\,\Psi_L \text{ and} \\ \Psi_R \to \Psi'_R &= e^{ig'\theta(x)\cdot\frac{Y}{2}}\,\Psi_R\,, \end{aligned} \tag{1.16}$$

with an arbitrary one-dimensional function $\theta(x)$ and the rotation parameters $\epsilon_k(x)$. Using the standard representation, the Pauli matrices σ_k ($k = 1,2,3$) and the hypercharge Y denote the generators of the $SU(2)_L$ and $U(1)_Y$ symmetry transformations, respectively, and g and g' represent the corresponding coupling constants. The covariant derivative ensuring gauge invariance of the Lagrangian under local $SU(2)_L \times U(1)_Y$ phase transformation is given by

$$\mathcal{D}_\mu = \partial_\mu + ig\frac{\sigma_k}{2}W^k_\mu + ig'\frac{Y}{2}B_\mu\,. \tag{1.17}$$

W^k_μ and B_μ represent the gauge fields associated to the $SU(2)_L$ and $U(1)_Y$ group, respectively. The field strength tensors $B_{\mu\nu}$ and $W^k_{\mu\nu}$ are defined by equation (1.10). Since the $U(1)_Y$ structure constant is zero, corresponding to a commuting gauge field, the gauge field B_μ couples to fermions but not to itself. The non-zero structure constants in the field strength tensors $W^k_{\mu\nu}$ of $SU(2)_L$ gauge fields however lead to interactions of gauge bosons among themselves. The gauge invariance of the electroweak theory thus induces the introduction of the four gauge bosons B^0 and W^k, where the latter only couple to left-handed fermion doublets and interact among themselves. The electroweak Lagrangian is given by

$$\mathcal{L}_{\text{EW}} = i\bar{\Psi}_L\gamma^\mu\mathcal{D}_\mu\Psi_L + i\bar{\Psi}_R\gamma^\mu\mathcal{D}_\mu\Psi_R - \frac{1}{4}B_{\mu\nu}B^{\mu\nu} - \frac{1}{4}W^k_{\mu\nu}W^{k\mu\nu}\,, \tag{1.18}$$

where Ψ_L denotes left-handed fermion doublets and Ψ_R the corresponding right-handed singlets. Two of the $SU(2)_L$ gauge fields can be linearly combined into the physically observable charged fields

$$W_\mu^\pm = \frac{1}{\sqrt{2}}\left(W_\mu^1 \mp iW_\mu^2\right) , \tag{1.19}$$

whose quanta are observed as $W^\pm$ bosons. The remaining charge-neutral $SU(2)_L$ field mixes with the $U(1)_Y$ field through the weak mixing angle θ_W, which results in the fields A_μ and Z_μ via a mass matrix diagonalisation given by

$$\begin{aligned} A_\mu &= B_\mu \cos\theta_\mathrm{W} + W_\mu^3 \sin\theta_\mathrm{W} \text{ and} \\ Z_\mu &= -B_\mu \sin\theta_\mathrm{W} + W_\mu^3 \cos\theta_\mathrm{W} . \end{aligned} \tag{1.20}$$

Requiring the quanta of the A_μ field to correspond to the massless photons, the weak mixing angle is defined by $g \sin\theta_\mathrm{W} = g' \cos\theta_\mathrm{W} = e$, with the elementary electric charge e. On the other hand, the quanta of the Z_μ field are observed as Z^0 bosons. The relation between the weak mixing angle, also referred to as the Weinberg angle, and the coupling constants is given by

$$\tan(\theta_\mathrm{W}) = \frac{g'}{g} . \tag{1.21}$$

Quantum chromodynamics is formulated in a manner analogous to the electroweak theory. The appropriate gauge group for the description of the strong interaction is the $SU(3)_C$ symmetry group, with the subscript C denoting colour. Restoring the gauge invariance of the theory with respect to local $SU(3)_C$ phase-space transformation invokes the introduction of eight gauge fields, corresponding to the eight generators of the $SU(3)_C$. In the standard representation, these eight generators are given by the 3×3 Gell-Mann matrices λ_k $(k = 1, \ldots, 8)$ acting on quark colour triplets. The covariant derivative in QCD is given by

$$\mathcal{D}_\mu = \partial_\mu + ig_3 \frac{\lambda_k}{2} G_\mu^k , \tag{1.22}$$

where G_μ^k represents the eight gauge fields and g_3 the associated coupling constant. Gluons are the quanta of the gauge fields and are thus referred to as the force mediators introduced into the theory by requiring $SU(3)_C$ gauge invariance. Similar to $SU(2)_L$, the commutator relations of the $SU(3)_C$ group generators exhibit non-zero structure constants. This non-Abelian character ensures the self-interaction of gluons. In contrast to $SU(2)_L \times U(1)_Y$, the $SU(3)_C$ colour symmetry however is unbroken leading to the prediction of massless gluons. Finally, the Lagrangian of the strong interaction is given by

$$\mathcal{L}_\mathrm{QCD} = i\bar{q}_f \gamma^\mu \mathcal{D}_\mu q_f - \frac{1}{4} G_{\mu\nu}^k G_k^{\mu\nu} , \tag{1.23}$$

with colour triplets q_f of quarks of flavour f and $G_{\mu\nu}^k$ denotes the field strength tensors.

The requirement of gauge invariance under local $SU(2)_L \times U(1)_Y$ phase transformation led to the introduction of four gauge fields whose field quanta can be connected to the photon γ, and the three bosons $W^{\pm}$ and Z^0. However, the gauge fields and the implied gauge bosons introduced are predicted to be strictly massless, which is in contradiction with the measured $W^{\pm}$ and Z^0 boson masses. Introducing explicit mass terms for gauge bosons into the Lagrangian would break the $SU(2)_L \times U(1)_Y$ gauge invariance and is therefore not an option. The Higgs mechanism on the other hand can be used to solve this obstacle using the idea of spontaneous symmetry breaking. One simple and elegant way for breaking the $SU(2)_L \times U(1)_Y$ gauge symmetry is to introduce a scalar field into the SM Lagrangian. Using the doublet representation of $SU(2)_L$, this complex scalar field is given by

$$\phi = \begin{pmatrix} \phi^+ \\ \phi^0 \end{pmatrix} = \frac{1}{\sqrt{2}} \begin{pmatrix} \eta_1 + i\eta_2 \\ \eta_3 + i\eta_4 \end{pmatrix} , \tag{1.24}$$

wherein the complex fields ϕ^+ and ϕ^0 can be written in terms of the four real fields η_i. Unlike the gauge fields introduced by requiring gauge invariance, there is no corresponding gauge group responsible for the Higgs field. The Lagrangian density for such a complex scalar field can be written with a specific potential $V(\phi)$ in the form

$$\begin{aligned} \mathcal{L}_{\text{Higgs}} &= (\mathcal{D}^\mu \phi)^\dagger (\mathcal{D}_\mu \phi) - V(\phi) \\ &= (\mathcal{D}^\mu \phi)^\dagger (\mathcal{D}_\mu \phi) - \mu^2 (\phi^\dagger \phi) - \lambda (\phi^\dagger \phi)^2 , \end{aligned} \tag{1.25}$$

where $\mathcal{D}_\mu$ is the electroweak covariant derivative given in equation (1.17), which thus introduces coupling terms between the Higgs field and the weak gauge bosons. μ^2 denotes a mass parameter and $\lambda > 0$ the strength of the Higgs boson field's self-interaction. For $\mu^2 > 0$, the potential $V(\phi)$ has a global minimum for $\phi = 0$. However, if $\mu^2 < 0$ is required, the minimum of the potential is no longer unique but exhibits a value on a continuous ring in the complex plane shown in figure 1.2. In this ring the vacuum expectation value v of the field ϕ is equal to

$$\langle 0|\phi|0\rangle = -\frac{|\mu^2|}{2\lambda} = \frac{v^2}{2} . \tag{1.26}$$

Hence, the ground state is not symmetric, whereas the Lagrangian in $SU(2)_L \times U(1)_Y$ is symmetric, a feature referred to as spontaneous symmetry breaking. Using the a priori arbitrary choice $\eta_3 = v$ and $\eta_1 = \eta_2 = \eta_4 = 0$ for the vacuum, an expansion around the minimum leads to the transformation of equation (1.24) into

$$\phi = \frac{1}{\sqrt{2}} \begin{pmatrix} 0 \\ v + H(x) \end{pmatrix} , \tag{1.27}$$

wherein $H(x)$ represents the Higgs boson field, whose quanta are called Higgs bosons. In this altered representation, only one of the four degrees of freedom of the original Higgs doublet remains. The other three fields η_i $(i = 1, 2, 4)$ appear as longitudinal degrees of freedom for the three gauge bosons $W^{\pm}$ and Z^0, which thus acquire masses given by

$$\begin{aligned} m_{W^\pm} &= \frac{1}{2} v g \quad \text{and} \\ m_{Z^0} &= \frac{1}{2} v \sqrt{g^2 + g'^2} , \end{aligned} \tag{1.28}$$

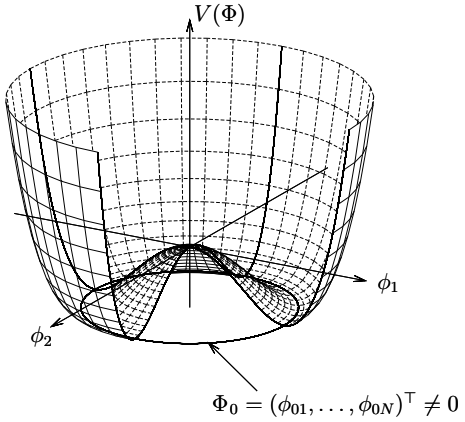

Figure 1.2: Scalar potential $V(\phi)$ of the Higgs field with $\lambda > 0$ and $\mu^2 < 0$ adapted from [67]. With this particular choice of the vacuum, the minimum of the potential is a circle in the complex plane. The vacuum expectation value of the Higgs field is hence not unique, and therefore the symmetry of the field spontaneously broken.

or simply $m_W = m_Z \cos\theta_W$. The vacuum expectation value of the Higgs field can thus be deduced from measurements of the $W^\pm$ mass and of the coupling constant g, leading to a numerical value of $v = 246$ GeV. The last term in equation (1.25) induces self-interactions of the Higgs field. Therefore, the Higgs boson H^0 also acquires mass $m_{H^0} = \sqrt{-2\mu^2}$, which has to be determined experimentally due to the appearance of the essentially free parameter $\mu^2 < 0$.

In contrast to the boson masses, the masses of the fermions are not generated by a gauge principle. They are rather included via introduction of additional gauge invariant terms into the Lagrangian, resulting in an increase of free parameters in the Standard Model. These Yukawa terms describe the couplings of the fermionic fields to the Higgs field. For example the Yukawa terms for top quarks are given by

$$g_Y^t \left(\bar{\Psi}_L \phi t_R + \bar{t}_R \phi^\dagger \Psi_L \right) , \tag{1.29}$$

wherein Ψ_L denotes the third-generation left-handed quark doublet, t_R the right-handed top singlet as shown in table 1.3, and g_Y^t is the corresponding Yukawa coupling constant. In the specific representation of equation (1.27) this can be written as

$$\frac{g_Y^t v}{\sqrt{2}} t\bar{t} + \frac{g_Y^t}{\sqrt{2}} t\bar{t}H . \tag{1.30}$$

The first term denotes the top quark mass term, while the second term specifies the coupling of the top quark to the Higgs boson. The top quark mass is given by $m_t = g_Y^t v/\sqrt{2}$ with the top quark coupling to the Higgs boson being m_t/v. Similar Yukawa terms are introduced for the other quarks and the charged leptons. The couplings of charged leptons and quarks to the Higgs boson are proportional to the fermion masses. Hence, the Yukawa coupling constants, or equivalently the fermion masses, appear as free parameters in the Standard Model. The extremely high mass, and therewith its strong coupling to the Higgs boson, grants the top quark a special role for indirect predictions of the Higgs boson mass.

1.2. The Top Quark

The top quark was discovered by the CDF and DØ collaborations at the Fermilab Tevatron in 1995 [1, 2]. This observation of top quark pair production via the strong interaction is however not the only production mode predicted by the Standard Model. Electroweak production of single top quarks also constitutes a Standard Model production mechanism, which was experimentally observed only two years ago [5, 6]. Since the first observation of this heaviest fundamental particle currently known, the mass of the top quark has been measured with ever increasing precision. The most recent combination by the Tevatron Electroweak Working Group for the top quark mass yields a value of 173.3 ± 1.1 GeV/c^2 [3]. Since it is about 40 times heavier than the next heaviest quark and nearly as massive as a gold nucleus, the large mass of the top quark leads to conjectures about whether this observed particle might not correspond to the weak isospin partner of the b quark in the Standard Model. It would then rather be an exotic quark carrying an electric charge of $-\frac{4}{3}\,e$ [68]. A recent measurement [69], however, disfavours this hypothesis of such an exotic quark with this particular electric charge. Since the Yukawa coupling of the top quark is close to unity, as can be deduced from the second term of equation (1.30), the top quark mass is in the range of the electroweak symmetry breaking scale. Therefore, this heaviest fermion might play a role in the process of electroweak symmetry breaking [70, 71]. One further peculiarity based on the large mass of the top quark is its very short lifetime. Although it decays exclusively via the weak interaction, the large mass induces a lifetime of $\tau_t \approx 5 \cdot 10^{-25}$ s [72], which is about two orders of magnitude smaller than the typical time scale for hadronisation processes $\Lambda_{\mathrm{QCD}}^{-1} \approx 3 \cdot 10^{-23}$ s. Consequently, top quarks on average decay before top-flavoured hadrons can be formed, which offers the unique possibility to study quasi-free quarks. Moreover, in contrast to the lighter quarks whose spins are depolarised by chromomagnetic interactions within the bound states, there is insufficient time for depolarisation of the top quark spin. Thus, the spin of the top quark remains undisturbed by the strong interaction and is directly transferred to its decay products [73]. Detailed reviews on the current status and prospects of top quark physics can for example be found in [72, 74] and references therein.

1.2.1. Top Quark Production via the Strong Interaction

The Standard Model predictions are not limited to the existence of the fundamental particles, but additionally include information on their production probability in a given experimental collider setup. Based on an analogy to classical scattering experiments, the cross section of a given process is a measure of the effective surface area seen by a striking particle. Cross sections are therefore expressed in units of area, with the most commonly quoted unit is barn, defined by $1\ \mathrm{b} = 10^{-28}\ \mathrm{m}^2$, or its corresponding sub-multiples like $1\ \mathrm{pb} = 10^{-12}\ \mathrm{b}$. In the collision of two particles, the cross section is a measure of the probability for an interaction to occur. For a transition of two incoming particles i and j into two outgoing particles k and l, the cross section in the centre-of-mass system can be calculated via

$$\sigma(ij \to kl) = \int \frac{1}{4Wp} \left|\mathcal{M}\right|^2 \cdot d\Phi(s; p_k, p_l)\,, \tag{1.31}$$

with $W^2 = s$, i.e. the four-momentum transfer squared $s = (p_i + p_j)^2$, the initial particle momentum $p = |\vec{p}_{i,j}|$, and a Lorentz-invariant phase-space factor $d\Phi(s; p_k, p_l)$. Of special importance is the matrix element $\mathcal{M}$, which can be determined from the Lagrangian using perturbation theory. For this purpose, the matrix element can be written in terms of a perturbation series expansion in the coupling constant of the corresponding interaction. Feynman diagrams constitute graphical representations for the individual terms in this series. Moreover, these diagrams allow for a translation into the corresponding formulae by application of the appropriate Feynman rules, which are given by the Lagrangian. Including only terms of the lowest non-vanishing order in the coupling constant yields a leading order (LO) computation of the matrix element. The inclusion of diagrams exhibiting one order more in the coupling constant results a next-to-leading order (NLO) calculation and so on. For the calculation of cross sections, the inclusion of terms beyond leading order in the coupling constant leads to divergences, which can be treated using the technique of renormalisation. Therein, divergences are avoided by defining physical quantities like a coupling constant as a combination of the bare quantity appearing in the Standard Model Lagrangian $\mathcal{L}_{\mathrm{SM}}$ and the divergent contributions. For renormalisable theories, like the Standard Model, the unobservable value of the bare quantity can be chosen such that divergences to all orders in perturbation theory are cancelled. Consequently, the value of the coupling constant depends on the energy scale, which is also referred to as the renormalisation scale μ_R. This scale defines which higher-order contributions are absorbed into the redefined quantities of the Lagrangian and which are taken into account using perturbation theory. Hence renormalised coupling constants are referred to as running coupling constants obeying the so-called renormalisation group equation. If the complete perturbation series could be calculated, the result for the cross section would be independent of μ_R. However, since calculations are performed at finite orders, the cross section depends on the renormalisation scale μ_R. In general, a good choice $\hat{\mu}_R$ is a scale that minimises the size of higher-order corrections. Therefore, usually a scale characteristic for the hard scattering is used. The renormalisation scale uncertainty denotes the uncertainty of a computation due to this non-unique choice. Conveniently, this uncertainty is evaluated as the effect of varying the renormalisation scale between $\frac{1}{2}\,\hat{\mu}_R$ and $2\,\hat{\mu}_R$.

The dominant production mechanism for top quarks at hadron colliders is the production of top-antitop quark pairs via the strong interaction. Although $t\bar{t}$ production can also be accomplished via Z^0 boson or photon exchange, these contributions can be neglected in hadron-hadron collisions. Furthermore, the Standard Model predicts the production of single top quarks via the electroweak interaction, which will be reviewed in section 1.2.2.

Partonic Cross Section

The cross sections $\hat{\sigma}$ of the hard parton-parton processes $ij \to t\bar{t}$ can be calculated for all possible initial-state partons i and j in perturbative QCD. The leading order (Born) cross sections for heavy quark production were calculated in the late 1970s [75–80]. The leading-order processes, contributing with the square of the strong coupling constant α_s to the perturbation series, are quark-antiquark annihilation ($q\bar{q} \to t\bar{t}$) and gluon-gluon fusion ($gg \to t\bar{t}$). Feynman diagrams for these LO processes are depicted in figure 1.3. Application of the corresponding Feynman rules allows for the calculation of the transi-

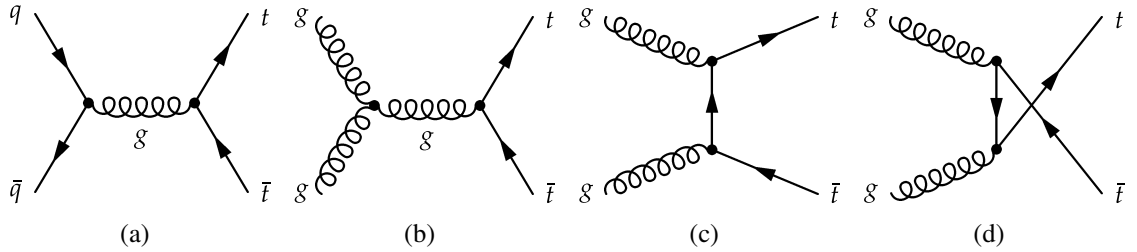

Figure 1.3: Leading order Feynman diagrams for the production of top quark pairs via quark-antiquark annihilation (a) and via gluon-gluon fusion (b), (c), and (d).

tion amplitudes and thus for the computation of the differential hard cross sections $\frac{d\hat{\sigma}}{d\hat{t}}$. The LO differential cross sections for quark-antiquark annihilation and gluon-gluon fusion are given by

$$\frac{d\hat{\sigma}}{d\hat{t}}(q\bar{q} \to t\bar{t}) = \frac{4\pi\alpha_s^2}{9\hat{s}^4} \cdot \left[\left(m_t^2 - \hat{t}\right)^2 + \left(m_t^2 - \hat{u}\right)^2 + 2m_t^2\hat{s} \right] \quad \text{and} \tag{1.32}$$

$$\begin{aligned} \frac{d\hat{\sigma}}{d\hat{t}}(gg \to t\bar{t}) = \quad & \frac{\pi\alpha_s^2}{8\hat{s}^2} \cdot \left[\frac{6\left(m_t^2 - \hat{t}\right)\left(m_t^2 - \hat{u}\right)}{\hat{s}^2} - \frac{m_t^2\left(\hat{s} - 4m_t^2\right)}{3\left(m_t^2 - \hat{t}\right)\left(m_t^2 - \hat{u}\right)} \right. \\ & + \frac{4}{3} \cdot \frac{\left(m_t^2 - \hat{t}\right)\left(m_t^2 - \hat{u}\right) - 2m_t^2\left(m_t^2 + \hat{t}\right)}{\left(m_t^2 - \hat{t}\right)^2} \\ & + \frac{4}{3} \cdot \frac{\left(m_t^2 - \hat{t}\right)\left(m_t^2 - \hat{u}\right) - 2m_t^2\left(m_t^2 + \hat{u}\right)}{\left(m_t^2 - \hat{u}\right)^2} \\ & - 3 \cdot \frac{\left(m_t^2 - \hat{t}\right)\left(m_t^2 - \hat{u}\right) + m_t^2\left(\hat{u} - \hat{t}\right)}{\hat{s}\left(m_t^2 - \hat{t}\right)} \\ & \left. - 3 \cdot \frac{\left(m_t^2 - \hat{t}\right)\left(m_t^2 - \hat{u}\right) + m_t^2\left(\hat{t} - \hat{u}\right)}{\hat{s}\left(m_t^2 - \hat{u}\right)} \right], \end{aligned} \tag{1.33}$$

with the top quark mass m_t and the Lorentz-invariant Mandelstam variables $\hat{s}$, $\hat{t}$, and $\hat{u}$ of the process. They are defined as $\hat{s} = (p_i + p_j)^2$, $\hat{t} = (p_i - p_t)^2$, and $\hat{u} = (p_i - p_{\bar{t}})^2$, where p_i and p_j represent the four-momenta of parton i and j, i.e. of the quarks q and $\bar{q}$ or of the two gluons, respectively. The four-momenta of the top and the anti-top quark are given by p_t and $p_{\bar{t}}$. The Mandelstam variables $\hat{s}$, $\hat{t}$, and $\hat{u}$ can be identified with the square of the partonic centre-of-mass energy and with the squares of the momentum transfers from the initial parton to the top quark or to the anti-top quark, respectively. The cross sections in equations (1.32) and (1.33) are quoted in the form given in [81].

Parton Distribution Functions

The differential cross sections given in equations (1.32) and (1.33) describe the LO $t\bar{t}$ production via quark-antiquark annihilation and gluon-gluon fusion. However, at the Large Hadron Collider compound particles are collided. Assuming the collision of hadron A

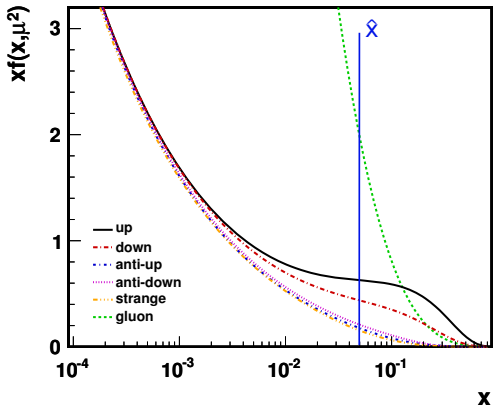

Figure 1.4: Parton distribution functions of u quarks, d quarks, $\bar{u}$ quarks, $\bar{d}$ quarks, s quarks and gluons inside the proton. The parametrisation used is CTEQ6.6 [84] and the scale at which the PDFs are evaluated is chosen to $\hat{\mu} = 172.5$ GeV. A typical value for $t\bar{t}$ production at the LHC with a centre-of-mass energy of $\sqrt{s} = 7$ TeV is $\hat{x} = 0.05$, which is indicated by the vertical blue line.

and B, the momentum of each hadron is shared among its constituents. A proton for example consists of two u quarks and one d quark. These three valence quarks are bound by virtual gluons, which can fluctuate into quark-antiquark pairs, so-called sea quarks. The parton distribution function (PDF) $f_{i/A}(x_i, \mu)$ describes the probability density for finding a parton i inside hadron A, where parton i carries a longitudinal momentum fraction $x_i = \frac{p_i}{p_A}$ of the total hadron momentum p_A. Parton distribution functions depend on the factorisation scale μ_F which describes the typical energy scale of the considered interaction. Since the factorisation scale μ_F and the previously discussed renormalisation scale μ_R are to some extend arbitrary parameters, they are customarily set to one single scale $\mu = \mu_R = \mu_F$. For the calculation of top quark production cross sections, μ is usually set to the top quark mass m_t. For example, figure 1.4 depicts PDFs in the CTEQ6.6 [82, 83] parametrisation at a scale $\hat{\mu} = 172.5$ GeV for the valence quarks (u and d), the sea quarks (here: $\bar{u}$, $\bar{d}$, and s) and gluons inside the proton. Using the momentum fractions x_i and x_j, the square of the total energy of the partonic sub-process $\hat{s}$ can be obtained from the square of the total hadronic centre-of-mass energy $s = (P_A + P_B)^2$ via

$$\hat{s} = (p_i + p_j)^2 = (x_i P_A + x_j P_B)^2 \approx 2 x_i x_j P_A P_B \approx x_i x_j s\,, \tag{1.34}$$

where the residual masses of the two incoming hadrons are neglected. For top quark pair production, the energy in the partonic interaction has to exceed the minimal value of $\hat{s}_{\text{min}} = 4m_t^2$, leading together with the approximation $x_i \approx x_j = \hat{x}$ to a typical value of $\hat{x} \approx \frac{2m_t}{\sqrt{s}}$ for $t\bar{t}$ production at the kinematic threshold. Hence, the centre-of-mass energy of the Large Hadron Collider induces $t\bar{t}$ production in the low x regime, with a typical value $\hat{x} \approx 0.05$, given the centre-of-mass energy of 7 TeV. Since the PDF for gluons in this region is very much enhanced compared to those of the valence or sea quarks, the dominant production sub-process, with a contribution of about 90%, is gluon-gluon fusion.

Total Hadronic Cross Section (The Factorisation Ansatz)

Finally, the total hadronic cross section σ for $t\bar{t}$ production in hadron-hadron collisions is given by the convolution of the parton distribution functions of the colliding hadrons and the hard parton-parton cross section $\hat{\sigma}_{ij}$

$$\sigma(AB \to t\bar{t}) = \sum_{i,j} \int dx_i dx_j f_{i/A}(x_i, \mu^2) f_{j/B}(x_j, \mu^2) \cdot \hat{\sigma}_{ij}(ij \to t\bar{t}; \hat{s}, \mu^2)\,, \qquad (1.35)$$

summed over all pairs of initial partons contributing to the process. While the next-to-leading order corrections to top quark pair production at hadron colliders have been calculated for unobserved spins in [85, 86] and with the full top quark spin dependency in [87, 88], a complete analytical result for the NLO partonic cross section was published only recently [89]. Moreover, approximations towards a full NNLO result have been obtained by several groups [8, 9, 90–93]. Based on the techniques deduced in [8, 9], the HATHOR [10] package allows for the calculation of the $t\bar{t}$ production cross section. Setting the renormalisation and factorisation scales to $\hat{\mu} = 172.5$ GeV and using the CTEQ6.6 [84] PDF parametrisation, this procedure results in a predicted value of

$$\sigma(pp \to t\bar{t}) = \left(164.6^{+11.4}_{-15.7}\right) \text{ pb}\,, \qquad (1.36)$$

for the $t\bar{t}$ production cross section at the LHC. The uncertainty of about 10% on this prediction includes scale and PDF uncertainties. For the evaluation of the scale uncertainty, the scale μ is varied to $\frac{1}{2}\hat{\mu}$ and $2\hat{\mu}$, respectively. In order to determine the uncertainty induced by the used parton distribution functions, the 22 orthogonal eigenvectors in the CTEQ6.6 PDF set are separately varied to their 90% confidence interval boundary value and the resulting deviations are added in quadrature. For the design centre-of-mass energy $\sqrt{s} = 14$ TeV of the Large Hadron Collider, an enhanced cross section value for top quark pair production of $\sigma(pp \to t\bar{t}) = 918^{+64}_{-41}$ pb [92, 94] is expected, based on the MSTW2008 NNLO PDF [82, 83] parametrisation and a scale $\hat{\mu} = 173$ GeV.

1.2.2. Top Quark Production via the Electroweak Interaction

Besides the production of top quark pairs involving the strong interaction, the production of single top quarks via the electroweak interaction is predicted by the Standard Model. Since electroweak top quark production proceeds via a Wtb vertex, it facilitates a direct measurement of the magnitude of the CKM matrix element V_{tb}. Figure 1.5 illustrates the LO Feynman diagrams for the three different modes for single top quark production, i.e. the t-channel, the s-channel, and the associated production. For a centre-of-mass energy of 7 TeV, recent results on the approximated NNLO cross sections for s-channel production of top quarks and of anti-top quarks yield [95]

$$\begin{aligned} \sigma^{t}_{s\text{-chan}} &= \left(3.17 \pm 0.06^{+0.13}_{-0.10}\right) \text{ pb and} \\ \sigma^{\bar{t}}_{s\text{-chan}} &= \left(1.42 \pm 0.01^{+0.06}_{-0.07}\right) \text{ pb}\,, \end{aligned} \qquad (1.37)$$

at $\hat{\mu} = 173$ GeV and using the MSTW2008 NNLO PDF set. While the first uncertainty is determined by varying the scale μ, the second uncertainty accounts for PDF uncertainties.

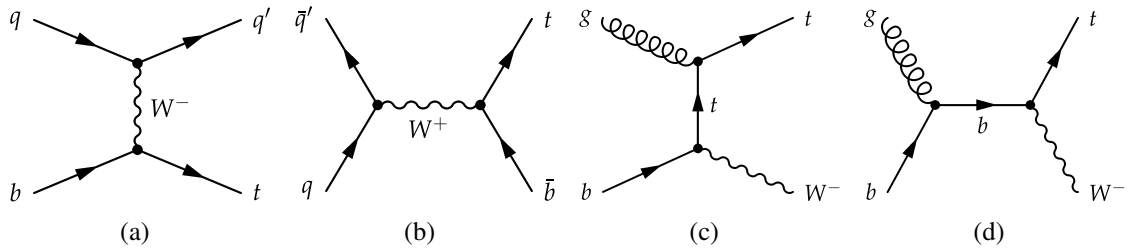

Figure 1.5: Leading order Feynman diagrams for the electroweak production of single top quarks via the t-channel (a), the s-channel (b), and the associated Wt production (c) and (d).

Given these small cross section values, a sub-leading role is ascribed to s-channel single top quark production compared to pairwise production of top quarks at the LHC.

The t-channel production mode on the other hand exhibits a larger cross section value of about [96]

$$\begin{aligned} \sigma^{t}_{t\text{-chan}} &= \left(42.6^{+0.9}_{-0.8} \pm 2.2\right) \text{pb and} \\ \sigma^{\bar{t}}_{t\text{-chan}} &= \left(22.6^{+0.6}_{-0.3} \pm 0.8\right) \text{pb}, \end{aligned} \tag{1.38}$$

where the MCFM [97] package with $\hat{\mu} = 172.5$ GeV and the CTEQ6M PDF has been employed to derive NLO cross section values. Due to this moderate value compared to the predicted $t\bar{t}$ production cross section given in equation (1.36), the t-channel production mode has to be considered as background contribution in the analysis of $t\bar{t}$ production. However, the different final state topologies of the two processes can be used to distinguish top quark pair production from the single top t-channel production mode.

The third single top quark production mode is characterised by the associated production of a top quark and an on-shell (or close to on-shell) charged $W^{\pm}$ boson, which is therefore also referred to as Wt production. For this production mechanism, the approximate NNLO cross section calculation yields [98]

$$\sigma_{Wt} = \left(15.6 \pm 0.4^{+1.0}_{-1.2}\right) \text{pb}, \tag{1.39}$$

where the uncertainties again include scale and PDF uncertainties. The associated production is of particular importance for the analysis of $t\bar{t}$ events, since this process interferes at next-to-leading order with $t\bar{t}$ production at leading order [99]. In phase-space regions where the final state Wb system is close to the top mass, this interference becomes large, due to the large propagator value for the intermediate top quarks in this particular phase-space region. In order to estimate the interference between Wt and $t\bar{t}$ production, two definitions of the Wt mode are given in [99]. The first approach is called Diagram Removal (DR), wherein all diagrams in the NLO Wt amplitudes are removed, which are doubly resonant in the sense that the intermediate top quark can be on-shell. In the second definition, called Diagram Subtraction (DS), the NLO Wt cross section is modified by implementing a subtraction term designed to locally cancel the $t\bar{t}$ contributions. Hence, the comparison of results obtained from the two complementary definitions can be used to estimate the impact of the interference on the analysis.

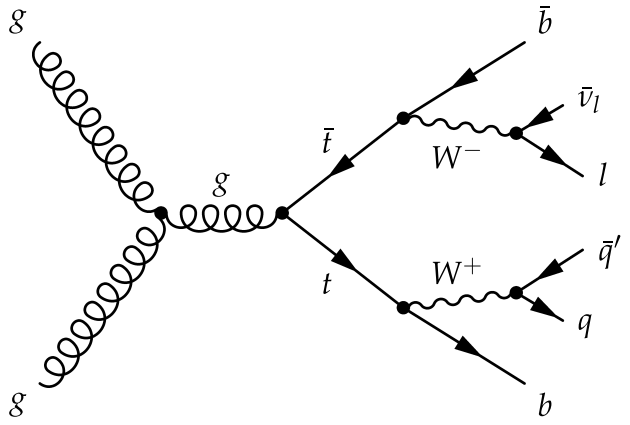

Figure 1.6: LO Feynman diagram for $t\bar{t}$ production via gluon-gluon fusion and subsequent top quark decays. This example shows the lepton+jets event topology, wherein the W^- boson originating from the anti-top quark decays leptonically into a charged lepton l^- and the corresponding anti-neutrino $\bar{\nu}_l$. The W^+ boson from the top quark on the other hand subsequently decays hadronically into a $q\bar{q}'$ quark pair.

1.2.3. Decay of the Top Quark

Constituting the up-type quark of the third generation, the top quark could in principle decay into an electrically charged W boson and any down-type quark of one of the three generations. However, the decay into a quark of the first or second generation is strongly suppressed by the small values for the corresponding CKM matrix elements V_{tu} and V_{tc} given in equation (1.2). The matrix element V_{tb} is close to one, implying an almost exclusive decay of the top quark into a W boson and a b quark. Since the top quark mass exceeds the sum of the masses of its decay products, the top quark decays into a real W boson, which is one of the reasons for the extremely short lifetime of top quarks. Figure 1.6 depicts again the LO Feynman diagram for $t\bar{t}$ production via gluon-gluon fusion, including the decay of the top quarks. The electrically charged W bosons subsequently decay either leptonically into a charged lepton and the corresponding neutrino or into a quark-antiquark pair. Top quark pair event topologies can thus be distinguished by the W boson decay modes. All-hadronic events are characterised by the hadronic decay of both W bosons, whereas in dilepton events both W bosons decay leptonically. A third possibility is provided in the lepton+jets event topology, where one W decays leptonically, while the other decays hadronically into a quark-antiquark pair as depicted in figure 1.6. Disregarding mass differences, the universality of the electroweak interaction implies equal probabilities for the different fermionic decay modes. However, due to the three different quark colour charges, the decay into quark-antiquark pairs is enhanced by a factor of three, leading to a LO branching ratio of $1/9$ for each of the three leptonic decay modes and LO branching ratios of $3/9$ for decays into a $u\bar{d}'$ or $c\bar{s}'$ quark pair. The branching ratios for the various decay channels are depicted in figure 1.7. While the all-hadronic channel exhibits a high branching ratio, large background contributions from processes like QCD multijet production are expected. The dilepton channel in turn is characterised by its small branching ratio and low expected background contributions. A compromise providing low background contributions on the one hand while exhibiting a moderate

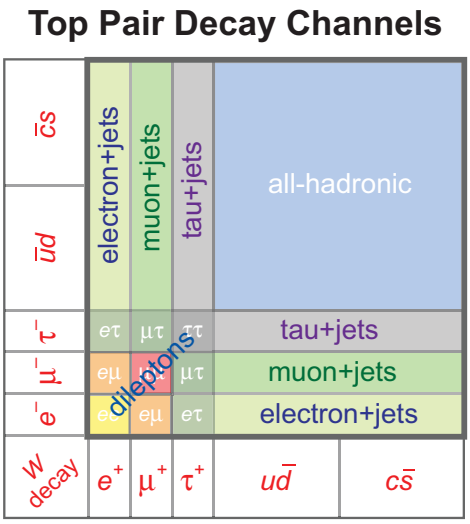

Figure 1.7: Decay channels for $t\bar{t}$ events [100]. The graphic shows the three different $t\bar{t}$ event topologies, i.e. the all-hadronic, the lepton+jets, and the dilepton channel. The branching ratios for the various channels are thereby indicated by the size of the different areas.

branching ratio on the other hand is provided by the lepton+jets event topology. The analysis presented in this thesis is therefore performed in the muon+jets channel, which, in combination with the electron+jets channel, is habitually called the golden channel.

Chapter 2

The CMS Experiment at the Large Hadron Collider

Top quarks, like the other fermions of the second and third generation, do not constitute ordinary matter. The production of these higher-generation fermions can however be achieved in collider experiments, where the interaction of particles exhibiting sufficient kinetic energy facilitates the production of new particles. For a detailed observation of such collision events and the detection of the particles produced, dedicated detectors are required, which are installed hermetically around the interaction point.

Since the first intentional proton-proton collisions at a centre-of-mass energy of 7 TeV on March 30$^{\text{th}}$ 2010, the Large Hadron Collider (LHC) operated by the European Organisation for Nuclear Research (CERN) near Geneva, Switzerland, constitutes the highest energetic collider ever built. Revealing its discovery potential within the next decade, the LHC is expected to answer several open questions in particle physics, such as the nature of electroweak symmetry breaking or existence and properties of physics beyond the Standard Model. One of the two general-purpose particle detectors at the LHC is the Compact Muon Solenoid (CMS) apparatus, which has been designed to meet the versatile requirements implied by the rich physics goals of the Large Hadron Collider.

2.1. The Large Hadron Collider

Revealing phenomena at decreasing length scales requires increasing energy densities in collider experiments. The resolved length scale probed in an interaction is given by the de Broglie wavelength $\lambda = {}^{h}/_{p}$ of a probe particle with momentum p. Over the past decades many accelerator facilities with increasing centre-of-mass energies have allowed the exploration of matter and interactions at scales in the order of 10^{-18} m, where two kinds of collider experiments have been performed. In the collision of structureless particles like electrons, the entire energy of the colliding particles is available in the centre-of-mass of the collision. On the other hand, in the collision of composite particles like protons, high-energetic interactions take place between the constituents of the colliding protons. According to the parton density functions discussed in section 1.2.1, these constituents carry only a fraction of the total proton momentum, effectively leading to a reduced centre-of-mass energy. This has to be considered in the design of a hadron collider in order to be well above the production energy threshold for a desired process. This apparent drawback however implies the advantage of a wide spectrum of effective collision energies. Hadron colliders thus constitute ideal discovery machines, whereas electron-positron colliders serve better for precision measurements at fixed energy scales.

Besides the centre-of-mass energy, high interaction rates are required for precision measurements and searches for rare phenomena, which typically exhibit very small cross sections. In general, the event rate of a certain physics process is given by the product of

its cross section σ and the luminosity $\mathcal{L}$ of the collider via $\frac{dN}{dt} = \sigma \cdot \mathcal{L}$. The acceleration of particles at colliders is commonly performed using radio frequency (RF) cavities, in which oscillating electric fields of adequate frequencies lead to accelerating effects. For this reason, particles cannot be accelerated in continuous particle beams but are rather grouped into so-called bunches, which generally exhibit high particle densities. For a head-on collision of two bunches, A and B, comprising N_A and N_B particles, the luminosity is given by [101]

$$\mathcal{L} = f \frac{N_\mathrm{A} N_\mathrm{B}}{4\pi\sigma_x\sigma_y}\,, \tag{2.1}$$

where σ_x and σ_y characterise the approximately Gaussian beam profiles in horizontal and vertical directions at the interaction point and f denotes the revolution frequency. Taking into account some more realistic assumptions, the luminosity for the collision of n_b proton bunches containing N_p protons each can be expressed as [102]

$$\mathcal{L} = f \frac{\gamma n_b N_p^2}{4\pi\epsilon_n\beta^*} F\,, \tag{2.2}$$

where γ is the Lorentz factor and ϵ_n represents the normalised transverse emittance, which is a measure of the phase-space area associated with either of the two transverse degrees of freedom of the beams. The amplitude function at the interaction point is denoted by β^* and F is a reduction factor due to a finite bunch crossing angle.

The Large Hadron Collider [102, 103] is a hadron-hadron collider employed by the European Organisation of Nuclear Research (CERN) near Geneva, Switzerland. Currently operated at an unprecedented centre-of-mass energy of $\sqrt{s} = 7$ TeV (a factor of two below the design value of $\sqrt{s} = 14$ TeV) the LHC constitutes the most powerful proton-proton collider to date. It is hosted in a tunnel of 26.7 km circumference, located between 45 m and 170 m below the surface on a plane inclined at 1.4% sloping towards Lake Geneva. The tunnel was originally built for the Large Electron-Positron collider (LEP) [104], which was been operated at CERN from 1989 until 2000. LEP provided electron-positron collisions at a centre-of-mass energy of up to 209 GeV and facilitated precision measurements of the $W^\pm$ and Z^0 gauge boson properties by the four LEP experiments [105, 106]. One major constraint for the centre-of-mass energy at LEP was the beam particles' energy loss induced by synchrotron radiation. The energy loss per turn is given by [107]

$$\Delta E = \frac{4\pi\alpha_\mathrm{em}}{3R}\beta^3\gamma^4\,, \tag{2.3}$$

where R denotes the effective dipole bending radius of the accelerator and α_em is the electromagnetic fine-structure constant. The Lorentz factor γ is given by $\gamma \approx \frac{E}{mc^2}$ and in the ultra-relativistic scenario $\beta \approx 1$. The energy loss per turn is thus inversely proportional to the fourth power of the energy-mass ratio of the accelerated particles. Accordingly, an electron with an energy of 100 GeV at LEP radiated about 2.3% of its energy per turn, which had to be compensated for by the accelerator facility. One possibility for the reduction of this energy loss is to increase the radius of the accelerator, with the optimal realisation being a linear collider. For the design of the Large Hadron Collider an alternative approach has been chosen. Protons exhibit a 2,000 times higher rest mass than

Table 2.1: Summary of proton energies at the different acceleration stages from the proton source to the Large Hadron Collider.

Acceleration stage	Final proton energy [GeV]
RFQ	$7.5 \cdot 10^{-4}$
LINAC2	$5.0 \cdot 10^{-2}$
PSB	1.4
PS	26
SPS	450
LHC	up to 7,000

electrons. Therefore, synchrotron radiation is negligible for the acceleration and storage of protons due to the increased energy-mass ratio.

Further, the LHC design comprises an envisaged luminosity of $\mathcal{L} = 10^{34}$ cm^{-2}s^{-1}. To attain such high luminosities, bunches of $1.15 \cdot 10^{11}$ protons are collided every 25 ns, corresponding to a collision frequency of 40 MHz. Collimation of the proton bunches to a transverse size of about 16 μm at the interaction points further enhances the collision probability. However, a small luminosity reduction is caused by the finite bunch crossing angle of 285 μrad, which is needed for the beam-beam separation in order to avoid unintended collisions near the dedicated interaction regions. The beam intensity required for the high design luminosity of the LHC excludes the use of antiproton beams. Choosing a proton-proton collider however does not significantly restrict the physics potential of the accelerator, as interactions involving a few hundred GeV momentum transfer are mostly gluon-initiated.

Due to the high luminosities envisaged at the LHC, several proton-proton collisions are expected to occur during the same bunch crossing. In general, only one of these collisions contains a hard interaction of interest, while the other superimposed interactions typically constitute soft minimum-bias collisions. These soft interactions are collectively referred to as pile-up collisions, while an event denotes the total of all proton-proton collisions occurring in the same bunch crossing. The average number of pile-up collisions is proportional to the instantaneous luminosity of the accelerator, leading to a total of about 20 pile-up collisions per event at nominal LHC luminosity.

2.1.1. Production and Pre-acceleration of Protons

Before entering the LHC, protons traverse the CERN pre-accelerator complex [108] depicted in figure 2.1. This injection facility had already served for other experimental purposes for decades and has been extensively modified and upgraded for operating with the LHC. The accelerator chain consists of the proton source and several facilities for the subsequent increase of proton energies as summarised in table 2.1. A duoplasmatron source is used for the production of protons, where interactions of high-energetic electrons lead to the ionisation of hydrogen atoms. The protons obtained are extracted by applying a high voltage and transferred to the Radio Frequency Quadrupole (RFQ) of about 1.75 m length, serving as a linear accelerator. In the RFQ, protons are accelerated, focused and grouped into bunches, which finally leave this acceleration stage with

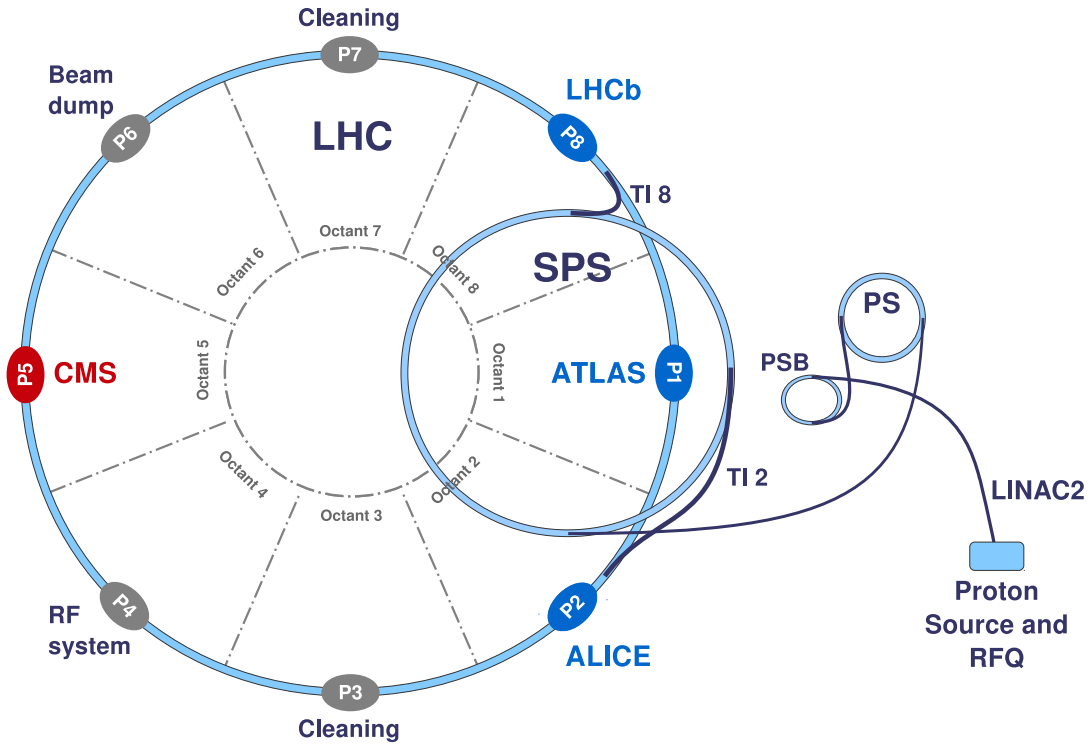

Figure 2.1: Schematic view of the CERN accelerator complex (not to scale). Starting on the right hand side at the proton source, protons are accelerated via the Radio Frequency Quadrupole (RFQ), the linear accelerator LINAC2, the Proton Synchrotron Booster (PSB), the Proton Synchrotron (PS), and the Super Proton Synchrotron (SPS). Finally, the proton bunches are injected as two counter-rotating beams into the Large Hadron Collider via the two transfer lines TI 2 and TI 8. The LHC is depicted, superimposed with the octant structure comprising eight arcs and eight straight sections, where each octant is centred around a straight insertion. Four of these straight sections are dedicated to utility insertions, i.e. two for cleaning of the LHC beams, one for the beam dump systems, and one for the RF systems. The general-purpose detectors, CMS and ATLAS, are located at P5 and P1, while the special purpose detectors ALICE and LHCb can be found at P2 and P8, respectively.

an energy of 750 keV. Also based on radio frequency technology, the linear accelerator LINAC2 constitutes the consecutive acceleration stage. Over a length of 30 m, the proton energy is enhanced to 50 MeV. The first circular accelerator in the chain is the Proton Synchrotron Booster (PSB), where the energy of the protons is increased to 1.4 GeV before entering the Proton Synchrotron (PS), which has a circumference of about 630 m. Finally, protons emerging from the PS with an energy of 26 GeV are injected into the Super Proton Synchrotron (SPS), constituting the final pre-acceleration stage. Between 1981 and 1984, the SPS was named Sp$\bar{\text{p}}$S and served as proton-antiproton collider, leading to the discovery of the $W^{\pm}$ and Z^0 bosons by the UA1 and UA2 collaborations [109–112]. In the LHC pre-accelerator chain, the SPS serves for the acceleration of proton bunches to an energy of 450 GeV before being injected as two counter-rotating beams into the LHC main ring via the transfer lines TI 2 and TI 8.

2.1.2. The LHC Main Ring

The Large Hadron Collider has been designed to fit into the existing LEP tunnel. Therefore, the centre-of-mass energy of the LHC is limited by the maximal attainable magnetic dipole field required to compensate for the centrifugal force experienced by charged beam particles. Since the LHC consists of several arcs and straight sections imposed by the tunnel geometry, the effective bending radius in the ring is 2.8 km. Hence, in order to keep particles with a design energy of 7 TeV in the beam pipe, specially-designed superconducting dipole magnets are employed providing a vertical magnetic field of 8.33 T [102, 103]. The magnet coils are made of copper-clad niobium-titanium (NbTi) cables and are cooled down for operation to a temperature of 1.9 K. The cooling is performed using superfluid helium which ingresses all excavations due to its negligible viscosity. In the copper-clad NbTi construction, copper provides rapid conduction of local heat generated by small surface defects or impurities. The advantage of this design compared to the use of solid niobium thus lies in the reduced susceptibility to quenching, which denotes the transition of the superconductor to the normal-conducting or resistive state. The choice of a proton-proton collider precluded the particle-antiparticle collider configuration of a common magnet system for both circulating beams, which exploits the opposite charges of the beam particles. At the Large Hadron Collider, the two beams of protons are therefore accelerated and stored in two separate beam pipes in the main arcs with common sections only at dedicated interaction regions. A beneficial effect of this architecture is the reduction of beam-beam interactions and collisions outside the interaction regions, which is needed to achieve the high LHC design luminosity. Instead of using two completely separate proton rings, the limited available space in the tunnel necessitated the design of twin-bore magnets comprising two sets of superconducting coils and beam pipes within a common mechanical structure and cryostat. A disadvantage of this twin-bore design, however, is the magnetic and mechanical coupling of the rings, which adversely affects the flexibility and results in a complicated magnetic structure. In addition to the 1,232 superconducting dipole magnets, a total of about 7,000 normal- and superconducting magnets are used for cleaning and focusing the beams, and to correct their trajectories.

The LHC consists of eight arcs and eight straight sections, which can be grouped into octants centred around the straight sectors, as depicted in figure 2.1. Each of the eight straight sections serves as a possible interaction point, referred to as Point 1 to Point 8, where experimental or utility insertions can be installed. At four of these possible interaction regions, the beams are forced to collide and particle detectors are installed in underground caverns to record such collisions. The two high luminosity insertions Point 1 and Point 5 are located at diametrically opposite straight sections, where the two general-purpose detectors ATLAS (A Toroidal LHC Apparatus) [113] and CMS [114, 115] are installed. In addition, the LHC hosts two special-purpose detectors located at the experimental insertions in Octant 2 and Octant 8, which also include the two beam injection systems. ALICE (A Large Ion Collider Experiment) [116] is dedicated to heavy ion physics and the LHCb (Large Hadron Collider beauty) [117] experiment has been specially-designed to investigate flavour physics. In addition, the comparatively small experiment LHCf (Large Hadron Collider forward) [118] will measure particle production very close to the beam pipes using detectors located about 140 m away from the ATLAS

Table 2.2: List of important LHC machine parameters for the phase of high luminosity running at the design centre-of-mass energy of 14 TeV adapted from [102] and for the current operation mode at a centre-of-mass energy of 7 TeV.

Quantity	Design	Current Operation
Luminosity $\left[\mathrm{cm}^{-2}\mathrm{s}^{-1}\right]$	10^{34}	$2 \cdot 10^{32}$
Number of bunches per proton beam	2,808	312
Number of protons per bunch	$1.15 \cdot 10^{11}$	$1.15 \cdot 10^{11}$
Normalised transverse emittance ϵ_n [μm]	3.75	1.6
Amplitude function β^* [m]	0.55	3.5
Crossing angle at interaction point [μrad]	285	100
Nominal bunch separation [ns]	25	75
Nominal energy of protons [GeV]	7,000	3,500
Number of main superconducting dipoles	1,232	1,232
Peak magnetic dipole field [T]	8.33	4.17
Dipole operating temperature [K]	1.9	1.9
Stored energy per beam [MJ]	362	24

interaction point. Similarly, the TOTEM (Total Elastic and Differential Cross Section Measurement) experiment [119] is designed to measure the total proton-proton cross section. For this purpose, forward detectors are employed which are installed at distances between 150 m and 400 m away from the CMS interaction point. The remaining four straight sections in Octant 3, 4, 6, and 7 are not intended for beam crossings but host utility insertions. Point 3 and Point 7 are dedicated to collimation systems, serving for momentum cleaning of both beams. Particles with a large momentum offset or large amplitude function are scattered and absorbed by dedicated collimators located at the two cleaning insertions. The straight section in Octant 4 contains two independent RF and feed-back systems for the two LHC beams. Protons entering the LHC main ring via one of the two transfer lines are accelerated to their nominal energy of 7,000 GeV using the superconducting copper-clad niobium radio frequency cavity system. The independent acceleration systems for the two beams are equipped with eight 400 MHz RF cavities each, accelerating the beams in total by 0.5 MeV/turn in an electric field of 5.5 MV/m. Finally, the straight insertion in Octant 6 is equipped with two independent beam abort systems. Therein, the two LHC beams can be independently extracted from the machine using dedicated fast-pulsed kicker magnets. The beams are then deflected away from the machine components to absorbers located in a beam dump cavern about 750 m away from the extraction magnets. Carbon has been chosen as absorbing material for the 362 MJ LHC beams due to its high sublimation temperature and thermal shock resistance. A list of important LHC machine parameters can be found in table 2.2, including design values for proton-proton collisions at a centre-of-mass energy of $\sqrt{s} = 14$ TeV and for the current operation mode at $\sqrt{s} = 7$ TeV.

In addition to the proton-proton operation, the LHC can also provide heavy ion collisions. For this purpose bunches of $7 \cdot 10^7$ lead nuclei Pb^{82+} can be collided at a centre-of-mass energy of about 5.5 TeV/nucleon. The design luminosity for heavy ion operation

is $\mathcal{L} = 10^{27}$ cm^{-2}s^{-1} with a bunch separation time of 100 ns. Ion-ion collisions are primarily provided at Point 2 for the specialised ALICE detector, but the CMS and ATLAS collaborations also study these collisions with similar luminosities. The CMS heavy ion physics program [120] is however not further discussed here, since the study presented in this thesis concentrates on results obtained from proton-proton collisions.

The injection of beams into the different facilities of the CERN accelerator complex is accomplished by special fast-ramping magnets called injection kickers. The rise times of these injection kickers entail gaps of missing bunches in the beams. At nominal operation, the 25 ns bunch spacing is induced by the 40 MHz RF system of the Proton Synchrotron leading to a total of 3,564 RF buckets over the entire LHC ring. These RF buckets, denoting the specific phase-space regions for acceleration of protons by the oscillating fields, limit the maximum number of bunches per beam. At nominal operation the SPS is filled from three to four PS batches, where each batch consists of 72 bunches and eight empty buckets due to the SPS injection kicker rise time of 220 ns. The LHC is then filled from twelve SPS batches of 5.48 µs or 7.86 µs duration, to be successively deposited over the machine circumference. Due to the LHC injection kicker rise time of 0.94 µs, the SPS batches are injected with gaps of 38 RF buckets. One final gap of 3.0 µs allows for the fall time of the injection kickers and the rise time of the beam dump kickers to be able to dump the LHC beams in a controlled manner within one revolution. This leads in total to 2,808 bunches of $1.15 \cdot 10^{11}$ protons filling the 3,564 available RF buckets per LHC beam. The minimum time required for filling both LHC beams from multiple cycles of the involved accelerators, and acceleration to their nominal energy of 7 TeV is estimated to about seventy minutes.

The luminosity is not constant over a physics run, but decays due to the depletion of intensities and emittances of the circulating beams. The main reason for the luminosity reduction during nominal LHC operation is the beam loss from collisions. Other contributions emerge from Touschek scattering and from particle losses due to emittance blow-up, which can be caused by the scattering of beam particles on residual gas, the non-linear force of the beam-beam interaction, intra-beam scattering, or RF noise. Flux monitors are used for the measurement of the instantaneous luminosity, for optimisations, and for the equalisation of the two beams at the interaction regions. In order to suppress the beam loss related background, gas ionisation chambers are employed to detect the flux of showers generated by neutral particles emerging from the proton-proton collisions. These luminosity flux monitors are installed inside the TAN (Target Absorber Neutral) devices, which serve to protect machine elements from neutral particles. For this purpose, the TAN absorbers are located in front of the dipole magnets guiding the beams from the interaction regions into the two separate beam pipes. The LHC luminosity lifetime at the design value of $\mathcal{L} = 10^{34}$ cm^{-2}s^{-1} and a centre-of-mass energy of 14 TeV is estimated to be about fifteen hours before the luminosity has degraded and necessitates a dump and refill procedure of the Large Hadron Collider.

Since the first intentional proton-proton collision on May 30$^{\text{th}}$, the Large Hadron Collider has been operated as pp collider at a centre-of-mass energy of 7 TeV until November 2010. Shortly thereafter, a period of about one month was dedicated to lead-lead collisions which finally demonstrated the successfully commissioning of the LHC machine.

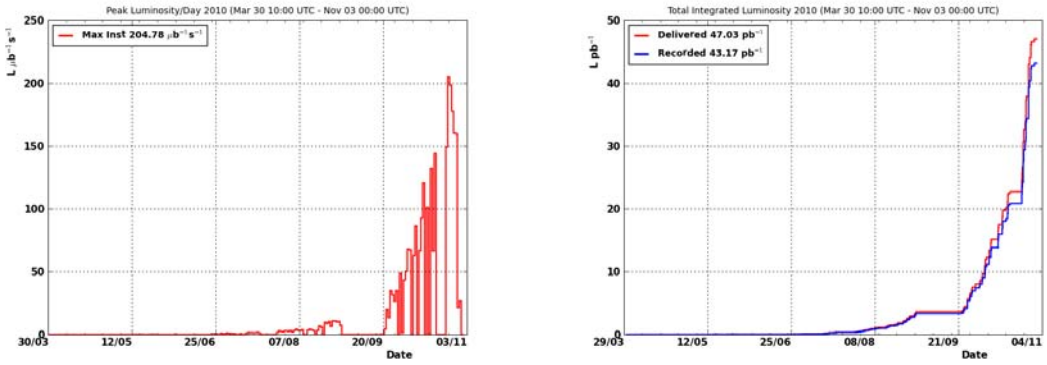

(a) (b)

Figure 2.2: Instantaneous and integrated luminosity of the LHC [123]. The instantaneous luminosity as a function of time is depicted in (a), leading to a peak luminosity of $2.0 \cdot 10^{32}$ cm^{-2}s^{-1}. Of special interest for physics analyses is the integrated luminosity given in (b). Therein, the integrated luminosity delivered by the LHC is represented by the red curve and the blue curve indicates the luminosity successfully recorded with CMS detector, corresponding to 43.2 pb^{-1}.

The reduction of the centre-of-mass energy for pp collisions to half of the design value has been devised for the operation in 2010 [121, 122]. During a one year shut-down in 2012, the LHC will presumably be prepared for operation at the design parameter values. Besides the lower centre-of-mass energy, several other parameters have been altered in the LHC start-up phase. A comparison between the design values and the ones most recently achieved is given in table 2.2. Accordingly, a maximum of 312 bunches per beam, each consisting of $1.15 \cdot 10^{11}$ protons, have been collided and the amplitude function at the CMS interaction point was enlarged to $\beta^* = 3.5$ m. The performance of the machine in this configuration is depicted in figure 2.2, where the instantaneous luminosity is given as a function of time. Additionally, the integrated luminosity of the LHC and the corresponding value for the recorded luminosity by the CMS experiment are shown. Until November 2010, the LHC provided an integrated luminosity of 47.0 pb^{-1}, among which 43.2 pb^{-1} have been successfully recorded with the CMS apperatus.

2.2. The CMS Experiment

The observation and detailed analysis of proton-proton collisions requires the application of large-scale general-purpose detectors to explore the versatile physics opportunities provided by the Large Hadron Collider. Multi-purpose particle detectors are typically designed forward-backward and azimuthally symmetric, and comprise a cylindrical barrel and end cap structure aiming for a 4π solid angle coverage. This hermetic angular coverage is important for identification and measurement of a large phase-space of final state particles emerging from the interaction region. Several specially-designed sub-systems for the detection of different types of particles are arranged concentrically around each other in an onion-like structure, exemplarily depicted in figure 2.3. Closest to the interaction region is a tracking system featuring measurements for the reconstruction of charged

particle trajectories. A homogeneous magnetic field with field lines parallel to the beam axis furthermore leads to a bending of these trajectories, which facilitates the determination of the particles' momentum and the sign of their charges. Calorimetry systems based on electromagnetic and hadronic calorimeters surrounding the tracking volume serve to absorb particles and to measure their deposited energy. Electromagnetic calorimeters are designed to measure the energy of particles interacting primarily via the electromagnetic force like electrons or photons. Electrons penetrating the electromagnetic calorimeter radiate highly energetic bremsstrahlung photons, which in turn convert into e^+e^- pairs. This results in a cascade of secondary particles of decreasing energy referred to as electromagnetic showers. The radiation length X_0, defined as the distance over which a high-energetic electron looses all but $1/e$ of its energy by bremsstrahlung, is the characteristic length scale for the description of the longitudinal electromagnetic calorimeter thickness. For high-energetic photons, the radiation length corresponds to $7/9$ of the mean free path for e^+e^- pair production. Similar to the electromagnetic showers, hadronic showers result from strong interactions of hadrons with heavy nuclei in the material of the hadronic calorimeter. Here, the typical length scale for characterising the hadronic calorimeter thickness is the nuclear interaction length λ_I, which denotes the mean free path length of a high-energetic hadron before interacting with the traversed material. Finally, the muon system constitutes the outermost part of a typical general-purpose detector. Due to their higher rest mass, muons emit significantly less bremsstrahlung compared to electrons and do not strongly interact within the hadronic calorimeter. Therefore, muons deposit only a small fraction of their energy in the calorimeter system and penetrate the muon system, which is used for their detection and identification.

The Compact Muon Solenoid [114, 115] experiment hosted in an underground cavern about 100 m below surface at Point 5 near Cessy, France, is one of the two competing general-purpose particle detectors at the Large Hadron Collider. The CMS apparatus has an overall length of 21.6 m, a diameter of 14.6 m, and a total weight of 12,500 t, which can almost entirely be ascribed to the enormous weight of the 10,000 t iron yoke. Since the excavation of the underground cavern was not completed until 2004, the CMS detector has been build on the surface in fifteen separate sections, which have then been lowered into the experimental cavern for assembly and installation. In contrast to its competitor ATLAS, the CMS detector thus features a modular concept of several discs as depicted in figure 2.4, permitting the simultaneous work on different detector parts and an easy accessibility for maintenance work during regularly scheduled LHC shut-down phases. Despite its huge weight the CMS apparatus is comparatively compact, at least compared to ATLAS, which exhibits twice the volume of CMS but only half of its weight.

The design of the CMS experiment has been driven by the requirements imposed by the envisaged physics goals of the Large Hadron Collider. The prime motivation of the LHC is to elucidate the nature of electroweak symmetry breaking and to examine the consistency of the Standard Model at energy scales above 1 TeV, where various alternatives to the SM invoke new symmetries, new forces, or constituents. The main focus in the Higgs boson search at CMS lies in final states including leptons or photons, such as $H^0 \to ZZ^* \to \mu\mu\mu\mu$ or $H^0 \to \gamma\gamma$, whereas physics beyond the Standard Model could lead to discoveries of supersymmetric particles, extra dimensions, or novel massive vector particles like a Z' boson involving a forward-backward asymmetrically dileptonic decay.

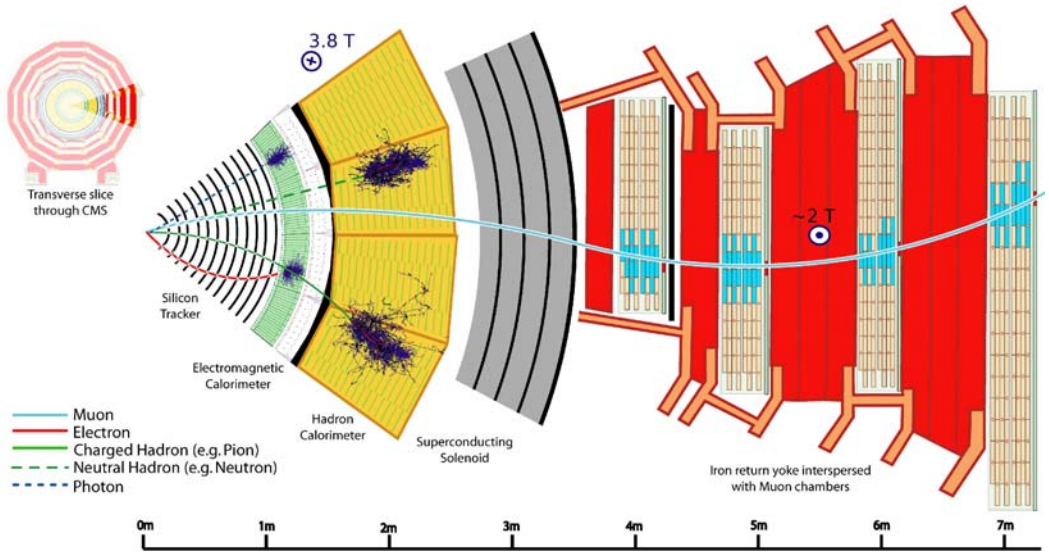

Figure 2.3: Transverse slice through the CMS detector exhibiting the onion-like structure of a typical general-purpose collider detector [12]. Additionally, some typical signatures like particle trajectories and electromagnetic and hadronic showers are depicted, originating from primary electrons, muons, charged and neutral hadrons, and photons. Electrons and photons deposit their entire energy in the electromagnetic calorimeter, whereas hadrons pass this detector component and induce hadronic showers in the hadronic calorimeter. Muons traversing the detector material are identified in the muon system in the outermost part of the detector. Charged particles furthermore exhibit curved trajectories due to the applied magnetic field.

A significant amount of missing transverse energy constitutes the signature of supersymmetric processes. Due to momentum conservation, the vector sum of all transverse momenta must be balanced in a proton-proton collision. The non-vanishing part of this sum is therefore called missing transverse energy and is an indirect measure for neutrinos or exotic particles which interact only weakly within the detector material. To accomplish the versatile requirements, a hermetic and compact design with a strong central magnetic field has been chosen for the CMS detector, aiming for an excellent muon identification and muon momentum resolution up to $p_{\mathrm{T}} = 1$ TeV/c over a wide geometric range. Furthermore, the CMS apparatus design aspires a good reconstruction efficiency and momentum resolution for charged particles in the inner tracking system, an accurate diphoton and dielectron invariant mass resolution of 1% at 100 GeV/c^2 with high angular coverage, efficient photon and lepton isolation at high luminosities, and efficient π^0 meson rejection. Additionally, a hadronic calorimeter with optimal hermetic coverage is required for an accurate missing transverse energy determination and fine lateral segmentation for a good dijet mass resolution.

Prior to the observation of proton-proton collision events, the CMS experiment was extensively tested in an exercise known as Cosmic Run At Four Tesla (CRAFT). Operating at nominal detector conditions, about 270 million cosmic muon triggered events were recorded, serving for detector performance studies, the commissioning of the alignment and calibration techniques, and to make several cosmic ray measurements [124]. As result of this exercise, the Compact Muon Solenoid apparatus has been well prepared and the

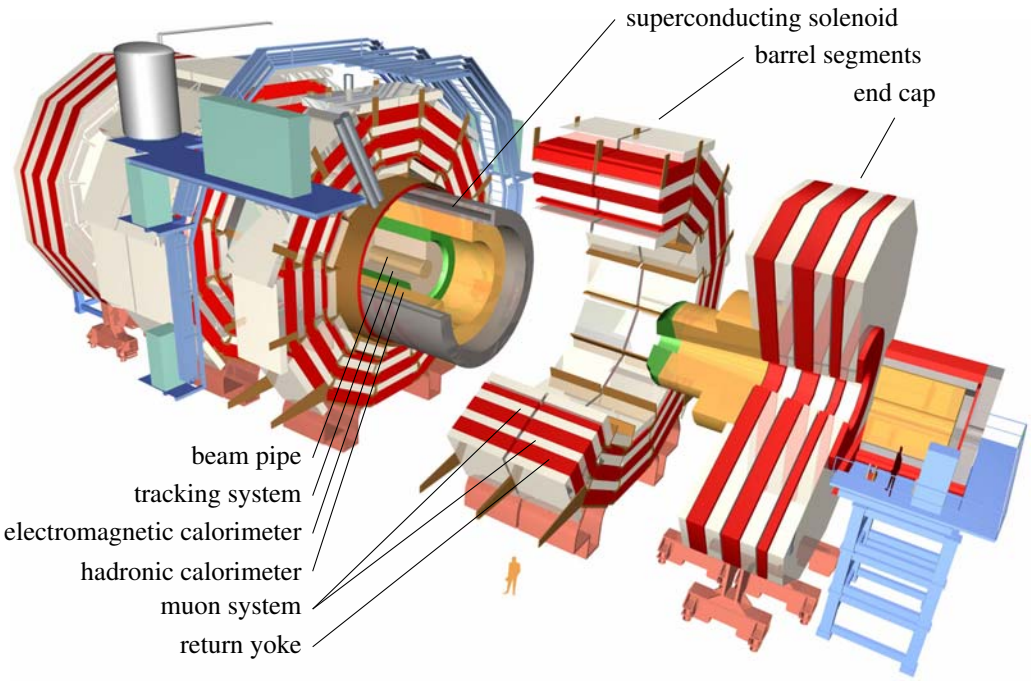

Figure 2.4: Schematic view of the Compact Muon Solenoid apparatus with the typical onion-like structure of a collider detector and the 4π solid angle design with a barrel part and two end caps [12]. The beam line in the innermost part is surrounded by the tracking system, the electromagnetic and hadronic calorimeters, and the superconducting solenoid. The muon system in the outermost part is inserted in excavations of the iron return yoke. The modular concept of several barrel segments and two end cap discs facilitates an easy accessibility for possible detector maintenance work during regularly scheduled LHC shut-down phase.

first meaningful physics results from proton-proton collisions were obtained by the CMS collaboration shortly after the LHC resumed operation at reduced centre-of-mass energies in November 2009 [125].

The coordinate system adopted for the description of the CMS detector geometry is depicted in figure 2.5 with the origin centred at the nominal collision point inside the experiment. The y axis points vertically upwards and the x axis points radially inwards towards the centre of the LHC. Thus, in order to obtain a right-handed coordinate system, the z axis points from Point 5 along the beam direction towards the Jura mountains. The azimuthal angle ϕ is measured from the x axis in the $x-y$ plane, the polar angle θ is defined with respect to the z axis, and r denotes the radial distance to the beam pipe. Another commonly used quantity in particle physics is the rapidity y defined as

$$y = \frac{1}{2} \ln \left(\frac{E + p_z}{E - p_z} \right) , \tag{2.4}$$

where E is the energy of the particle and p_z the z component of its momentum vector. An advantage of this dimensionless quantity is the invariance of rapidity differences Δy under Lorentz boost in the z direction. For massless particles, as well as for massive particles in the ultra-relativistic limit, the rapidity y is equal to the purely geometrically defined

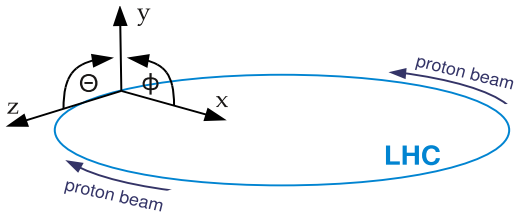

Figure 2.5: Coordinate system for the description of the CMS detector geometry with the origin centred at the nominal proton-proton interaction point.

pseudorapidity η given by

$$\eta = -\ln\left(\tan\frac{\theta}{2}\right), \tag{2.5}$$

which is typically used to describe detector geometries and particle directions. The azimuthal angle ϕ and the pseudorapidity η can then be used to define the angular distance between two point-like objects in the detector volume as $\Delta R = \sqrt{(\Delta\eta)^2 + (\Delta\phi)^2}$. The transverse energy and the transverse momentum of a particle are defined as $E_{\mathrm{T}} = E \cdot \sin\theta$ and $p_{\mathrm{T}} = p \cdot \sin\theta$, respectively, and can be computed from the corresponding x and y components.

The required performance of the inner tracking and the muon system, and therefore the required bending of charged particle tracks drives the design of the detector layout through the choice of the magnetic field configuration. A superconducting solenoid constitutes the core of the CMS detector. With an inner diameter of 5.9 m and a length of 12.9 m, the superconducting magnet is large enough to envelope the inner tracking and calorimetry systems. Operated at a nominal current of about 19.5 kA, the superconducting niobium-titanium coil provides a magnetic field of 3.8 T along the beam axis, leading to a total stored field energy of 2.7 GJ. Its return field with a strength of about 2 T saturates 1.5 m of iron in the return yoke allowing for the insertion of four muon stations. The individual sub-systems depicted in figures 2.3 and 2.4 are briefly discussed in the following sections, starting with the tracking system at the innermost part of the detector.

2.2.1. Tracking System

The inner tracking system [126, 127] of the CMS apparatus is designed to provide a robust, efficient, and precise measurement of charged particle trajectories emerging from proton-proton collisions and the accurate reconstruction of primary and secondary vertices. One important constraint for the design of the tracking system is the high particle density. At nominal LHC luminosity, an average of about 1,000 particles per bunch crossing are expected to traverse the tracker volume. Therefore, a tracking device with high granularity and fast response is required for reliable identification of trajectories and to attribute them to the correct bunch crossing. The intense particle flux will also cause severe radiation damage to the tracking system, which demanded the development of detector components able to operate in this harsh environment for an expected lifetime of about ten years of operation. Furthermore, the amount of material in the tracker has to be kept at a minimum in order to limit multiple scattering, photon conversion, and nuclear interactions. For these various reasons, an all-silicon detection technology has been chosen for

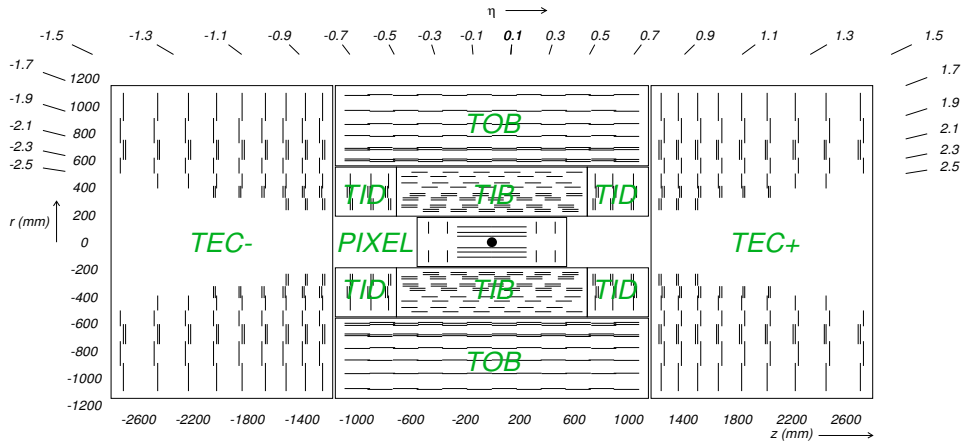

Figure 2.6: Schematic longitudinal view of the CMS tracking system. The innermost part is instrumented with the pixel detector comprising a three-layered barrel tracking device and two end cap discs on each side. The silicon micro-strip detector is divided into the Tracker Inner Barrel (TIB) and the Tracker Outer Barrel (TOB) in the barrel part, while the end cap system includes the Tracker Inner Disc (TID) and the Tracker End Caps (TEC). Each line represents a detector module, whereas stereo modules are indicated by double lines.

the inner tracking system, which exhibits a length of 5.8 m and a diameter of 2.5 m leading to a tracking coverage of up to $|\eta| = 2.5$. With an overall active silicon area of about 200 m^2, the CMS tracking system is the largest silicon tracker ever built. The tracking system, schematically illustrated in figure 2.6, can be divided into two main sub-systems employing two different silicon designs. All detector elements are housed in the tracker support tube and the whole tracking volume is operated at a temperature of about $-10°$C.

The region closest to the interaction point is instrumented with a silicon pixel detector comprising three barrel layers and two end cap discs on each side. The barrel layers are arranged in concentric rings at radii of 4.4 cm, 7.3 cm, and 10.2 cm and have a length of 53 cm each. The two end cap discs located at $z = \pm 34.5$ cm and $z = \pm 46.5$ cm exhibit a turbine-like geometry with blades rotated by 20° and a radial expansion of $(6 - 15)$ cm. Driven by the desired resolution and occupancy of the detector, a total of 66 million pixels with a size of 100×150 μm^2 cover an area of 1 m^2 over the entire pseudorapidity range $|\eta| < 2.5$. The expected single point resolution of the pixel detector is about 10 μm for an $r - \phi$ measurement and about 15 μm in the z coordinate.

At intermediate distances from the beam pipe, the reduced particle flux allows the use of a micro-strip detector composed of 9.3 million silicon strips. Constituting the second component of the CMS tracking system, the silicon strip detector is also designed with barrel layers and end cap discs and covers the region 20 cm $< r <$ 116 cm. In the barrel part the Tracker Inner Barrel (TIB) with four layers of silicon strips covers a region up to $|z| = 65$ cm and extends in radius towards $r = 55$ cm. The Tracker Outer Barrel (TOB) comprises six detection layers and extends up to $|z| = 110$ cm. The end cap structure of the micro-strip detector include two Tracker End Cap (TEC) discs in the region 120 cm $< |z| <$ 280 cm and 22.5 cm $< r <$ 113.5 cm with nine layers each and three layers in the Tracker Inner Disc (TID) closing the gap between TIB and TEC. With a single point resolution of $(23 - 35)$ μm for the TIB and of $(35 - 53)$ μm for the TOB,

a total of ten $r-\phi$ measurements are provided. Furthermore, the end caps allow twelve ϕ measurements to be performed per particle trajectory. As can be seen in figure 2.6, several layers are equipped with stereo modules. In these cases, a second module is mounted back-to-back with a stereo angle of 100 mrad in order to provide a measurement of the second coordinate, i.e. the z coordinate in the barrel and r in the discs. The typical single point resolutions for a measurement of the z coordinate ranges between 230 µm and 530 µm in the TIB and the TOB, respectively. This tracker layout ensures at least nine hits per particle trajectory in the silicon strip tracker in the full range of $|\eta| < 2.4$ with at least four of them being two-dimensional measurements.

The expected transverse momentum resolution for a high-momentum charged particle of $p_{\mathrm{T}} \approx 100$ GeV/c is about $(1-2)\%$ up to $|\eta| = 1.6$, while at lower momenta the resolution is decreased due to multiple scattering within the tracker material. The efficiency for muons is expected to be about 99% over most of the acceptance with slight inefficiencies at $|\eta| > 2.1$, due to the reduced coverage of the pixel end cap discs.

2.2.2. Calorimetry System

The calorimetry system of the CMS apparatus is equipped with electromagnetic and hadronic calorimeters to perform energy measurements of final state particles leaving the tracker volume. The electromagnetic calorimeter (ECAL) [128, 129] provides an energy measurement of electrons, photons, and charged hadrons, and is placed hermetically around the silicon tracker. The hadronic calorimeter (HCAL) [130] in turn enfolds the ECAL and is designed to measure the energy of charged and neutral hadrons. A schematic view of the calorimetry system completed by the relative location of the tracking system and the muon chambers can be found in figure 2.7.

The homogeneous, compact, and high granularity design of the ECAL has been driven by the need for excellent diphoton resolution. Lead tungstate ($PbWO_4$) scintillating crystals are used as detector material due to its high density of 8.28 $\mathrm{g/cm^3}$ and radiation hardness. Correlated to this high density is a small radiation length of $X_0 = 0.89$ cm and a Molière radius of $R_{\mathrm{M}} = 2.2$ cm, where the latter defines the radius of a cylinder containing on average 90% of the shower energy and hence characterises the transverse scale of an electromagnetic shower. Furthermore, fast energy measurements are facilitated by the scintillation decay time of $PbWO_4$, which is of the same order of magnitude as the LHC bunch crossing time, leading to approximately 80% light emission within 25 ns.

Like the tracking system, the ECAL exhibits the characteristic barrel and end cap structure. The Electromagnetic Barrel (EB) covers the region $|\eta| < 1.479$ and consists of 61,200 tapered-shaped $PbWO_4$ crystals mounted in a quasi-projective geometry to avoid cracks aligned with particle trajectories. Each barrel crystal covers an area of $\Delta\eta \times \Delta\phi = 0.0174 \times 0.0174$ with an inner front-face cross-section of about 22×22 mm^2 and a length of 230 mm corresponding to 25.8 X_0. Another 14,648 lead tungstate crystals instrument the two Electromagnetic End caps (EE) with an angular coverage of $1.479 < |\eta| < 3.0$. Located at $z = \pm 315.4$ cm, the positioning of the EE takes into account an estimated shift of 1.6 cm towards the interaction point once the solenoidal magnetic field is switched on. The EE consists of identically shaped crystals, which are installed in an $x-y$ grid slightly off-point from the nominal vertex position. Each crystal

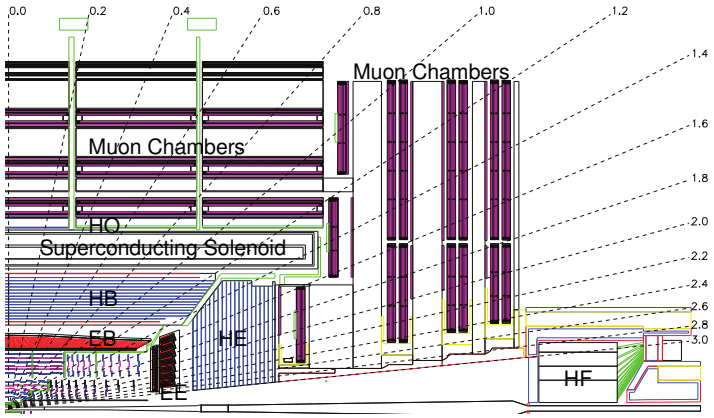

Figure 2.7: Longitudinal view of one quarter of the CMS detector [115]. The tracking system is surrounded by the electromagnetic and the hadronic calorimeters located inside the superconducting solenoid coil, except for the Hadronic Outer (HO) and the Hadronic Forward (HF) calorimeters. The barrel part of the calorimetry system is equipped with the Electromagnetic Barrel (EB) and the Hadronic Barrel (HB) calorimeters, while in the end caps the Electromagnetic End caps (EE) and the Hadronic End caps (HE) are installed. Furthermore, the ECAL preshower detector is mounted in front of the EE. In the outermost part of the detector, the iron return yoke is interspersed with several muon chambers.

has a front-face cross-section of 28.62×28.62 mm^2 with a length of 22 cm corresponding to 24.7 X_0. Despite the obvious advantages of lead tungstate it has a comparatively low light emittance and thus requires the adoption of photodetectors with intrinsic gain. The magnetic field configuration and the expected level of radiation led to the choice of avalanche photodiodes in the barrel part, due to their insensitivity to high magnetic fields, whereas the high particle flux in the end cap region favoured specially-designed vacuum phototriodes with higher quantum efficiency. For the identification of neutral pions in the ECAL end caps within the fiducial region $1.653 < |\eta| < 2.6$, a silicon preshower detector (ES) is located between TEC and EE. It furthermore assists in the identification of electrons and improves the position determination of electrons and photons. The ES is a sampling calorimeter comprising two layers of lead radiators and silicon strip sensors. While the lead radiators serve for initiation of electromagnetic showers from incoming photons or electrons, the two orthogonally aligned silicon sensors are installed behind each radiator to measure the deposited energy and the transverse shower profile. The total thickness of the preshower detector at $|\eta| = 1.653$ is 20 cm, corresponding to a material budget of 2 X_0 and 1 X_0 in front of the first and second sensor layer, respectively. Therefore, about 90% of incident photons in this geometrical region produce a e^+e^- pair before reaching the second sensor layer.

The energy resolution of the ECAL was tested with electron beams of $(20 - 250)$ GeV in 2004, leading to a typical value of $\frac{\sigma(E)}{E} = \frac{2.8\%}{\sqrt{E}} \oplus 0.3\%$ [131], with the energy E measured in GeV. Another challenge is the ECAL calibration, including the absolute energy calibration and the inter-calibration, which have to be taken into account due to crystal-to-crystal variations of the scintillation light yield. Initial inter-calibrations have been performed using cosmic rays and high-energy electron test beam data [132]. The ultimate inter-calibration precision can then be achieved *in situ* with physics events, for example by

comparison with trajectory measurements in the tracking system or with electrons from $W^{\pm} \to e\nu$ boson decays. Furthermore, $Z \to e^+e^-$ and $Z \to \mu^+\mu^-\gamma$ decay processes provide information about photon conversions and bremsstrahlung radiation.

The hadronic calorimeter enfolding the electromagnetic calorimeter is particularly important for measurements of hadronic particle jets in conjunction with the ECAL and for the estimation of the missing transverse energy. The design of the HCAL has mainly been driven by the magnetic properties of the material and the requirement to place the calorimeter inside the bore of the solenoid, which constrains the total amount of shower absorbing material in terms of interaction lengths. To provide sufficient absorber material, a sampling calorimeter is employed with non-magnetic brass absorbers interspersed with scintillator tiles as active material. Due to its high density of 8.53 $\mathrm{g/cm^3}$, brass exhibits a radiation length of $X_0 \approx 1.5$ cm and a nuclear interaction length of $\lambda_\mathrm{I} = 16.42$ cm. Wave length shifting fibres are employed to collect and transport the emitted light to hybrid photodiodes (HPD). In contrast to the ECAL, most of the energy is deposited in the absorber material and only a fraction of the energy is actually measured, resulting in a decreased energy resolution of the HCAL.

The Hadronic Barrel (HB) calorimeter covering $|\eta| < 1.3$ consists of 36 identical azimuthal wedges constructed of flat brass absorber plates aligned parallel to the beam axis, while the inner- and outermost plates are made of stainless steel for structural strength. The plastic scintillator system is divided into 16 η sectors, resulting in a segmentation of $\Delta\eta \times \Delta\phi = 0.087 \times 0.087$. The Hadronic End caps (HE) covers the region $1.3 < |\eta| < 3.0$ with a granularity of $\Delta\eta \times \Delta\phi = 0.087 \times 0.087$ for $|\eta| < 1.6$, increasing to $\Delta\eta \times \Delta\phi \approx 0.17 \times 0.17$ for higher pseudorapidities. Here, the design is driven by the need to minimise cracks between the HB and HE, rather than the single-particle energy resolution. Since the HE is inserted into the ends of the solenoid, the same absorber material has been chosen as for the HB, resulting in a total HE absorber thickness of about $10\,\lambda_\mathrm{I}$ including the ECAL material. The effective thickness of the HB increases from $5.82\,\lambda_\mathrm{I}$ at $\eta = 0$ to $10.6\,\lambda_\mathrm{I}$ at $|\eta| = 1.3$, while the ECAL adds an additional material budget of $1.1\,\lambda_\mathrm{I}$. In order to ensure adequate sampling in the central region, the hadronic calorimeter is extended outside the solenoid coil by the Hadron Outer (HO) calorimeter. Covering the region $|\eta| < 1.26$, the HO closely follows the barrel calorimeter segmentation. The HO consists of one to two scintillator tiles mounted outside the vacuum tank of the magnet coil using the solenoid as additional absorbing material. Its purpose is to detect the tails of the hadronic shower and the missing transverse energy measurements, by sampling the energy leakage of deeply penetrating hadron showers at the rear of the barrel calorimetry system. Thus, the HO extends the minimum absorber thickness to $11.8\,\lambda_\mathrm{I}$, except at the barrel end cap boundary region. The HCAL coverage at $3.0 < |\eta| < 5.0$ is provided by the Hadronic Forward (HF) calorimeter, which is mainly designed to withstand the large particle flux in this region. This led to the choice of steel absorber plates interspersed with quartz fibres as active medium. The signals are generated in form of Cherenkov light, rendering the detector mostly sensitive to the electromagnetic component of the hadronic showers. The HF is designed as a cylindrical steel absorber structure with a radial expansion of 12.5 cm $< r <$ 130 cm and the front-face of the calorimeter is located at $|z| = 11.2$ m. The quartz fibres run parallel to the beam axis, and provide a segmentation of $\Delta\eta \times \Delta\phi = 0.175 \times 0.175$ which becomes coarser for higher pseudo-

rapidities. Fast photomultiplier tubes shielded with steel and polyethylene are used for amplification of the Cherenkov light signals, facilitating real-time luminosity measurements with the Hadronic Forward calorimeter.

2.2.3. Muon System

The muon system [133] of the Compact Muon Solenoid apparatus is designed for the momentum and charge reconstruction of muons over the entire kinematic range of the Large Hadron Collider and provides a full geometric coverage for muon identification up to $|\eta| = 2.4$. Good muon momentum resolution and trigger capability is facilitated by the high solenoidal magnetic field and its flux return yoke, where the latter also serves as hadron absorber and therefore improves the muon identification. As depicted in figure 2.8, the muon system comprises three different types of gaseous detectors embedded in the iron return yoke. The particular choice of detector technologies has been driven by the requirement for fast response, excellent resolution, coverage of a very large total surface, and the need to operate in dense radiation environments.

Like the tracking and calorimetry systems, the muon system comprises a barrel part and two planar end caps. In the barrel region covering $|\eta| < 1.2$, the neutron induced background is small. Therefore, the anticipated low rate, combined with the comparatively low strength of the residual magnetic field, allows for the use of 250 drift tube (DT) chambers arranged concentrically around the beam line. Each of the first three barrel muon stations, called MB 1 to MB 3, contains eight chambers for the measurement of muon trajectory coordinates in the $r-\phi$ bending plane and four chambers for the measurement in z direction. In contrast, the fourth muon station MB 4 does not include the z measurement planes. The number of chambers in each station and their orientation have been chosen to provide a good efficiency for linking muon hits recorded with the different stations into a single muon track, while efficiently rejecting background hits. In each DT chamber, several drift tube cells are arranged in two or three superlayers, which in turn consist of four layers of drift tubes. Two of these superlayers have anode wires parallel to the beam line, providing an $r-\phi$ measurement for each particle trajectory. In between, the third superlayer has a perpendicular orientation and thus provides a measurement of the z coordinate. This design facilitates a 95% trajectory reconstruction efficiency for high-p_{T} muons in $|\eta| < 0.8$ and momentum measurements solely derived with the barrel muon system. Furthermore, the mechanical precision of the muon chamber construction aims at a resolution of 100 µm for an $r-\phi$ measurement.

The two end caps covering the region $0.9 < |\eta| < 2.4$ are equipped with 468 Cathode Strip Chambers (CSCs), as they can withstand the enhanced muon rates and background levels, and the largely non-uniform magnetic field. Similar to the barrel region, the trapezoidal CSCs are arranged in four layers, called ME 1 to ME 4, positioned perpendicularly to the beam axis and interspersed between the flux return yoke. CSCs are multi-wire proportional chambers comprising six anode wire planes interleaved among seven cathode panels. While the wires are installed azimuthally and provide an r measurement for particle trajectories, the cathode panels, segmented into strips of constant $\Delta\phi$ width, run approximately perpendicular to the wires. Thus, induced charges on the strips provide a measurement of the ϕ coordinate. The muon system typically shows a $(95-99)\%$ offline reconstruction efficiency obtained from simulated single-muon samples. Small inefficien-

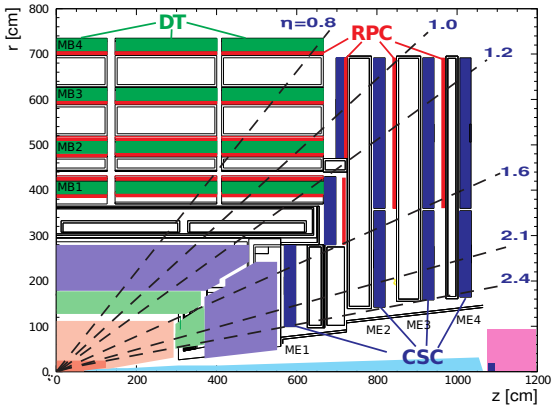

Figure 2.8: Longitudinal view of one quarter of the CMS Muon System adapted from [114]. In the barrel region Drift Tubes (DT) and Resistive Plate Chambers (RPC) are employed, while the end cap region is equipped with RPCs and Cathode Strip Chambers (CSC). In total four barrel muon stations, MB 1 to MB 4, and four end cap muon stations, ME 1 to ME 4, are installed.

cies at $|\eta| = 0.25$, $|\eta| = 0.8$, and $|\eta| = 1.2$ can be ascribed to the region between two DT wheels and the barrel end cap transition region, respectively. The best spatial resolution is provided at the centre of the charge distribution on the CSC strips and is typically about 200 µm, while the resolution in ϕ is of the order of 1 mrad.

In addition to the CSC and DT chambers, a complementary system of Resistive Plate Chambers (RPCs) is installed in the barrel and the end cap region. RPCs are double-gap chambers operated in avalanche mode to ensure reliable operation at high rates. While the DT and CSC sensors yield precise position measurements, RPCs exhibit a very fast response and are thus particularly suited to unambiguously identify the correct bunch crossing to which a trajectory is to be associated. Moreover, they provide position information in the barrel end cap overlap region, which has typically few measurements from the other systems. In the initial stage of the CMS experiment, the RPCs will cover the region $|\eta| < 1.6$, which will then be extended to the region $|\eta| < 2.1$. As can be seen in figure 2.8, this initial coverage is provided by six layers of RPCs, among which two chambers are installed in each of the first two muon stations, MB 1 and MB 2, and one RPC in each of the two last stations, MB 3 and MB 4. The end cap region is instrumented with one RPC in each of the first three stations, ME 1 to ME 3, in order to exploit coincidences between the stations for background reduction, to improve the time resolution for bunch crossing identification, and to achieve a good p_{T} resolution.

Due to multiple scattering in the detector material in front of MB 1, the offline muon momentum resolution for transverse momenta up to $p_{\mathrm{T}} = 200$ GeV/c in the central region is about 9% for the muon system, while, at $p_{\mathrm{T}} = 1$ TeV/c, this resolution varies between $(15 - 40)\%$ depending on $|\eta|$. A global momentum reconstruction based on muon system and inner tracking system information can be used to improve these resolutions. Employing this alternative approach yields a momentum resolution of about 1% or better for central muons with $p_{\mathrm{T}} < 100$ GeV/c and about $(5 - 10)\%$ at $p_{\mathrm{T}} = 1$ TeV/c, again depending on $|\eta|$. The entire muon system layout reaches a reconstruction efficiency of 90% for muons with a transverse momentum larger than 100 GeV/c in the full geometric range of $|\eta| < 2.4$.

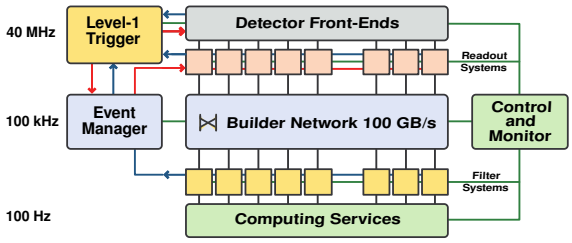

Figure 2.9: Architecture of the CMS Data Acquisition System [115] comprising detector electronics, the first level trigger processors, the readout network, and an online CPU filter farm executing the high-level trigger software. With the two applied filter steps, the enormous data volume induced by the 40 MHz LHC bunch crossing frequency can be reduced to a manageable level of 100 events/s, which are then transferred for permanent archiving and further processing.

2.2.4. Data Acquisition and Trigger System

The LHC bunch crossing rate of 40 MHz entails about 10^9 interactions per second, resulting in about 100 TB/s of data. The trigger and data acquisition system [134, 135] serves for the reduction of this enormous amount of data to a manageable level by selecting interesting events among the huge amount of background events. In order to achieve this reduction, the data acquisition system depicted in figure 2.9 consists of the detector electronics, the first level (Layer-1) trigger processors, the readout network, and an online CPU filter system, which executes the high-level trigger (HLT) software. The Level-1 trigger is based on customised programmable hardware aiming for a data reduction to about 100 kHz. For this purpose, the Level-1 trigger is divided into the calorimeter trigger, the muon trigger, and the global trigger. In a first step, the first two of these triggers involve algorithms for the reconstruction and ranking of calorimeter and muon objects. The four best candidates of each type are then passed to the global trigger, which also receives the total and missing transverse energy measurements and the jet multiplicity above certain programmable thresholds from the calorimeter trigger. According to configurable trigger conditions, the global trigger finally selects the interesting events based on the presence of several different objects with energies or momenta above predefined thresholds. In order to allow a dead-time free data acquisition, the entire event information is stored in pipeline memories while the trigger decision is being taken. The depth of these pipeline buffers is limited to 128 LHC bunch crossings, leading to a total Layer-1 trigger latency of 3.2 µs. The readout network has to handle a data volume of about 100 GB/s, which is transferred to the online computing farm running the HLT software. For the high-level trigger, more detailed information and sophisticated reconstruction algorithms are used providing the possibility for a full reconstruction of the event topologies and filtering according to several desired physics goals. Due to this trigger software approach, a maximum flexibility in terms of the optimisation of selection algorithms and trigger thresholds can be obtained. Moreover, the usage of standard computer hardware allows to profit from the fast evolution of computing technology during the years of operation. Finally, the application of the high-level trigger reduces the overall data volume to an event rate of a few 100 Hz, which is then transferred for permanent archiving to a central storage system located at CERN.

Although the CMS trigger system allows for an event rate reduction by five orders of magnitude, the overall amount of data will reach several petabytes per year. This huge

data volume necessitates the connection of computing services and storage resources all around the world via the Grid computing network. Based on Grid middleware, denoting a standardised interface to storage and CPU facilities, the CMS computing model [136] has been designed as a fully distributed system with common Grid services at centres defined and managed through the Worldwide LHC Computing Grid (WLCG) project [137]. This WLCG project is a collaboration between the LHC experiments, computing centres, and Grid middleware providers. The CMS computing model defines a hierarchy comprising three interconnected layers of computing centres referred to as Tier-0, Tier-1 and Tier-2, providing different resources and services. Of central importance for the CMS computing model and therefore for the CMS software framework (CMSSW) is the Event Data Model (EDM). Therein, all possible information belonging to a particular collision event can collectively been stored in one common data format. Physically stored as persistent ROOT files [138], these information may include raw digitised data up to high-level objects for real or simulated bunch crossings. Additional provenance information like the software configuration, detector conditions, and calibration setups used, further allows the unambiguous identification of each individual event contributing to a final analysis. The CMS computing model provides several dedicated data format layers in order to reduce the required storage space and computing time for the individual reconstruction and analysis steps. The RAW data format comprises detector information like individual pixel hits, which are needed for the reconstruction of high-level objects like electrons or muons. The Tier-0 centre located at CERN provides archiving for RAW events and serves for initial calibration and reconstruction. Based on immutable trigger information, events are divided into primary data-sets, stored at the Tier-0 and distributed to at least one Tier-1 centre. Currently eight Tier-1 centres serve for a redundant copy of the RAW events and provide extensive CPU power for re-reconstruction and calibration. Several levels of pattern recognition and compression algorithms are applied for the event reconstruction, which constitutes the most CPU intensive activity in the CMS data processing chain. The resulting RECO format is transferred to the Tier-1 centres and contains high-level physics objects, a full record of the reconstructed hits and clusters used to produce them, and sufficient information to allow subsequent application of new calibrations or algorithms without recourse to RAW data. Therefore, the RECO format is still too large for frequent transfer and contains more information than required by most analyses. As a sub-set of the RECO format, the Analysis Object Data (AOD) represents the third data format layer. Requiring about 100 kB/event, the AOD format is designed to facilitate a wide range of physics analyses while occupying sufficiently small storage for distribution to several Tier-2 centres. At these Tier-2 centres, substantial CPU and storage resources are provided for the individual analyses. Data processing is thereby enabled via the Grid by remote job submission to the Tier-2 centres hosting the specific data-sets. Based on fair-share basis, the jobs are executed at computing nodes and the resulting output files are transferred to a user-selected storage element for final analysis. Furthermore, using the AOD or RECO format as input, a fourth data format is provided by the Physics Analysis Toolkit (PAT), which serves for data processing common to most high-level analyses.

Chapter 3

Generation, Simulation, and Reconstruction of Events

Top quark pairs can be produced via an elementary hard parton-parton interaction in proton-proton collisions. The full structure of such events however is complex and generally not predictable from first principles. Besides the hard interaction, radiation and hadronisation processes, as well as subsequent particle decays lead to the production of hundreds of outgoing particles in a typical $t\bar{t}$ event. Based on electronic signals from the tracking devices, the calorimeters, and the muon system, specially-designed algorithms are employed for the reconstruction of these emerging particles, aspiring to a comprehensive analysis of the underlying hard parton-parton interaction.

Dedicated simulations of proton-proton collision events can be used for the development of analysis strategies, the estimation of efficiencies, acceptances, and kinematic distributions. Therein, the hard interaction and the evolution of emerging particles are provided by Monte Carlo event generators, while the interactions of particles within the material and the magnetic field inside the apparatus are emulated in the subsequent CMS detector simulation. Finally, observed and simulated events exhibit the same data format and are therefore subject to the same reconstruction algorithms, facilitating a direct comparison between simulated processes and observed collision data.

3.1. Event Generation

Due to the quantum mechanical character of nature, an event-by-event prediction for proton-proton collisions is unfeasible. Rather the expected probability distributions, obtained by averaging over a large number of events, can be used for the comparison with observed collision data. Therefore, event generators employ Monte Carlo (MC) techniques, wherein choices based on random numbers are made, intended to reproduce the quantum mechanical probabilities arising in the generation process. As depicted in figure 3.1, the simulation of the complex event structure can be factorised into several consecutive generation stages, roughly corresponding to increasing scales of distances and time. Some of these generation steps can be described from first principles, while for others purely phenomenological models are required with parameters tuned to data.

Calculation of the corresponding cross section constitutes the initial generation stage. Following the factorisation ansatz in equation (1.35), the cross section is given by the convolution of the partonic cross section and the parton distribution functions of the colliding protons. Since the scattering process usually takes place at large momentum-transfer scales, where the strong coupling constant α_s is small, the partonic cross section can be computed by means of perturbation theory. This typically yields a small number of final state particles which include the decay products of primarily produced particles in case of top quark or weak gauge boson production.

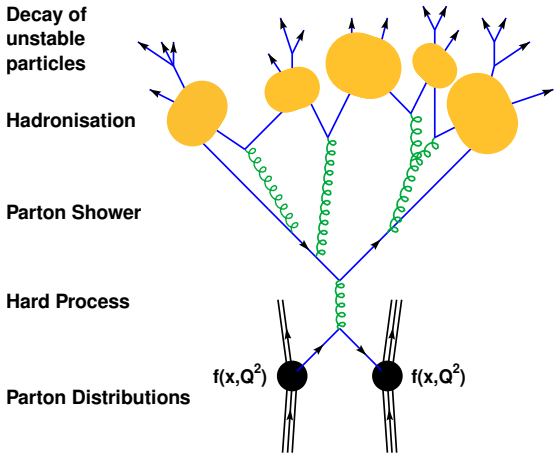

Figure 3.1: Illustration of consecutive event generation steps in proton-proton collisions adapted from [139]. Incoming protons are characterised by parton distribution functions and the hard process can be computed by means of perturbation theory. Colour-charged initial and final state particles generally allow for gluon radiation processes, resulting in cascades of emerging particles, called parton showers. In the subsequent hadronisation stage, observable colourless hadrons are formed and, finally, unstable particles are decayed in the last event generation step.

The accelerated colour-charges involved in proton-proton collisions entail the possibility of gluon radiation in the initial or final state, referred to as Initial State Radiation (ISR) and Final State Radiation (FSR), respectively. Two approaches exist to either compute or estimate the effects of these higher-order perturbative corrections to the elementary hard process. In the Matrix Element (ME) method a given number of additional emissions is included based on exact leading order matrix element calculations of the hard scattering process. Due to the perturbative treatment, however, the ME approach is limited to interactions at large momentum-transfer scales. Therefore, only diagrams corresponding to real emissions like hard gluon radiations can be taken into account. In contrast to the ME approach, the Parton Shower (PS) method is based on approximations derived by simplifying kinematics and interferences, rather than using the full matrix element expressions. Thus, higher-order corrections in this approach are implemented via iterative parton splittings, leading to initial or final state parton showers. To account for the inclusive effects of initial state radiations, evolved parton distribution functions can be employed. In general, the PDF $f_{i/p}(x_i, Q^2)$ for a parton i inside the proton p is a function of the momentum fraction x_i and the scale Q^2 as discussed in section 1.2.1. By numerically solving the DGLAP evolution equations [140–142], a given parton distribution function at fixed scale Q_0^2 can be used to derive the PDF at an arbitrary scale Q^2. For this purpose, partons are iteratively split according to the perturbative splitting functions describing the processes $g \to gg$, $g \to q\bar{q}$, and $q \to qg$. This procedure results in additional parton production that constitute the initial state parton showers. Employing such evolved PDFs, initial state parton showers in the PS approach can be approximated by space-like parton showers, which are modelled within the backward-evolution scheme. Starting from an incoming parton in the hard scattering process, the shower is traced backwards in time to the shower initiator using sequences of increasing Q^2 scales. Final state parton showers

in turn are approximated by time-like parton showers starting from final state partons in the elementary hard scattering process. For this procedure, sequences of decreasing Q^2 scales are used along the positive time axis. Since the branching processes involved might emerge from soft and collinear gluon emissions, the mathematical description of parton showers contains singularities. This requires the implementation of a generator dependent lower cut-off scale to justify the perturbative treatment. However, a reasonably low cut-off value is desirable to ensure an adequate description of soft parton showers.

These two approaches for the inclusion of higher-order perturbative corrections serve for the description of complementary aspects. The parton shower approach facilitates the modelling of multi-parton final states without an explicit upper limit on the number of emerging partons, resulting in an accurate description for soft gluon emissions. While the PS method is therefore well-suited for modelling the internal structure of jets in the low transverse momentum region, it has only limited predictive power for the rates of well-separated jets originating from hard gluon radiations. Such phenomena, however, take place at higher momentum-transfer scales, where an appropriate description can be obtained from matrix element methods. To benefit from the advantages of both approaches and to obtain a most adequate description over the whole phase space, typically, combinations of the two methods are employed. Several matching techniques have therefore been developed to resolve possible ambiguities in the final state configurations and to preclude gaps in the phase space coverage. The most prominent matching schemes available are the CKKW [143, 144] and the MLM [145] algorithms, and the modified subtraction method implemented in MC@NLO [146].

In the previous event generation stages, short distances and high momentum-transfer scales facilitated the application of perturbative methods. However, as partons recede from each other, the lower momentum-transfer scales imply large values for the strong coupling constant α_s, rendering perturbative treatments useless. Confinement effects like the evolution of colour-charged partons into experimentally observable colourless hadrons, referred to as fragmentation or hadronisation, can therefore not be perturbatively described from first principles based on the QCD Lagrangian. Consequently, the description of hadronisation processes is accomplished by purely phenomenological models which comprise model parameters that have to be tuned to data. Among the most prominent descriptions for hadronisation processes are the string fragmentation model [147] and the cluster fragmentation model [148].

In the string fragmentation model, also referred to as the Lund string model, colour-singlet partons are converted into colour-neutral objects via an iterative string break-up scheme. Therein, the separation of final state partons moving away from their common production vertex leads to an increase of stored energy in their interconnecting colour-flux tube. This increase in potential energy may result in the production of a $q'\bar{q}'$ pair and the system is split into two colour-singlet systems as depicted in figure 3.2. One or both emerging colour-flux tubes might then be subject to further splitting processes until only on-mass-shell hadrons remain.

In contrast to the Lund string model, the cluster fragmentation model exploits the so-called preconfinement [149] property of perturbative QCD. This denotes the tendency of partons generated in iterative branching processes to be arranged in colour-singlet clusters with limited extension in both coordinate and momentum space. Therefore, perturbative

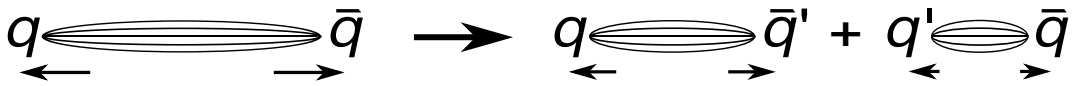

Figure 3.2: Illustration of colour-flux tube splitting in the Lund string model. While the two partons q and $\bar{q}$ are moving apart, their interconnecting colour-flux tube is stretched leading to an increase of stored potential energy. Above a certain distance and potential energy threshold, a $q'\bar{q}'$ pair is produced and the string is split. One or both resulting colour-flux tubes might then be subject to further splitting processes.

QCD does not directly provide information on confinement mechanisms, but predicts that the hadronisation process depends only on local structures, and is independent of the hard elementary process and its energy scale. Colour-singlet clusters then constitute the basic units out of which hadrons arise non-perturbatively, and the invariant mass of a given cluster determines the multiplicity of hadrons emerging from the fragmentation process.

Many particles produced in the preceding generation stages are unstable and decay further into experimentally observable particles. To facilitate proper description and modelling of these decay processes according to the available phase space, known branching ratios and decay models are implemented in the event generator programs. Depending on the actual decay package used, further information like the spin of the decaying particle is taken into account. Finally, charged leptons, neutrinos, photons, and hadrons like pions, kaons, protons, and neutrons emerge from this last event generation stage.

Besides the hard elementary process, interactions of proton remnants and additional proton-proton collisions in the same bunch crossing have to be taken into account by the MC generators to ensure realistic event simulation. Additional proton-proton interactions, so-called minimum bias or pile-up collisions, typically lead to the production of soft hadrons that have to be added to the final state. For the treatment of proton remnants and multiple interactions (MI) of partons, collectively referred to as the underlying event, more sophisticated techniques are required. Since the energy consumed by the partons partaking in the elementary hard process constitutes only a small fraction of the available proton energy, high energetic proton remnants are entailed. Due to colour-connections, these remnants are part of the same hadronisation system as the hard interaction. Moreover, the composite nature of the colliding beam particles allows for the occurrence of several parton-parton interactions per proton-proton collision, while each of these interactions implies ISR and FSR processes. Underlying event activity thus typically yields additional soft contributions to the final state and requires a dedicated description based on phenomenological models tuned to data.

Depending on the particular simulation techniques involved, two types of event generators can be distinguished. General-purpose parton shower and hadronisation event generators like PYTHIA [150] or HERWIG [151] provide full event simulations, including the modelling of hadronisation and decay processes. Matrix element event generators like MADGRAPH/MADEVENT [152], ALPGEN [153], or MC@NLO [146], on the other hand, provide simulations which typically include leptons, quarks, and gluons in the final generation stage. Employing proper matching techniques, these ME generators thus need to be interfaced to an MC generator of the first type to obtain a complete event simulation.

In the following paragraphs, some aspects of the event generators relevant for the analysis presented in this thesis are briefly discussed.

MADGRAPH/MADEVENT
One of the most commonly used ME event generators is the multi-purpose tree-level generator MADEVENT, which is powered by MADGRAPH [152]. For a given process including up to eight particles in the final state, MADGRAPH automatically identifies all relevant Feynman graphs and generates the squared amplitudes for these diagrams as well as the mappings needed for the subsequent MC phase space integration. These process-dependent information are then passed to MADEVENT which produces stand-alone code for the subsequent calculation of cross sections and the unweighted generation of events. Generated events may then be passed to any parton shower and hadronisation event generator using matching approaches like the MLM or the CKKW prescription.

ALPGEN
The matrix element generator ALPGEN [153] is dedicated to the study of hard processes in hadron collisions with special emphasis on final states comprising high jet multiplicities. For a large set of parton level processes in QCD and electroweak interactions, ALPGEN performs the calculation of the exact matrix elements at leading order perturbation theory. The generation of events can then either be performed in a weighted or an unweighted operation mode. The weighted event generation mode is thereby well-suited for parton-level studies and for the calculation of total cross sections in the presence of some overall generation cuts, e.g. production rates of jets above a given threshold. In the second operation mode, the unweighted generation of events can be used for subsequent evolution via parton shower and hadronisation programs. For this purpose, the second mode features matrix element calculations including the full flavour and colour information needed for a subsequent shower evolution. As with MADEVENT, a proper matching of matrix elements and parton showers in ALPGEN is performed using the MLM approach.

MC@NLO
The most ambitious approach in some aspects is provided by MC@NLO [146], in which next-to-leading order matrix element calculations for a given QCD process are matched to parton shower simulations provided by HERWIG. MC@NLO thus allows to obtain NLO results for most observables formally expanded in powers of α_s, especially the calculation of cross sections is accurate to next-to-leading order in perturbation theory. This is achieved in the MC@NLO approach, by treating hard emissions as in ME computations at next-to-leading order, while soft and collinear emissions are handled by PS simulations. The necessary matrix element and parton shower matching procedure in MC@NLO is provided by a modified subtraction method which, however, disadvantageously features negative weights for a small fraction of generated events.

PYTHIA
The general-purpose parton shower and hadronisation event generator PYTHIA [150] is dedicated to the description of multi-particle production in elementary hard interactions, in particular those provided by e^+e^-, pp, $p\bar{p}$, and ep colliders. For the generation of events including all simulation stages, PYTHIA comprises theory predictions and models

for a number of physics aspects including hard and soft interactions, parton distribution functions, initial and final state parton showers, multiple interactions, fragmentation, and decays. While the program is largely based on original research, further knowledge and many formulae are incorporated from the literature. For the treatment of hadronisation processes, an implementation of the Lund string model is used. Furthermore the large number of parameters in PYTHIA, which can be used to develop tunes that optimally describe certain physics aspects of collision data, like the underlying event structure or contributions from pile-up collisions, are of particular interest.

HERWIG
Another commonly used general-purpose parton shower and hadronisation event generator is HERWIG [151]. It is dedicated to the simulation of lepton-lepton, lepton-hadron and hadron-hadron collisions with special emphasis on detailed QCD parton shower simulations. For this purpose, HERWIG comprises a large set of $2 \rightarrow n$ scattering processes for both the Standard Model and its supersymmetric extensions. Moreover, the description of processes includes initial and final state radiations based on angular-ordered parton showers, hadronisation, hadron decays, and a dedicated underlying event simulation. Using the angular-ordered parton shower approach for initial and final state gluon radiation, HERWIG facilitates the inclusion of colour-coherence effects and azimuthal correlations within and between jets. In contrast to the Lund string model used in PYTHIA, HERWIG employs a cluster fragmentation model for jet hadronisation and a similar model for soft and underlying hadronic events. Furthermore, for most processes full spin correlations are implemented using the approach described in [154] for the simulation of particle decays.

3.2. Detector Simulation

The generation of events described so far is, in principle, valid for any of the LHC experiments, since the simulated particle-level processes are solely defined by initial conditions like the centre-of-mass energy and the types of colliding particles. For an aspired comparison with observed collision data, simulated events are thus further subject to a dedicated CMS detector simulation. Two alternative approaches exist for this purpose. In the standard simulation, also referred to as full simulation, the interactions of generated particles within the material and the magnetic field inside the apparatus are emulated. The CMS detector simulation is based on the GEANT4 package [155] which includes a rich set of physics processes to model electromagnetic and hadronic interactions of particles with matter within a magnetic field. Furthermore, GEANT4 features tools for detailed modelling of the CMS detector geometry including information on sensitive detector parts as well as on support structures and cabling material. Interfaces for particle tracking procedures are also implemented in the GEANT4 package, facilitating the retrieval of information from various detector sub-systems and the magnetic field. Since the full detector simulation is, however, very time consuming and for some processes several million events have to be generated in order to obtain statistically reliable estimates, an alternative approach has been developed for the CMS detector simulation. This so-called fast simulation [156] employs techniques that allow for large-scale event simulations on

reasonable time scales while exhibiting an accuracy comparable to the GEANT4-based simulation. The lower computing time in the fast simulation is facilitated by several simplified assumptions regarding detector geometry, a number of dedicated parametrisations, and optimised algorithms. For the validation of this alternative approach and the tuning of involved parameters, comparisons with detailed GEANT4-based simulations can be used. Moreover, both detector simulations are extensively compared with observed collision data in order to validate the employed techniques.

Finally, both detector simulations yield low-level detector objects like energy deposits in individual calorimeter cells or tracking hits. Since the resulting objects are provided in the same format as those obtained from observed pp collision data, common reconstruction procedures can be applied to obtain high-level analysis objects.

3.3. Event Reconstruction

The analysis of an elementary hard parton-parton interaction occurred in proton-proton collisions requires a comprehensive reconstruction of emerging particles belonging to this particular event. This is accomplished by a multitude of dedicated algorithms implemented in CMSSW, which aim for a successive reconstruction of the entire event. The information acquired at each reconstruction step is thereby consistently stored in a single data format, based on the Event Data Model described in section 2.2.4. In an initial stage, electronic signals from the tracking devices, the calorimetry systems, and the muon chambers are used for the reconstruction of high-level detector objects like charged particle trajectory candidates or energy deposits. Using combined information from various detector systems, these objects can then further be associated with physics object candidates that constitute the basic input objects for most physics analyses. Of particular interest for the analysis presented in this thesis is the complex $t\bar{t}$ lepton+jets event topology comprising several different physics objects as discussed in section 1.2.3. The investigation of such elementary hard processes therefore necessitates the reconstruction of electron, muon, jet, and neutrino candidates.

3.3.1. Reconstruction of Charged Particle Trajectory Candidates

Charged particles traversing the CMS silicon tracking system entail discrete signals along their trajectories. The reconstruction procedures applied aspires to a proper combination of these measurable hits to reproduce the entire particle track. As the applied magnetic field inside the tracking volume leads to helical trajectories on which the charged particles move, the momentum and charge of the traversing particle can be determined from the curvature of the reconstructed helix. Of eminent importance for the performance of the applied algorithms is a good estimate for the proton-proton interaction region, referred to as beam spot. This measure constitutes an initial estimate of the elementary hard interaction point in the transverse region, prior to primary vertex or particle track reconstruction. Based on the beam spot and reconstructed hits within the pixel tracking devices, an initial trajectory and vertex reconstruction yields so-called pixel vertex candidates. These constitute the basic input objects for the standard trajectory reconstruction procedures. The default algorithm for the reconstruction of charged particle trajectories

within the CMSSW framework is the Combinatorial Track Finder (CTF) [157], which is modularised into four stages, namely seed generation, trajectory building, ambiguity resolution, and final track fit.

In the seed generation stage, possible trajectory candidates, including their uncertainties, are obtained either from hit triplets or from hit pairs compatible with a given beam spot or pixel vertex. Here, hits reconstructed in the pixel tracking devices provide the best track seeding, due to the fine granularity and low occupancy of the pixel detector. Moreover, this procedure implicitly favours trajectories evoking pixel hits, which facilitates the tracking precision required at the hard interaction region.

In the second stage, the resulting seeds are used for a recursive trajectory building procedure, which is based on a standard Kalman filter pattern recognition approach [158, 159]. Starting from a coarse estimate of the track parameters provided by the seed, the filter proceeds iteratively, layer-by-layer, and subsequently includes information obtained on the successive detection layers. In the most often used procedure, known as inside-out tracking, trajectory candidates are grown from the first pixel layer to the outermost layer of the silicon strip tracker. In this procedure, the initial seed trajectory is extrapolated to the next compatible layer by taking into account the equations of motion for charged particles in a constant magnetic field, multiple scattering processes, and energy loss in the traversed material. Based on a χ^2 constructed from the predicted trajectory state and compatible measured hit positions on this successive detection layer, the track parameters and their corresponding uncertainties are updated according to the Kalman filter formalism, leading to a new trajectory candidate. Since several hits on this current layer may be compatible with the predicted trajectory, this procedure can result in a full set of new trajectory candidates. To account for the possibility that the traversing particle did not leave any hit on this particular layer, one further trajectory candidate is created for which no measured hit, a so-called invalid hit, is used. Finally, to limit the number of combinations, the updated trajectories are rated based on their χ^2 values and the number of invalid hits. Only those trajectories exhibiting a small χ^2 value are kept for further propagation, while possible ambiguities among tracks sharing a substantial number of hits are resolved in favour of the highest quality trajectories. In order to have an unbiased result, all resulting trajectory candidates are then propagated in parallel to the successive tracking layer and the procedure is repeated until either the outermost layer of the tracker is reached, no more compatible hits can be found, or a stopping condition is satisfied. This latter procedure is typically applied to achieve very fast CPU performance suitable for use in the HLT software. In turn, the high track finding efficiencies and accurate determination of trajectory parameters required for offline analyses favour use of the full set of available measured hits.

As a given seed may result in more than one trajectory candidate or a given trajectory may be reconstructed from two different seeds, the candidate collection resulting from the trajectory building stage may exhibit ambiguities or mutually exclusive tracks. The third trajectory reconstruction stage is therefore dedicated to resolve these ambiguities and thus to avoid double counting of tracks. For this purpose, the number of hits shared among two trajectory candidates and their assigned qualities are determined. If more than 50% of hits are shared, the trajectory candidate with fewer associated hits or, if both exhibit the same number of hits, the trajectory with the higher χ^2 value is discarded.

For each trajectory candidate, the building stage results in a collection of hits and estimated track parameters, which might be biased by constraints introduced in the seeding stage. Therefore, each trajectory is subject to a final track fit which is based on a two-layered least squares approach implemented in the CTF algorithm. In the first stage, a standard Kalman filter is initialised at the location of the innermost hit assigned to the trajectory candidate. By processing the list of assigned hits iteratively in the inside-out direction, this filter serves to remove the approximations and biases introduced in the seeding and building stage. A consecutive smoothing stage complements this procedure by applying a second Kalman filter, proceeding outside-in towards the beam line, which yields optimum track parameter estimates at the origin vertex. Since the updated parameters of the second filter at each intermediate tracking layer are combined with the predicted parameters of the first filter, this two-layered filtering and smoothing procedure also yields the best estimates at each tracking layer. Parameter estimates on other surfaces can then be derived by extrapolating the trajectory candidates starting from the hit closest to the desired surface.

The standard trajectory reconstruction procedure at CMS employs an iterative approach involving multiple applications of the CTF algorithm. After the first iteration, a high-purity filter is applied to the reconstructed trajectory candidates, resulting in a first track collection. Hits associated with these high-purity tracks are then removed and remaining hits are subjected to further CTF iterations that subsequently differ in their seeding and filtering criteria. While the first iterations are dedicated to the reconstruction of prompt tracks, progressively including those at lower momenta, subsequent iterations are intended to find trajectory candidates originating from displaced vertices or those not exhibiting any pixel hits. Compared to a single iteration, this procedure facilitates a faster and more efficient reconstruction of charged particle tracks, e.g. about 5% of additional trajectory candidate can be recovered in simulated $t\bar{t}$ events [160].

3.3.2. Reconstruction of Primary Vertex Candidates

An accurate determination of the primary vertex to infer the hard elementary interaction point is essential for the reconstruction of kinematic properties and hence for the comprehensive analysis of the entire event. Due to the finite volume of the colliding hadron bunches, the exact position of the elementary hard interaction varies on an event-by-event basis. This requires the reconstruction of primary vertex candidates for each event individually, which is accomplished in CMSSW by a two-step approach. Starting from a given set of reconstructed tracks, the vertex finding stage is dedicated to the grouping of trajectory candidates into subsets that share a common point of origin. In the subsequent vertex fitting stage, the vertex parameters, including the covariance matrix, are iteratively estimated from a given set of tracks.

As for the track reconstruction procedures, the particular vertex finding algorithm applied depends on the particular use case. While a fast vertex finding algorithm is needed for implementation in the HLT software, offline physics analyses demand approaches yielding high efficiencies and accurate results for the primary vertex reconstruction. Therefore, the latter uses fully reconstructed tracks with certain quality criteria like the number of associated hits in the tracking devices, the reduced χ^2 of the trajectory fit, and their transverse momenta with respect to the beam line. Another important quantity in this

context is the impact parameter (IP), denoting the minimum distance between the trajectory candidate and a given reference point. The associated impact parameter significance is defined as the IP divided by its uncertainty. For the reconstruction of primary vertex candidates, only tracks below a maximal transverse IP significance with respect to the beam spot are considered in order to reject tracks that are not compatible with the primary interaction point of the event. Finally, primary vertex candidates are obtained in the vertex finding stage by clustering these preselected tracks along the beam line.

The resulting candidates are then subjected to a vertex fitting procedure. For this purpose, the CMSSW framework features several algorithms based on Kalman filter techniques. The algorithms mainly differ in their sensitivity to outlying tracks resulting either from mis-measured track parameters or from tracks originating from another vertex. A reduced sensitivity to outlying tracks can be achieved with non-linear algorithms which do not simply reject outlying tracks but rather down-weight the outliers depending on their compatibility with the vertex candidate. Two non-linear algorithms have been developed at CMS, the Trimmed Kalman Vertex Fitter [135] and the Adaptive Vertex Fitter (AVF) [161], whereas the latter represents the default primary vertex fitting algorithm. The AVF is an iterative weighted Kalman filter, wherein each track is weighted by a function of the reduced distance between the track and the vertex candidate. Vertex fitting is then accomplished by minimising the weighted least sum of squares and iteratively computing the vertex position and the involved weights. The candidates obtained are then filtered according to their compatibility with the beam spot and the χ^2 value of the vertex fit. Finally, the resulting primary vertex candidates are ranked by the scalar p_{T}^2 sum of their associated trajectory candidates.

3.3.3. Reconstruction of Electron Candidates

The experimental signature of an electron produced at the interaction point comprises a charged particle track in combination with a localised energy deposit within the electromagnetic calorimeter. Electron reconstruction techniques can therefore, in principle, be summarised as the procedure for matching two such objects. However, the large material budget of the silicon tracking system and the applied solenoidal magnetic field complicate the determination of the two ingredients. Electrons traversing the silicon tracking layers radiate bremsstrahlung photons along their helical trajectory, leading to a significant spread of ECAL energy deposits in the ϕ direction. To account for this energy loss in the tracker material and to collect the bremsstrahlung energy, dedicated trajectory reconstruction and energy clustering algorithms are applied for the reconstruction of electron candidates [162]. The specialised clustering procedure results in the formation of so-called ECAL superclusters (SCs). Seeds for the subsequent reconstruction of electron trajectory candidates can then be obtained by combining superclusters with two compatible hits in the inner tracker layers. This so-called supercluster driven pixel-seed finding is very efficient for isolated electrons with $p_{\mathrm{T}} \geq 10$ GeV$/c$, where reliable SC energy and position estimates can be obtained, and kinks originating from the emission of bremsstrahlung photons do not significantly impair track reconstruction. For electrons with lower transverse momenta or electrons within jets, the SC driven seeding strategy is complemented by a tracker driven algorithm. In this approach, short track segments with at least three assigned hits are loosely matched to energy deposits in the electromagnetic

calorimeter. Finally, seeds provided by the two complementary approaches are merged into a single collection to benefit from the advantages of both seeding techniques.

The emission of bremsstrahlung photons, in general, introduces non-Gaussian contributions to the event-by-event fluctuations of calorimetry and tracking measurements. Therefore, a specially-designed Gaussian Sum Filter (GSF) algorithm [163, 164] with a dedicated Bethe-Heitler energy loss model [165] is employed for the electron trajectory building and fitting procedure. In contrast to standard Kalman filters, the GSF algorithm facilitates proper handling of highly non-Gaussian tails in the position predictions for the electron trajectory state on the successive tracking layers. As with the standard tracking procedure, this dedicated approach yields accurate estimates for track momenta at the interaction vertex as well as at the ECAL surface. Furthermore, the determination of the electron energy fraction emitted by bremsstrahlung photons can be determined through the comparison of the outermost and innermost track momentum estimates. Finally, electron candidates are built by associating a GSF track with a compatible supercluster. Here, the energy of the electron candidate is obtained by averaging the supercluster energy and the track momentum, weighted by their corresponding uncertainties.

Once electron candidates have been reconstructed, additional requirements can be applied to distinguish between electrons and charged hadrons or other objects, which exhibit a similar signature. For this purpose, dedicated electron identification methods have been developed [166], which classify the obtained candidates based on observables sensitive to the pattern of bremsstrahlung emission and electromagnetic showering in the tracker material. Available track-cluster observables, such as the transverse energy of the superclusters or the ratio of deposited energies in the hadronic and electromagnetic calorimeters, can thus be used to further select the candidates obtained from the electron reconstruction procedure.

3.3.4. Reconstruction of Muon Candidates

Muons produced at the interaction region leave two characteristic footprints while traversing the CMS detector. As charged particles, their helical trajectories can be reconstructed in the silicon tracker and, due to their minimum ionising nature, muons are capable to penetrate the muon system. The reconstruction of muon candidates therefore aspires to properly combine the information from these two sub-detectors. Moreover, the small fraction of muon energy deposited in the calorimetry system allows further identification of the reconstructed candidates. Muon reconstruction and identification in CMSSW is accomplished by several complementary approaches [114, 167], collectively based on standard Kalman filter techniques. The final collection of muon candidates obtained with this multi-faceted reconstruction procedure comprises three different categories of candidates. Standalone muon candidates are obtained using only detector information from the muon system, while the supplementation of silicon tracker information facilitates the reconstruction of global muon candidates. The third type of reconstructed objects comprises tracker muon candidates that result from the standard trajectory reconstruction by additionally requiring compatible information from the muon system.

Prior to the so-called standalone reconstruction of trajectory candidates in the muon system, a local reconstruction of track segments is performed from the combination of

individual hits in each CSC and DT chamber. Resulting track segments and hit information from the RPCs are then used to generate seeds, which serve to initiate the standalone trajectory building stage. In the standard configuration, the seed trajectory state parameters are propagated to the innermost compatible muon detection layer. Trajectory building is then performed using the track segments and RPC hits in an inside-out pattern recognition procedure similar to the standard tracking approach. The propagation of track parameters at each step takes into account the non-uniform magnetic field and energy loss induced by ionisation processes, multiple scattering, and emission of bremsstrahlung photons. Finally, trajectory smoothing is applied in the form of a backward pattern recognition procedure employing the individual hit information, composed of the previously used track segments. The obtained track parameters are then extrapolated to the point of closest approach to the beam line, where a constraint to the nominal interaction point can be imposed to further improve track momentum resolution.

Following the concept of global muon reconstruction, the most accurate muon description can be obtained by combining information from the silicon tracker and the muon system. Therefore, trajectory candidates resulting from the standard track reconstruction procedure are linked to those obtained from the standalone reconstruction omitting any vertex compatibility constraints. The first global muon reconstruction stage is dedicated to identifying silicon tracker tracks compatible with a given standalone muon trajectory candidate. Due to the large multiplicity of reconstructed trajectory candidates in the silicon tracking device, this selection is performed in two steps. First, a subset of candidates is selected based on their rough correspondence to a standalone muon track in momentum and position space. For this initial track matching procedure, a so-called region of interest is defined, denoting a rectangular region in the $\eta - \phi$ space. In the second step, more stringent spatial and momentum matching criteria are applied to select the silicon tracker track for the subsequent combination with the standalone muon trajectory candidate. Ideally, this matching procedure is performed after propagating the two tracks onto a common reference surface, where two competing objectives determine the choice of this particular surface. While the covariance matrices of the propagated track parameters should be minimal, only a small number of matches per standalone trajectory candidate are desirable. Since the propagation of tracks through a lot of material typically involve large uncertainties in the propagated track parameters, natural choices for the common reference surface include the outer boundary of the silicon tracking system, the inner boundary of the muon system, or a specific cylindrical layer in between. After the matching and subsequent trajectory candidate selection procedures have been performed, the next reconstruction stage is dedicated to a global track fit involving standard Kalman filter techniques. This procedure however does not perform any additional pattern recognition. Rather, the global reconstruction algorithm combines the collections of hits associated with the two trajectory candidates and initiates a trajectory fitting and smoothing procedure. The resulting global muon candidates are then checked for ambiguities and the χ^2 value of the fit is used to select, at most, one global muon candidate per standalone muon track.

The tracker muon reconstruction constitutes a complementary approach, dedicated to the reconstruction of muons with low transverse momenta or muons lost by geometrical effects like gaps in the muon system. For this purpose, the algorithm starts from the standard collection of silicon trajectory candidates above a given momentum threshold.

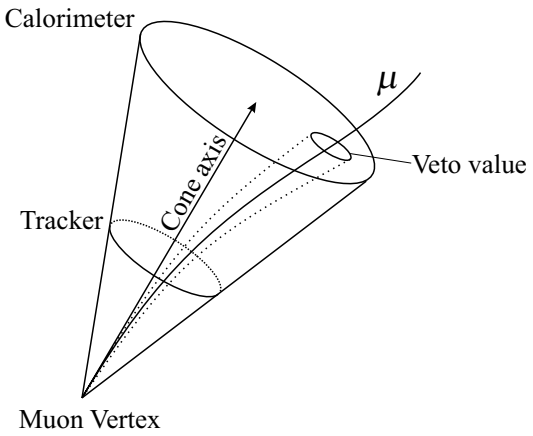

Figure 3.3: Schematic illustration of the muon isolation cone [114]. The cone axis is defined by the muon direction at the vertex position. Transverse momenta of tracks or energy deposits inside the cone are then used to define muon isolation variables, whereas the contributions from the muon itself are omitted through the applied inner veto cone. The so-called veto values in turn can be used to test the muon candidate for compatibility with a minimum ionising particle.

These reconstructed tracks are then propagated into the muon system and positively classified as muon candidates if at least one compatible track segment in the muon system can be found. In contrast to the global reconstruction approach, however, no final track refit is performed. The momentum vector of the tracker muon candidate is thus identical to the one obtained from the standard trajectory reconstruction. The resulting collection comprises muon candidates in combination with compatibility value which indicate the probability of the track being a muon. This additional information is stored for each candidate and can be used for muon identification techniques.

Muon Identification

In addition to the collection of candidates, the three muon reconstruction techniques provide additional information which can be used in offline physics analyses to further select and identify the reconstructed objects. Based on this additional information, muon identification algorithms have been developed [167] which try to minimise the probability of mis-identification while maintaining high efficiencies. These identification algorithms involve track quality information like the number of hits associated with any of the three types of trajectory candidates, the χ^2 values of the various track fits, and the number of invalid hits. Furthermore, energy deposits in the ECAL crystals and HCAL cells are recorded while propagating the muon trajectory candidates through the calorimetry system. This is of special interest for analyses involving prompt muons originating from hard elementary interactions, in contrast to muons emerging from decays of B mesons, pions, or kaons. As these non-prompt muons are typically accompanied by nearby hadronic activity, the energy deposit within a cone around the muon track is usually much larger compared to prompt muon tracks. This feature is exploited by isolation algorithms, wherein the scalar sum of energy deposits or track momenta within a cone of $R = 0.3$ in the $\eta - \phi$ plane around the muon track is calculated as depicted in figure 3.3. The application of

a small inner cone, called veto cone, serves to exclude the contributions from the muon itself. The radii of this veto cone are $R = 0.07$ and $R = 0.1$ for the electromagnetic and the hadronic calorimeters, respectively. Moreover, the energy deposits inside this inner cone can be used to test the muon candidate for compatibility with a minimum ionising particle.

3.3.5. Reconstruction of Jets

Colour-charged partons emerging from the interaction region underlie the confinement principle of QCD and therefore hadronise into collimated streams of colour-neutral objects, called particle jets that can be observed as energy deposits in the calorimetry system. The evolution from the hard elementary interaction to energy deposits in the electromagnetic and hadronic calorimeters is schematically depicted in figure 3.4. Jet reconstruction techniques are employed to cluster all energy deposits which are supposed to originate from one individual outgoing parton, to ultimately provide information about the final state quarks and gluons from the hard interaction. Besides the aspired correspondence between parton level and hadron level, a well-behaved jet reconstruction algorithm has to be collinear and infrared safe. Collinear safety ensures that additional collinear gluon splittings within parton showers do not alter the result of the jet reconstruction algorithm. The demand for collinear safety can thus be achieved if the reconstruction algorithm is invariant under the interchange of an input object with two adjacent objects that add up to the original input. Infrared safety on the other hand denotes the stability of the jet clustering results against the addition of soft partons. This is motivated by the large probability of soft gluon radiation processes in parton showers, soft contributions arising from the underlying event, and instrumental contributions like calorimeter noise. Furthermore, from the theoretical point of view, infrared and collinear safety is essential to obtain meaningful finite perturbative calculations and to maintain the relation between the Born or low-order partonic structure of the event and the experimentally observable jets.

Jet reconstruction algorithms typically involve abstract implementations which facilitate their application to any set of four-vector-like input objects, called pseudo-particles. This simplifies the comparison of jets reconstructed from detector objects such as energy deposits in the calorimeters, simulated partons, or generated stable particles after hadronisation and decay. Hence, from the technical point of view, a jet is just defined by the clustering algorithm used, its parameters, and the applied recombination scheme which determines the method used to combine the individual jet constituents to form the four-vector of the jet. Thus, since jet finding is not a unique procedure, several different algorithms have been developed which can typically be categorised either as cone-type or as sequential recombination algorithms.

Cone-type algorithms are inspired by the idea of defining a jet as an angular cone around some direction of dominant energy flow. Therefore, jets are constructed as the sum of all pseudo-particles within a stable cone of given radius R in the $\eta - \phi$ plane. The term stable in this context indicates that the jet axis coincides with the four-momentum sum of its constituents. The most straight-forward implementation for this kind of jet finder is provided by the Iterative Cone (ICONE) algorithm [114], wherein all pseudo-particles above a certain configurable transverse energy threshold are used as seeds for the iterative search of stable cones. Starting with the seed exhibiting the highest transverse energy as the ini-

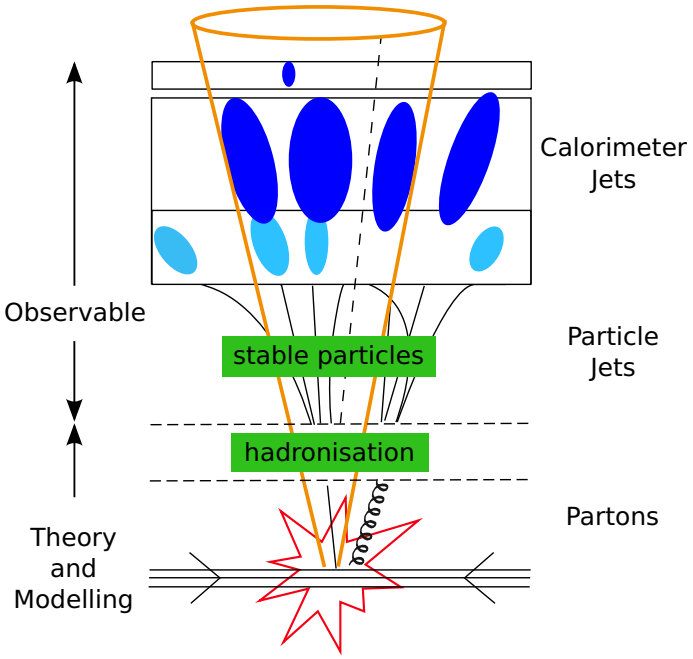

Figure 3.4: Schematic illustration of a hadronisation process with the subsequent formation of jets. The light and dark blue ellipses indicate energy deposits in the calorimetry systems, which can be used as input objects for jet reconstruction algorithms. Cone-type jet finders then define jets by a cone of given radius R around the dominant direction of energy flow.

tial cone axis, all pseudo-particles inside a cone of radius R centred around this initial axis are combined to obtain a new estimate for the cone axis. This procedure is iteratively repeated until the cone axis converges to yield a stable cone. The associated pseudo-particles are then combined according to the applied recombination scheme. Rather than using the stable cone kinematics that are typically obtained from the E_{T} weighted sum of all jet constituents, the so-called E scheme is applied in CMSSW to calculate the jet four-vector. In this recombination scheme, the N pseudo-particles comprising the jet are treated as massless particles and the sum of their four-momenta p_i yields the reconstructed jet four-momentum

$$p_{\mathrm{jet}} = (E_{\mathrm{jet}}, \vec{p}_{\mathrm{jet}}) = \sum_{i=1}^{N} (E_i, \vec{p}_i)\,. \tag{3.1}$$

The pseudo-particles associated with this jet are then removed from the input collection and the jet finding procedure is reinitiated until no seeds above the given energy threshold remain. Possible overlaps between two stable cones are thus prevented by this so-called progressive removal procedure. Due to the comparably low execution time and the good p_{T} resolution achieved, the ICONE algorithm is ideally suited for its extensive use in the HLT software. However, like most commonly used cone-type algorithms due to the application of energy threshold dependent seeds, it is neither collinear nor infrared safe. One approach to fix this behaviour is to search for all stable cones in the event omitting the application of seeds, and afterwards run a split-merge procedure on all stable cones to account for ambiguities arising from possible overlaps. Employing appropriate split-merge procedures, such algorithms are infrared and collinear safe [168]. Disadvantageously

however, straight-forward implementations of such procedures yield very time consuming algorithms due to the large set of cones that have to be checked for stability. This required the development of advanced approaches like the Seedless Infrared Safe Cone (SISCONE) algorithm [168]. Implemented with a dedicated split-merge procedure and employing an exhaustive non-iterative procedure to provably find all stable cones in the event, the SISCONE algorithm is infrared and collinear safe to all orders of perturbative QCD, while providing a moderate execution time.

Sequential recombination algorithms constitute the second class of iterative jet finding procedures. Complementary to cone-type approaches, these algorithms introduce a distance measure between pseudo-particles and recombine pair-wise those exhibiting the smallest distance. For this purpose, the clustering algorithm exhibits a testing variable to decide whether two objects should be combined and a dedicated recombination scheme. Starting from a set of input objects, the clustering algorithm calculates the distances $d_{i,j}$ between each pair of pseudo-particles i and j, and the distance $d_{k,B}$ of any pseudo-particle k to the beam axis,

$$d_{i,j} = \min\left(p_{\mathrm{T},i}^{2p}, p_{\mathrm{T},j}^{2p}\right)\frac{\Delta_{ij}^2}{D^2}, \tag{3.2}$$

$$d_{k,B} = p_{\mathrm{T},k}^{2p}, \tag{3.3}$$

where $\Delta_{ij} = \sqrt{(y_i + y_j)^2 + (\phi_i + \phi_j)^2}$, and $p_{\mathrm{T},i}$, y_i and ϕ_i are the transverse momentum, rapidity, and azimuth of pseudo-particle i, respectively. The clustering algorithm then identifies the smallest distance among all $d_{i,j}$ and $d_{k,B}$ in the list of input objects. In case the smallest value is among the set of $d_{i,j}$ distances, the two objects are combined to form a new pseudo-particle with four-momentum $p = p_i + p_j$ according to the E scheme. On the other hand, if $d_{k,B}$ constitutes the smallest value, particle k is removed from the list of input objects and defined as a jet. After this step is performed, all distances are recalculated and the procedure is iteratively repeated until no pseudo-particles are left to be clustered. The configurable jet size parameter D in equation (3.2) serves to rescale the distances $d_{i,j}$ of two pseudo-particles such that any pair of jets a and b are at least separated by $\Delta_{a,b} = D$. According to the general definition of the clustering metrics in equations (3.2) and (3.3), the parameter p governing the relative power of energy versus geometrical scale, can be used to distinguish between several algorithms. Well-known examples of these jet cluster algorithms are the k_{T} algorithm [169] and the Cambridge/Aachen algorithm [170, 171], which are defined by $p = 1$ and $p = 0$, respectively. Furthermore, recent developments lead to an implementation with $p = -1$, which is known as the anti-k_{T} algorithm [172]. Thus, the only difference between the three sequential clustering algorithms is the actual distance definition, while all three of them are collinear and infrared safe. From the experimental point of view, jets are defined by the applied clustering algorithm and the type of pseudo-particles used. In this context, CMS provides three complementary jet reconstruction procedures. The most commonly used approach is the so-called calorimeter jet reconstruction employing as input objects the unweighted sum of energy deposits in the electromagnetic and hadronic calorimeters, so-called calorimeter towers. Due to the finer granularity of the electromagnetic calorimeter, each HCAL cell thereby corresponds to 5×5 ECAL crystals. The second approach aspires to improve

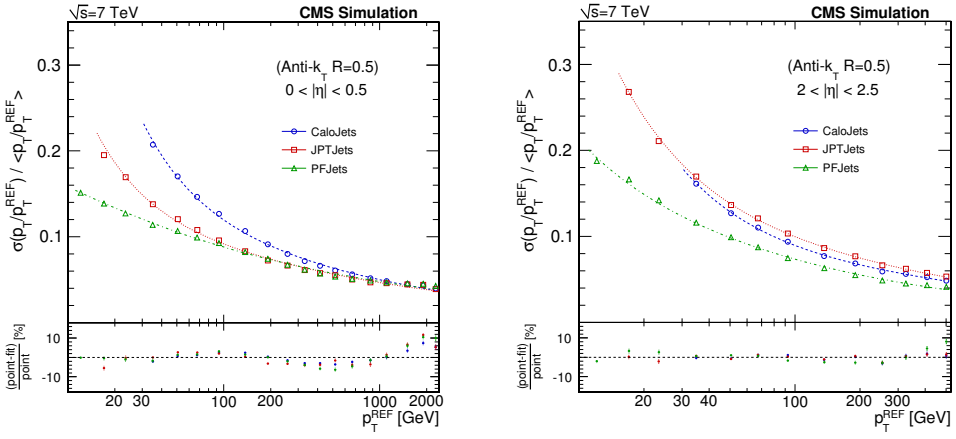

Figure 3.5: Transverse momentum resolutions of calorimeter-based, JPT and PF jets as functions of $p_{\mathrm{T}}^{\mathrm{REF}}$ for the ranges $0 < |\eta| < 0.5$ and $2 < |\eta| < 2.5$ taken from [173]. The transverse momenta p_{T} and $p_{\mathrm{T}}^{\mathrm{REF}}$ correspond to the reconstructed jet and its matched reference generator jet, respectively. Due to the incorporated tracking information, JPT and PF jets exhibit improved resolutions compared to calorimeter jets. Moreover, the PF jet reconstruction does not rely on combined ECAL and HCAL input objects and thus benefits from the fine ECAL granularity.

the transverse momentum information of calorimeter jets by exploiting the kinematics of associated charged particle tracks. This procedure is known as the Jet Plus Tracks (JPT) algorithm [174]. After reconstruction of charged particle trajectories and calorimeter jets, the algorithm associates reconstructed tracks with calorimeter jets based on their spatial distance in the $\eta - \phi$ plane and the track momenta at the interaction vertex. Associated tracks are then propagated to the calorimeter surface, where a classification as in-cone or out-cone tracks is performed depending on whether they point towards a region inside or outside the jet cone. The momenta of both track types are then added to the energy of the corresponding calorimeter jet. Furthermore, the expected average calorimeter energy deposit for in-cone tracks is subtracted based on the track momentum and the hypothesis that the track originated from a charged pion. Finally, the jet axis of the original calorimeter jet is also corrected. The third jet reconstruction approach implemented in CMSSW is based on the so-called Particle Flow (PF) algorithm [175] which attempts to reconstruct, identify, and calibrate every single particle in the event individually, prior to the reconstruction of jets. For this purpose, object candidates are reconstructed from the combined information of the tracking devices, the electromagnetic and hadronic calorimeters, and the muon system. Subsequently, the resulting candidates are identified as electron, muon, photon, charged hadron, or neutral hadron candidates based on the detector systems involved in their reconstruction. Depending on the assigned particle type, the energy of each reconstructed object is calibrated, assuming hadrons as pions. In contrast to the calorimeter jet approach, the PF algorithm thus yields calibrated input objects for the jet reconstruction. Moreover, the PF jet reconstruction benefits from the excellent momentum resolution of the silicon tracking system and the fine ECAL granularity as no a priori combination of ECAL and HCAL clusters is performed. The comparison of transverse momentum resolutions for the three different jet reconstruction procedures in two exemplary $|\eta|$ ranges can be found in figure 3.5.

Jet Energy Corrections

To accomplish the original aim of estimating the underlying parton properties, several corrections have to be applied to the reconstructed jets. For example, a given jet of certain energy and direction leads to a reconstructed jet energy that depends on the electromagnetic fraction of the jet. This results from the non-compensating nature of the CMS calorimetry system, which exhibits a higher response, i.e. ratio of measured to true energy, to the electromagnetic than to the hadronic component of jets. Moreover, calorimeter jets have to be corrected for the energy-dependent calorimeter response, instrumental effects, and for radiation and fragmentation processes. The jet correction procedure at CMS is factorised into seven sequential steps [176], also referred to as correction levels, where each level adresses a certain effect. Among this sequence, the first three correction levels aim to cover all instrumental effects and to correct for any non-linearity and inefficiency in the calorimeter response. These jet energy corrections can be determined either from Monte Carlo simulations or in-situ from data-driven approaches like dijet-balancing or Z/γ-jet p_{T} balancing techniques [173].

Level 1: Offset corrections [177] account for increased jet energies induced by pile-up collisions and electronic noise. The average amount of these additional contributions is therefore subtracted from the measured jet energies.

Level 2: To account for the non-uniform calorimeter response in η, arising from the non-compensating behaviour and possible inefficiencies caused by uninstrumented regions in the detector acceptance, so-called relative corrections [178] are applied. This correction level aims to equalise the jet response as a function of jet η with respect to the response in a central region $|\eta| < 1.3$.

Level 3: Absolute jet energy corrections [173] are applied to account for the p_{T} dependent calorimeter response, aiming for a uniform jet response as a function of p_{T}. In combination with the two preceding correction levels, the application of Level 3 corrections account for all instrumental effects. The first three levels therefore provide corrected jet energies comparable to the underlying particle jets as defined in figure 3.4.

Level 4 to Level 7: Four optional correction levels exist to further estimate the momentum and energy of underlying partons. Level 4 is dedicated to correcting for variations arising from the different electromagnetic fractions of jets. Since gluons exhibit higher probabilities for radiation induced energy loss, light quark (u, d, s) initiated jets typically yield higher energy responses in the calorimeters compared to gluon-induced jets. This is accounted for by flavour-dependent jet corrections, provided in Level 5. Energy deposits originating from the underlying event activity are assumed to be almost independent from the direction and energy scale of the hard elementary final state. This additional energy is therefore subtracted from the jet energy by application of Level 6 corrections. Finally, parton corrections can be applied in Level 7, which consider possible differences between the energies of an initial parton and its corresponding particle jet.

Identification of b Jets

One special feature in the hadronisation process can be exploited to distinguish between jets initiated by light quarks or gluons and those originating from b quarks. This is of particular interest for the classification of event topologies and to select certain processes that

comprise b quarks in the final state. Emerging b quarks fragment into B hadrons which typically carry most of the transverse momentum of the initial quark. Since these hadrons predominantly decay via the weak interaction, they exhibit a considerably long lifetime of about $\tau = 1.6$ ps which might result in an experimentally observed transverse decay length of several millimetres. This property of B hadrons can be exploited to identify b quark induced jets, a procedure known as b-tagging. CMSSW features several different b-tagging algorithms [179] which aspire to the identification of b jets based on a displaced secondary vertex, on the high invariant mass of b jets compared to light quark jets, or on the presence of a soft charged lepton inside the jet, originating from semileptonic B hadron decays.

3.3.6. Reconstruction of the Missing Transverse Energy

Neutrinos emerging from the hard elementary process interact only weakly with matter and thus escape the CMS apparatus undetected. Since the initial particles in the hard elementary interaction exhibit no transverse momenta, the vector sum of all final state transverse momenta must also vanish due to momentum conservation. An imbalance in this vector sum can therefore be attributed to the presence of neutrinos or other weakly interacting particles. Due to its high angular coverage, the calorimetry system is ideally suited to providing a measure of this imbalance. For this purpose, the so-called missing transverse energy $\vec{\not{E}}_{\mathrm{T}}$ is reconstructed as the vector sum of all transverse energy deposits in the calorimetry system [180]

$$\vec{\not{E}}_{\mathrm{T}} = -\sum_{n=1}^{N} \left(E_n \sin\theta_n \cos\phi_n \hat{x} + E_n \sin\theta_n \sin\phi_n \hat{y} \right) , \tag{3.4}$$

where the index n runs over all calorimeter input objects and $\hat{x}$ and $\hat{y}$ denote the unit vectors in the x and y directions, respectively. Finally, several corrections have to be applied for an accurate determination of the missing transverse energy. Since reconstructed jets are corrected for the calorimeter response, this has to be taken into account in the calculation of $\vec{\not{E}}_{\mathrm{T}}$. For this purpose, the missing transverse energy is corrected for the jet energy scale by vectorially subtracting these corrections

$$\left(\vec{\not{E}}_{\mathrm{T}}\right)_{\mathrm{corr}} = \vec{\not{E}}_{\mathrm{T}} - \sum_{i=1}^{N_{\mathrm{jets}}} \left(\vec{p}_{\mathrm{T},i}^{\,\mathrm{corr}} - \vec{p}_{\mathrm{T},i}^{\,\mathrm{raw}} \right) , \tag{3.5}$$

where $\vec{p}_{\mathrm{T},i}$ denotes the transverse momentum of jet i before and after applying the jet energy corrections. Since the corrections for low-p_{T} jets are known to have large uncertainties, the correction in equation (3.5) only considers jets above $p_{\mathrm{T}} = 10\ \mathrm{GeV}/c$. Energy deposits from electrons on the other hand are well-measured by the calorimeters and are therefore not corrected. However, jet reconstruction procedures potentially cluster energy deposited by electrons which would lead to spurious corrections of $\vec{\not{E}}_{\mathrm{T}}$. Therefore, jets above a certain electromagnetic fraction are also excluded for the corrections defined in equation (3.5). Muons traversing the detector are minimally ionising particles and thus deposit, on average, only a few GeV in the calorimetry system, which potentially leads to a significant contribution to the missing transverse energy. This requires a specific muon

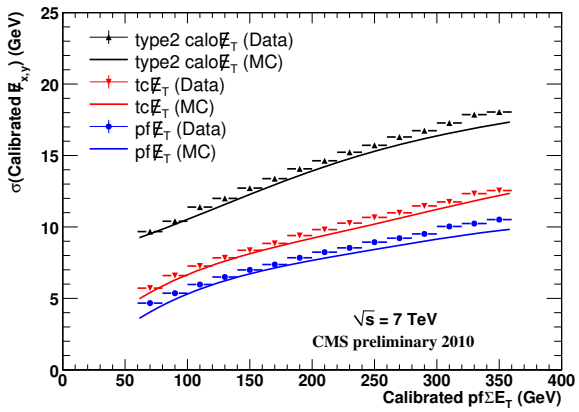

Figure 3.6: Calibrated $\not\!\!E_T$ resolution versus the calibrated E_T sum of particle flow objects taken from [182]. Depicted are the resolution values for Type-II corrected calorimeter-based (calo$\not\!\!E_T$), track-corrected (tc$\not\!\!E_T$), and particle flow (pf$\not\!\!E_T$) missing transverse energy in data and the corresponding values for Monte Carlo simulations. Compared to the calorimeter-based missing transverse energy, both alternative reconstruction techniques show improved $\not\!\!E_T$ resolutions.

correction procedure, wherein the transverse momenta of all muons in the event are subtracted from $\vec{\not\!\!E}_T$, while their estimated calorimeter energy deposits are added in order to avoid double counting. The combination of jet energy and muon corrections yields the so-called Type-I correction, while the optional Type-II correction is dedicated to further account for effects arising from pile-up collisions and the underlying event activity.

There exist two alternative approaches in CMS to measure the missing transverse energy. Similarly to the Jet Plus Tracks algorithm, additional tracker information can be used for the determination of $\vec{\not\!\!E}_T$. This approach is known as track-corrected missing transverse energy (TCMet) reconstruction [181]. Starting from the standard $\vec{\not\!\!E}_T$ calculation, the TCMet algorithm extends the vector sum in equation (3.4) by including the transverse momenta of reconstructed silicon tracker tracks, while subtracting their inferred calorimeter energy deposits under the assumption that the track was initiated by a pion. The third approach for the reconstruction of missing transverse energy is based on particle flow objects, similar to the reconstruction of PF jets. Instead of using energy deposits in the calorimetry system, the so-called PFMet algorithm [175] calculates the negative vector sum of all reconstructed PF objects in the event to determine the missing transverse energy. As shown in figure 3.6, both alternative missing transverse energy reconstruction techniques show a significantly improved $\not\!\!E_T$ resolution [182], where $\not\!\!E_T = |\vec{\not\!\!E}_T|$ denotes the magnitude of the missing transverse energy.

Chapter 4

Selection of Candidate Events

The expected top quark pair production cross section is about nine orders of magnitude smaller than the total inelastic proton-proton cross section of about 60 mb, as illustrated in figure 4.1. Therefore, only one among more than 300 million events constitutes signal for the analysis of top quark pair production. The characteristic final state topology of $t\bar{t}$ events in the muon+jets channel, however, can be used to select a signal-enriched sample, aspiring a good signal-to-background ratio, while maintaining a high signal selection efficiency. For the development of event selection strategies, Monte Carlo simulations of signal and background processes are employed. These samples of simulated events can furthermore be used to estimate selection efficiencies and candidate event yields. Complementary information from data-driven techniques are used to minimise the dependency on these simulation-based yield estimates. Finally, observed and estimated event yields as well as kinematic distributions are compared to validate the employed simulation techniques, which play a crucial role in the search for top quark pair production and the corresponding cross section measurement. For this analysis, pp collision data corresponding to an integrated luminosity of $L = (36.1 \pm 4.0)$ pb^{-1} is available, which has been recorded with the CMS apparatus at a centre-of-mass energy of $\sqrt{s} = 7$ TeV between June and October 2010.

4.1. Analysed Data Sample

The analysis of top quark pair production presented in this thesis focuses on the muon+jets channel, where muon refers to a muon or its corresponding antiparticle. The appearance of a high-energetic muon in the event topology facilitates to start the selection of candidate events already at the stage of data-taking by means of the CMS trigger system introduced in section 2.2.4. So-called trigger streams are defined by a combination of several HLT software triggers, leading to primary data sets which comprise data accepted by at least one of the incorporated triggers. Before being analysed by the different physics analysis groups, the primary data sets are split into secondary data sets (SD) according to specific HLT paths accepting the particular events. For the analysis of $t\bar{t}$ muon+jets events, the secondary data set `SD_Mu` is investigated which comprises events accepted by one of the high-p_{T} muon triggers.

An LHC fill is usually divided into several cycles of CMS data-taking, denoted as runs, which typically end when a detector subsystem fails, rendering full detector read-out temporarily impossible. Each run is furthermore divided into luminosity section, defined as the subsection of a run during which the instantaneous luminosity is considered constant. This period is defined by about 2^{20} orbits which corresponds to approximately 93 s. Depending on the particular physics analysis topic, the impeccable operation of different

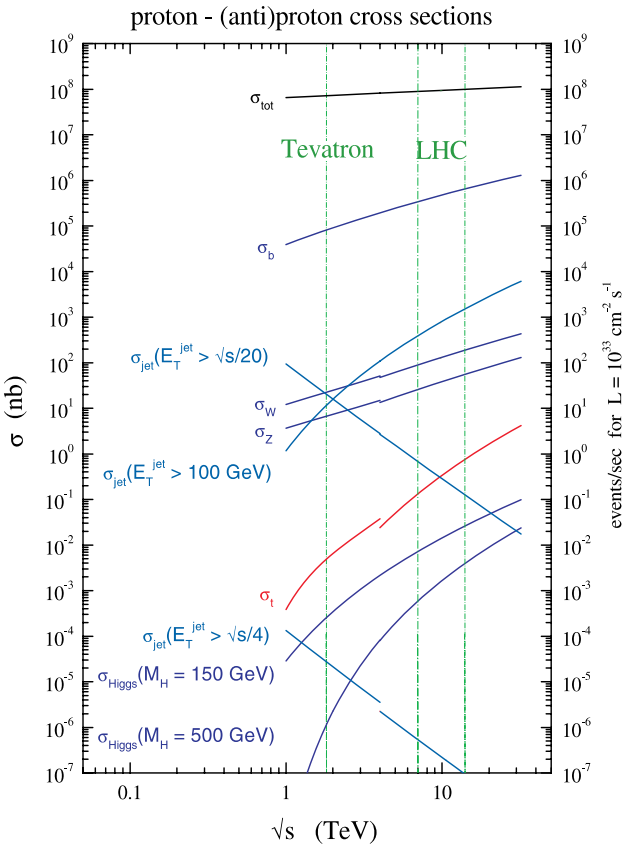

Figure 4.1: Next-to-leading order cross sections for several processes as a function of $\sqrt{s}$ in $p\bar{p}$ (for $\sqrt{s} < 4$ TeV) and pp (for $\sqrt{s} > 4$ TeV) collisions adapted from [183]. The centre-of-mass energies of the Tevatron ($\sqrt{s} = 1.96$ TeV), the design value of the LHC ($\sqrt{s} = 14$ TeV), and the current operation value of the LHC ($\sqrt{s} = 7$ TeV) are indicated by the dashed green lines. The expected $t\bar{t}$ production cross section at $\sqrt{s} = 7$ TeV is about nine orders of magnitude smaller than the total inelastic proton-proton cross section, requiring dedicated selection criteria to obtain a $t\bar{t}$ signal-enriched sample. Moreover, the values for W and Z boson production are about two to three orders of magnitude larger compared to the $t\bar{t}$ production cross section.

detector components during the run is essential. The recorded data for each run is therefore verified online and offline. Since the analysis of top quark events requires a fully functional tracking, calorimetry, and muon system, only data with a fully operational detector are investigated. A listing of runs and luminosity sections which are considered usable for the given requirements is provided by so-called JSON files, which can be used to select a subset of the given `SD_Mu` data set. For the analysis presented in this thesis, the JSON file `Cert_136033-149442_7TeV_Nov4ReReco_Collisions10_JSON` [184] is employed, which comprises all certified pp collision data recorded with the CMS apparatus at a centre-of-mass energy of $\sqrt{s} = 7$ TeV between June and October 2010.

As summarised in table 4.1, the acquired pp collision data is divided into two data-taking periods, in between which a technical stop of the LHC allowed for several major software upgrades, e.g. of the HLT software. Applying the filtering procedure based on the corresponding JSON file, the data set usable for analysis corresponds to an integrated luminosity of $L = (36.1 \pm 4.0)$ pb^{-1} [11]. The determination of the integrated luminos-

Table 4.1: Summary of analysed CMS data sets. The data-taking periods, run ranges, and corresponding integrated luminosities are listed. Application of the filtering procedure using the corresponding JSON file, the total accumulated luminosity by the CMS apparatus at a centre-of-mass energy of $\sqrt{s} = 7$ TeV in 2010 is $L = (36.1 \pm 4.0)$ pb^{-1}.

Period	Run Range	Integrated Luminosity $\left[\text{pb}^{-1}\right]$
Run2010A	$135821 - 144114$	3.2 ± 0.3
Run2010B	$146240 - 149709$	32.9 ± 3.6
Total	$135821 - 149709$	36.1 ± 4.0

ity is based on signals from the hadronic forward calorimeter. In the so-called zero counting method, the average fraction of empty calorimeter towers is used to infer the mean number of interactions per bunch crossing. This method provides a relative luminosity measurement, which is complemented by an approach to obtain the absolute luminosity. For this purpose, horizontal and vertical separation scans, namely Van der Meer scans [185], are employed to measure the beam size in the interaction region. According to equation (2.1) in chapter 2, the beam size in combination with beam current measurements can then be used to determine an absolute luminosity value. Using this approach, an accuracy of 11% for the measurement of the integrated luminosity is achieved, whereas the dominating uncertainty of about 10% is attributed to the beam current measurements [11].

Finally, after the reconstruction or re-reconstruction stage and the filtering for certified data according to the JSON file, dedicated cleaning procedures are applied to pp collision. In order to reject anomalous HCAL noise signals arising due to instrumentation issues associated with the employed photo multipliers, a so-called `HB/HE-NoiseFilter` algorithm [186] is applied to all reconstructed data events. Moreover, in events with more than 10 associated tracks, at least 25% of these tracks have to be qualified as high purity tracks. This event veto is dedicated to the rejection of so-called beam scraping events.

4.2. Modelling of Signal and Background Processes

The final state of $t\bar{t}$ events in the muon+jets channel comprises a high-p_{T} muon and a neutrino from the leptonically decaying W boson, two light quarks from the hadronically decaying W boson, and two b quarks. This is exemplarily shown in figure 4.2, depicting a Feynman diagram for $t\bar{t}$ production and the subsequent decay of top quarks and W bosons. The experimental signature of four jets, a high-p_{T} muon and missing transverse energy is, however, not unique. Several other Standard Model processes can exhibit a similar experimental signature, which might lead to erroneous classification as signal events. Therefore, an event selection is applied, exploiting differences in kinematic observables and characteristic properties of signal and background processes, in order to obtain a signal-enriched sample of candidate events. For the development of such event selection techniques, Monte Carlo simulations are employed to model the $t\bar{t}$ signal and the expected background processes.

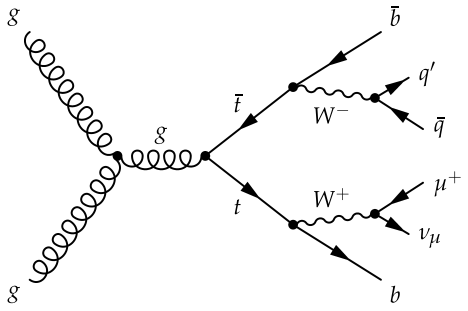

Figure 4.2: LO Feynman diagram for $t\bar{t}$ production via gluon-gluon fusion and the subsequent decay of top quarks in the muon+jets channel. Both top quarks decay into a b quark and a charged W boson. The W^+ boson originating from the top quark then decays leptonically into a μ^+ and its corresponding neutrino ν_μ, while the W^- boson from the $\bar{t}$ quark subsequently decays hadronically into a $\bar{q}q'$ pair. Throughout the analysis, the charge conjugated decays are implicitly included.

4.2.1. Expected Background Processes

Given the characteristic muon+jets event topology, only certain Standard Model processes are expected to potentially counterfeit the experimental signature of $t\bar{t}$ events and thus constitute significant background contributions. Among these expected background processes are W boson, Z boson, and electroweak single top quark production, which can exhibit prompt muons in the final state. Produced in association with additional jets, the experimental signature of these processes is similar to $t\bar{t}$ muon+jets events. Furthermore, QCD multijet production has to be considered as background contribution as well, since falsely identified or secondarily produced muons in such events might lead to a signal-like experimental signature.

Electroweak Production of Single Top Quarks

Due to the top quark in the final state of the hard interaction, electroweak production of single top quarks provides the most $t\bar{t}$ signal-like event topology. This process is accomplished via one of the three production modes discussed in section 1.2.2, and for which exemplary tree-level Feynman diagrams including the decay of top quarks are depicted in figure 4.3. Including higher-order effects leading to additional partons in the final state, single top quark production exhibits a similar experimental signature as $t\bar{t}$ events. Especially the hadronic decay of a W boson in the associated production provides three final state quarks already at leading order. Among electroweak production of single top quarks, the Wt-channel thus constitutes the most significant background contribution for the analysis of $t\bar{t}$ events in the muon+jets channel.

W+Jets and Z+Jets Production

Given the sizable cross sections for vector boson production illustrated in figure 4.1, the production of on-shell W bosons or Z bosons is expected to constitute the most dominant background contribution to top quark pair production in the muon+jets channel. Figure 4.4 illustrates leading order and exemplary two higher-order Feynman diagrams for

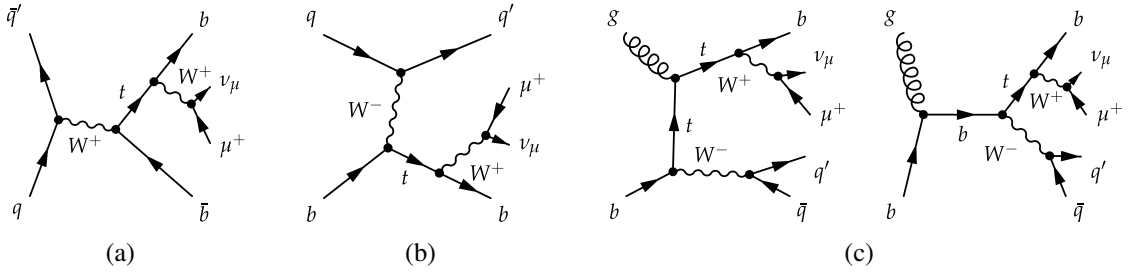

Figure 4.3: Leading order Feynman diagrams for the electroweak production of single top quarks. The s-channel and t-channel production modes can be found in (a) and (b), respectively, while the associated production of a top quark and a W boson is depicted in (c). In each diagram, the top quark decays into a b quarks, a muon, and the corresponding neutrino, while the associatively produced W boson in (c) decays hadronically into a $\bar{q}q'$ pair. If produced in association with additional partons, these processes lead to final state configurations similar to those of $t\bar{t}$ events.

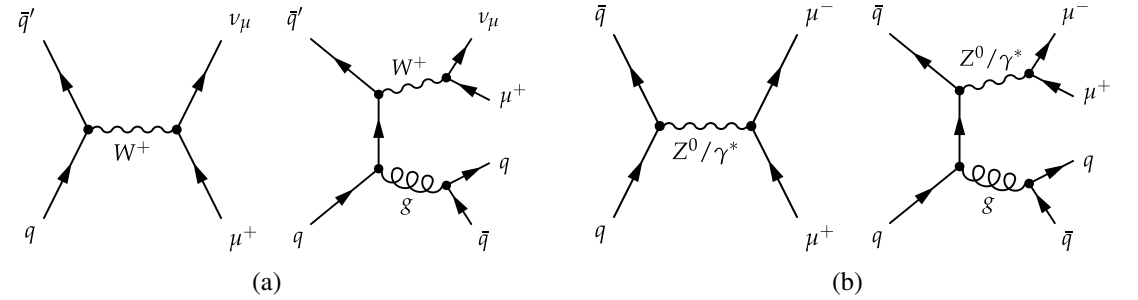

Figure 4.4: Feynman diagrams for the production of W bosons and Z bosons including decays involving muons. Besides the LO production of W bosons in (a) and of Z bosons in (b), exemplary higher-order contributions with additional partons in the final state configurations are depicted. Including these higher-order effects, the production of W bosons and Z bosons in association with additional jets can exhibit a $t\bar{t}$ signal-like experimental signature and therefore constitutes background in the analysis of top quark pair production in the muon+jets channel.

these processes, wherein only W boson and Z boson decays including muons are considered. If produced in association with additional jets emerging from higher-order effects, these processes can exhibit a similar experimental signature as $t\bar{t}$ muon+jets events. Of special importance is the production of W bosons in association with jets, since the leptonic W boson decay into a muon and the corresponding neutrino leads to a $t\bar{t}$ signal-like experimental signature. Compared to W+jets events, Z boson production in association with additional jets is expected to constitute a less significant background contribution, since a requirement on the presence of exactly one muon minimises contributions from $Z \to \mu\mu$ decays. On the other hand, Z+jets events in the $Z \to \tau\tau$ decay mode exhibit a similar experimental signature as the $t\bar{t}$ muon+jets event topology, if one tau lepton decays into a muon and its corresponding neutrino, while the other decays hadronically.

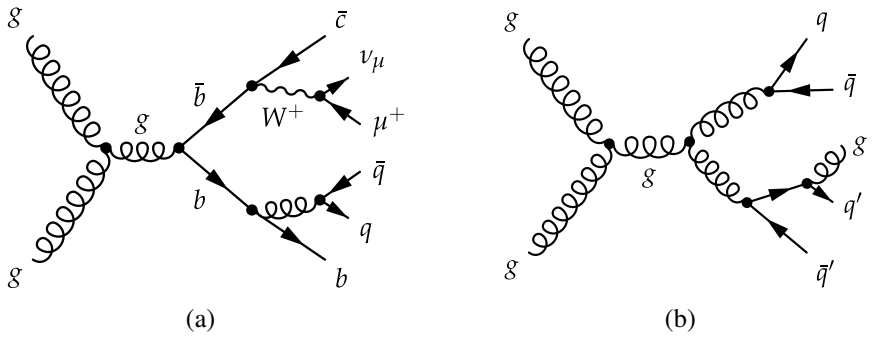

Figure 4.5: Exemplary Feynman diagrams for QCD multijet production processes. The production of a $b\bar{b}$ pair is illustrated in (a). While the b quark decays hadronically, the $\bar{b}$ quark decays in the process of hadronisation via the weak interaction into a $\bar{c}$ quark, a muon, and the corresponding neutrino. Another QCD multijet production mode is depicted in (b), leading to a final state configuration comprising four quarks and one gluon. In the process of fragmentation, one of these five partons might entail a decay-in-flight muon, emerging from the decay of a charged pion or kaon in the jet. Alternatively, one jet might lead to an erroneously identified muon signature induced by hadrons penetrating the muon system, a so-called punch-through muon.

QCD Multijet Processes

The expected background processes discussed so far each contain prompt muons from W boson or Z boson decays. In addition, processes including secondarily produced muons have to be considered. These muons might emerge from heavy flavor decays during the hadronisation process, e.g. via the decay of hadrons containing b or c quarks. Furthermore, so-called decay-in-flight muons might emerge from pion or kaon decays, produced in any hadron shower and decayed in the detector volume. The decay-in-flight muon produces a track in the muon system, which might be matched to some nearby inner track and thus leads to a global muon signature. Another possibility for a counterfeited muon signature arises from hadrons penetrating the muon system, so-called punch-through muons. Hits associated to the deeply-penetrating hadrons might be combined to a standalone muon track and matched to an inner track, where the latter originates from charged hadrons composing the punched-through jet. Although the probability for this erroneous identification of muons and the probability for secondary muons to pass stringent quality criteria is very small, processes with large cross sections might still constitute a non-negligible background contribution in the analysis of $t\bar{t}$ production. A potential source for secondarily produced or mis-identified muons is multijet production via the strong interaction, for which exemplary Feynman diagrams can be found in figure 4.5. The hard final state parton configurations of such processes comprise solely quarks and gluons, while muons or muon-like objects originate from radiation or particle decays during the hadronisation process.

4.2.2. Simulation-Based Modelling of Signal and Background Processes

For the development of event selection strategies and to estimate acceptances and efficiencies, Monte Carlo simulations of top quark pair production and the expected background processes are employed. The aspired statistical accuracy of yield estimates and the modelling of kinematic distributions thereby leads to the requirement of a sufficiently large number of simulated events per contributing process. For the comparison with observed collision data and to obtain yield estimates corresponding to a certain integrated luminosity, the events of the simulated samples are weighted with a process-dependent factor w

$$w = \frac{L \cdot \sigma \cdot \epsilon_{\text{filter}}}{N_{\text{gen}}}, \tag{4.1}$$

which accounts for the integrated luminosity L, the number of simulated events N_{gen} in the given Monte Carlo sample, and the corresponding production cross section σ. If available, NNLO or NLO cross section values are used for the calculation of the weighting factor w. Furthermore, the amount of generated events which are presumably rejected by an applied event selection can be reduced in favour of enriching certain phase-space regions relevant for the analysis of $t\bar{t}$ production. For this purpose a filter on generator level can be applied, which is accounted for in equation (4.1) via the filter efficiency ϵ_{filter}.

The Monte Carlo samples investigated for the analysis presented in this thesis have been generated with the 38X cycle of the CMSSW framework and the full simulation has been employed for the simulation of the CMS detector. As discussed in section 3.1, for an adequate description of certain physics aspects of pp collision data, like the underlying event structure, phenomenological models with parameters tuned to data are required. For this purpose, the PYTHIA tune D6T [187] has been used in the simulation of signal and background processes, except for electroweak single top quark and QCD multijet production, for which the PYTHIA tune Z2 [187] has been employed.

Modelling of $t\bar{t}$ Signal Events and Single Top Background Processes

For the simulation of top quark pair production and electroweak single top quark production, MADGRAPH/MADEVENT is employed with a top quark mass of 172.5 GeV/c^2. Using the matrix element generator MADGRAPH, the production of top quarks in association with up to three additional hard partons in the final state is facilitated. To provide higher statistics for analyses involving leptons in the final state, the simulation of the single top quark s-channel and t-channel production modes is furthermore restricted to leptonic top quark decays, i.e. $t \to bW \to bl\nu_l$, where l denotes an electron, a muon, a tau, or the corresponding antiparticles. For the simulation of hadronisation processes and the subsequent decay of unstable particles, the hard parton configurations provided by MADGRAPH/MADEVENT are passed to the parton shower generator PYTHIA, employing the MLM matching prescription. Table 4.2 lists the cross sections, numbers of simulated events, and the weighting factors for an integrated luminosity of 36.1 pb^{-1} for $t\bar{t}$ and single top quark production. Since the leading order branching ratio $\text{BR}(W \to l\nu) = 1/9$ instead of the experimentally determined value $\text{BR}(W \to l\nu) = 0.1080 \pm 0.0009$ [4] for leptonic W boson decays has been employed in the generation of $t\bar{t}$ signal and Wt single top quark production, selected events are

Table 4.2: Summary of cross sections, numbers of generated events, and weighting factors corresponding to an integrated luminosity of 36.1 pb^{-1} for $t\bar{t}$ production and electroweak production of single top quarks. All samples have been produced using MADGRAPH/MADEVENT interfaced to PYTHIA and $\hat{\mu} = 172.5$ GeV has been adopted for the renormalisation and factorisation scale. While the simulation of $t\bar{t}$ production and the Wt single top quark production mode includes all SM final state configurations, only leptonic top quark decays, i.e. $t \to bl\nu_l$ with $l = e, \mu, \tau$, are considered for the simulation of the s-channel and t-channel single top quark production modes. For top quark pair production, the cross section value is obtained from approximate NNLO calculations [8–10] as discussed in section 1.2.1. The filter efficiency and cross section values for electroweak single top quark production are adopted from [96], whereas MCFM [97] has been employed for the calculation of NLO cross section values.

Process	$\sigma \cdot \epsilon_{\text{filter}}$ [pb]	Generated Events N_{gen}	Event Weight w
$t\bar{t}$, inclusive	$164.6^{+11.4}_{-15.7}$	1,306,182	0.0046
s-channel, $t \to bl\nu_l$	1.40 ± 0.06	494,967	0.0015
t-channel, $t \to bl\nu_l$	$20.48^{+1.08}_{-1.01}$	484,060	0.0001
Wt-channel, inclusive	10.6 ± 0.8	494,961	0.0008

weighted by a factor f_{BR}, which depends on the decay mode of the W boson. In particular, events involving two leptonic or two hadronic W boson decays are weighted by a factor $f_{\text{BR}} = (0.108 \cdot 9)^2$ or $f_{\text{BR}} = (0.676 \cdot \frac{3}{2})^2$, respectively. Accordingly, semileptonic $t\bar{t}$ events and Wt events in which one W decays leptonically while the other decays hadronically are weighted by $f_{\text{BR}} = (0.108 \cdot 9) \cdot (0.676 \cdot \frac{3}{2})$.

Modelling of W+Jets and Z+Jets Background Processes

Similar to top quark production processes, the generation of W boson and Z boson production is accomplished using MADGRAPH/MADEVENT interfaced to PYTHIA. According to the MLM scheme, the hard parton configurations with up to four additional partons in the final state are matched to parton showers provided by PYTHIA. In order to enhance the number of events presumably selected in $t\bar{t}$ lepton+jets analyses, only leptonic decays of W bosons and Z bosons are accounted for in the generation process. The interference of Z boson and virtual photon production is furthermore taken into account by including the matrix elements containing a virtual photon, leading to Z/γ^* production, which is also referred to as Drell-Yan production. The cross section for Drell-Yan production is very large for small invariant masses $m_{l^+l^-}$ of the final state leptons. Such events, however, are likely rejected by an event selection applied in the analysis of $t\bar{t}$ muon+jets events, leading to the application of a generator-level cut of $m_{l^+l^-} > 50$ GeV/c^2. A summary of the cross section values, numbers of generated events, and process-dependent weighting factors can be found in table 4.3.

Modelling of QCD Multijet Background Processes

The most demanding process in terms of simulation-based modelling of background contributions in $t\bar{t}$ muon+jets analyses is QCD multijet production. Due to the large cross

Table 4.3: Summary of cross sections, numbers of generated events, and weighting factors corresponding to an integrated luminosity of 36.1 pb^{-1} for W boson and Z boson production in association with additional final state partons. Both samples have been generated using MADGRAPH/MADEVENT interfaced to PYTHIA. The given product of cross section times filter efficiency accounts for branching fractions, since only leptonic decays $W \to l\nu_l$ and $Z \to l^+l^-$ with $l = e, \mu, \tau$ are considered. The production of Z bosons furthermore includes matrix elements including virtual photons and therefore a generator-level cut on the invariant mass of the final state leptons $m_{l^+l^-} > 50$ GeV/c^2 is applied. The cross section and filter efficiency values are adopted from [96], providing NNLO cross section calculations based on FEWZ [188].

Process	$\sigma \cdot \epsilon_{\text{filter}}$ [pb]	Generated Events N_{gen}	Event Weight w
W+jets, $W \to l\nu_l$	31314 ± 1558	14,805,546	0.076
Z+jets, $Z \to l^+l^-$	3048 ± 132	2,543,727	0.043

Table 4.4: Summary of cross section, filter efficiency, number of generated events, and weighting factor corresponding to an integrated luminosity of 36.1 pb^{-1} for QCD multijet production. For this sample, the parton shower generator PYTHIA has been used, employing additional generator-level cuts on $\hat{p}_{\text{T}} > 20$ GeV/c and on the occurrence of at least one muon with $|\eta| < 2.5$ and $p_{\text{T}} > 15$ GeV/c. To account for the simulation of decay-in-flight muons, PYTHIA has been configured to include decays of long-lived kaons and pions within a cylinder of radius $r = 2$ m and length $l = 8$ m around the beam axis. The cross section and filter efficiency values are adopted from [189], whereas PYTHIA has been used to calculate the LO cross section value.

Process	$\sigma \cdot \epsilon_{\text{filter}}$ [pb]	Generated Events N_{gen}	Event Weight w
InclusiveMu15	84679	29,504,866	0.10

section values involved, a huge number of events has to be generated in order to achieve statistically accurate event yield estimates. Moreover, the small probability for secondarily produced muons or decay-in-flight muons to survive stringent event selection criteria, requires the application of filters on generator level. The third category of background contributions possibly arising from QCD multijet production processes are events comprising punch-through muons. The selection probability of such events is, however, very small and its proper modelling demands an excellent understanding of details and even unusual effects in the detector. Therefore, only the production of secondary muons and decay-in-flight muons are considered for the simulation of QCD multijet background processes. The simulation of QCD multijet production is performed using PYTHIA for the generation, simulation, hadronisation, and decay of unstable particles. For this purpose, PYTHIA is configured for the generation of so-called minimum bias events, which consist of all $2 \to 2$ processes with q, $\bar{q}$, and g as initial and final state particles. In order to reduce the number of events in phase-space regions which are likely rejected by selection criteria applied in a $t\bar{t}$ muon+jets analysis, a filter on generator level is applied to all generated events before being subject to the CMS detector simulation. As can be inferred from figure 4.1, at low $\hat{s}$ values the cross section for QCD multijet production strongly increases, however, low selection efficiencies are expected for events in this phase-space region.

Therefore, a requirement on generator level is applied on the transverse momentum of the hard process $\hat{p}_{\mathrm{T}} = \sqrt{\frac{\hat{t}\cdot\hat{u}}{\hat{s}}} > 20$ GeV$/c$, with the partonic Mandelstam variables $\hat{s}$, $\hat{t}$, and $\hat{u}$. The commonly used generation of very short-lived particles, which cannot reach the detector, has to be extended in order to incorporate the simulation of events comprising decay-in-flight muons. For this purpose, PYTHIA is configured to include the decay of long-lived pions and kaons within a cylinder of radius $r = 2$ m and length $l = 8$ m around the beam axis. Finally, to further enhance the number of events including muons in the final state, a generator-level filter is applied on the occurrence of at least one muon with $|\eta| < 2.5$ and $p_{\mathrm{T}} > 15$ GeV$/c$, taking into account multiple-step decays. A summary of details on the simulated QCD multijet sample can be found in table 4.4, evincing a weighting factor $w = 0.10$ despite the large number of generated events. Therefore, the sample of simulated events can only be used to obtain a rough estimate for the amount of the QCD multijet background contribution, while the description of kinematic distributions might suffer from low statistics after the application of dedicated event selection criteria.

4.3. Selection Criteria

The characteristic experimental signature of a high-p_{T} muon, missing transverse energy, and several jets in a typical $t\bar{t}$ muon+jets event can be used to select a signal-enriched sample of candidate events. For this purpose, the occurrence of the characteristic objects is required and differences in kinematic observables and characteristic properties of signal and background events are exploited. The applied selection criteria are driven by the requirement on an effective rejection of events originating from background processes, while maintaining a high signal selection efficiency. Therefore, the event selection developed for the analysis presented in this thesis employs requirements on the trigger, the primary vertex, the muon candidate, and on the number of jets, where each object candidate is required to satisfy several quality criteria. Furthermore, candidate events with additional lepton candidates are rejected. This event veto allows for the selection of candidate event samples, which are statistically orthogonal to the selected samples investigated by $t\bar{t}$ analyses using other decay channels, namely the $t\bar{t}$ production cross section analysis in the electron+jets channel [15] or the corresponding analysis in the dilepton channel [14]. The detailed description of selection criteria in the following paragraphs furthermore represents the reference event selection for the measurement of the $t\bar{t}$ production cross section in the muon+jets channel presented in Ref. [15, 190].

Trigger Requirements

Driven by the procedure applied on pp collision data, the first stage of the event selection accounts for trigger information provided by the HLT software. Observed and simulated events are required to pass the HLT trigger path `HLT_Mu9`, which is part of the trigger stream defining the secondary data set `SD_Mu`. The trigger path `HLT_Mu9` represents a single muon trigger, accepting events based on the occurrence of a muon object candidate in the trigger acceptance above a kinematic threshold of $p_{\mathrm{T}} = 9$ GeV/c. Starting from pp collision run number 147197, the high initial LHC luminosities and therewith the high

trigger rates of HLT_Mu9, necessitated a prescaling of this particular trigger path. Consequently, only one event among several positive HLT_Mu9 trigger decisions is recorded and subject to event reconstruction and further analysis. In order to prevent event selection inefficiencies induced by this trigger prescaling, an alternative trigger path is exploited. For this purpose, a positive decision of the single muon trigger HLT_Mu15_v1 is required for pp collision data starting from run 147197. This trigger path is similar to the HLT_Mu9, except for the transverse momentum thresholds on the muon object candidates, which is set to $p_{\mathrm{T}} = 15\ \mathrm{GeV}/c$ as indicated by the path name.

Primary Vertex Requirements

The primary vertex provides an estimate for the location of the hard partonic interaction and is therefore of central importance for the analysis of $t\bar{t}$ muon+jets events, for which only the top quark decay products can be experimentally observed. Moreover, object candidates originating from pile-up events might further complicate the analysis of the $t\bar{t}$ topology. The primary vertex candidate with the highest scalar p_{T}-sum of tracks is deemed to provide the best estimate for the location of the hard partonic interaction and its occurrence is therefore used to select events for further considerations. Besides the mere occurrence, a requirement on the number of degrees of freedom $n_{\mathrm{dof}} > 4$ is imposed on the primary vertex candidate, where n_{dof} denotes the weighted sum of tracks used for the reconstruction of the primary vertex candidate. In addition, the PV candidate has to be located in a central region of the CMS detector, which is defined by $\Delta z(\mathrm{PV}, \mathrm{IP}) < 24$ cm and $\Delta\rho(\mathrm{PV}, \mathrm{IP}) < 2$ cm with respect to the nominal interaction point (IP).

Muon Selection Criteria

The key elements in the applied event selection are the identification and selection requirements imposed on the reconstructed muon object candidates. First of all, muon candidates have to be identified as tracker muons as well as global muons, which reduces the probability for falsely identified muon objects. Muon candidates passing this identification criteria are further required to exhibit a transverse momentum of $p_{\mathrm{T}} > 20$ GeV/c and to fall within the trigger acceptance, which is ensured by requiring $|\eta| < 2.1$. In addition, the selected candidates are required to fulfil the so-called GlobalMuonPromptTightID. This implies a value of $\chi^2_{\mathrm{red}} < 10$ for the reduced χ^2 of the global fit in the muon trajectory reconstruction, and the occurrence of at least one valid hit in the muon system, which can be matched to the reconstructed global muon trajectory. To further enrich the purity of the muon selection, the number of valid hits in the silicon tracking system is required to exceed a value of $N_{\mathrm{hits}} = 10$. Moreover, there has to be at least one pixel hit found for the track reconstruction in the inner tracking system, and the global muon reconstruction has to exhibit at least two segments matched to the global muon fit. This latter requirement is imposed, since the trigger information provided by the drift tube chambers requires at least two muon track segments. Besides these identification requirements imposed to minimise the probability for erroneous classification of reconstructed object candidates as muons, additional requirements aim for the selection of muon candidates emerging the hard interaction and to reject muon candidates originating from pile-up

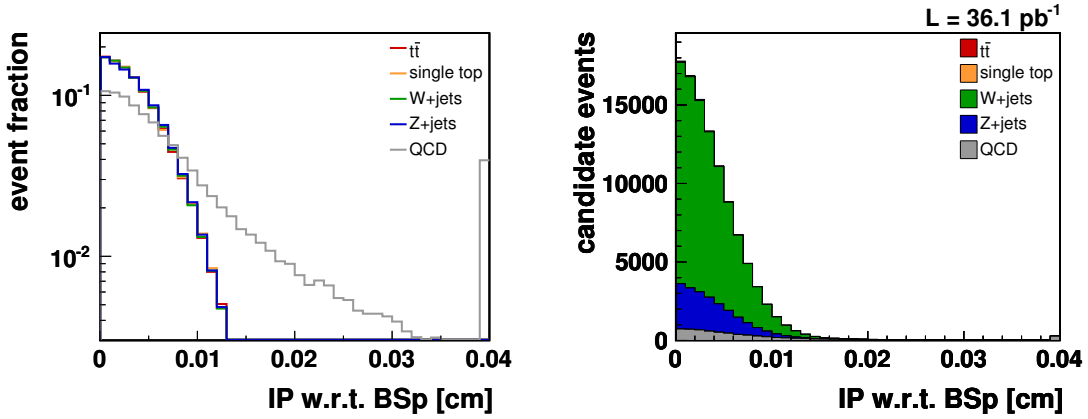

(a) (b)

Figure 4.6: Distribution of the muon transverse impact parameter with respect to the beam spot in a selected event sample without explicit jet multiplicity criteria. The muon candidate is required to complying with the full set of muon selection criteria, except for the requirement on the presented observable. The shape comparison in (a) demonstrates smaller values for this characteristic observable in processes comprising prompt muons, i.e. for $t\bar{t}$, electroweak single top quark, W+jets, and Z+jets production. QCD multijet production processes in turn exhibit larger transverse impact parameter values, which can be ascribed to secondarily produced muons. Therefore, muon candidates are required to exhibit an impact parameter of less than 0.02 cm. In (b), the expected distribution scaled to an integrated luminosity of 36.1 pb^{-1} is shown.

events. Therefore, the distance between the muon vertex obtained using the track reconstruction within the inner tracking system and the primary vertex candidate is required to be $\Delta z(\mu, \mathrm{PV}) < 1$ cm. Furthermore, to reject secondarily produced muons, which are typically close to a nearby jet, muon candidates are required to be well-separated from jets in the event

$$\Delta R(\mu, \mathrm{jet}_{30}) > 0.3\,, \tag{4.2}$$

where jet_{30} denotes a jet with $p_{\mathrm{T}} > 30$ GeV/c and dedicated quality criteria applied, which will be discussed on page 74. Two more selection criteria have been developed to reduce contamination from background events comprising secondarily produced muons or muons emerging from decay-in-flight processes. Such muons typically exhibit large values for the impact parameter with respect to the primary vertex candidate or to the beam spot. The distribution of this characteristic observable can be found in figure 4.6, where e.g. $t\bar{t}$ or W+jets events are deemed to comprise prompt muons, while secondarily produced muons are expected in QCD multijet events. In order to select prompt muons and hence to reduce background contributions involving secondarily produced muons, the impact parameter of the muon track reconstructed from silicon tracking measurements with respect to the beam spot is required to be smaller than 200 µm. Another characteristic property of prompt muons is exploited in the isolation algorithms discussed in section 3.3.4. These algorithms can be used to construct a combined relative isolation variable I_{rel} from the summed contributions of tracker, ECAL, and HCAL energies,

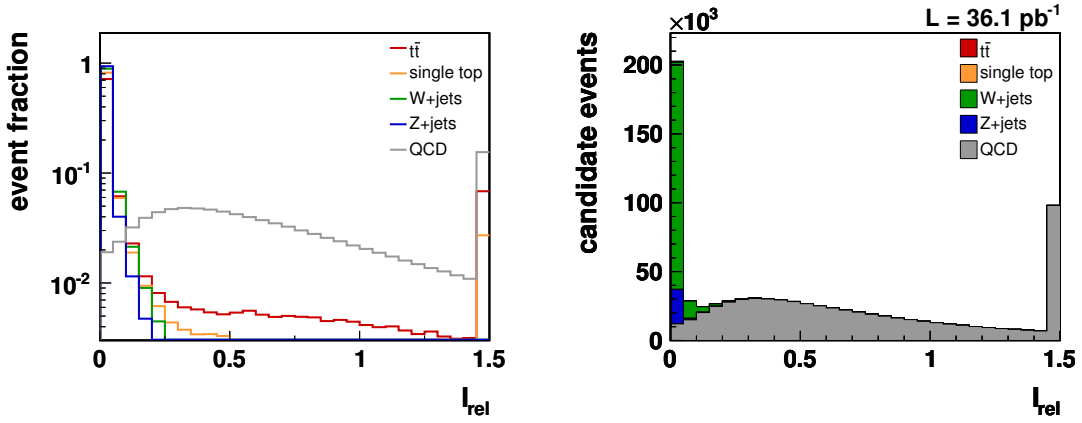

(a) (b)

Figure 4.7: Distribution of the relative isolation for muons in a selected event sample without explicit jet multiplicity criteria. The muon candidate is required to complying with the full set of selection criteria, except for the requirement on the presented observable. The shape comparison in (a) demonstrates smaller values for this characteristic quantity in processes comprising prompt muons, i.e. for $t\bar{t}$, electroweak single top quark, W+jets, and Z+jets production. Due to the contribution of non-muon+jets decay modes, a tail towards higher values in the I_{rel} distribution is observed for simulated $t\bar{t}$ signal and Wt single top quark events. In contrast to processes comprising prompt muons, QCD multijet production processes exhibit larger values, which can be ascribed to secondarily produced muons. Therefore, muon candidates are required to exhibit a relative isolation of less than 0.05. In (b), the expected distribution of the relative isolation for an integrated luminosity of 36.1 pb^{-1} is shown.

divided by the transverse momentum of the muon candidate

$$I_{\text{rel}} = \frac{I_{\text{Trk}} + I_{\text{ECAL}} + I_{\text{HCAL}}}{p_{\text{T}}} \,. \tag{4.3}$$

The tracker isolation energy I_{Trk} is defined as the sum of the transverse momenta of tracks with $p_{\text{T}} > 1$ GeV/c within a cone of radius $R = 0.3$ around the muon, while omitting the track corresponding to the muon candidate. Similarly, the calorimeter isolation energies are calculated by summing the deposited transverse energies in the ECAL crystals or HCAL cells in a cone of $R = 0.3$ around the muon. To remove the energy deposits originating from the muon candidate, inner veto cones of $R = 0.07$ and $R = 0.1$ are applied in the ECAL and HCAL, respectively. A shape comparison of this relative isolation variable for $t\bar{t}$ signal and several background processes is depicted in figure 4.7, together with the simulation-based expectation for an integrated luminosity of 36.1 pb^{-1}. Signal and background events involving prompt muons exhibit small values for this relative isolation variable, while for QCD multijet events higher values are expected. Therefore, the total isolation energy of muon candidates is required to be less than 5% of the muon transverse momentum, leading to a muon selection criterion of $I_{\text{rel}} < 0.05$.

Employing the discussed requirements, only events with exactly one reconstructed muon candidate satisfying all described selection and identification criteria are subject to further considerations.

Loose Lepton Veto

In order to minimise background contributions originating from Drell-Yan or $t\bar{t}$ production in the dilepton channel, a veto is applied on events comprising additional, more loosely defined muon candidates. The rejection of $t\bar{t}$ dilepton events is of particular importance to ensure the statistical independence of the $t\bar{t}$ muon+jets and the $t\bar{t}$ dimuon channel, in order to facilitate a straight forward comparison or combination of results obtained in the two individual channels. The same motivation for statistical orthogonality holds for the rejection of events comprising electron candidates, which are selected by analyses investigating $t\bar{t}$ electron+jets or dileptonic electron+muon event topologies.

For the rejection of events comprising additional muons, a veto on the occurrence of an additional global muon candidates with $p_{\mathrm{T}} > 10$ GeV$/c$, $|\eta| < 2.5$, and relative isolation $I_{\mathrm{rel}} < 0.2$ is imposed. Similarly, events containing an electron candidate with certain quality criteria are rejected. For this event veto, electron candidates reconstructed with the standard GSF algorithm discussed in section 3.3.3 are required to exhibit a transverse energy of $E_{\mathrm{T}} > 15$ GeV, $|\eta| <2.5$, and a relative isolation of $I^{e}_{\mathrm{rel}} < 0.2$. The definition of the relative isolation I^{e}_{rel} for electrons [15] is similar to the corresponding isolation variable used for muon candidates, except for the radii of the inner veto cones and the use of the transverse energy of the electron, rather than using its transverse momentum.

Jet Requirements

The reconstruction of jets is performed using the anti-k_{T} clustering algorithm on particle flow objects with a jet size parameter $D = 0.5$, resulting in so-called particle flow jets. To account for the non-uniform calorimeter response in η and p_{T}, the reconstructed PF jets are corrected employing Level 2 and Level 3 jet energy correction levels described on page 58. Due to the abstract implementation of jet clustering algorithms discussed in section 3.3.5, the collection of particle flow jets comprise a non-negligible contamination of muons. Therefore, the ΔR distance between each jet and the selected muon candidate is determined, whereas all selection criteria are applied to the muon candidate, except for the criterion in equation (4.2). If the distance between the jet and the selected muon candidate is $\Delta R(\mu, \mathrm{jet}) < 0.1$, the jet is removed from the collection of particle flow jets. Furthermore, in the determination of Layer 2 jet energy corrections [191], the jet energy resolution has been determined to be about 10% worse in data compared to simulation-based expectations. To account for this jet energy resolution (JER) bias, all jets in the simulated samples are matched to generator-level jets, based on a $\Delta R(\mathrm{jet, gen\ jet}) < 0.4$ and a $\frac{\Delta p_{\mathrm{T}}(\mathrm{jet, gen\ jet})}{p_{\mathrm{T,\ gen\ jet}}} < 3.0$ criterion. For all reconstructed jets in the simulated samples, which can be matched to a generator-level jet above a transverse momentum threshold of $p_{\mathrm{T}} = 15$ GeV$/c$, the difference between the transverse momentum of the reconstructed and the generator-level jet is increased by 10% and the four-momentum of the jet is corrected accordingly. Due to the correlation of jets and the missing transverse energy, which is reconstructed from particle flow objects as well, this JER bias correction has to be properly propagated to $\not\!\!E_{\mathrm{T}}$. For this purpose, the missing transverse energy is modified for this JER bias based on so-called uncorrected jets, i.e. particle flow jets without Layer 2 and Layer 3 jet energy corrections applied. In particular, prior to the application of the

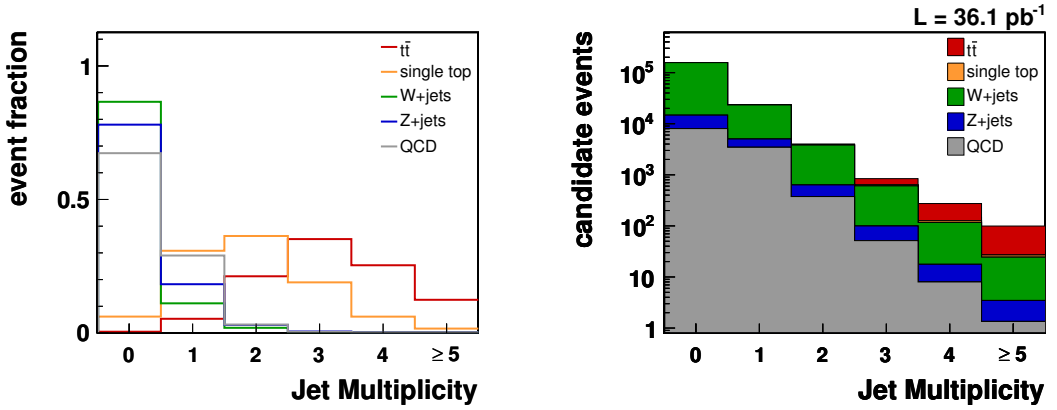

(a) (b)

Figure 4.8: Distribution of the particle flow jet multiplicity with all selection and identification requirements imposed on the reconstructed jets. Moreover, the selection of exactly one tight muon candidate, and the veto on loose lepton candidates are applied. The shape comparison in (a) illustrates high event fractions for $t\bar{t}$ events with three or more jets, while the background processes typically exhibit smaller jet multiplicities. In (b), the expected jet multiplicity distribution for an integrated luminosity of 36.1 pb^{-1} is shown. While the lower multiplicities are dominated by QCD multijet and W+jets production processes, a significant $t\bar{t}$ signal contribution is expected in events with three or more jets.

JER bias correction the transverse momenta of the uncorrected jets are vectorially added to the missing transverse energy and subtracted again after the JER bias correction has been employed.

After this dedicated cleaning and correction procedures, only Layer 2 and Layer 3 corrected jets above a lower transverse momentum threshold of $p_{\mathrm{T}} = 30$ GeV/c within the tracker acceptance of $|\eta| < 2.4$ are selected for further considerations. Furthermore, all jets are required to pass dedicated jet identification criteria, designed to minimise the erroneous identification of electrons, photons, single pions, or high-energetic ECAL or HCAL noise as jet candidates. In particular, the neutral electromagnetic, the neutral hadronic, and the charged electromagnetic fraction of jets are required to exhibit values below 99% each. The charged hadronic fraction and the multiplicity of charged constituents in turn must exceed a value of zero. Finally, there have to be at least two constituents per reconstructed jet candidate. The multiplicity of jets with the full set of selection and identification criteria applied can be found in figure 4.8. Therein, the mere shape comparison of $t\bar{t}$ signal and expected background processes would lead to an event selection requirement of at least three jets per event. Using the additional information provided by the expected jet multiplicity distribution normalised to an integrated luminosity of 36.1 pb^{-1}, significant background contamination in candidate event samples with a requirement of exactly three jets is expected. In order to benefit from both phase-space regions, requirements on exactly three or at least four jets per event have been chosen, leading to statistically orthogonal samples of candidate events for the analysis of $t\bar{t}$ production.

Despite the occurrence of two b quarks in the final state topology of $t\bar{t}$ events, no explicit requirement on information provided by b-tagging algorithms is employed. Instead, an alternative ansatz has been chosen for the selection of $t\bar{t}$ muon+jets events. Therefore, the analysis of top quark pair production presented in this thesis is commonly referred to as untagged analysis [15].

4.4. Estimation of Selection Efficiencies

Applying the elaborated event selection criteria to simulated signal and background events, selection efficiencies can be estimated based on these simulations. Moreover, using the process-dependent weighting factor w defined in equation (4.1), candidate yield estimates corresponding to a particular integrated luminosity can be obtained. These yield estimates could then in principle be used for a comparison with observed collision data. However, in order to reduce the dependency on simulation-based estimates, supplementary information from data-driven techniques can be used to correct the simulation-based lepton reconstruction, selection, and trigger efficiencies. For this purpose, the tag-and-probe method is employed which investigates a distinct mass resonance exhibiting a $\mu^+\mu^-$ final state. Imposing stringent quality criteria on one of the two decay products facilitates to measure various efficiencies by application of reconstruction, selection, or trigger requirements on the other decay product of the given resonance. But before addressing these data-driven techniques, simulation-based selection efficiencies and yield estimates will be discussed.

4.4.1. Simulation-Based Selection Efficiencies and Yield Estimates

The impact of sequentially imposing the various event selection criteria discussed in section 4.3 on simulated signal and background events is shown in table 4.5. Therein, the simulation-based efficiency estimates are given with respect to the full statistic of the event samples under investigation. Requiring exactly one well-identified and isolated muon candidate effectively reduces the QCD multijet background selection efficiency to less than 1%, while other background processes evince efficiencies in the order of $(13-20)\%$. In turn, the efficiency for selecting $t\bar{t}$ events is 55% in the muon+jets channel and 4.7% for other $t\bar{t}$ decay modes. Application of the consecutive veto on events comprising additional, more loosely defined muon or electron candidates serves for the reduction of the selection efficiency for Z+jets background events and $t\bar{t}$ contributions in non-muon+jets decay modes. The highest simulation-based background selection efficiencies after application of these loose lepton event vetoes are observed for electroweak production of single top quarks and W+jets events, exhibiting values of 19% and 15%, respectively. The cross section for electroweak production of single top quarks is, however, small compared to the corresponding value for top quark pair production. Large selection efficiencies in combination with a large production cross section value for W+jets events, on the other hand, lead to a significant background contribution. Therefore, an effective reduction of this particular background contribution is aspired, which can be accomplished by a jet multiplicity requirement. The highest signal selection efficiency and most effective background rejection is found for requirements on exactly three or at least

Table 4.5: Simulation-based event selection efficiencies for $t\bar{t}$ signal and expected background processes. The individual efficiencies listed are with respect to the overall number of simulated events per sample. Therefore, the event selection efficiencies for all background processes except from the Wt production mode of single top quarks are intrinsically biased, due to the applied filters on generator level discussed in section 4.2.2. The overall selection efficiencies for $t\bar{t}$ events including all decay channels is estimated to about 3.6% and 3.8% for requirements on exactly three or at least four jets per event. In turn, less than 1% selection efficiency is expected for all background processes, except for the Wt single top quark production mode with overall efficiencies of 3.3% and 1.5%, respectively.

Requirement	$t\bar{t}$ muon+jets	$t\bar{t}$ other	single top t-chan.	single top Wt-chan.	W+jets	Z+jets	QCD
Trigger	84.98%	22.20%	34.73%	27.34%	22.47%	31.33%	84.85%
PV	84.96%	22.19%	34.71%	27.34%	22.38%	31.26%	84.81%
Tight Muon	55.30%	4.73%	19.60%	12.95%	14.56%	13.25%	0.39%
Loose μ veto	55.15%	4.25%	19.56%	12.50%	14.56%	7.95%	0.39%
Loose e veto	53.90%	2.67%	19.18%	10.78%	14.53%	7.76%	0.39%
$\geq$ 1 jet	53.81%	2.62%	17.56%	10.55%	1.95%	1.71%	0.13%
$\geq$ 2 jets	52.21%	2.17%	10.01%	8.84%	0.34%	0.29%	0.01%
$\geq$ 3 jets	42.95%	1.32%	3.11%	4.85%	0.06%	0.05%	0.002%
$\geq$ 4 jets	23.06%	0.54%	0.80%	1.52%	0.01%	0.01%	0.0003%

four jets per event, respectively. Using all these selection criteria, overall selection efficiencies of 3.6% and 3.8% are expected for $t\bar{t}$ events with requirements on exactly three or at least four jets, whereas the separately investigated efficiency for the $t\bar{t}$ muon+jets channel yields estimates of 19% and 23% respectively. In turn, the simulation-based selection efficiencies for all background processes are well below 1%, except for the Wt mode of electroweak single top quark production with expected selection efficiencies of about 3.3% and 1.5% in events with exactly three or at least four jets. However, as discussed in section 4.2.2, all background processes except for the Wt single top quark production are preselected for leptonic final states, while an inclusive simulation has been performed for top quark pair production processes. The simulation of QCD multijet production furthermore employs filter criteria on generator level to select events comprising muons. Therefore, the comparison of selection efficiencies for signal and background processes is intrinsically biased, with systematically higher selection efficiencies for all background processes, except for Wt single top quark production.

The decomposition of finally selected $t\bar{t}$ events passing the full set of selection criteria including the requirement on exactly three or at least four jets per event comprises 88.1% or respectively 81.6% $t\bar{t}$ muon+jets events. The remaining fraction of 18.4% and 11.9% are dominated by contributions from $t\bar{t}$ decay modes involving tau leptons, namely 6.1% and 6.3% are provided by the tau+jets channel and 8.4% and 3.7% stem from dileptonic muon+tau decay processes after imposing requirements on exactly three jets or at least four jets per event. For illustration, the decomposition of selected $t\bar{t}$ events with a requirement on at least four jets can be found in figure 4.9.

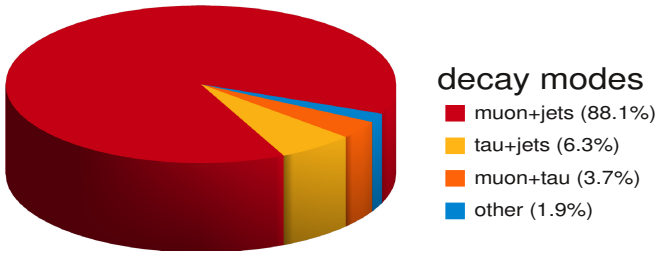

Figure 4.9: Pie chart of $t\bar{t}$ decay modes contributing to the candidate sample obtained after employing the full set of event selection criteria on simulated $t\bar{t}$ events, including the requirement on at least four jets. The dominant fraction of 88% originates from $t\bar{t}$ muon+jets events, while the remaining fraction of 12% mainly comprise decay modes involving tau leptons, namely tau+jets and muon+tau decays.

Table 4.6: Simulation-based event yield estimates for $t\bar{t}$ signal and expected background processes, normalised to an integrated luminosity of 36.1 pb^{-1}. Applying the full set of event selection criteria, including the requirement on exactly three or at least four jets per event, a total of about 851 and 383 candidate events are expected, among which 214 and 230 events are deemed to originate from $t\bar{t}$ production. The dominating background contribution is W+jets production with about 507 and 120 events, respectively.

Requirement	$t\bar{t}$	single top t-channel	single top Wt-channel	W+jets	Z+jets	QCD
Tight Muon	726.3	145.1	49.6	164832.4	14600.1	12047.4
Loose μ veto	700.5	144.8	47.9	164825.3	8755.0	12034.0
Loose e veto	609.2	142.0	41.3	164472.2	8549.4	11929.4
$\geq$ 1 jet	606.3	130.0	40.4	22090.8	1879.8	3897.0
$\geq$ 2 jets	573.9	74.1	33.9	3816.1	317.9	436.0
$\geq$ 3 jets	444.5	23.1	18.6	627.4	59.9	60.8
$\geq$ 4 jets	230.3	5.9	5.8	120.1	11.8	9.3

In addition to the estimated selection efficiencies, simulation-based yield estimates for $t\bar{t}$ signal and all expected background processes can be obtained through the application of the process-dependent weighting factor w defined in equation (4.1). Assuming an integrated luminosity of 36.1 pb^{-1}, the estimated candidate event yields can be found in table 4.6. Imposing selection criteria on exactly three or at least four jets per event, a total of about 851 and 383 candidate events are expected. Among these candidate events, about 214 and 230 events are expected to originate from top quark pair production. The dominating background contribution emerges from W+jets production, with an expectation of about 507 and 120 events, respectively. In addition, a contribution of about 51 and 9 events from QCD multijet production processes are expected for the two selection criteria. However, due to the large weighting factor, low selection efficiencies, and the demanding modelling procedures applied during simulation, large uncertainties are expected for this simulation-based yield estimate. Therefore, the expected background contribution from QCD multijet production can only be considered as rough estimate, while particularly for this estimation data-driven methods are preferable.

4.4.2. Estimation of Muon Reconstruction, Selection, and Trigger Efficiencies

The accurate and reliable estimation of object reconstruction, event selection, and trigger efficiencies is a key element for the search of top quark pair production and the analysis of the $t\bar{t}$ production cross section. Simulation-based efficiency estimates, however, might suffer from imperfect modelling of signal and background processes, or from an imprecise description of the detector response. Therefore, supplementary information from data-driven techniques are used to correct the simulation-based efficiency estimates. A well-established data-driven approach to measure efficiencies is the so-called tag-and-probe (T&P) method, which employs a mass resonance to select a particular type of particle candidates. The efficiency estimates are then obtained by probing certain criteria on these objects. For this purpose, a so-called tag object is defined by imposing a set of stringent selection criteria. Since these requirements are designed to select a particular type of particles, the rate of other objects erroneously passing the tag selection criteria should be negligible. In a second step, probe object candidates with less stringent selection criteria are selected by pairing these probe candidates with a tag object such that the invariant mass of the tag-and-probe pair is consistent with the mass of the considered resonance. Especially for rather loose probe selection criteria, this object pairing might involve contamination from background processes or combinatorial background. These background contributions can be taken into account using an analytical fit to the mass resonance, or by subtraction of background contributions, estimated from dedicated side-band region studies. The efficiency determination for a selection criterion in the tag-and-probe approach is then obtained from the number of probe objects passing this particular requirement N_{pass} and the total number of probe objects N_{all} via

$$\epsilon = \frac{N_{\text{pass}}}{N_{\text{all}}} \,. \tag{4.4}$$

In case a probe object also passes the stringent tag selection criteria, this specific tag-and-probe pair induces a double pairing in the same event, which is accounted for in the definition of the efficiency ϵ. Consequently, the determined efficiency does not represent a selection efficiency per event, but rather the efficiency per probe object, e.g. a reconstruction, selection, or trigger efficiency per muon candidate. Due to the correlation between numerator and denominator in equation (4.4), binomial uncertainties for the efficiency ϵ are expected. The mere calculation of binominal uncertainties might, however, lead to an underestimation of the uncertainties, especially for small numbers of probe candidates or for efficiencies close to unity. In order to prevent undercoverage, a Clopper Pearson interval construction [192] is used to obtain 68% confidence level intervals for the estimation of the statistical uncertainty on the efficiency ϵ.

For the estimation of muon efficiencies in the analysis of top quark pair production, the Z boson mass resonance in the $Z \to \mu\mu$ decay mode is used for the selection of tag-and-probe candidates. The overall efficiency $\epsilon_{\text{overall}}$, can thereby be factorised into three sequentially measured efficiencies, namely the muon reconstruction efficiency ϵ_{reco}, the muon selection efficiency ϵ_{sel}, and the trigger efficiency $\epsilon_{\text{trigger}}$

$$\epsilon_{\text{overall}} = \epsilon_{\text{reco}} \cdot \epsilon_{\text{sel}} \cdot \epsilon_{\text{trigger}} \,. \tag{4.5}$$

In order to facilitate this factorisation, the probe muon candidates for each sequential measurement are defined with respect to the previous requirements. For example, the probe objects for trigger efficiency measurements are required to pass the muon reconstruction and selection criteria, which are probed in the preceding stages of the efficiency determination.

The efficiency estimates obtained by application of the tag-and-probe method to observed and simulated events, denoted by $\epsilon^{\text{data}}_{\text{T\&P}}$ and $\epsilon^{\text{MC}}_{\text{T\&P}}$, respectively, are then used to correct simulation-based efficiencies in a data-driven way

$$\frac{\epsilon^{\text{data}}_{\beta}}{\epsilon^{\text{MC}}_{\beta}} \overset{\text{Assumpt.}}{=} \frac{\epsilon^{\text{data}}_{\text{T\&P}}}{\epsilon^{\text{MC}}_{\text{T\&P}}} \qquad \Rightarrow \qquad \epsilon^{\text{data}}_{\beta} = \frac{\epsilon^{\text{data}}_{\text{T\&P}}}{\epsilon^{\text{MC}}_{\text{T\&P}}} \cdot \epsilon^{\text{MC}}_{\beta} = \kappa \cdot \epsilon^{\text{MC}}_{\beta} \,, \tag{4.6}$$

wherein β denotes any simulated signal or background process, i.e. $t\bar{t}$, electroweak single top quark, W+jets, Z+jets, or QCD multijet production. This approach is based on the assumption, that the ratio of efficiencies in observed and simulated Z boson events is equal to the corresponding ratio for all other processes under investigation. Therefore, the correction factor κ is employed to obtain an estimate for the efficiencies in data $\epsilon^{\text{data}}_{\beta}$ by weighting the simulation-based efficiencies $\epsilon^{\text{MC}}_{\beta}$. The uncertainty on the correction factor κ is given by propagation of the individual uncertainties. Moreover, to account for possible inefficiencies in certain phase-space regions, the correction factor κ can be determined as a function of a muon specific observable like η. This parametrised approach allows to correct simulated processes, according to their phase-space specific distributions. In the following paragraphs the individual methods for the determination of the correction factor κ from the application of the tag-and-probe method to estimate muon reconstruction, muon selection, and trigger efficiencies will be discussed.

Muon Reconstruction Efficiency

For the determination of the muon reconstruction efficiency ϵ_{reco}, tag muons are defined as global muon candidates, which pass the muon trigger requirements. The definition of probe candidates takes into account all reconstructed tracks within the silicon tracking system with an additional requirement, that the probe object has the signature of a minimum-ionising particle in the calorimeters [167]. Using the Z boson mass resonance, probe candidates are paired with an oppositely-charged tag muon. To account for background contamination, the invariant mass of the tag-and-probe pairs for both categories, passing as well as failing probes, are subject to an analytical fit. For this purpose, an appropriate signal-shape and category-dependent background-shapes are used to model the invariant mass spectrum. Finally, the muon reconstruction efficiency is estimated from the number of passing probes divided by the sum of passing and failing probe categories. Since no significant deviations between $\epsilon^{\text{data}}_{\text{reco, T\&P}}$ and $\epsilon^{\text{MC}}_{\text{reco, T\&P}}$ in certain phase-space regions have been observed, overall efficiency values are determined. The resulting efficiency values in data and simulation can be found in table 4.7, leading to an overall correction factor $\kappa = 0.990 \pm 0.007$ [193].

Table 4.7: Summary of muon reconstruction efficiencies in data and simulation obtained via the tag-and-probe (T&P) method, adopted from [193]. In addition, the value for the corresponding correction factor κ is given in the last column.

$\epsilon^{\text{data}}_{\text{reco, T\&P}}$ [%]	$\epsilon^{\text{MC}}_{\text{reco, T\&P}}$ [%]	Corr. Factor κ
95.5 ± 0.6	96.52	0.990 ± 0.007

Muon Selection Efficiency

The definition of tag muons for the determination of the muon selection efficiency ϵ_{sel} comprises reconstructed muon candidates with the full set of identification and selection requirements applied as for the analysis of $t\bar{t}$ muon+jets events. Moreover, the tag muons are required to match an `hltSingleMu9L3Filtered9` trigger object, which corresponds to the `HLT_Mu9` trigger path. For the data-taking period in which this HLT trigger has been prescaled and the alternative trigger path `HLT_Mu15_v1` is employed, tag muons for the determination of $\epsilon^{\text{data}}_{\text{sel, T\&P}}$ are required to match an `hltSingleMu15L3Filtered15` trigger object. For both trigger object matching procedures, a geometrical distance between the tag muon and the trigger object of $\Delta R < 0.2$ is required. The collection of probe objects includes muon candidates reconstructed as global and tracker muons above a transverse momentum threshold of $p_{\text{T}} = 20$ GeV/c within the trigger acceptance $|\eta| < 2.1$. Only oppositely-charged tag-and-probe combinations with an invariant mass close to the Z boson pole mass are taken into account, i.e. $|M(\mu\mu) - M(Z)| < 15\,\text{GeV}/c^2$. Since the tight tag selection criteria renders the background contributions negligible, dedicated background subtraction methods are omitted. Alternatively, the muon selection efficiency is directly determined from the number of probe objects passing the selection criteria and the total number of probe candidates. Due to isolation requirements, the selection efficiency ϵ_{sel} is expected to depend on the hadronic activity in the vicinity of the muon. Since $t\bar{t}$ events typically exhibit more hadronic activity compared to Z boson events, this dependency could be estimated using for example the tag-and-probe method in $Z + n$ jets events ($n = 1, 2, 3, \ldots$). However, the expected amount of tag-and-probe combinations in the higher jet bins are small, leading to large statistical uncertainties. Using an alternative ansatz, this dependency is accounted for by a differential determination of ϵ_{sel} in a variable measuring hadronic activity. For this purpose, ϵ_{sel} is given as a function of the distance between the muon and the closest jet in the event, leading to $\Delta R(\mu, \text{jet})$ dependent efficiencies and correspondingly, a $\Delta R(\mu, \text{jet})$ dependent weighting factor κ. Results for the muon selection efficiencies in data and simulation and the corresponding correction factors κ can be found in figure 4.10 (c) and figure 4.10 (d). Due to the low statistics for the tag-and-probe method in events with at least one jet per event, which is necessary to determine the ΔR dependent efficiencies, no significant deviations from an overall correction factor are observed. Therefore, the determination of muon selection efficiencies is repeated as a function of the pseudorapidity of the given probe muons. As can be seen in figure 4.10 (a), comparable efficiencies are determined in data and simulation, leading to a flat behaviour of the correction factor depicted in figure 4.10 (b). The determined overall values for the efficiencies in observed and simulated event samples and the corresponding correction factor of $\kappa = 0.995 \pm 0.003$ are summarised in table 4.8.

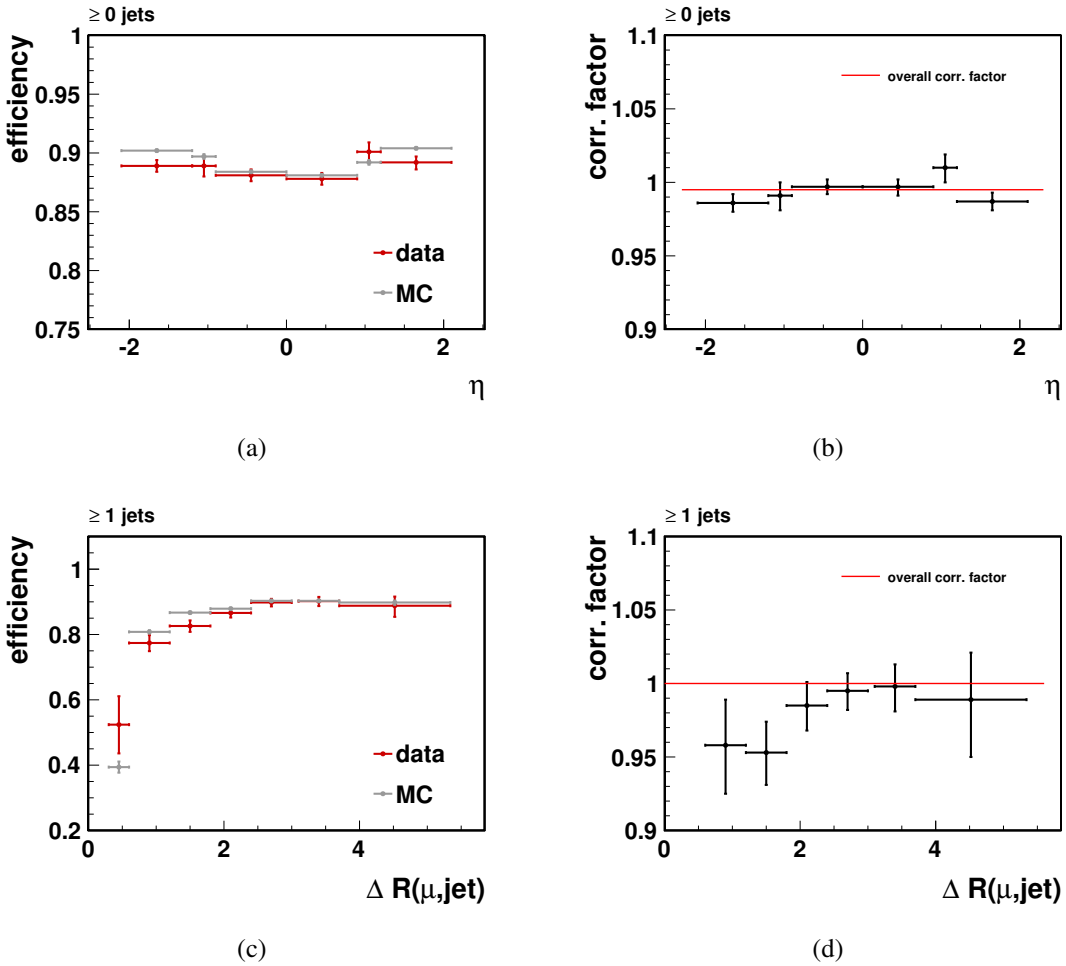

Figure 4.10: Comparison of muon selection efficiencies in data and simulation obtained via the tag-and-probe method in (a) and (c). The corresponding correction factors κ can be found in (b) and (d), respectively. Due to isolation requirements applied, the selection efficiency is expected to depend on the hadronic activity in the vicinity of the muon. To account for this dependency, the selection efficiency ϵ_{sel} and the corresponding correction factor κ in (c) and (d) are determined as a function of ΔR between the muon and the closest jet. Since no significant deviations from an overall flat correction factor, indicated by the horizontal red lines, have been observed within the given statistical uncertainties, the determination of ϵ_{sel} and κ have been repeated as a function of the pseudorapidity of the probe muon candidates in (a) and (b). Since this alternative selection efficiency determination can be performed in event samples without dedicated jet multiplicity requirements, lower statistical uncertainties on ϵ_{sel} and κ are observed, leading to an overall correction factor $\kappa = 0.995 \pm 0.003$.

Table 4.8: Summary of muon selection efficiencies in data and simulation obtained via the tag-and-probe method in events without dedicated jet requirement and with a requirement of at least one jet per event. Moreover, the corresponding correction factors κ are given in the last column. Due to smaller statistical uncertainties for the tag-and-probe method applied to the sample without the jet multiplicity requirement, the overall correction factor $\kappa = 0.995 \pm 0.003$ is used for the correction of simulation-based yield estimates.

range	$\epsilon^{\text{data}}_{\text{sel, T\&P}}$ [%]	$\epsilon^{\text{MC}}_{\text{sel, T\&P}}$ [%]	Corr. Factor κ
≥ 0 jets	88.2 ± 0.2	88.43 ± 0.05	0.995 ± 0.003
≥ 1 jets	82.6 ± 0.7	82.6 ± 0.1	1.000 ± 0.009

Trigger Efficiency

For the determination of the trigger efficiency $\epsilon_{\text{trigger}}$, the definition of tag muons is identical to the one used for estimating the muon selection efficiency. Probe muon candidates are required to pass the full set of muon selection criteria and are paired with oppositely-charged tag muons, if the invariant mass of the tag-and-probe combination is compatible with the Z boson pole mass, i.e. $|M(\mu\mu) - M(Z)| < 15$ GeV/c^2. The trigger efficiency $\epsilon_{\text{trigger}}$ is then obtained analogously to the selection efficiency from the number of probe candidates passing the trigger requirements, divided by the total number of probe objects. The trigger requirements on probe candidates are checked via a ΔR matching to a corresponding trigger object. For this purpose, the distance between the probe muon candidate and the corresponding HLT trigger object is required to be $\Delta R < 0.2$. For observed and simulated events, `hltSingleMu9L3Filtered9` trigger objects are considered, which correspond to the `HLT_Mu9` trigger path. For the data-taking period in which the alternative trigger path `HLT_Mu15_v1` is applied, a matching between probe candidates and an `hltSingleMu15L3Filtered15` trigger object is required for passing probes. Similar to the procedure applied for the reconstruction efficiency, the trigger efficiency is determined in several η ranges of the probe muon candidate. Results for the `HLT_Mu9` trigger path before and after the technical stop of the LHC discussed in section 4.1, for the trigger path `HLT_Mu15_v1`, and for the simulation-based `HLT_Mu9` trigger path can be found in figure 4.11. Based on the luminosity-weighted mean of the individual trigger efficiencies in data, the correction factor κ can be found in figure 4.11 (b). As for the determination of the muon selection efficiency, no statistically significant deviations from an overall correction factor have been observed. The individual trigger efficiency values in data and simulation and the overall correction factor $\kappa = 0.969 \pm 0.004$ are summarised in table 4.9.

Table 4.9: Summary of muon trigger efficiencies in data and simulation obtained via the tag-and-probe method, and the corresponding correction factor κ. Depending on the run range, the HLT_Mu9 or the HLT_Mu15_v1 trigger path is used for the determination of the trigger efficiency in pp collision data, while for simulated events only the HLT_Mu9 trigger path is investigated. The efficiency for the HLT_Mu9 trigger path is furthermore obtained as the luminosity-weighted mean efficiencies before and after the technical stop of the LHC discussed in section 4.1. Accordingly, the correction factor κ is calculated from the trigger efficiency in the simulated sample and the luminosity-weighted mean of the individual trigger efficiencies in data.

$\epsilon^{\text{data,HLT\_Mu9}}_{\text{trigger, T\&P}}$ [%]	$\epsilon^{\text{data,HLT\_Mu15\_v1}}_{\text{trigger, T\&P}}$ [%]	$\epsilon^{\text{MC}}_{\text{trigger, T\&P}}$ [%]	Corr. Factor κ
90.4 ± 1.1	92.8 ± 0.2	95.20 ± 0.03	0.969 ± 0.004

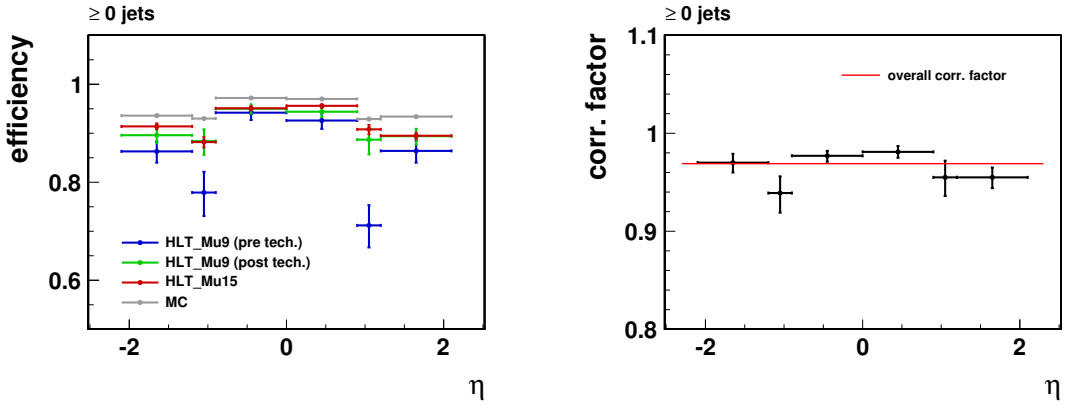

(a) (b)

Figure 4.11: Comparison of muon trigger efficiencies in data and simulation as a function of η obtained via the tag-and-probe method. In (a) observed trigger efficiencies for the trigger path HLT_Mu9 before and after the technical stop of the LHC, for the trigger path HLT_Mu15_v1, and for the simulation-based trigger path HLT_Mu9 are shown. Small trigger inefficiencies can be seen in the barrel end cap transition region, i.e. in the range $0.9 < |\eta| < 1.2$, especially for HLT_Mu9 prior to the technical stop. Calculating the luminosity-weighted mean of the individual trigger efficiencies in data, the correction factor κ as a function of the probe muon pseudorapidity in (b) is deduced. As in case of the muon reconstruction efficiency, no statistically significant deviations from an overall correction factor, indicated by the horizontal red line, is observed.

4.5. Comparison of Observed and Simulated Events

Finally, using the full set of event selection criteria elaborated in section 4.3, candidate event yields as well as kinematic distributions in observed and simulated pp collision data can be compared. This comparison is of central importance, since the expected kinematic distributions of $t\bar{t}$ signal and the expected background processes will play a crucial role in the search for top quark pair production and the measurement of the $t\bar{t}$ production cross section. The event yield comparison for observed and simulated pp collision data corresponding to an integrated luminosity of (36.1 ± 4.0) pb^{-1} can be found in table 4.10. Therein, the correction factor $\kappa = 0.955 \pm 0.008$ obtained from the three correction factors κ discussed in section 4.4.2 is taken into account for the yield estimates of $t\bar{t}$ signal and the expected background processes. Moreover, the jet resolution bias and the measured branching ratios for leptonic W boson decays have been used to derive these yield estimates. As can be deduced, especially in a selected event sample with exactly two or three jets per event, the overall yield estimates are about 20% lower than the observed number of candidate events. However, especially the yield estimates for QCD multijet production are considered unreliable. Moreover, the theory-predicted cross section values for W boson and Z boson production are accurate up to next-to-leading order. However, the generation of these processes is accomplished with the LO generator MADGRAPH using PYTHIA for the parton shower simulation. Therefore, the yield estimate of events with higher jet multiplicities might suffer from this overall rescaling to NLO theory predictions for the cross section values of W boson and Z boson production.

Applying the requirement on exactly three or at least four jets per event, a total of about 812 and 366 events is expected, among which 204 and 220 events are deemed to originate from $t\bar{t}$ production. This corresponds to expected signal-to-background ratios of $S/B = 0.34$ and $S/B = 1.51$ and pseudo-significances of $S/\sqrt{B} = 8.3$ and $S/\sqrt{B} = 18.2$, respectively.

Table 4.10: Comparison of event yields for observed and simulated pp collision data. The yield estimates for simulated signal and background processes are scaled to an integrated luminosity of $L = 36.1$ pb^{-1} and account for the overall correction factor $\kappa = 0.955 \pm 0.008$, the jet resolution bias, and the measured branching ratios for leptonic W boson decays. In the second-to-last column, the sum over all signal and background event yields is given, which can be compared to the observed yields in pp collision data. As can be deduced, especially in a selected event sample with exactly two or three jets per event, the overall yield estimates are about 20% lower compared to the observed number of candidate events. However, especially the yield estimate for QCD multijet production is considered unreliable. Moreover, the yield estimates for W boson and Z boson production might suffer from improper knowledge on the corresponding production cross section for events with higher jet multiplicities.

Requirement	$t\bar{t}$	single top	W+jets	Z+jets	QCD	Sum	Data
$=1$ jet	30.9	59.6	17443.4	1490.9	3303.5	22328.3	25661
$=2$ jets	123.5	63.3	3043.6	246.3	358.1	3834.9	5001
$=3$ jets	204.5	28.6	484.2	45.9	49.1	812.3	1064
≥ 4 jets	219.8	11.2	114.6	11.3	8.9	365.8	423

Figures 4.12 to 4.15 show comparisons of several kinematic distributions for observed and simulated candidate events. Similar to the event yields presented in table 4.10, the distributions of simulated events are weighted to the integrated luminosity of 36.1 pb^{-1} and account for the various correction factors κ. Figure 4.12 is dedicated to the comparison of the jet multiplicity and the so-called M3 variable, which is defined as the invariant mass of three jets in the event, exhibiting the highest vectorial-summed transverse momentum. This observable provides a simple and rough estimate for the invariant mass of the three jets originating from the hadronically decaying top quark. Although this simple approach is not expected to substitute an elaborated procedure for the correct reconstruction of hadronically decaying top quarks in $t\bar{t}$ events, the resulting M3 distributions allows for a fast and easy check of signal contamination in the selected sample of events. Moreover, this observable in a selected sample of events with a requirement of at least four jets depicted in figure 4.12 (c) will play a central role in the search for top quark pair production and the measurement of the $t\bar{t}$ production cross section. The comparison of p_{T} and η distributions for the leading, second-, and third-leading jet can be found in figure 4.13, visualising again the discrepancy between observed and estimated candidate event yields. However, the transverse momentum distributions suggest that these excesses of observed candidate events can be ascribed to background processes, rather than an underestimation of signal contributions. The comparison of kinematic distributions for the selected muon candidate and the missing transverse energy with the requirement of exactly three or at least four jets per event can be found in figure 4.14 and figure 4.15, respectively. Besides the p_{T} and η distributions of the selected muon candidate, the missing transverse energy, reconstructed with the particle flow algorithm, and the reconstructed transverse W boson mass $M_{\text{T,W}}$ are depicted. This observable is defined from the momentum components of the muon and the neutrino as

$$M_{\text{T,W}} = \sqrt{(p_{\text{T},\mu} + p_{\text{T},\nu})^2 - (p_{x,\mu} + p_{x,\nu})^2 - (p_{y,\mu} + p_{y,\nu})^2}\,, \tag{4.7}$$

where the momentum components of the neutrino, $p_{x,\nu}$, $p_{y,\nu}$, and $p_{\text{T},\nu}$, are approximated using the corresponding components of the missing transverse energy. Finally, the sum of the transverse momentum of the selected muon candidate and the missing transverse energy are used to construct $H_{\text{T,lep}}$, for which distributions in events with a requirement of exactly three or at least four jets are shown in the corresponding figures. Of particular interest in figure 4.15 is the distribution of the missing transverse energy, which, in combination with the M3 distribution, will play a central role in the search for top quark pair production and for the measurement of the $t\bar{t}$ production cross section in chapter 5.

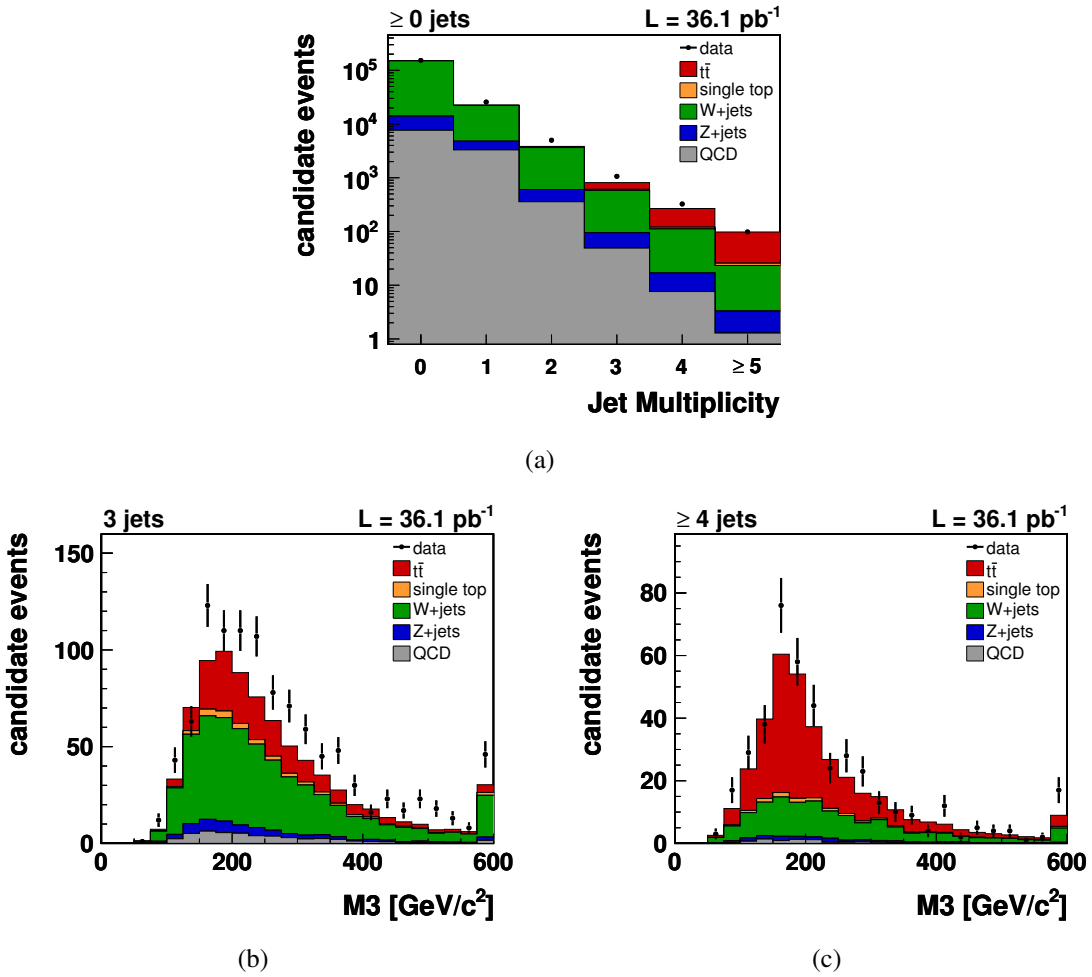

Figure 4.12: Comparison of kinematic distributions for observed and simulated pp collision data, normalised to the predictions given in table 4.10. In (a) the jet multiplicity distribution is shown for events with the full event selection applied, except for the requirement on at least four jets. Demanding for exactly three or at least four jets per event leads to the M3 distributions depicted in (b) and (c), respectively, where the latter represents a simple estimator for the reconstructed mass of the hadronically decaying top quark.

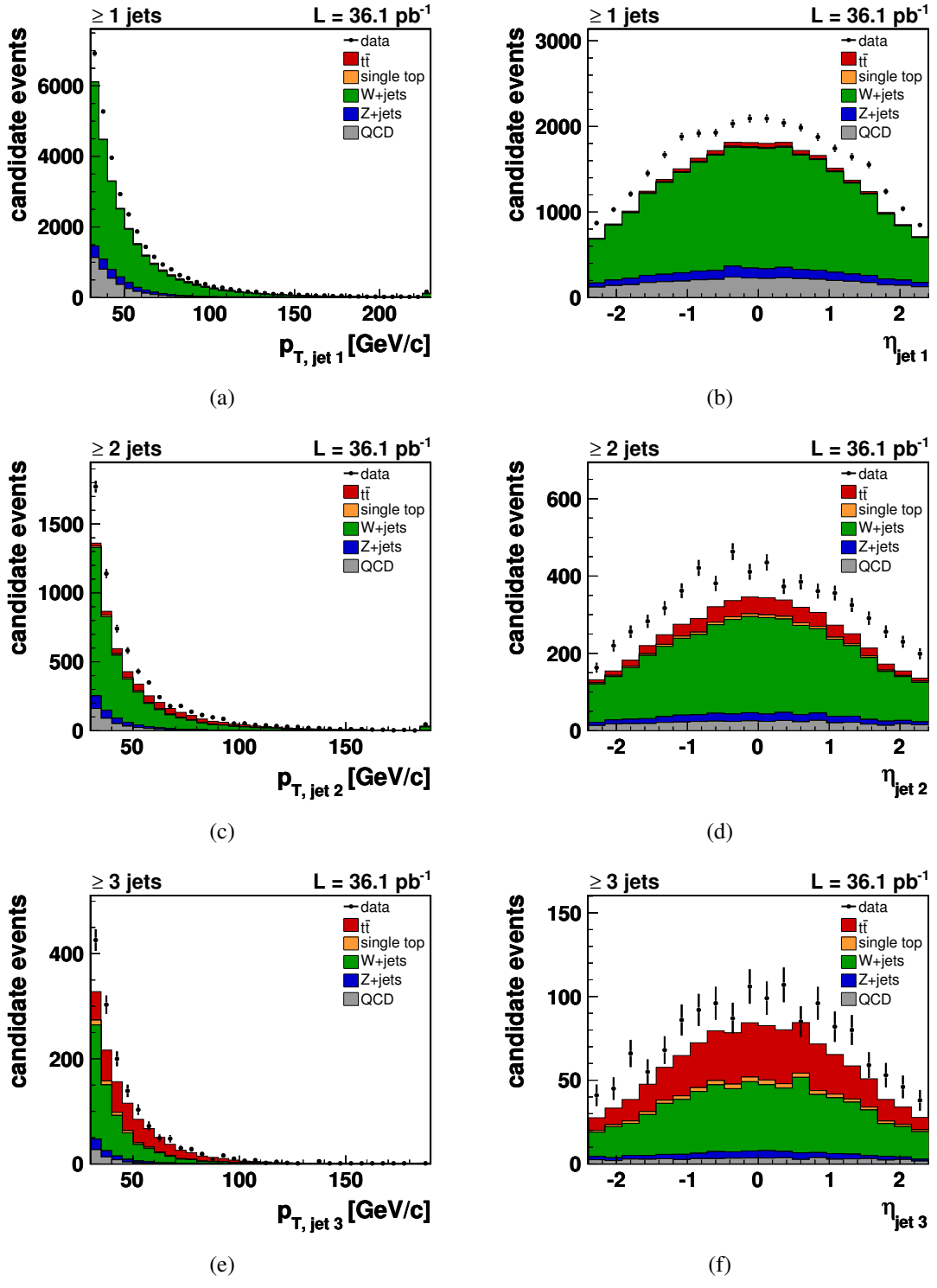

Figure 4.13: Comparison of kinematic distributions for observed and simulated pp collision data, normalised to the predictions given in table 4.10. In (a), (c), and (e), the transverse momentum distribution of the leading, second-, and third-leading jet can be found. The corresponding η distributions for these jets are depicted in (b), (d), and (f), respectively. The comparison of these kinematic distributions visualises again the discrepancy between observed and estimated candidate event yields. However, especially the transverse momentum distributions suggest underestimated background contributions.

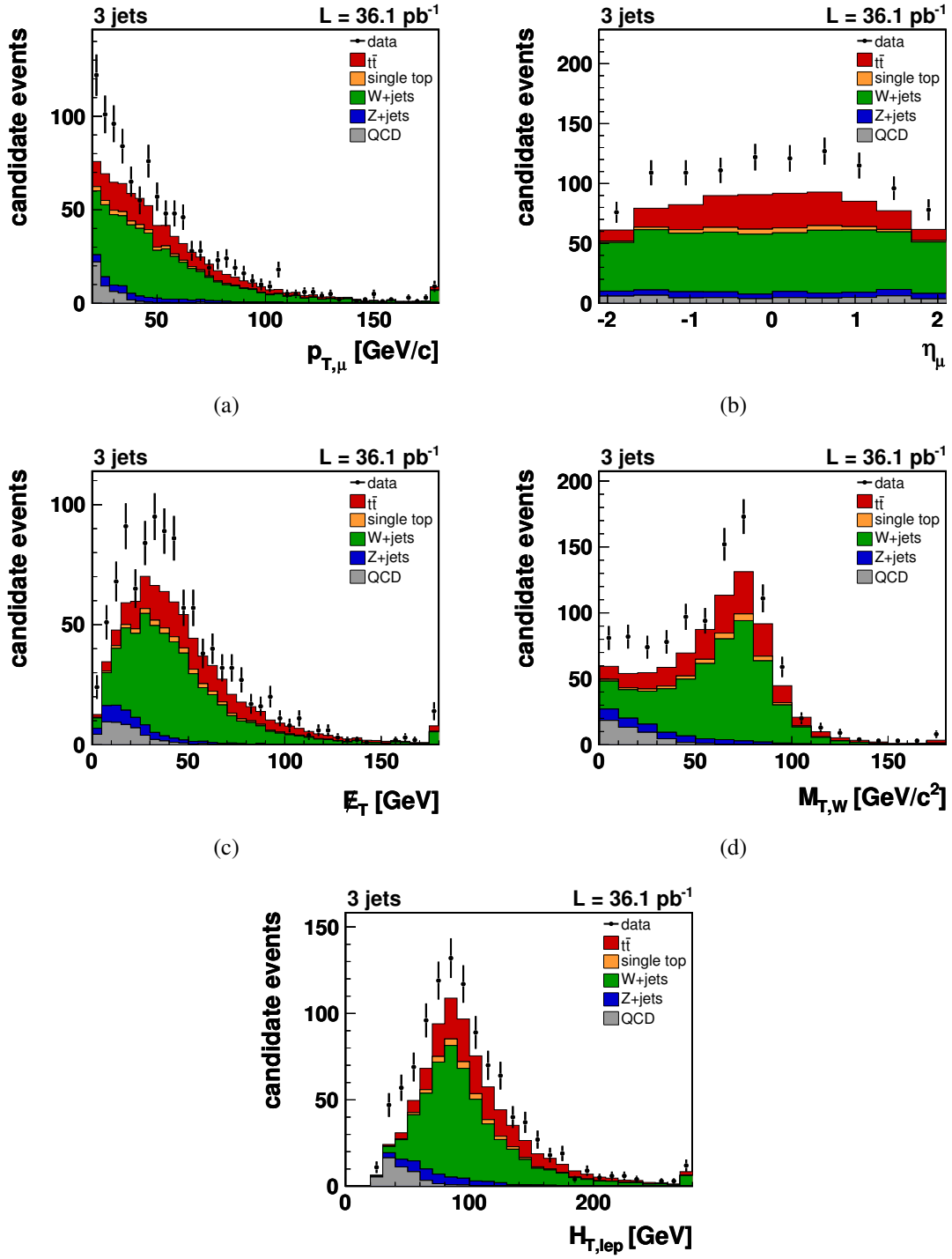

(a) (b) (c) (d) (e)

Figure 4.14: Comparison of kinematic distributions for observed and simulated pp collision data in a selected sample with exactly three jets per event and normalised to the predictions given in table 4.10. The transverse momentum and pseudorapidity distribution of the selected muon candidate can be found in (a) and (b), respectively. In (c), (d), and (e) the distributions of the missing transverse energy, of the transverse W boson mass, and of $H_{\mathrm{T,lep}}$ are depicted. Of particular importance is the $\not\!\!E_{\mathrm{T}}$ distribution in (c), since this observable will play a central role in the search for top quark pair production and the measurement of the $t\bar{t}$ production cross section in chapter 5.

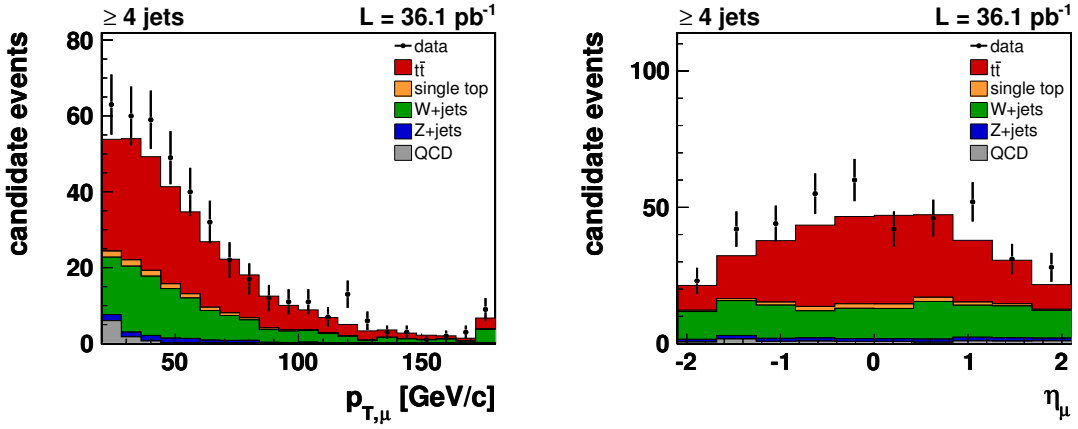

(a)

(b)

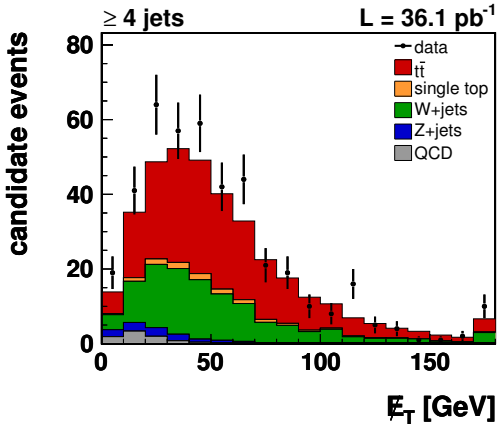

(c)

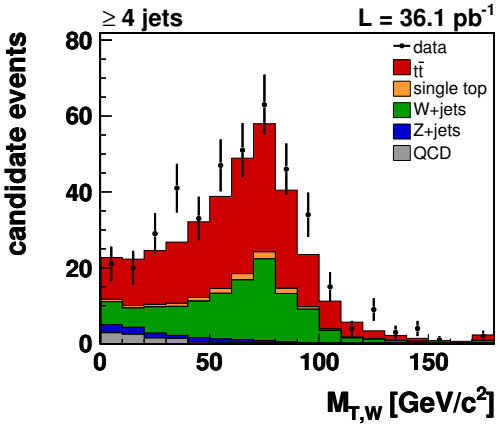

(d)

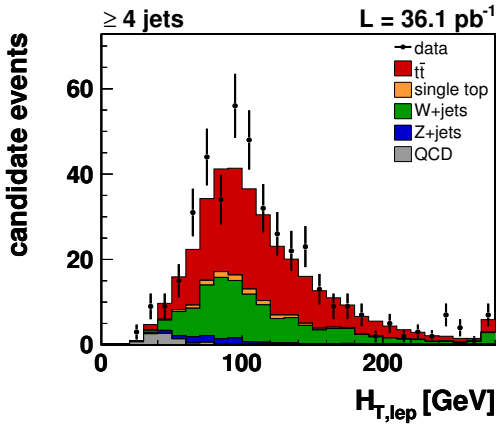

(e)

Figure 4.15: Comparison of kinematic distributions for observed and simulated pp collision data in a selected sample with at least four jets per event and normalised to the predictions given in table 4.10. The transverse momentum and pseudorapidity distribution of the selected muon candidate can be found in (a) and (b), respectively. In (c), (d), and (e) the distributions of the missing transverse energy, of the transverse W boson mass, and of $H_{\mathrm{T,lep}}$ are depicted.

Chapter 5

Search for Top Quarks and Measurement of the $t\bar{t}$ Production Cross Section

The ultimate aim of the analysis presented in this thesis is the observation of top quark pair production and the measurement of its cross section in the muon+jets channel. For these purposes, the fraction of $t\bar{t}$ events $f_{t\bar{t}}$ in a given data set comprising $N_{\text{data}}^{\text{obs}}$ observed candidate events is extracted by means of a binned likelihood fit to the distributions of appropriate observables which facilitate the discrimination between signal and background processes. Comparing the observed value of $f_{t\bar{t}}$ with expectations obtained by employing the binned likelihood fit procedure to a hypothetical model neglecting any $t\bar{t}$ signal contributions, the sensitivity of the $t\bar{t}$ search can be determined. Moreover, the top quark pair production cross section can be extracted from $f_{t\bar{t}}$ via

$$\sigma_{t\bar{t}} = \frac{f_{t\bar{t}} \cdot N_{\text{data}}^{\text{obs}}}{(A \cdot \epsilon)_{t\bar{t}} \cdot L}\,, \tag{5.1}$$

where L is the integrated luminosity and $(A \cdot \epsilon)_{t\bar{t}}$ denotes the product of acceptance times efficiency for $t\bar{t}$ events. Before applying the elaborated procedures to observed pp collision data, Monte Carlo techniques are employed to estimate the sensitivity of the $t\bar{t}$ search and the statistical uncertainty on the cross section measurement. Furthermore, uncertainties in the theoretical modelling and in the experimental techniques might adversely affect the determination of $f_{t\bar{t}}$. Therefore, potential sources of systematic uncertainties are taken into account and their impact on the applied analysis methods is investigated. Finally, the sensitivity of the top quark search and the cross section for $t\bar{t}$ production at a centre-of-mass energy of $\sqrt{s} = 7$ TeV are determined, based on the full set of pp collision data acquired with the CMS detector in 2010, corresponding to an integrated luminosity of $L = (36.1 \pm 4.0)\ \text{pb}^{-1}$.

5.1. Discriminating Observables

The determination of the fraction $f_{t\bar{t}}$ of $t\bar{t}$ events in a given data set by means of a binned likelihood fit procedure requires the selection of observables which allow to separate signal from background processes. For this purpose, a two-layered approach has been adopted for the analysis presented in this thesis. First, an observable is chosen which facilitates the discrimination between top quark pair production and the most significant background contribution in the muon+jets channel, namely W+jets production. To further reduce the uncertainty on the determination of this main background contribution, a second observable is selected, devoted to the separation of W+jets production from remaining background contributions.

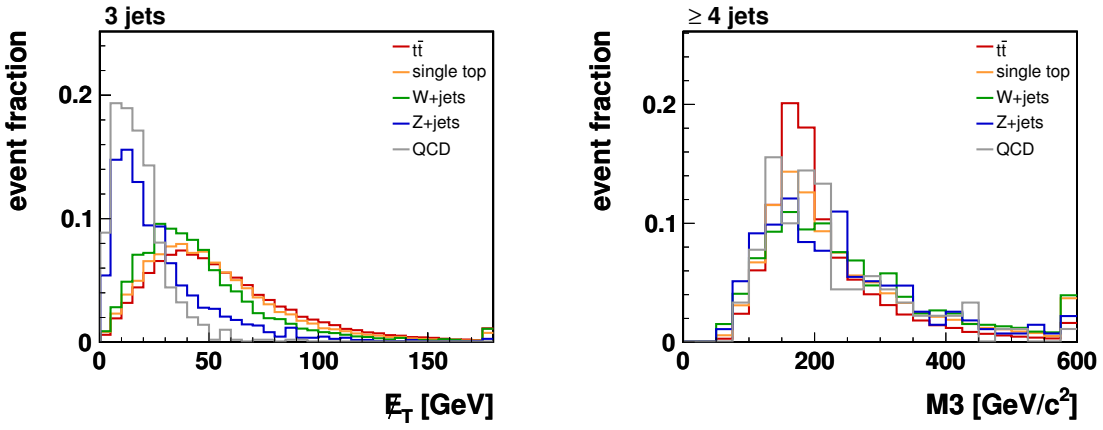

(a) (b)

Figure 5.1: Shape comparisons of the $\not\!\!E_T$ and M3 distributions for signal and background processes. The distribution of the missing transverse energy with a requirement on exactly three jets per event, is shown in (a). Since $t\bar{t}$, electroweak single top quark, and W+jets production processes comprise neutrinos from leptonic decays of on-shell W bosons in the event topology, these processes feature higher $\not\!\!E_T$ values compared to Z+jets or QCD multijet production. In (b) the distribution of M3 is shown after imposing the requirement on at least four jets per event. Due to its sensitivity to the top quark mass, the M3 distribution for $t\bar{t}$ signal and for electroweak production of single top quarks exhibit a prominent peak around the top quark mass, while all other background processes show broader M3 distributions.

As discussed in section 4.4.1, the highest signal-to-background ratio is expected in a sample of candidate events with the full set of selection criteria are applied, including the requirement on at least four jets per event. Therefore, an observable sensitive to characteristic signal properties in this phase-space region provides a promising candidate for the separation of $t\bar{t}$ and W+jets production. Due to its sensitivity to the top quark mass, the chosen discriminating observable is M3, denoting the invariant mass of those three jets per event which exhibit the highest vectorial-summed transverse momentum as introduced in section 4.5. The separation power of M3 can be deduced from figure 5.1 (b), depicting a shape comparison of M3 distributions for $t\bar{t}$ production and the expected background processes. Compared to top quark pair production, all background processes, except for electroweak production of single top quarks, exhibit broader M3 distributions with maxima around the top quark mass, but without the prominent peak observed in $t\bar{t}$ events. Since the production of single top quarks also comprises a top quarks in the final state topology, the M3 distribution is very signal-like and thus hardly distinguishable from the distribution in $t\bar{t}$ events. However, this background process is theoretically well-understood and the contribution induced by single top quark production is comparatively small.

The second observable is dedicated to the separation of W+jets and the remaining background contributions to $t\bar{t}$ production in the muon+jets channel, namely QCD multijet and Z+jets production. For this purpose, a characteristic property in the leptonic decay of on-shell W bosons can be exploited to select an appropriate discriminating observable. Due to emerging neutrinos, events comprising such leptonic W boson decays are expected to exhibit substantial amounts of missing transverse energy ($\not\!\!E_T$). In contrast, for QCD mul-

tijet and Z+jets production less missing transverse energy is predicted. Depending on the particular QCD multijet production process involved, the $\not\!\!E_{\mathrm{T}}$ contribution emerges from semileptonic decays of hadrons comprising b or c quarks in the process of hadronisation, from processes involving decay-in-flight muon production, or merely from the finite energy resolution provided by the calorimetry system. Similar arguments hold for Z+jets events, where significant amounts of missing transverse energy are only expected in $Z \to \tau\tau$ events with a subsequent $\tau \to \mu\nu_\mu\nu_\tau$ decay. Applying the event selection criterion on exactly one well-identified and isolated muon candidate to simulated Z+jets events, however, yields relative fractions of about 70% and 30% for $Z \to \mu\mu$ and $Z \to \tau\tau$ decays, respectively. Consequently, $\not\!\!E_{\mathrm{T}}$ constitutes an appropriate observable for the separation of W+jets production and background contributions emerging from Z+jets and QCD multijet production processes. Moreover, since the final state topology of $t\bar{t}$ events in the muon+jets channel comprise neutrinos emerging from an on-shell W boson decay as well, the use of missing transverse energy as discriminating observable facilitates to further improve the separation of $t\bar{t}$ signal and these background contributions. As can be deduced from table 4.6, the contribution of W+jets production is enhanced in candidate event samples for which altered jet multiplicity requirements applied. In order to perpetuate a phase-space region close to the one selected for the separation of $t\bar{t}$ and W+jets production, and hence to profit from an additional $t\bar{t}$ contribution, the criterion on exactly three jets per event is used. Figure 5.1 (a) shows the missing transverse energy distributions for $t\bar{t}$, W+jets, and all other considered background processes for these event selection criteria. As expected, QCD multijet and Z+jets events exhibits on average smaller values for the missing transverse energy compared to W+jets, $t\bar{t}$, or electroweak single top quark production.

5.1.1. Data-Driven Modelling of QCD Multijet Production Processes

Despite the large number of generated events, the sizable weighting factor w for the simulation-based modelling of QCD multijet production processes presented in table 4.4, renders statistically accurate predictions of kinematic distributions for this background contribution unfeasible. Moreover, demanding modelling procedures are required for an accurate description of the various contributing QCD multijet production processes, which collectively feature small selection efficiencies. Consequently, the $\not\!\!E_{\mathrm{T}}$ and M3 distributions, as well as the expected event yields, provided by the simulation-based modelling of QCD multijet production processes can only be considered as coarse estimates. To circumvent intricacies induced by statistical fluctuations related to an insufficient number of generated events and to minimise the dependency on simulation-based predictions, a data-driven procedure is employed to model the $\not\!\!E_{\mathrm{T}}$ and M3 distribution of events originating from QCD multijet production processes. For this purpose, the applied selection criteria are modified, aiming for the selection of a candidate event sample which is highly enriched in QCD multijet events. By appropriately choosing these altered selection criteria, events populating this so-called side-band region are assumed to emulate the $\not\!\!E_{\mathrm{T}}$ and the M3 distribution of QCD multijet production processes in the signal region, which is defined by the standard event selection criteria. As depicted in figure 4.7, the isolation requirement imposed on muon candidates effectively reduces contributions from QCD multijet production processes which comprise secondarily produced or erroneously identified

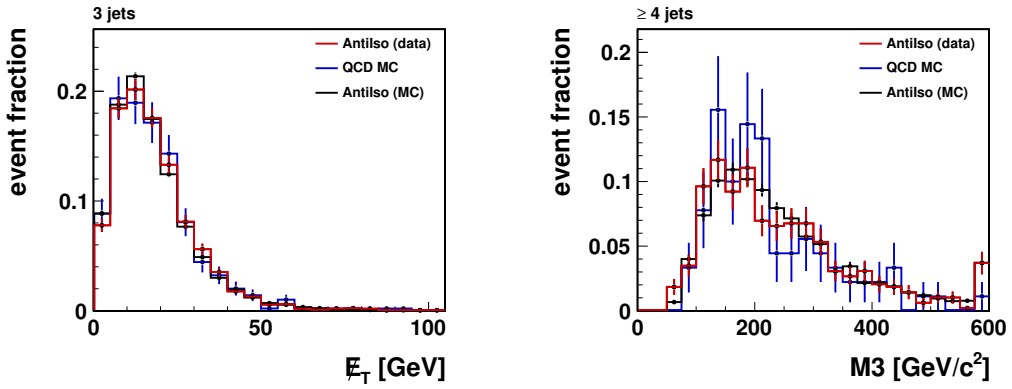

(a) (b)

Figure 5.2: Comparison of $\not\!\!E_T$ and M3 distributions for QCD multijet production processes obtained from simulation-based and data-driven models. In order to obtain such a data-driven model, the isolation requirement in the event selection applied to observed pp collision data is modified to $0.2 < I_{\text{rel}} < 0.5$, leading to a so-called AntiIso sample. As consistency check, this AntiIso selection is additionally applied to the full set of simulated events of all considered signal and background processes, denoted by AntiIso (MC). Within the statistical uncertainties, good agreement is observed for the $\not\!\!E_T$ and M3 distributions obtained from the simulated sample of QCD multijet events and the AntiIso selection in observed and simulated pp collision data.

muon candidates. Therefore, altering the event selection such that the selected muon candidate satisfies all requirements except for the $I_{\text{rel}} < 0.05$ requirement is well-suited to provide a sample of events enriched in QCD multijet production processes. However, instead of merely inverting the isolation requirement, a criterion of $0.2 < I_{\text{rel}} < 0.5$ is imposed on the muon candidate. The motivation for the lower boundary in this so-called AntiIso selection is to reduce potential contamination of $t\bar{t}$ signal or other considered background processes in this side-band region. On the other hand, due to the correlation between I_{rel} and the transverse momentum of the selected muon candidate, the kinematic behaviour of events with large I_{rel} values is expected to be different from events in the signal region. Therefore, the upper boundary of $I_{\text{rel}} = 0.5$ is applied to maintain a sample of candidate events, covering a phase-space region similar to the one selected by the standard event selection criteria. Apart from the described modifications, the default event selection criteria including the loose lepton vetoes and the requirements of exactly three or at least four jets per event are imposed. Hence, employing this AntiIso selection to observed pp collision data provides a so-called AntiIso sample of candidate events which can be used to emulate kinematic distributions for QCD multijet production processes. As can be seen in figure 5.2, the $\not\!\!E_T$ and M3 distributions obtained via this data-driven procedure and the corresponding simulation-based distributions show good agreement within the statistical fluctuation. Moreover, an additional consistency check is performed by application of the AntiIso selection to the full set of simulated events for all considered signal and background processes. The corresponding $\not\!\!E_T$ and M3 distributions for this simulation-based AntiIso sample are depicted in figure 5.2 as well, exhibiting good agreement with the data-driven distributions obtained by application of the AntiIso selection to observed pp collision data.

Table 5.1: Expected composition of the AntiIso sample. The given contributions are estimated from employing the AntiIso selection, defined by a modified isolation requirement of $0.2 < I_{\text{rel}} < 0.5$, to the full set of simulated events for all signal and considered background processes. Accordingly, an event sample highly enriched in QCD multijet production processes is expected for both jet multiplicity requirements. In addition, the last column comprises candidate event yields, obtained by employing the AntiIso selection to observed pp collision data, corresponding to an integrated luminosity of 36.1 pb^{-1}.

requirement	$t\bar{t}$	W+jets	Z+jets	QCD	observed events
$=3$ jets	0.7%	0.5%	0.4%	98.3%	2158
≥ 4 jets	4.7%	0.6%	0.5%	94.1%	488

Applying the AntiIso selection to the full set of simulated events furthermore allows to estimate the composition of the AntiIso sample as listed in table 5.1. Accordingly, the expected purity of QCD multijet production processes in the AntiIso sample with a requirement of exactly three or at least four jets per event is 98.3% and 94.1%, respectively. Moreover, table 5.1 comprises the candidate event yields obtained by employing the AntiIso selection to observed pp collision data, corresponding to an integrated luminosity of $L = 36.1$ pb^{-1}. Compared to the unweighted number of simulated events after imposing the standard selection criteria, the data-driven AntiIso sample thus provides about two times more events for the modelling of QCD multijet production processes.

5.2. Statistical Methods

The search for top quark pair production can be formally related to the concept of statistical significance, wherein the significance level quantifies the probability for observing signal events based on a mere fluctuation of expected background contributions. A well-established procedure for the determination of this significance level is provided by hypothesis testing. In this procedure, the probability for the rejection of a hypothesis without signal contributions is computed, assuming this so-called null hypothesis were true. Moreover, for the determination of the $t\bar{t}$ production cross section according to equation (5.1), the fraction $f_{t\bar{t}}$ of $t\bar{t}$ events in a given data set with $N_{\text{data}}^{\text{obs}}$ candidate events has to be extracted. Both analysis techniques are based on a binned likelihood fit procedure which simultaneously investigates the observed $\not{E}_{\text{T}}$ and M3 distributions in statistically orthogonal candidate events with requirements on exactly three or at least four jets, respectively. To accomplish this approach, a likelihood function and appropriate models for the description of the observed kinematic distributions are required. The number of $t\bar{t}$ events as well as the expected background contributions are incorporated in the likelihood function as model parameters and can thus be determined by maximising the likelihood function. Prior to the application of the elaborated techniques to the $\not{E}_{\text{T}}$ and M3 distributions in observed pp collision data, the significance level of the $t\bar{t}$ search and the statistical uncertainty on the cross section measurement can be estimated using ensemble test comprising pseudo-experiments. Therein, Monte Carlo techniques are used to derive so-called pseudo-data distributions from the expected signal and back-

ground processes. Applying the analysis procedures to the $\not\!\!E_{\mathrm{T}}$ and M3 distributions in each pseudo-experiment therefore allows to obtain ensemble-averaged expectations. For the implementation of the binned likelihood fit procedure and to perform ensemble tests, theta [194] is used, a framework for template-based modelling and inference.

5.2.1. Modelling and Binned Likelihood Fit Procedure

The modelling of $\not\!\!E_{\mathrm{T}}$ and M3 distributions in observed pp collision data is based on simulated samples of $t\bar{t}$, electroweak single top quark, W+jets, and Z+jets production, as well as on the data-driven AntiIso sample introduced in section 5.1.1. In particular, a linear combination of all contributing processes k ($k = t\bar{t}$, t, W, Z, and QCD) is used to predict the event yield in bin i of the distribution of observable o ($o =$ M3, $\not\!\!E_{\mathrm{T}}$) via

$$\mu_i(\nu_k) = \sum_k \mu_{ik} = \sum_k \nu_k \cdot \mathcal{T}_{ik} \,. \tag{5.2}$$

The event yield of process k is given by the corresponding model parameter ν_k, and $\mathcal{T}_{ik}$ denotes the relative fraction of events for process k in bin i. Alternatively, the probability distributions $\mathcal{T}_k$ can be conceived as histograms normalised to unit area which fulfil the normalisation condition $\sum_i \mathcal{T}_{ik} = 1 \;\forall\, k$. Depending on the investigated discriminating observable, $\not\!\!E_{\mathrm{T}}$ or M3, the parameters ν_k represent Poisson means of the expected number of events emerging from $t\bar{t}$, single top quark, W+jets, Z+jets, or QCD multijet production in a candidate event sample with an applied requirement of exactly three or at least four jets per event, respectively. The electroweak production of single top quarks, denoted by $k = t$, thereby comprise a combination of the Wt- and the t-channel production mode according to theory predictions.

A simultaneous investigation of $\not\!\!E_{\mathrm{T}}$ and M3 as discriminating observables can be accomplished by combining the two individual models used for the description of the $\not\!\!E_{\mathrm{T}}$ and M3 distribution. For this purpose, the relative fraction of event yields for applied selection criteria of exactly three and at least four jets per event, are fixed to the predictions obtained from table 4.10. Consequently, the model used for the description of observed $\not\!\!E_{\mathrm{T}}$ and M3 distributions in pp collision data comprises only five model parameters ν_k, corresponding to the number of $t\bar{t}$ signal, electroweak single top quark, W+jets, Z+jets, and QCD multijet production events. To furthermore facilitate a direct comparison of model parameters with given predictions, the parameters β_k can be introduced via

$$\beta_k = \frac{\nu_k}{\hat{\nu}_k} = \frac{\sigma_k}{\sigma_k^{\mathrm{theory}}} \,, \tag{5.3}$$

representing the ratio of measured to predicted event yields, whereas the yield estimates $\hat{\nu}_k$ are taken from the corresponding rows of table 4.10. Moreover, the parameters β_k can be interpreted as the ratio of measured to theory-predicted cross section values. Using this alternative parametrisation, the predicted event yield μ_i can be rewritten as

$$\mu_i(\beta_k) = \sum_k \beta_k \cdot \hat{\nu}_k \cdot \mathcal{T}_{ik} \,. \tag{5.4}$$

Using this elaborated model, the investigation of observed $\not\!\!E_{\mathrm{T}}$ and M3 distributions in pp collision data facilitates the determination of the model parameters β_k by means of a

maximum likelihood procedure. For this purpose, the MINUIT package [195] is used to minimise the negative logarithm of a likelihood function which depends on the observed distributions and the model parameters β_k. Given an observed distribution d of observable o with n_i events per bin i, the likelihood function can be defined as

$$L(\beta_k;\Delta_k|d) = \prod_{i=1}^{N_{\text{bins}}} P\left(n_i|\mu_i\right) \cdot G(\beta_k;\Delta_k)\,, \tag{5.5}$$

where N_{bins} denotes the total number of bins used for the distribution of observable o. In particular, $N_{\text{bins}} = 36$ and $N_{\text{bins}} = 24$ have been chosen for the distribution of $\not\!\!E_{\text{T}}$ and M3, respectively. The first term in equation (5.5)

$$P\left(n_i|\mu_i\right) = \frac{\mu_i^{n_i} \cdot e^{-\mu_i}}{n_i!}\,, \tag{5.6}$$

represents the Poisson probability of observing n_i events, given a Poisson mean μ_i. The second term in equation (5.5) introduces a Gaussian constraint

$$G(\beta_k;\Delta_k) = \frac{1}{\sqrt{2\pi\Delta_k^2}} e^{-\frac{(\beta_k-1)^2}{2\Delta_k^2}}\,, \tag{5.7}$$

facilitating the incorporation of a priori knowledge such as estimated background event yields. This allows for a more robust application of the maximum likelihood technique in terms of avoiding free floating model parameters β_k for certain background processes, or maximisation issues in case the separation power provided by the discriminating observables is insufficient. As discussed in section 5.1, the distributions of $\not\!\!E_{\text{T}}$ and M3 for $t\bar{t}$ signal and electroweak single top quark production are quite similar, potentially leading to computational issues in the applied maximisation technique. Due to this similarity, to the small number of expected single top quark events, and to the fact that this process is theoretically well-understood and described, a constraint on the amount of electroweak single top quark events is employed. Therefore, a Gaussian constraint $G(\beta_t;0.30)$ is applied, whereas the predictions $\hat{v}_t$ are taken from table 4.10. Due to the discrepancy between observed and expected event yields discussed in section 4.5, the width $\Delta_t = 0.30$ incorporates a conservatively estimated uncertainty of 30% on the expected event yields. In addition, the separation between W+jets and Z+jets production might suffer from the similarity of the expected M3 distributions for these two processes and from the similarity of the $\not\!\!E_{\text{T}}$ distributions in Z+jets and QCD multijet production events. Therefore, a second constraint $G(\beta_W/\beta_Z;0.30)$ is introduced on the ratio of theory-predicted cross section values for W+jets and Z+jets production. Thus, substituting the ratio of model parameters β_W/β_Z for the single parameter β_k in equation (5.7), a constraint is applied with a width of $\Delta_{W/Z} = 0.30$. Moreover, all model parameters β_k in equation (5.5) are constrained to non-negative values in order to prevent unphysical results for event yields or cross section values.

Finally, the product of two likelihood functions is used in the search for top quark pair production and for the measurement of the $t\bar{t}$ production cross section

$$L(\beta_k;\Delta_k|d) = L_3(\beta_k;\Delta_k|d_3) \cdot L_4(\beta_k;\Delta_k|d_4)\,. \tag{5.8}$$

Except for the Gaussian constraints $G(\beta_t; 0.30)$ and $G(\beta_W/\beta_Z; 0.30)$ which only appear once in this product, the likelihood functions L_3 and L_4 are defined according to equation (5.5), based on observed distributions d_3 and d_4, corresponding to the observed $\not{E}_{\mathrm{T}}$ and M3 distributions, respectively. For the determination of the model parameter values $\hat{\beta}_k$, the likelihood function $L(\beta_k; \Delta_k|d)$ is maximised with respect to all model parameters β_k. However, prior to a detailed discussion about the application of this binned likelihood fit procedure in the search for top quark pair production in section 5.2.3 and for the measurement of the $t\bar{t}$ production cross section in section 5.2.4, the concept of ensemble testing will be described.

5.2.2. Ensemble Testing

In order to estimate central values and uncertainties of a statistical method prior to its application to observed collision data, the procedure of ensemble testing can be employed. For this purpose, pseudo-experiments are performed, wherein a particular model is used to obtain so-called pseudo-data distributions by means of Monte Carlo techniques. The term ensemble in this context denotes the collection of pseudo-experiments based on the same a priori knowledge used to derive the pseudo-data distributions. In each pseudo-experiment, the pseudo-data distribution of observables o, namely the $\not{E}_{\mathrm{T}}$ and M3 distributions, are then subject to the elaborated binned likelihood fit procedure, resulting in a determination of values for the various model parameters β_k. Performing a large number of pseudo-experiments, ensemble-averaged expectations can be obtained, e.g. the expected statistical uncertainty on the measurement of the $t\bar{t}$ production cross section.

The most straight forward application of this ensemble testing procedure is to derive pseudo-data distributions from the same model used to describe the observed $\not{E}_{\mathrm{T}}$ and M3 distributions. For this purpose, a random number ν'_k per pseudo-experiment and process k is drawn according to a Poisson distribution with predicted mean $\hat{\nu}_k$. To additionally incorporate uncertainties on the expected background event yields, $\hat{\nu}_k$ is modified to $\hat{\nu}_k \cdot \delta_k$ for all background processes k. The parameters δ_k are drawn according to a Gaussian distribution centred around zero with a process-dependent width Δ_k^{exp}, as given in table 5.2. The ν'_k events are then drawn from the corresponding probability distributions $\mathcal{T}'_k$, which are in the given example identical to the nominal distributions $\mathcal{T}_k$. This leads to a pseudo-data distribution of observable o with μ'_i events per bin i according to the linear combination

$$\mu'_i = \sum_k \nu'_k \cdot \mathcal{T}'_{ik} \,. \tag{5.9}$$

On the other hand, the definition of the likelihood function is not modified for these altered predictions. Consequently, possible modifications like altered yield estimates ν'_k or altered probability distributions $\mathcal{T}'_k$ are only accounted for in the preparation of pseudo-data distributions. This consideration of a priori information in the generation of pseudo-experiments leads to so-called prior-predictive ensembles.

5.2.3. Hypothesis Testing

The determination of the significance level in the search for $t\bar{t}$ production is based on a hypothesis testing procedure. Therein, the probability for rejecting a hypothetical model

Table 5.2: Expected background uncertainties Δ_k^{exp} used for prior-predictive ensembles. Based on the uncertainties of theory-predicted cross section values for single top quark, W+jets, and Z+jets production, and to account for the differences between observed and simulated event yields, conservative rate uncertainties of 30% are assumed. Since the simulation-based modelling of QCD multijet production processes is considered particularly unreliable and thus merely provides coarse event yield estimates, an uncertainty of 100% is assumed on this expectation.

Δ_t^{exp}	Δ_W^{exp}	Δ_Z^{exp}	$\Delta_{\text{QCD}}^{\text{exp}}$
0.30	0.30	0.30	1.00

without signal contributions is computed, given this hypothesis were true. This hypothesis testing thus allows to determine whether observed candidate events can be ascribed to a mere fluctuation of background contributions, or to the occurrence of the investigated signal. To accomplish this determination, two distinct models are introduced for the description of observed $\not\!\!E_{\text{T}}$ and M3 distributions. The first model comprises signal and background contributions, corresponding to the so-called signal-plus-background hypothesis H_1, and is identical to the model introduced in equation (5.4). The alternative model, in turn, is based on a background-only assumption, also referred to as null hypothesis H_0. For this purpose, the signal parameter is fixed to $\beta_{t\bar{t}} = 0.0$ in this second model. Given observed $\not\!\!E_{\text{T}}$ and M3 distributions in data d, the maximisation of the two likelihood functions corresponding to the two alternative models can be used to define a likelihood ratio

$$Q = \sqrt{-2.0 \cdot \ln \frac{L(\hat{\beta}_{t\bar{t}}, \hat{\beta}_k | d)}{L(\beta_{t\bar{t}} = 0.0, \hat{\beta}'_k | d)}}\,, \tag{5.10}$$

where the numerator is obtained by maximising the likelihood function defined in equation (5.8) with respect to all model parameters β_k. On the other hand, the denominator is determined from the maximisation with respect to the background parameters β_k, while the signal parameter is fixed to $\beta_{t\bar{t}} = 0.0$. Since this latter procedure corresponds to the null hypothesis, a small value of this likelihood ratio in data indicates compatibility with a mere fluctuation of background processes, while a large Q value favours the signal-plus-background hypothesis. The use of the likelihood ratio Q as test statistic is motivated by the Neyman-Pearson lemma [13] which indicates that a likelihood ratio is the most sensitive observable for separating hypotheses.

In order to quantify the rejection of the null hypothesis, and thus to determine the significance level of the $t\bar{t}$ search, the value $\widehat{Q}_{\text{obs}}$ obtained from the likelihood fit to the $\not\!\!E_{\text{T}}$ and M3 distributions in observed pp collision can be compared to the Q value distribution q_0 of the background-only assumption. For this purpose, an ensemble test is performed using the null hypothesis as model to obtain pseudo-data distributions for the discriminating observables $\not\!\!E_{\text{T}}$ and M3. Therein, the number of events ν'_k for each background processes k, is drawn from a Poisson distribution with mean $\hat{\nu}_k \cdot \delta_k$ and the ν'_k events are drawn from the corresponding probability distributions $\mathcal{T}_k$ as discussed in section 5.2.2. The determination of the Q value per pseudo-experiment then yields the distribution q_0 which can be

used to quantify the significance level of the $t\bar{t}$ search via the so-called p value

$$\hat{p}_{\text{obs}} = \frac{1}{A_q} \cdot \int_{\widehat{Q}_{\text{obs}}}^{\infty} q_0(Q')dQ' \,, \tag{5.11}$$

with $A_q = \int_{-\infty}^{\infty} q_0(Q')dQ'$. The p value determines the probability of observing a value Q at least as large as $\widehat{Q}_{\text{obs}}$, given the null hypothesis were true. Alternatively, the result of a hypothesis test can be reported in terms of standard Gaussian deviations σ, derived by converting the p value according to the integral expression

$$\sigma(p) = \sqrt{2} \cdot \text{Erf}^{-1}[1 - 2(1-p)] \quad \text{with} \quad \text{Erf}(z) = \frac{2}{\sqrt{\pi}} \int_0^z e^{-t^2} dt \,. \tag{5.12}$$

The used criterion for claiming observation of $t\bar{t}$ production is $\hat{p}_{\text{obs}} < 2.87 \cdot 10^{-7}$ which corresponds to a 5σ discrepancy between the observed likelihood ratio and the corresponding expectation based on a mere fluctuation of background contributions.

Prior to the evaluation of physical results, the expected significance of the applied procedure can be tested. For this purpose, an ensemble test based on the signal-plus-background hypothesis H_1 is performed. The model used to construct pseudo-data $\not{E}_{\text{T}}$ and M3 distributions therefore includes signal and background contributions. The median of the resulting Q value distribution q_1 can be used to determine an expected value $\widehat{Q}_{\text{exp}}$. The choice of this so-called median-expected Q value is motivated by a 50% probability for observing a value of $Q < \widehat{Q}_{\text{exp}}$, given the signal-plus-background hypothesis H_1 were true. Substituting $\widehat{Q}_{\text{exp}}$ for the observed value $\widehat{Q}_{\text{obs}}$ in equation (5.11), the expected p value $\hat{p}_{\text{exp}}$ can be obtained. However, several sources of systematic uncertainties might alter the Q value distributions q_0 and q_1 by affecting the probability distributions $\mathcal{T}_k$ or the expected event yields $\hat{\nu}_k$, subsequently leading to altered significance levels $\hat{p}_{\text{obs}}$ and $\hat{p}_{\text{exp}}$. Therefore, the impact of systematic uncertainties on the distribution q_0 and thus on the significance for $t\bar{t}$ production will be studied in section 5.3.10.

5.2.4. Cross Section Measurement

For the determination of the $t\bar{t}$ production cross section, a Neyman construction for central intervals is employed, using the maximum likelihood estimate for $\beta_{t\bar{t}}$ as test statistic. For this purpose, several ensemble tests are performed, wherein the models used to construct the prior-predictive ensembles systematically differ in the expected signal event yields $\hat{\nu}_{t\bar{t}}$. In contrast, the Poisson means $\hat{\nu}_k$ of the expected background event yields remain constant for the full set of ensemble tests. Employing the maximisation procedure to the likelihood function defined in equation (5.8) allows for the determination of the model parameter values $\hat{\beta}_k$ ($k = t\bar{t}$, t, W, Z, and QCD), yielding distributions of $\hat{\beta}_{t\bar{t}}$ for each particular value $\hat{\nu}_{t\bar{t}}$, or equivalently a true value $\beta_{t\bar{t}}^{\text{true}}$. The median values, and the 68% and 95% quantiles of these $\hat{\beta}_{t\bar{t}}$ distributions can then be used to estimate central values and to construct confidence belts, respectively. This is exemplarily shown in figure 5.3 (a) for a true value of $\beta_{t\bar{t}}^{\text{true}} = 1.0$. Performing this construction of central values and central confidence intervals in a $\beta_{t\bar{t}}^{\text{true}}$ range of $[0.0, 3.0]$, the Neyman construction depicted in figure 5.3 (b) can be obtained. Given observed $\not{E}_{\text{T}}$ and M3 distributions in pp collision data,

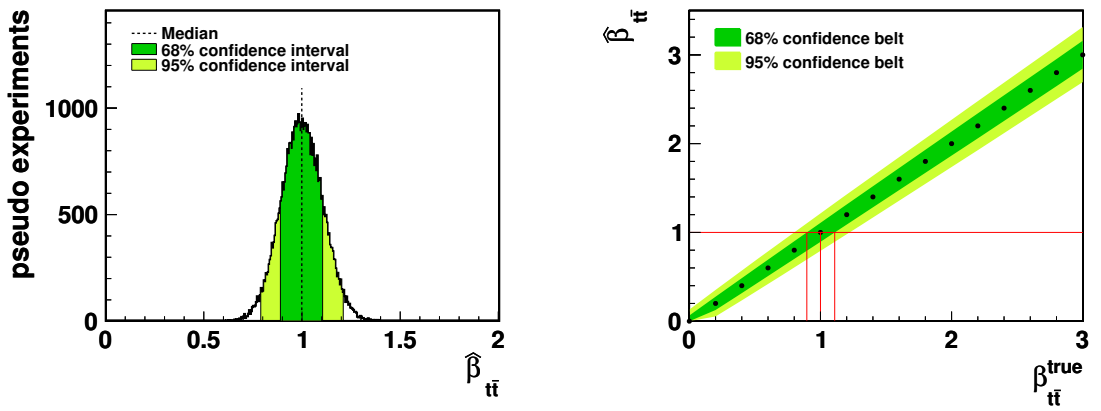

(a) (b)

Figure 5.3: Distribution of the maximum likelihood estimate for $\beta_{t\bar{t}}$ in an ensemble test based on $\beta^{\text{true}}_{t\bar{t}} = 1.0$ and the Neyman construction for the determination of the statistical uncertainty on $\sigma_{t\bar{t}}$, both assuming an integrated luminosity of $L = 36.1$ pb^{-1}. The dashed vertical black line and the filled green areas in (a) illustrate the extraction of the median, the 68%, and the 95% central confidence intervals which serve for the construction of central values and confidence belts in (b). Given this Neyman construction for central intervals based on the maximum likelihood estimate for $\beta_{t\bar{t}}$ as test statistic, the observed value $\hat{\beta}^{\text{obs}}_{t\bar{t}}$ in pp collision data can be used to determine the corresponding input value $\hat{\beta}^{\text{true}}_{t\bar{t}}$ as well as the statistical uncertainty. This determination is illustrated by the vertical red lines in (b), which indicates the intersections of a horizontal line at the median-expected value $\hat{\beta}^{\text{exp}}_{t\bar{t}} = 1.0$ with the central values and the boundaries of the 68% confidence belt. Accordingly, the estimated central value is $\hat{\beta}^{\text{true}}_{t\bar{t}}$ within statistical uncertainties of -10.4% and $+10.9\%$.

the determination of $\hat{\beta}^{\text{obs}}_{t\bar{t}}$ allows for the extraction of the corresponding input value $\hat{\beta}^{\text{true}}_{t\bar{t}}$ from this Neyman construction, as indicated by the intersection of the horizontal red line with the central values in figure 5.3 (b). Due to the linearity of the Neyman construction, the true value equals the observed value, i.e. $\hat{\beta}^{\text{true}}_{t\bar{t}} = \hat{\beta}^{\text{obs}}_{t\bar{t}}$. Moreover, the $\pm 1\sigma$ statistical uncertainties on this extracted value $\hat{\beta}^{\text{true}}_{t\bar{t}}$ can be obtained from the 68% confidence belt of the Neyman construction, as illustrated by the intersections of the horizontal red line with the boundaries of the inner confidence belt in figure 5.3 (b).

As for the determination of the significance level by means of hypothesis testing, several sources of systematic uncertainties might adversely effect the procedure for the extraction of the $t\bar{t}$ production cross section. However, the derived Neyman construction can be used to estimate the purely statistical uncertainty on the measurement of $\sigma_{t\bar{t}}$. For this purpose, the intersection of a horizontal red line at the median-predicted value $\hat{\beta}^{\text{exp}}_{t\bar{t}} = 1.0$ with the boundaries of the 68% confidence belt is used to determine the expected statistical uncertainty, as depicted in figure 5.3 (b). Consequently, the expected $\pm 1\sigma$ statistical uncertainties on the $t\bar{t}$ production cross section in a data set corresponding to an integrated luminosity of $L = 36.1$ pb^{-1} is -10.4% and $+10.9\%$.

5.3. Systematic Uncertainties

Several sources of systematic uncertainties might lead to a reduction of the significance level for the $t\bar{t}$ search, as well as to an increased uncertainty on the determination of the $t\bar{t}$ production cross section. These sources of systematic uncertainties are involved due to assumptions made in the simulation-based modelling of signal and background processes, like the parametrisation of the parton distribution functions or the parton shower configuration. Moreover, an inappropriate modelling of the considered processes might be induced by experimental uncertainties, for example on the determination of the jet energy scale or the jet energy resolution. Therefore, the systematic impact of uncertainties in the theoretical modelling and the experimental setup on the elaborated analysis techniques are investigated.

Since the source of a systematic uncertainty can affect the expected event yields for signal and background processes, as well as the probability distributions $\mathcal{T}_k$ of the investigated discriminating observables, the combined effect of altered rate and shape uncertainties has to be studied. For this purpose, the systematic impact on the measurements is evaluated by altering the modelling of the affected processes within the uncertainties of the given systematic, or by assigning a reasonable alternative model. As a result, relative changes of the event yields with respect to the nominal predictions $\hat{v}_k$ and altered probability distributions $\mathcal{T}_k'$ are obtained. Incorporating these altered predictions into the statistical methods, the impact of systematic uncertainties can be investigated. For this purpose, prior-predictive methods are used to incorporate systematic uncertainties into the hypothesis testing procedure, as well as into the Neyman construction. While this is straight-forward for the hypothesis testing procedure, also the Neyman construction allows for this inclusion via prior-predictive ensembles, since the method does not rely on asymptotic properties of the test statistic but yields per construction correct prior-averaged interval coverage. Finally, the expected sensitivity of the $t\bar{t}$ search and the uncertainty on the measurement of $\sigma_{t\bar{t}}$ including systematic uncertainties can be evaluated.

In order to estimate the systematic impact induced by the theoretical modelling of signal and background processes, several simulation-based samples have been produced with modified settings for the modelling of $t\bar{t}$, W+jets, and Z+jets production. A listing of these dedicated systematic samples can be found in appendix A.

5.3.1. Parton Distribution Functions

The simulation-based modelling of signal and considered background processes collectively depend on the parton distribution functions used to describe the colliding protons. Due to experimental uncertainties and employed evolution procedures based on the DGLAP equations, an imperfect knowledge of the applied parton distribution functions has to be assumed which potentially leads to systematic effects on the employed analysis techniques. To account for this uncertainty on the PDF modelling, the CTEQ6.6 [84] PDF set and the LHAPDF [196] package is used to perform a re-weighting procedure. Therein, each of the 22 orthogonal eigenvectors is separately altered to its 90% confidence interval boundary values. Calculating the difference between the nominal and these altered PDF values, an event-by-event weighting factor is obtained, which can be applied to the simulated events. Performing this re-weighting procedure with each of the 44 eigen-

vector variations, the relative deviations from the nominal yield estimates $\hat{v}_k$ depicted in figure 5.4 are obtained. Accordingly, maximal relative yield deviations of 0.6% and 0.4% are expected for $t\bar{t}$ events with selection criteria of exactly three or at least four jets, respectively. Similarly, small relative deviations are expected for single top quark production, while for W+jets and Z+jets production the most significant variations in terms of expected event yields are of the order of 3.3%. Table 5.3 summarises the maximal relative deviations of expected event yields for $t\bar{t}$ signal and the expected background processes for selection criteria of exactly three or at least four jets per event. Moreover, this re-weighting procedure leads to altered $\not{E}_{\mathrm{T}}$ and M3 probability distributions $\mathcal{T}_k'$ for $t\bar{t}$, single top quark, W+jets, and Z+jets production.

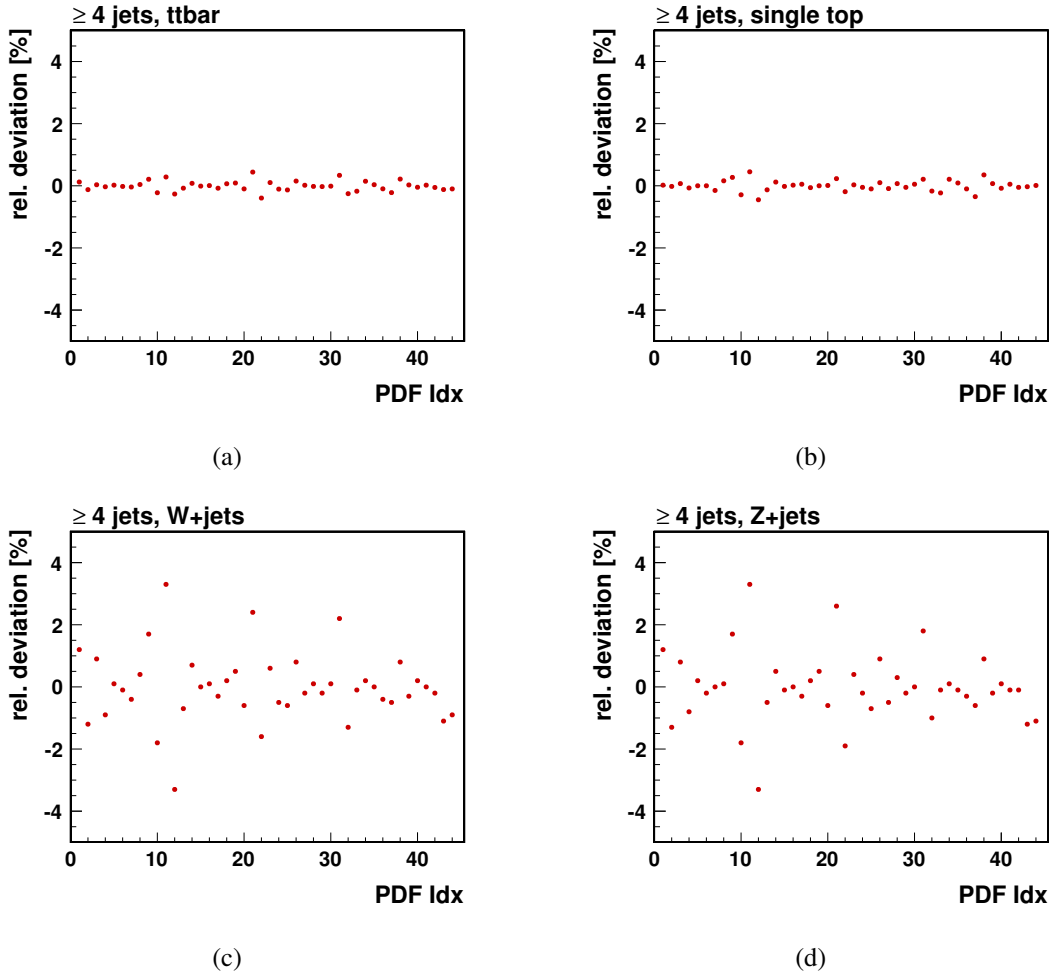

Figure 5.4: Impact of varying the values of the 22 orthogonal eigenvectors in the CTEQ6.6 PDF set within their 90% confidence interval boundaries on the expected event yields. In particular, the relative differences of expected event yields for the 44 eigenvector variations, denoted by PDF Idx, with respect to the central CTEQ6.6 PDF value are shown for $t\bar{t}$ (a), single top quark (b), W+jets (c), and Z+jets (d) production, employing a requirement on at least four jets per event.

Table 5.3: Impact of varying the values of the 22 orthogonal eigenvectors in the CTEQ6.6 PDF set within their 90% confidence interval boundaries on the expected event yields. The relative differences quoted are obtained as the maximal deviations between the nominal yield estimates and the ones derived from the 44 systematical variations. In particular, maximal yield differences for $t\bar{t}$, electroweak single top quark, W+jets, and Z+jets production are listed, corresponding to selection criteria of exactly three or at least four jets per event, respectively.

Requirement	$t\bar{t}$	single top	W+jets	Z+jets
$= 3$ jets	0.6%	0.7%	2.9%	2.4%
≥ 4 jets	0.4%	0.8%	3.3%	3.3%

5.3.2. Initial- and Final-State Radiation

Initial- and final-state radiation processes directly impact the jet topology of pp collision events. Therefore, uncertainties on the probability for initial- and final-state radiation to occur, represent potential sources of systematic uncertainties on the yield estimates $\hat{v}_k$, as well as on the simulation-based probability distributions $\mathcal{T}_k$ for the discriminating observables $\not{E}_{\mathrm{T}}$ and M3. In order to investigate the effect of higher or lower radiation probabilities, and thus the effect of reduced or increased initial- and final-state radiation in the simulation-based modelling of $t\bar{t}$ production, dedicated samples have been generated, for which several parameters in the parton-shower simulation provided by PYTHIA have been systematically varied. In particular, parameters governing the maximum parton virtuality, the maximal $p_{\perp}$ threshold of the parton shower, and Λ_{QCD} for the running coupling constant α_s have been adjusted. The impact of lower and higher probabilities for ISR/FSR processes on the expected $t\bar{t}$ event yields in selected candidate event samples including requirements of exactly three or at least four jets per event, can be found in table 5.4. Accordingly, differences up to -4.3% with respect to the nominal yield estimates are expected. In addition to this rate uncertainty, the impact on the shape of the $\not{E}_{\mathrm{T}}$ and the M3 probability distributions $\mathcal{T}_{t\bar{t}}$ are depicted in figure 5.5. Compared to the variation of expected event yields, the altered probability distributions $\mathcal{T}'_{t\bar{t}}$ exhibit minor differences compared to the nominal distributions.

Table 5.4: Impact of varying the amount of initial- and final-state radiation processes. The relative differences of yield estimates are derived from simulated $t\bar{t}$ event samples with lower (less) and higher (more) initial- and final-state radiation probability and the nominal $t\bar{t}$ sample. In particular, the differences in expected event yields correspond to selection criteria of exactly three or at least four jets per event, respectively.

Source	Requirement	$t\bar{t}$
less ISR/FSR	$= 3$ jets	$+0.6\%$
	≥ 4 jets	-0.1%
more ISR/FSR	$= 3$ jets	-4.3%
	≥ 4 jets	-4.2%

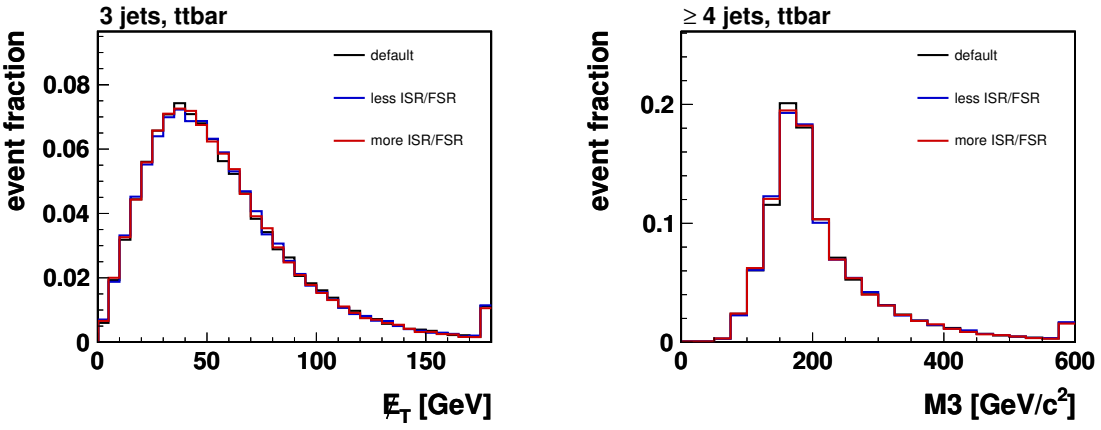

(a) (b)

Figure 5.5: Impact of varying the amount of initial- and final-state radiation processes on the probability distributions $\mathcal{T}_{t\bar{t}}$ of the discriminating observables. The comparison of the $\not\!\!E_T$ probability distributions for the nominal sample of simulated $t\bar{t}$ events and dedicated systematic samples with reduced and increased ISR/FSR probability is depicted in (a). Similarly, in (b) the corresponding shape comparison is shown for the distribution of the M3 distribution.

5.3.3. Uncertainty on Leptonic W Bosons Branching Ratios

As discussed in section 4.2.2, simulated $t\bar{t}$ signal and Wt single top quark events are weighted by a decay-mode specific factor f_{BR}, accounting for the measured leptonic W boson branching ratio $\mathrm{BR}(W \to l\nu) = 0.1080 \pm 0.0009$. The uncertainty of about 0.8% on this measurement thus entails uncertainties on the expected event yields as well as on the $\not\!\!E_T$ and M3 probability distributions for $t\bar{t}$ and single top quark production. In order to account for this uncertainty, f_{BR} is subject to a $\pm 1\sigma$ variation. Table 5.5 summarises the impact of employing the weighting procedure described in section 4.2.2 based on the $\pm 1\sigma$ varied factors f'_{BR} on the expected event yields. Moreover, the impact on the distributions of the discriminating observables for $t\bar{t}$ and Wt single top quark production has been investigated, yielding probability densities $\mathcal{T}'_k$ which are indistinguishable from the nominal distributions $\mathcal{T}_k$.

Table 5.5: Impact of varying the leptonic W boson branching ratio in the simulation-based modelling of $t\bar{t}$ and Wt single top quark events. The relative differences of yield estimates are derived from a $\pm 0.8\%$ variation of the measured branching ratio, technically implemented by a variation of the decay-mode specific fraction f_{BR}. In particular, the differences in expected event yields for selection criteria of exactly three or at least four jets per event are given.

Source	Requirement	$t\bar{t}$	Wt-channel
smaller f_{BR}	$= 3$ jets	-0.7%	-0.6%
	≥ 4 jets	-0.6%	-0.6%
larger f_{BR}	$= 3$ jets	$+0.7\%$	$+0.6\%$
	≥ 4 jets	$+0.6\%$	$+0.6\%$

Table 5.6: Impact of pile-up events in the generation of $t\bar{t}$ and W+jets production on the expected event yields, employing selection criteria of exactly three or at least four jets per event. The relative differences of yield estimates compared to the nominal expectations $\hat{\nu}_k$ are derived from samples of simulated events including additional hard interactions per bunch crossing. Since the amount of pile-up events in the given samples is slightly larger compared to expectations based on the observed SD_Mu data set, the listed yield differences represent conservative estimates on the expected rate uncertainties.

Source	Requirement	$t\bar{t}$	W+jets
Incl. pile-up events	$= 3$ jets	-3.5%	$+15.2\%$
	≥ 4 jets	$+3.2\%$	$+18.1\%$

5.3.4. Pile-Up Events

The samples of simulated events for $t\bar{t}$ signal and the expected background processes do not include the simulation of pile-up events. The assumption of negligible amounts of additional hard interactions per bunch crossing might be reasonable for early LHC data, however, for the most recent data the large instantaneous luminosity values lead to an expectation of about $4-5$ pile-up events. In order to estimate the effect of these additional hard interactions per bunch crossing, dedicated samples of simulated $t\bar{t}$ signal and W+jets background events have been generated. Although the average number of pile-up events in these samples is slightly larger compared to the given expectation, these samples of simulated events can be used to obtain a conservative estimate on the expected differences in terms of event yield estimates and probability distributions $\mathcal{T}_k'$. The impact on the expected yield estimates is summarised in table 5.6, exhibiting differences of up to 18% compared to the nominal expectations for W+jets production. In figure 5.6 shape comparisons of simulated events omitting and including effects of pile-up events on the expected $\not\!\!E_{\mathrm{T}}$ and M3 distributions for $t\bar{t}$ signal and W+jets production are shown. Compared to the sizable differences of event yield estimates, the probability distributions obtained from the systematically varied samples of simulated events evince less significant deviations compared to the nominal distributions $\mathcal{T}_k$.

5.3.5. Factorisation Scale and Matching Threshold

The simulation-based modelling of signal and background processes furthermore includes information on the factorisation and renormalisation scale, which are customarily set to a common scale $\hat{\mu} = \hat{\mu}_F = \hat{\mu}_R$ as discussed in section 1.2.1, and on the threshold value used in the MLM matching procedure. Since the particular parameter values used for the simulation of signal and background processes are to some extent arbitrary and might not be the optimal choice for the description of observed pp collision data, the impact of up- and downwards variations of these values are investigated. For this purpose, four additional event samples have been produced for the simulation-based modelling of $t\bar{t}$, W+jets, and Z+jets production, respectively. In particular, for the so-called scale systematic samples, the scale at which the running strong coupling constant α_s is evaluated is varied by a factor of 0.5 or 2.0, while the value of Λ_{QCD} used to calculate the running of

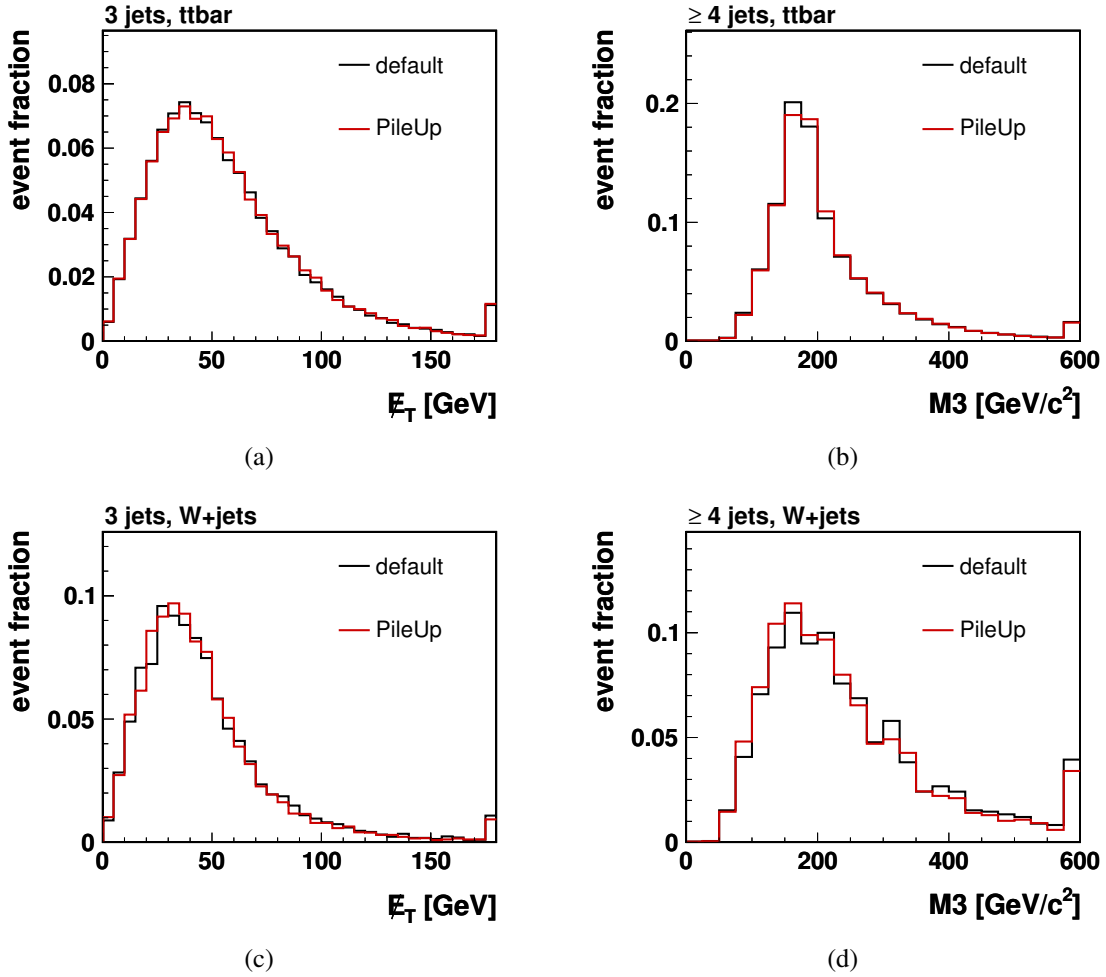

Figure 5.6: Impact of pile-up events in the generation of $t\bar{t}$ and W+jets production on the probability distributions $\mathcal{T}_k$ of the discriminating observables. Since the amount of pile-up events in the given samples of simulated events are slightly larger compared to expectations based on the observed SD_Mu data set, the comparison of nominal and systematically modified $\not\!\!E_T$ and M3 distributions represent conservative estimates on the expected shape uncertainties. In (a) and (c) the comparisons of $\not\!\!E_T$ distributions for the nominal samples and ones including the simulation of pile-up events are depicted for $t\bar{t}$ and W+jets production, respectively, using selection criteria of exactly three jets per event. The corresponding shape comparisons for the M3 distributions in selected samples with a requirement on at least four jets per event are shown in (b) and (d).

Table 5.7: Impact of varying the factorisation and renormalisation scale and the matching threshold for the simulation-based modelling of $t\bar{t}$, W+jets, and Z+jets production. The relative differences of yield estimates are derived from simulation-based samples with lower (down) and higher (up) values for the renormalisation and factorisation scale and for the matching threshold, respectively. In particular, the differences in expected event yields correspond to selection criteria of exactly three or at least four jets per event, respectively.

Source	Requirement	$t\bar{t}$	W+jets	Z+jets
Scale down	$= 3$ jets	-3.1%	$+102.7\%$	$+67.7\%$
	≥ 4 jets	$+9.1\%$	$+97.7\%$	$+81.7\%$
Scale up	$= 3$ jets	$+3.5\%$	-34.7%	-33.3%
	≥ 4 jets	-4.9%	-43.5%	-44.6%
Threshold down	$= 3$ jets	-0.3%	$+5.0\%$	-8.9%
	≥ 4 jets	$+1.8\%$	-0.4%	-0.3%
Threshold up	$= 3$ jets	$+1.3\%$	$+5.3\%$	-4.6%
	≥ 4 jets	-1.3%	-7.8%	-17.3%

α_s is simultaneously varied by a factor of 2.0 and 0.5, respectively. A similar procedure is used for the matching threshold, which has been varied by a factor 0.5 and 2.0 for the generation of the corresponding systematic samples. The effect of these variations on the expected event yields are summarised in table 5.7. Especially for W+jets and Z+jets production, variations of the factorisation and renormalisation scale lead to large differences of expected event yields with respect to the nominal yield estimates $\hat{v}_k$. For $t\bar{t}$ production, the corresponding yield differences are estimated to $(3-9)\%$. Compared to the scale uncertainty, the impact of varying the matching threshold induces minor differences in terms of event yield estimates. Furthermore, the effects of the scale and matching threshold variations on the $\not{E}_{\mathrm{T}}$ and M3 distributions $\mathcal{T}_k$ are depicted in figure 5.7 and figure 5.8, respectively.

Besides systematic effects induced by uncertainties in the theoretical modelling, experimental uncertainties might adversely effect the expectated event yields and the probability distribution of the discriminating observables. This second category of sources for systematic uncertainties will be discussed in the following sections.

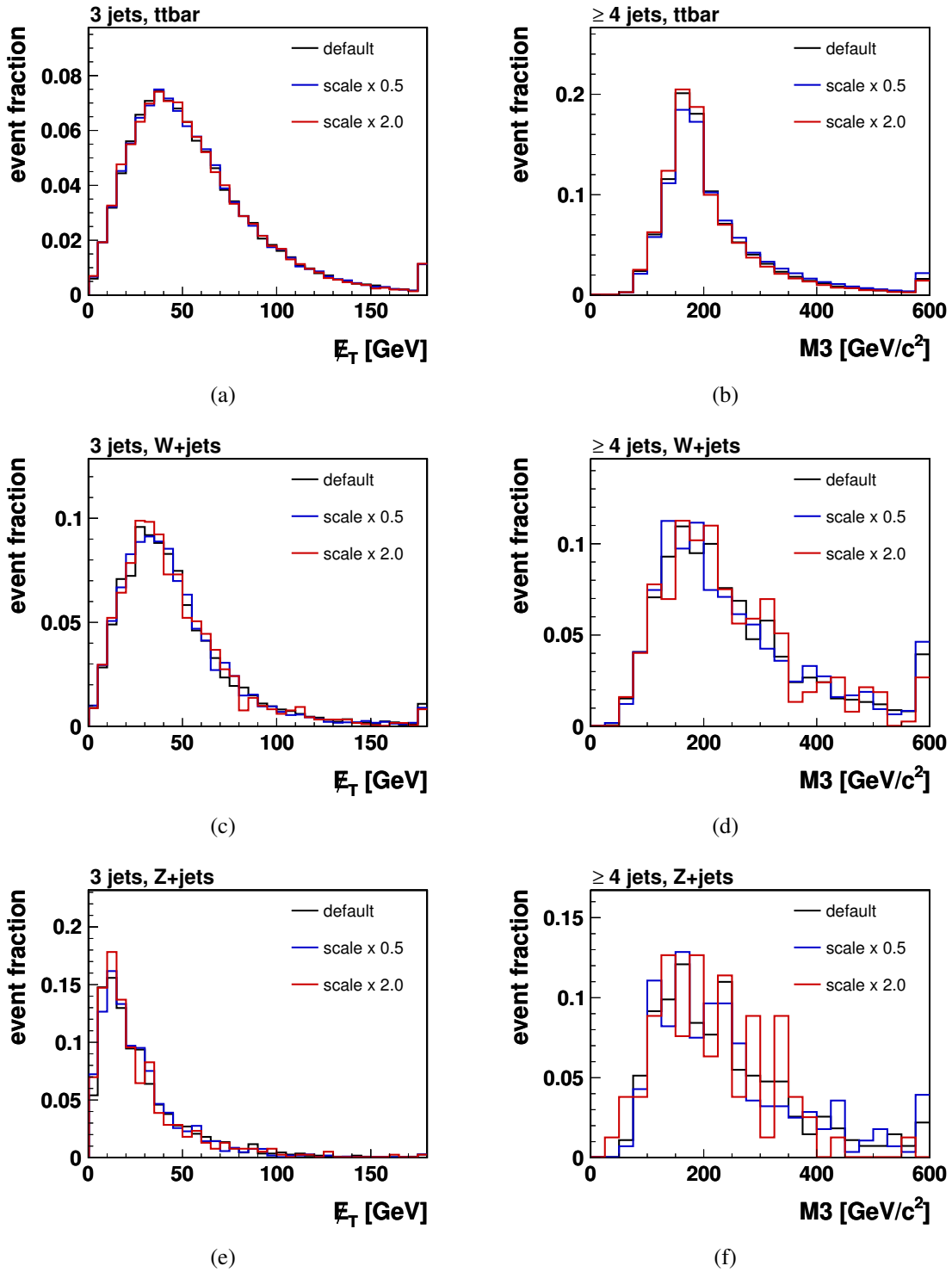

Figure 5.7: Impact of varying the renormalisation and factorisation scales on the probability distributions $\mathcal{T}_k$ of the discriminating observables. Shape comparisons of the nominal $\not\!\!E_{\mathrm{T}}$ distributions and the ones derived from the systematic samples are depicted in (a), (c), and (e) for $t\bar{t}$, W+jets, and Z+jets production, respectively. Similarly, in (b), (d), and (f), the corresponding shape comparisons for the M3 distributions are shown.

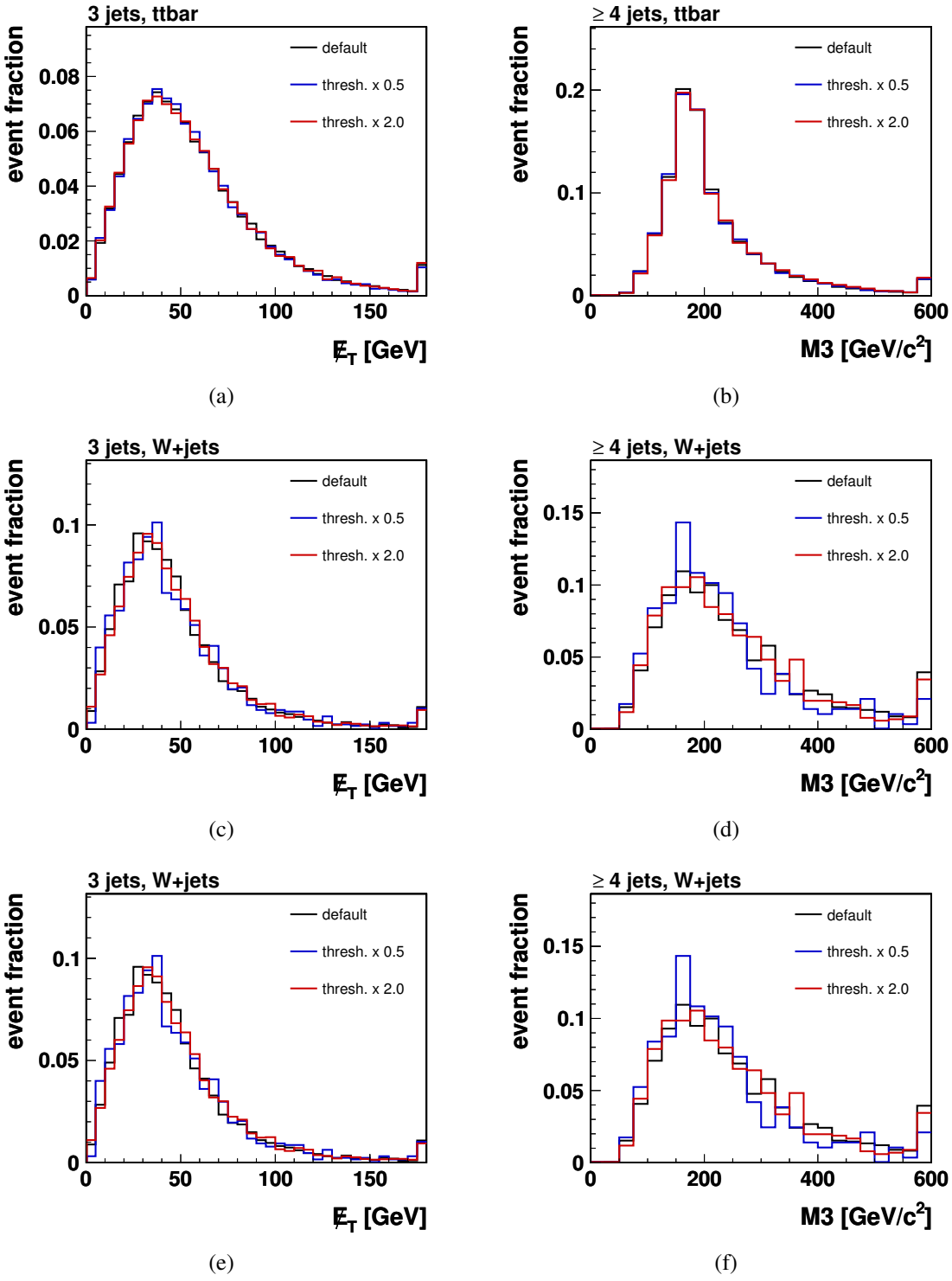

Figure 5.8: Impact of varying the matching threshold on the probability distributions $\mathcal{T}_k$ of the discriminating observables. Shape comparisons of the nominal $\not\!\!E_T$ distributions and the ones derived from the systematic samples are depicted in (a), (c), and (e) for $t\bar{t}$, W+jets, and Z+jets production, respectively. Similarly, in (b), (d), and (f), the corresponding shape comparisons for the M3 distributions are shown.

5.3.6. Jet Energy Scale and Jet Energy Resolution

The applied selection criteria of exactly three or at least four jets per event are based on jet objects which have been subject to Level 2 and Level 3 jet energy corrections as discussed in section 4.3. The experimental determination of these jet energy corrections induces an uncertainty which depends on the pseudorapidity and the transverse momentum of the reconstructed jet [191]. Since this determination is mostly based on gluon-induced jets, while the final state topology of $t\bar{t}$ events comprise quark- and particularly b quark-induced jets, an additional overall uncertainty of 5% is added in quadrature to these η- and p_{T}-dependent uncertainties. To account for this so-called jet energy scale (JES) uncertainty, the four-momentum of each jet candidate is subject to a $\pm 1\sigma$ variation, prior to the application of event selection criteria. Similar to the modification of the missing transverse energy entailed by the correction for the jet energy resolution bias correction discussed in section 4.3, this variation of the jet energy scale has to be propagated to the calculation of the missing transverse energy. For this purpose, the uncorrected jets are vectorially added to $\vec{\not{E}}_{\mathrm{T}}$ prior to the JES variation and subtracted again after the $\pm 1\sigma$ variation has been performed. The impact on the estimated event yields in terms of relative differences with respect to the nominal values $\hat{v}_k$ is summarised in table 5.8. Moreover, the probability distributions $\mathcal{T}_k$ of the discriminating observables $\not{E}_{\mathrm{T}}$ and M3 are modified as depicted in figure 5.9. While the $+1\sigma$ variation entails a shift towards higher values for the $\not{E}_{\mathrm{T}}$ and the M3 distributions of simulated $t\bar{t}$, W+jets, and Z+jets events, a similar effect but in opposite direction is observed for the corresponding -1σ variation.

Besides the jet energy resolution bias discussed in section 4.3, the experimental determination of the jet energy resolution entails an uncertainty of about $\pm 10\%$ on this quantity. In order to account for this source of systematic uncertainty and to properly handle the employed JER bias correction, variations of $\pm 9.1\%$ on the jet energy resolution are employed. Technically, this is again achieved via the ΔR and $\frac{\Delta p_{\mathrm{T}}}{p_{\mathrm{T}}}$ matching procedure described in section 4.3 and the corresponding propagation of corrections to the calculation of the missing transverse energy. The impact of these variations on the expected event yields for $t\bar{t}$ signal and the expected background contributions is given in table 5.8. In contrast to the variation of the absolute jet energy scale, a variation of the jet energy resolution leads to smaller deviations in terms of yield estimates. Figure 5.10 shows shape comparisons for the nominal and the systematically modified $\not{E}_{\mathrm{T}}$ and M3 distributions in $t\bar{t}$, W+jets, and Z+jets events.

5.3.7. Unclustered Energy

The variation of the jet energy scale and jet energy resolution discussed in the previous section only accounts for effects on the $\not{E}_{\mathrm{T}}$ probability distributions, induced by variations in energy measurements of objects clustered into jets. Similarly, the effects of a variation of the so-called unclustered energy might affect the $\not{E}_{\mathrm{T}}$ probability distributions and thus lead to an additional source of systematic uncertainties. Since the applied selection criteria, however, do not comprise a requirement on the amount of the missing transverse energy, only effects on the shape of the $\not{E}_{\mathrm{T}}$ distributions for signal and background processes are expected. To account for this potential source of systematic uncertainties, the

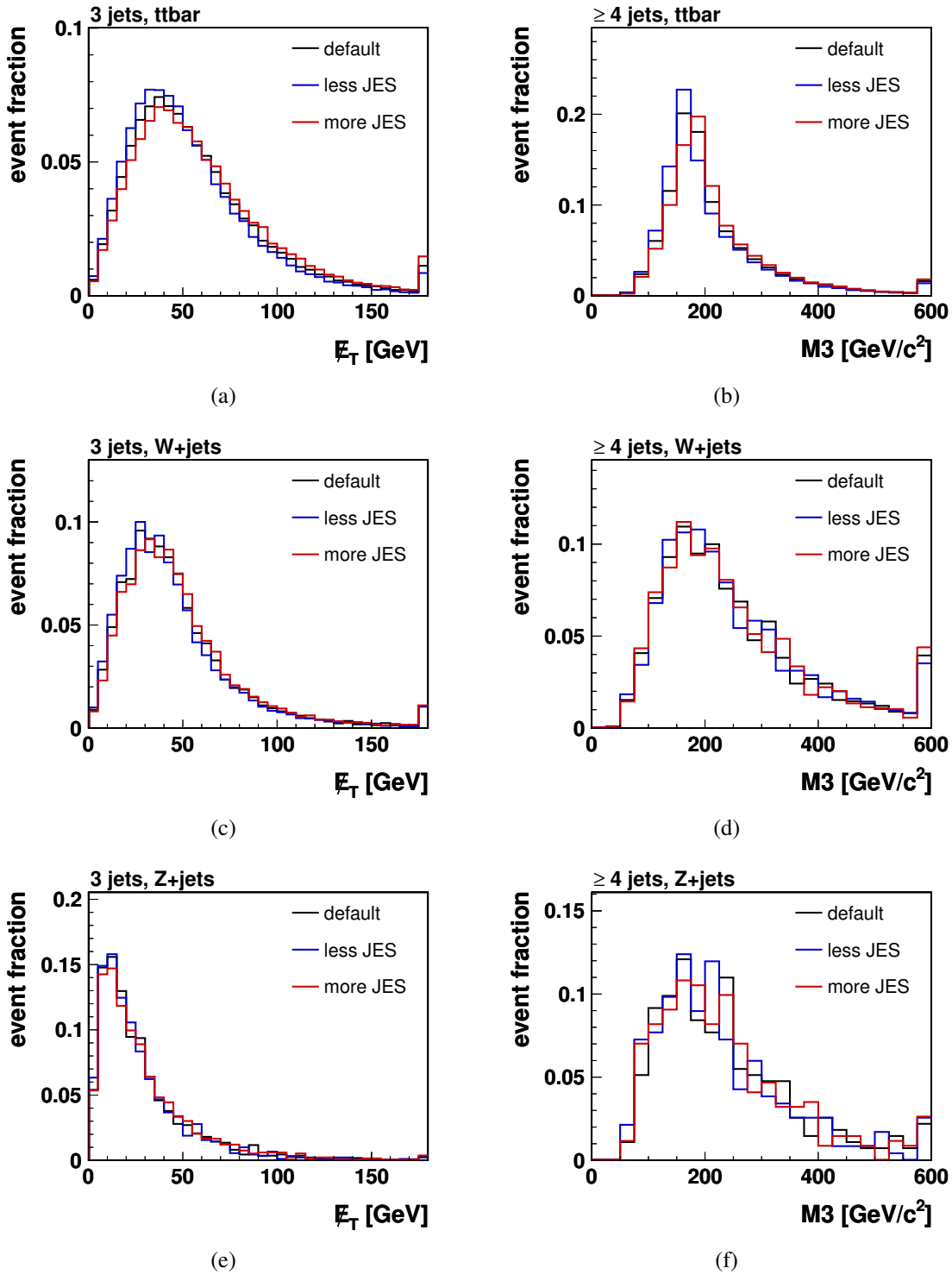

Figure 5.9: Impact of varying the jet energy scale (JES) on the probability distributions $\mathcal{T}_k$ of the discriminating observables. Shape comparisons between the nominal $\not\!\!E_T$ distributions and the ones derived by applying $\pm 1\sigma$ variations of the jet energy scale are depicted in (a), (c), and (e) for $t\bar{t}$, W+jets, and Z+jets production, respectively. Similarly, in (b), (d), and (f), the corresponding shape comparisons for the M3 distributions are shown.

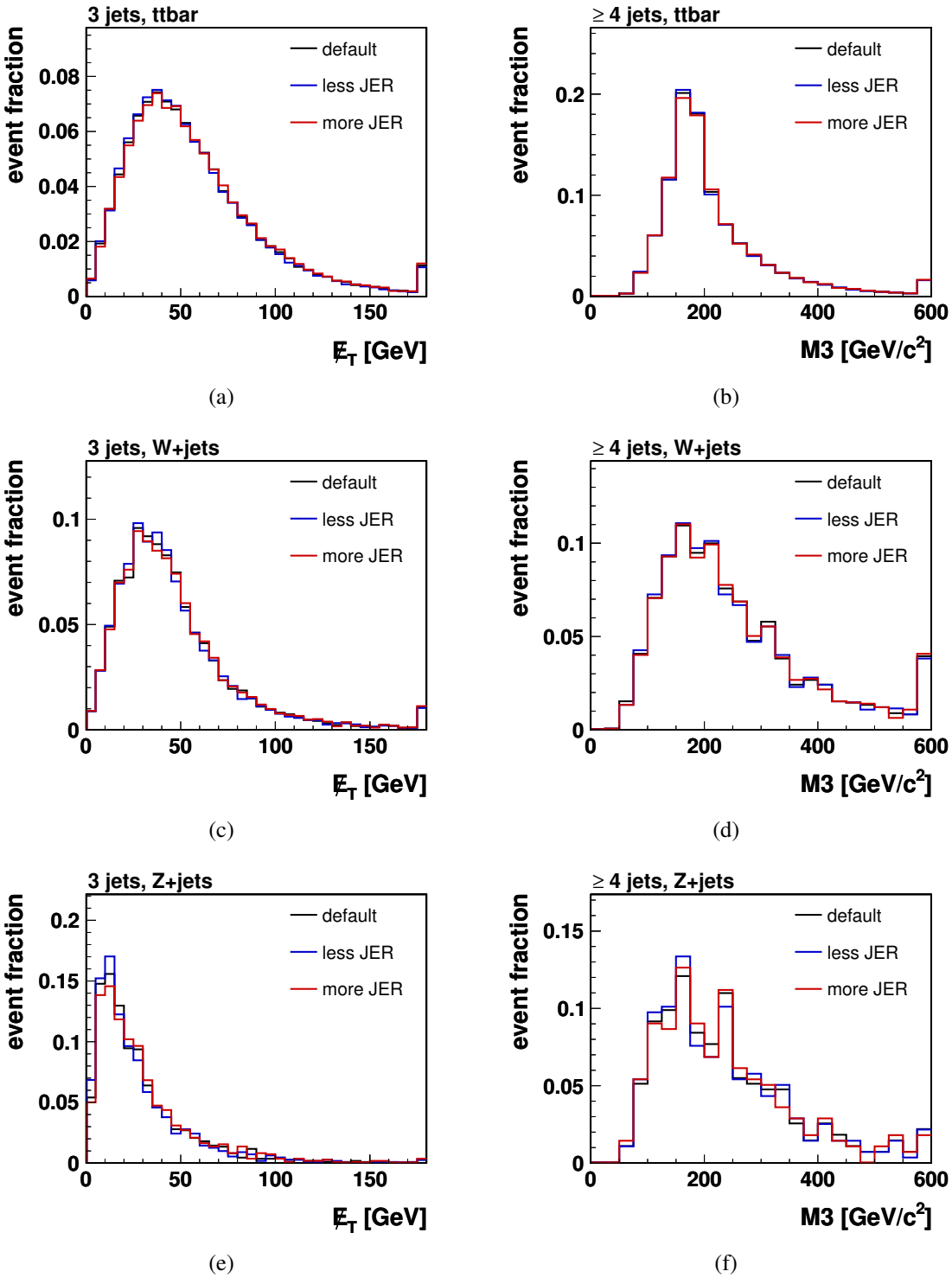

Figure 5.10: Impact of varying the jet energy resolution (JER) on the probability distributions $\mathcal{T}_k$ of the discriminating observables. Shape comparisons between the nominal $\not\!\!E_T$ distributions and the ones derived by applying $\pm 9.1\%$ variations of the jet energy resolution are depicted in (a), (c), and (e) for $t\bar{t}$, W+jets, and Z+jets production, respectively. Similarly, in (b), (d), and (f), the corresponding shape comparisons for the M3 distributions are shown.

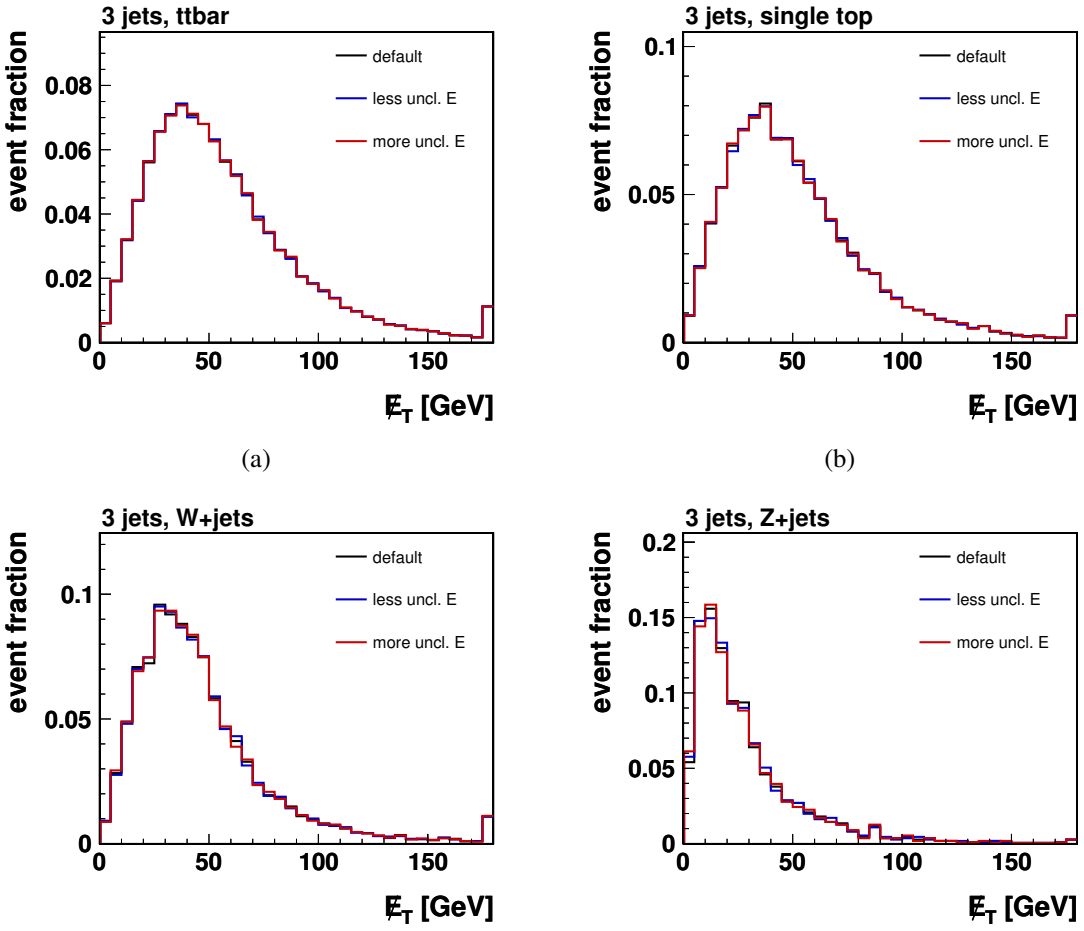

Figure 5.11: Impact of varying the unclustered energy on the $\not\!\!E_T$ probability distributions $\mathcal{T}_k$. Shape comparisons between the nominal $\not\!\!E_T$ distributions and the ones derived by applying a $\pm 10\%$ variation on the unclustered energy are depicted for $t\bar{t}$ (a), electroweak single top quark (b), W+jets (c), and Z+jets (d) events.

Table 5.8: Impact of varying the jet energy scale and the jet energy resolution. The relative differences of yield estimates are derived from $\pm 1\sigma$ variations of the jet energy scale (JES) and the jet energy resolution (JER), prior to the application of event selection criteria. In particular, the differences in the expected event yields for $t\bar{t}$, electroweak single top quark, W+jets, and Z+jets production are given, corresponding to selection criteria of exactly three or at least four jets per event, respectively.

Source	Requirement	$t\bar{t}$	single top	W+jets	Z+jets
JES−	$= 3$ jets	$+1.7\%$	-7.5%	-15.6%	-19.0%
	≥ 4 jets	-10.6%	-14.2%	-20.4%	-14.3%
JES+	$= 3$ jets	-2.4%	$+6.5\%$	$+17.5\%$	$+19.5\%$
	≥ 4 jets	$+9.9\%$	$+14.9\%$	$+23.3\%$	$+25.3\%$
JER−	$= 3$ jets	$+0.4\%$	$+0.4\%$	-1.0%	$+0.0\%$
	≥ 4 jets	$+0.8\%$	$+0.6\%$	$+0.0\%$	$+1.5\%$
JER+	$= 3$ jets	-0.3%	$+0.6\%$	$+0.5\%$	-1.1%
	≥ 4 jets	-0.9%	-0.6%	$+0.0\%$	$+1.5\%$

effects of $\pm 10\%$ variations on the unclustered energy are investigated. For this purpose, the four-momenta of all Level 2 and Level 3 uncorrected jets are vectorially added to the missing transverse energy and subtracted again after a variation of the resulting unclustered energy by a factor of 0.9 and 1.1, respectively. The expected impact of this $\pm 10\%$ variations on the $\not\!\!E_{\mathrm{T}}$ probability distributions for $t\bar{t}$ signal, W+jets, and Z+jets production is shown in figure 5.11. Similar to the effects observed for a variation of the absolute jet energy scale, the variation of the unclustered energy entails a shift of the $\not\!\!E_{\mathrm{T}}$ distribution towards smaller and higher mean values, respectively.

5.3.8. Data-Driven Modelling and Yield Estimates for QCD Multijet Production

The data-driven modelling of QCD multijet events by means of the AntiIso sample discussed in section 5.1.1 might be inappropriate for the description of $\not\!\!E_{\mathrm{T}}$ and M3 distributions of QCD multijet events, leading to an additional source of systematic uncertainties in the search for top quarks and the measurement of $\sigma_{t\bar{t}}$. For this purpose, the side-band region defined by the requirement of $0.2 < I_{\mathrm{rel}} < 0.5$ in the AntiIso selection is modified to criteria of $0.2 < I_{\mathrm{rel}} < 0.35$ and $0.35 < I_{\mathrm{rel}} < 0.5$, respectively. The comparison of the $\not\!\!E_{\mathrm{T}}$ and M3 distributions for the nominal AntiIso sample and the ones obtained via this segmentation procedure are shown in figure 5.12.

Moreover, according to the simulation-based yield estimates for QCD multijet production a value of $R_{4/3}^{\mathrm{exp}} = 0.25$ is expected for the ratio of event yields in selected samples with a requirement on exactly three or at least four jets. In turn, the corresponding value obtained from the AntiIso sample is $R_{4/3} = 0.23$. In order to account for this difference, an $\pm 8\%$ uncertainty is assumed on the ratio $R_{4/3}$ for QCD multijet events.

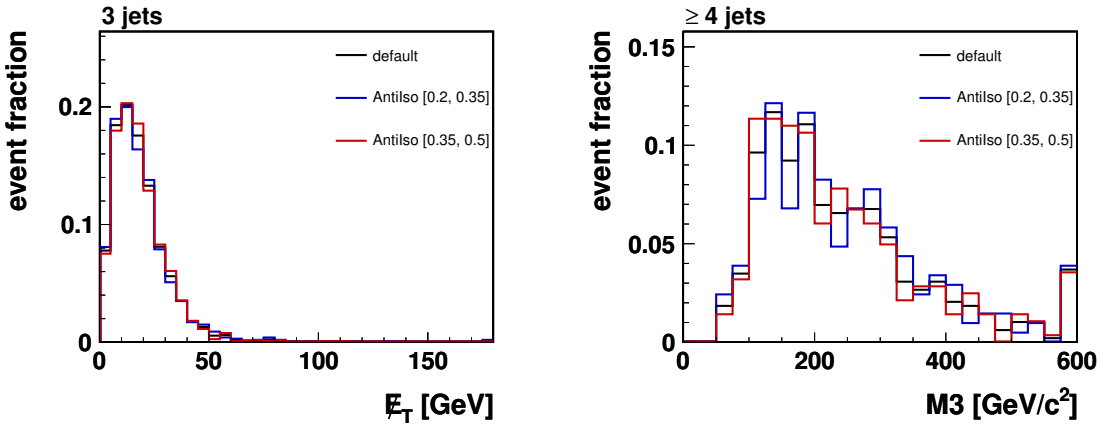

(a) (b)

Figure 5.12: Impact of varying the AntiIso selection on the data-driven modelling of $\not\!\!E_T$ and M3 probability distributions $\mathcal{T}_{QCD}$ for QCD multijet production. Shape comparison between the nominal $\not\!\!E_T$ and M3 distributions and the ones derived by altering the I_{rel} boundaries of the AntiIso selection are depicted in (a) and (b), respectively. While a requirement of $0.2 < I_{rel} < 0.5$ is imposed in the nominal AntiIso selection, the altered side-band regions are defined by the sub-ranges $[0.2, 0.35]$ and $[0.35, 0.5]$, respectively.

5.3.9. Integrated Luminosity and Efficiency Correction Factors

The uncertainty on the determination of the integrated luminosity described in section 4.1, induces an additional source of systematic uncertainties on the expected event yields $\hat{\nu}_k$. Since this uncertainty affects all signal and background processes uniformly over the entire phase-space, the difference between the systematically varied and the nominal yield estimates is $\pm 11\%$. Moreover, this overall rate uncertainty does not entail variations of the $\not\!\!E_T$ or M3 probability distributions $\mathcal{T}_k$.

The correction factors κ derived in section 4.4.2 have been applied to account for the differences between observed and simulation-based estimates of muon reconstruction, selection and trigger efficiencies. Therefore, the experimental uncertainties on κ induce a further source of systematic uncertainties on the estimated event yields $\hat{\nu}_k$. Similar to the uncertainty on the integrated luminosity, the usage of the overall correction factor $\kappa = 0.955 \pm 0.008$ affects signal and background processes uniformly over the entire phase-space, leading to an overall rate uncertainty of $\pm 0.8\%$ on the expected event yields.

5.3.10. Expected Impact on the Results

Given the various sources of systematic uncertainties, their impact on the significance level of the $t\bar{t}$ search and on the measurement of the $t\bar{t}$ production cross section have to be investigated. For this purpose, prior-predictive ensembles are employed which incorporate the various sources of systematic uncertainties in the model predictions used to construct the pseudo-data distributions of the discriminating observables. On the other hand, the statistical methods used to determine the significance level of the $t\bar{t}$ search and to measure the production cross section are not modified. In particular, for the description of observed or pseudo-data M3 and $\not\!\!E_{\mathrm{T}}$ distributions, the model defined in equation (5.4) remains unchanged and is therefore still based on the nominal yield estimates $\hat{\nu}_k$ and probability distributions $\mathcal{T}_k$. Thus, the a priori information about systematic uncertainties is solely accounted for in the preparation of pseudo-data distributions. The hypothesis testing procedure and the Neyman construction are then performed, based on these prior-predictive ensembles. Following this approach, the combined impact of statistical and systematic uncertainties on the expected value $\hat{p}_{\mathrm{exp}}$ and the uncertainty on $\hat{\beta}^{\mathrm{exp}}_{t\bar{t}}$ can be estimated, finally allowing for a comparison of observed and estimated results.

Technically, the incorporation of the various sources of systematic uncertainties is accomplished by additional model parameters δ_{syst}, governing the strength of the individual systematic uncertainties, and by substituting systematically modified estimates $\hat{\nu}'_k$ and $\mathcal{T}'_k$ for the nominal expectations $\hat{\nu}_k$ and $\mathcal{T}_k$. The individual strength parameters δ_{syst} in a large number of pseudo-experiments are assumed to comply with a Gaussian distribution centred around zero with a width $\Delta_{\mathrm{syst}} = 1.0$, except for δ_{PDF}, for which $\Delta_{\mathrm{PDF}} = 0.61$ is used to comply with the a priori information of 90% C.L. for the eigenvector values. For each pseudo-experiment, the values of the incorporated δ_{syst} parameters are then drawn according to the corresponding Gaussian distributions. Besides these model parameters δ_{syst}, the model used to generate the pseudo-data $\not\!\!E_{\mathrm{T}}$ and M3 distributions is based on the systematically altered Poisson means $\hat{\nu}'_k$ for the expected yield estimates of process k according to

$$\hat{\nu}'_k(\delta_{\mathrm{syst}}) = \hat{\nu}_k \cdot \left[1 + \sum_{j=1}^{N_{\mathrm{syst}}} |\delta_j| \cdot \left(H(\delta_j) \frac{\hat{\nu}^+_{jk}}{\hat{\nu}_k} + H(-\delta_j) \frac{\hat{\nu}^-_{jk}}{\hat{\nu}_k} - 1 \right)\right], \tag{5.13}$$

with the Heaviside step function $H(x)$ and the nominal event yield estimates $\hat{\nu}_k$. The expected event yields $\hat{\nu}^{\pm}_{jk}$ for the various source of systematic uncertainties j on process k, are determined from the dedicated samples or modifications discussed in section 5.3.1 to section 5.3.9 which account for up- and downwards fluctuations of the given uncertainties, e.g. a $\pm 1\sigma$ variation of the jet energy scale. Similarly, the systematically modified probability distributions $\mathcal{T}'_k$ are obtained from a bin-by-bin interpolation. Accordingly, the relative fraction of events in bin i of $\mathcal{T}'_k$ is obtained via

$$\mathcal{T}'_{ik}(\delta_{\mathrm{syst}}) = \mathcal{T}_{ik} \cdot \left[1 + \sum_{j=1}^{N_{\mathrm{syst}}} |\delta_j| \cdot \left(H(\delta_j) \frac{\mathcal{T}^+_{ijk}}{\mathcal{T}_{ik}} + H(-\delta_j) \frac{\mathcal{T}^-_{ijk}}{\mathcal{T}_{ik}} - 1 \right)\right], \tag{5.14}$$

using the nominal probability distribution $\mathcal{T}_k$ and the systematically modified distributions $\mathcal{T}^{\pm}_{jk}$, whereas the latter correspond to the distributions obtained by up- and downwards fluctuations of the systematic uncertainty under investigation.

Finally, the pseudo-data $\not\!\!E_{\mathrm{T}}$ and M3 distributions are drawn from the various processes k according to the given Poisson means $\hat{\nu}'_k$ and to the probability distributions $\mathcal{T}'_k$. In case the source of a systematic uncertainty affects several processes k, like the uncertainty on the correction factor κ derived in section 4.4.2, a 100% correlation of the corresponding model parameters δ_{syst} is used for the involved processes k. The only exceptions in this context are the uncertainty on the renormalisation and factorisation scale and the uncertainty on the matching threshold, incorporated via δ_{scale} and $\delta_{\mathrm{matching}}$, respectively, which apply to $t\bar{t}$, W+jets, and Z+jets production. Since the scale parameters $\hat{\mu}_k$, as well as the matching thresholds used for the simulation-based modelling of $t\bar{t}$ and V+jets ($V = W, Z$) production are not correlated, independent parameters δ_{scale} and $\delta_{\mathrm{matching}}$ are used to determine the strength of the corresponding systematic uncertainties on $t\bar{t}$ and V+jets production in the prior-predictive ensembles.

Expected Impact on the Significance Level

In order to estimate the combined impact of statistical and systematic uncertainties on the significance level of the $t\bar{t}$ search, the hypothesis testing procedure is performed based on the prior-predictive ensembles including the systematically modified expectations $\hat{\nu}'_k$ and $\mathcal{T}'_k$. For this purpose, all discussed sources of systematic uncertainties are taken into account for the generation of pseudo-experiments. The statistical evaluation of observed and expected significance levels is then accomplished using the procedures described in section 5.2.2. Consequently, the Q value distributions q_0 and q_1 are obtained, assuming the validity of the background-only or the signal-plus-background hypothesis, respectively. As depicted in figure 5.13, this simultaneous investigation of statistical and systematic uncertainties leads to a median-expected Q value of $\widehat{Q}_{\mathrm{exp}} = 10.87$ which could in principle be used to calculate the expected significance level $\hat{p}_{\mathrm{exp}}$ according to equation (5.11). However, the $2.22 \cdot 10^9$ pseudo-experiments performed to derive the distribution q_0 are insufficient for the determination of $\hat{p}_{\mathrm{exp}}$. Therefore, only an upper limit of $\hat{p}_{\mathrm{exp}} < 4.51 \cdot 10^{-10}$ can be estimated. In terms of standard Gaussian deviations, this corresponds to an expected lower limit on the significance level of 6.13σ, which is well above the aspired target for claiming observation of $t\bar{t}$ production. Additionally, the value $\widehat{Q} = 5.76$ corresponding to a statistical significance of 5σ is indicated in figure 5.13, illustrating the calculation of the corresponding p value $\hat{p} = 2.87 \cdot 10^{-7}$.

Expected Impact on the Cross Section Measurement

The impact of systematic uncertainties on the measurement of the $t\bar{t}$ production cross section is estimated using prior-predictive ensembles as well. In contrast to the procedure used for hypothesis testing, however, the impact of the uncertainty on the integrated luminosity is omitted in the prior-predictive procedure. Since the determination of the integrated luminosity entails an overall uncertainty of $\pm 11\%$ on the expected event yields $\hat{\nu}_k$ for all processes k, but does not affect the probability distributions $\mathcal{T}_k$, the impact of this systematic uncertainty on the observed value $\hat{\beta}^{\mathrm{true}}_{t\bar{t}}$, and consequently on the observed $t\bar{t}$ production cross section value, can be quoted separately. Including all other sources of systematic uncertainties to derive the Neyman construction depicted in figure 5.14, the determination of $\pm 1\sigma$ statistical-plus-systematic uncertainties closely follows the procedure

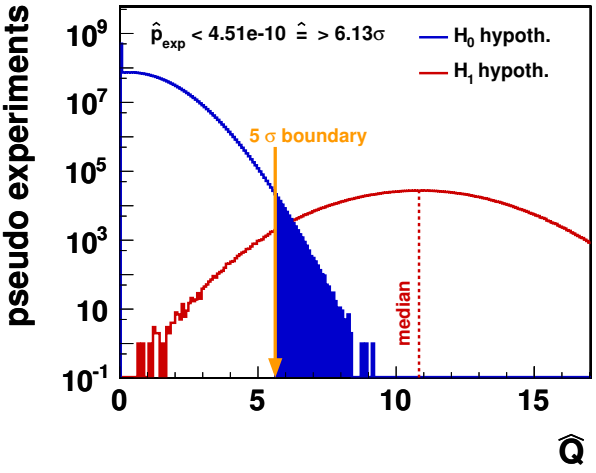

Figure 5.13: Expected Q value distributions for the background-only hypothesis (blue) and the signal-plus-background hypothesis (red) obtained from prior-predictive ensembles based on statistical and systematic uncertainties. Due to the insufficient number of pseudo-experiments for the null hypothesis H_0, the median-expected Q value obtained from an ensemble based on the H_1 hypothesis can only be used to estimate an upper limit of $\hat{p}_{\text{exp}} < 4.51 \cdot 10^{-10}$ on the expected significance level for the $t\bar{t}$ search. In terms of standard Gaussian deviations, this upper limit on $\hat{p}_{\text{exp}}$ thus yields a lower limit for the rejection of the background-only assumption of 6.13σ. To illustrate the formal determination of the p value based on the background-only Q value distribution q_0 and a particular value $\widehat{Q}$, the latter is indicated by the yellow line at $\widehat{Q} = 5.76$. Using the integral of q_0 indicated by the blue area, a value of $\hat{p} = 2.87 \cdot 10^{-7}$ is obtained which corresponds to a 5σ significance level.

discussed in section 5.2.4. The combined impact of statistical and systematic uncertainties can thus be estimated from the Neyman construction evaluated at $\hat{\beta}_{t\bar{t}}^{\text{exp}} = 1.0$, leading to expected uncertainties on the $t\bar{t}$ production cross section of -19.9% and $+24.9\%$.

To furthermore estimate which source of systematic uncertainties has to be reduced to significantly decrease the overall uncertainty on the determination of the $t\bar{t}$ production cross section, this prior-predictive approach and the subsequent determination of the $\pm 1\sigma$ uncertainties from the Neyman construction is repeated by neglecting individual sources of systematic uncertainties. Table 5.9 summarises the expected statistical-plus-systematic uncertainties on $\hat{\beta}_{t\bar{t}}^{\text{true}}$, given these so-called $N_{\text{syst}} - 1$ ensembles. The most significant reduction of the uncertainty is observed for the model omitting uncertainties on the jet energy scale, leading to statistical-plus-systematic uncertainties of about $\pm 15\%$. As already mentioned, the uncertainty on the integrated luminosity has to be taken into account as well which can be accomplished by either quoting the $\pm 11\%$ uncertainty separately or by adding this uncertainty in quadrature to the overall statistic-plus-systematic uncertainties.

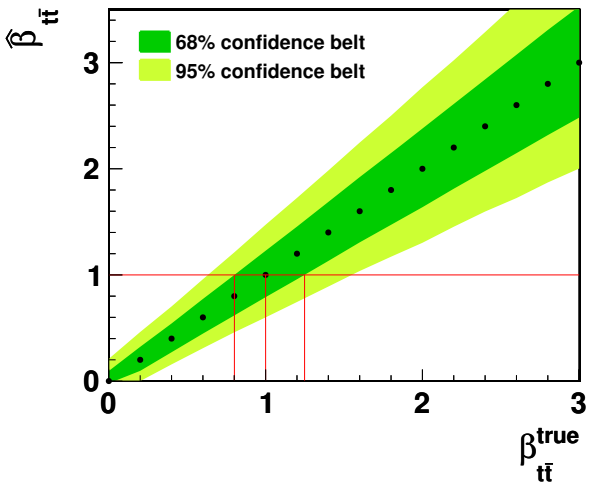

Figure 5.14: Neyman construction for the determination of statistical-plus-systematic uncertainties. To account for the various sources of systematic uncertainties, prior-predictive ensembles are employed, incorporating systematically modified expectations $\hat{\nu}'_k$ and $\mathcal{T}'_k$. Evaluating the Neyman construction at $\hat{\beta}^{\text{exp}}_{t\bar{t}} = 1.0$, expected $\pm 1\sigma$ uncertainty values of -19.9% and $+24.9\%$ are determined, compared to the purely statistical uncertainties of about $\pm 11\%$.

Table 5.9: Summary of expected statistical-plus-systematic uncertainties on the determination of the $t\bar{t}$ production cross section. The individual values are obtained from a Neyman construction evaluated at $\hat{\beta}^{\text{exp}}_{t\bar{t}} = 1.0$, wherein prior-predictive ensembles are used to incorporate the sources of systematic uncertainties. In addition, the potential reduction of the overall uncertainty is investigated by neglecting individual sources of systematic uncertainties, using so-called $N_{\text{syst}} - 1$ ensembles. Accordingly, the most significant reduction is expected for the model omitting uncertainties on the jet energy scale.

	stat.+syst. uncertainty [%]	
only stat.+bkg. uncertainty	-10.4%	$+10.9\%$
total stat.+syst. uncertainty	-19.9%	$+24.9\%$
w/o JES uncertainty	-13.8%	$+15.0\%$
w/o JER uncertainty	-19.8%	$+24.4\%$
w/o Unclustered energy uncertainty	-19.8%	$+24.4\%$
w/o ISR/FSR uncertainty	-19.6%	$+24.3\%$
w/o Scale uncertainty	-19.4%	$+23.3\%$
w/o Matching threshold uncertainty	-19.7%	$+24.0\%$
w/o BR($W \to l\nu$) uncertainty	-19.9%	$+24.9\%$
w/o κ Corr. factor uncertainty	-19.9%	$+24.9\%$
w/o QCD rate/shape uncertainty	-19.8%	$+24.7\%$
w/o Pile-up events	-19.9%	$+24.7\%$
w/o PDF uncertainty	-19.8%	$+24.9\%$

5.4. Significance of $t\bar{t}$ Production

Finally, the hypothesis testing procedure is applied to the $\not\!\!E_T$ and M3 distributions in observed pp collision data, corresponding to an integrated luminosity of (36.1 ± 4.0) pb^{-1}. As illustrated in figure 5.15, the resulting Q value is $\widehat{Q}_{\text{obs}} = 10.45$ and thus slightly smaller compared to the median-expected value $\widehat{Q}_{\text{exp}}$. However, the Q value distribution q_0 obtained from $2.22 \cdot 10^9$ pseudo-experiments discussed in section 5.3.10 still prevents a formal calculation of the p value according to equation (5.11). Consequently, the determination of the observed p value yields

$$\hat{p}_{\text{obs}} < 4.51 \cdot 10^{-10} \,. \tag{5.15}$$

Since the same Q value distribution q_0 is employed for the determination of $\hat{p}_{\text{obs}}$ and $\hat{p}_{\text{exp}}$, respectively, identical values are obtained for the two upper limits. According to equation (5.15), the probability for a mere fluctuation of considered background processes to describe the observed $\not\!\!E_T$ and M3 distributions in pp collision data can be rejected at a level exceeding 6.13σ. Consequently, the observed likelihood ratio allows to claim the observation of top quark pair production via the strong interaction.

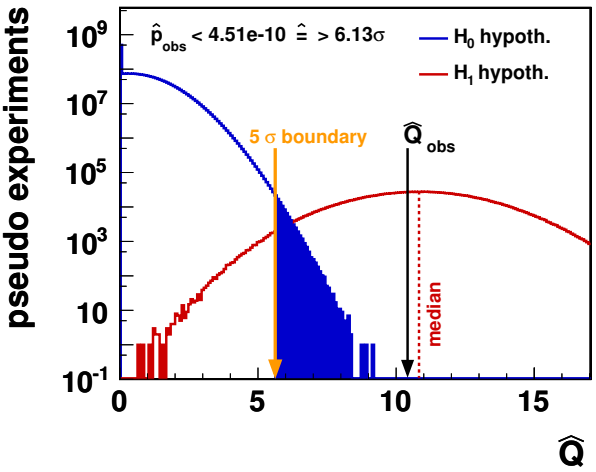

Figure 5.15: Observed Q value $\widehat{Q}_{\text{obs}}$ in pp collision data and expected Q value distributions for the background-only hypothesis H_0 (blue) and for the signal-plus-background hypothesis H_1 (red), both including statistical and systematic uncertainties via prior-predictive ensembles. As for the median-expected Q value in figure 5.13, the value $\widehat{Q}$ corresponding to a 5σ significance level is indicated by the vertical yellow line. Given the observed value $\widehat{Q}_{\text{obs}} = 10.45$, an upper limit on the observed p value of $\hat{p}_{\text{obs}} = 4.51 \cdot 10^{-10}$ can be determined. Consequently, in terms of standard Gaussian deviations the significance level of the $t\bar{t}$ search implies a rejection of the background-only assumption by $> 6.13\sigma$, and thus allows to claim observation of $t\bar{t}$ production.

5.5. Measurement of the $t\bar{t}$ Production Cross Section

For the determination of the $t\bar{t}$ production cross section, the observed $\not\!\!E_{\mathrm{T}}$ and M3 distributions in pp collision data are subject to a maximum likelihood fit procedure, using the likelihood function defined in equation (5.8). This yields the observed values $\hat{\beta}_k^{\mathrm{obs}}$ listed in table 5.10 for the various model parameters β_k. Therein, the quoted statistical uncertainties on the maximum likelihood estimate of the model parameter values $\hat{\beta}_k^{\mathrm{obs}}$ of the background contributions are provided by MINUIT, using the covariance matrix at the minimum of the negative logarithm of the likelihood function. As suggested by the discrepancy between observed and expected kinematic distributions in section 4.5, larger background contributions of W+jets, Z+jets, and QCD multijet production processes compared to the simulation-based expectations are observed. In particular, for W+jets and Z+jets production the observed maximum likelihood estimates lead to 36% and 33% higher event yields. The corresponding value for QCD multijet production results in an observed event yield which is about a factor of two larger compared to the simulation-based expectation. In contrast to this sizable discrepancies between observed and expected background contributions, the maximum likelihood estimate for the signal parameter $\beta_{t\bar{t}}$ is about 3% higher and thus in good agreement with the expected value $\hat{\beta}_{t\bar{t}}^{\mathrm{exp}} = 1.0$. In order to derive the central value $\hat{\beta}_{t\bar{t}}^{\mathrm{true}}$ and the corresponding statistical-plus-systematic uncertainty, the Neyman construction discussed in section 5.3.10 is evaluated at the observed value $\hat{\beta}_{t\bar{t}}^{\mathrm{obs}} = 1.03$ as depicted in figure 5.16. This procedure leads to $\hat{\beta}_{t\bar{t}}^{\mathrm{true}} = 1.03$ within statistical-plus-systematic uncertainties of -19.7% and $+24.7\%$.

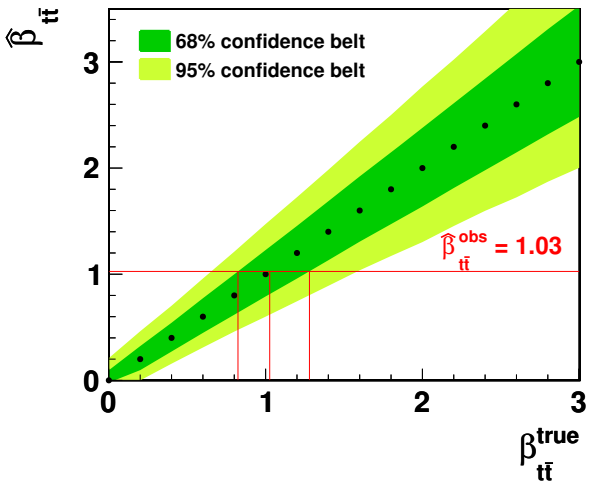

Figure 5.16: Neyman construction for the determination of the observed cross section value and the corresponding statistical-plus-systematic uncertainties. For the determination of the central value $\hat{\beta}_{t\bar{t}}^{\mathrm{true}}$ and the corresponding uncertainties, the Neyman construction is evaluated at the observed value $\hat{\beta}_{t\bar{t}}^{\mathrm{obs}} = 1.03$. This leads to an observed value of $\hat{\beta}_{t\bar{t}}^{\mathrm{true}} = 1.03$ with an uncertainty of -19.7% and $+24.7\%$ which can be used for the determination of the $t\bar{t}$ production cross section.

Table 5.10: Maximum likelihood estimates $\hat{\beta}_k^{\text{obs}}$, determined from the binned likelihood fit to observed $\not\!\!E_{\text{T}}$ and M3 distributions in pp collision data, corresponding to an integrated luminosity of $L = (36.1 \pm 4.0)$ pb^{-1}. The quoted uncertainties on the background parameter values $\hat{\beta}_k^{\text{obs}}$ are derived from the covariance matrix at the minimum of the negative logarithm of the likelihood function. Since these uncertainties do not include systematic uncertainties, these results cannot be considered as estimates for cross section measurements of the background processes. Moreover, in order to prevent ambiguity with these purely statistical uncertainties, the corresponding value on $\hat{\beta}_{t\bar{t}}^{\text{obs}}$ is omitted, since the statistical-plus-systematic uncertainty on $\hat{\beta}_{t\bar{t}}^{\text{obs}}$ is derived by means of the Neyman construction.

$\hat{\beta}_{t\bar{t}}^{\text{obs}}$	$\hat{\beta}_t^{\text{obs}}$	$\hat{\beta}_W^{\text{obs}}$	$\hat{\beta}_Z^{\text{obs}}$	$\hat{\beta}_{\text{QCD}}^{\text{obs}}$
1.03	1.00 ± 0.30	1.36 ± 0.10	1.33 ± 0.41	2.11 ± 0.58

Converting the maximum likelihood estimate $\hat{\beta}_{t\bar{t}}^{\text{obs}}$ by means of equation (5.3), the observed top quark pair production cross section at a centre-of-mass energy of 7 TeV in pp collision data corresponding to an integrated luminosity of $L = (36.1 \pm 4.0)$ pb^{-1} is

$$\sigma_{t\bar{t}} = 168.9^{+41.7}_{-33.3}\,(\text{stat.+syst.}) \pm 18.6\,(\text{lumi.})\ \text{pb}\ , \tag{5.16}$$

and thus in remarkably good agreement with theory predictions of $\sigma_{t\bar{t}}^{\text{theo.}} = 164.6^{+11.4}_{-15.7}$ pb, obtained from approximate NNLO calculations [8–10].

In addition, the maximum likelihood estimates $\hat{\beta}_k^{\text{obs}}$ can be used to re-weight the event yield estimates listed in table 4.10, in order to facilitate a final comparison of observed and estimated kinematic distributions. In figure 5.17 this comparison is depicted for the discriminating observables $\not\!\!E_{\text{T}}$ and M3 in candidate event samples with a requirement of exactly three and at least four jets per event, respectively. The good correspondence for these distributions, however, is achieved per construction, since the simulation-based modelling of $\not\!\!E_{\text{T}}$ and M3 distributions in $t\bar{t}$ signal, electroweak single top quark, W+jets, Z+jets production, and the AntiIso sample used to model the QCD multijet contributions are fit to the observed distributions in the applied maximum likelihood procedure. Therefore, given the selection requirements of exactly three or at least four jets per event, the comparison of kinematic distributions is additionally performed for the pseudorapidity of the selected muon candidate, the transverse W boson mass, and for $H_{\text{T,lep}}$ in figure 5.18. In summary, good agreement is observed for the expected and observed distributions of the various kinematic observables.

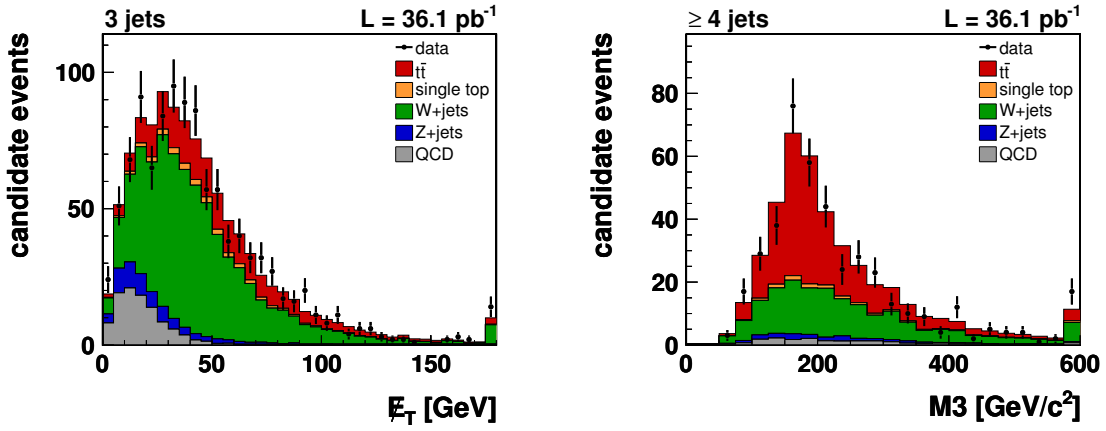

(a) (b)

Figure 5.17: Comparison of observed and estimated distributions of the discriminating observables, re-weighting the expected yield estimates $\hat{\nu}_k$ by the maximum likelihood estimates for β_k given in table 5.10. Good agreement between the observed and estimated distributions of $\not{E}_{\mathrm{T}}$ and M3 can be seen in (a) and (b), respectively. However, this comparison per construction allows for a good correspondence, since the maximum likelihood procedure investigates $\not{E}_{\mathrm{T}}$ and M3 as discriminating observables.

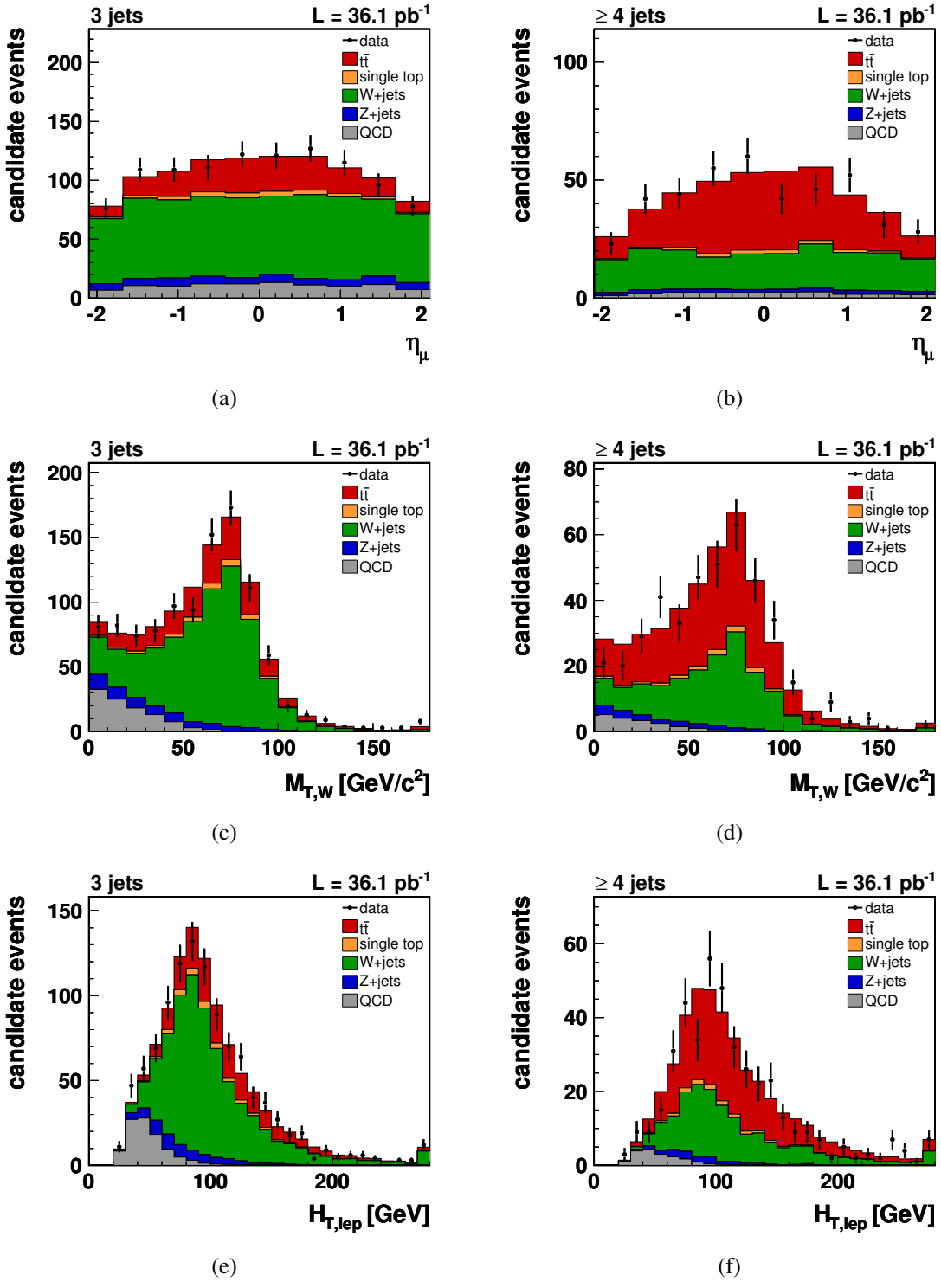

Figure 5.18: Comparison of observed and estimated kinematic distributions, re-weighting the expected yield estimates $\hat{\nu}_k$ by the maximum likelihood estimates for β_k given in table 5.10. In (a), (c), and (e), the comparison of observed and estimated pseudorapidity distributions of the selected muon candidate, of the transverse W boson mass, and of $H_{\mathrm{T,lep}}$ in a candidate event sample with exactly three jets per event are depicted. Similarly, (b), (d), and (f), show the corresponding comparisons in a candidate event sample with a requirement on at least four jets per event. In summary, good agreement between observed and expected distributions is found for the presented kinematic observables.

Summary and Discussion

The Standard Model (SM) of particle physics constitutes the most complete model currently known for the description of the elementary building blocks of matter and forces acting between them. Their interactions are ascribed to the exchange of force-mediating bosons which couple to the charges of the fermions. Depending on the interactions in which they partake, the twelve SM fermions can be divided into two main categories, namely quarks and leptons. Among these, quarks are affected by all Standard Model forces, while for leptons only electroweak interactions are predicted.

The heaviest among these elementary fermions is the top quark, which was first observed by the CDF and DØ collaborations at the Fermilab Tevatron in 1995 [1, 2]. With a mass of $m_t = 173.3 \pm 1.1\ \mathrm{GeV}/c^2$ [3], it is nearly as massive as a gold nucleus and about 40 times heavier than the b quark. Due to this exceptionally large mass, top quarks on average decay before top-flavoured hadrons can be formed, and so offer a unique possibility to study quasi-free quarks. Moreover, the observed mass value provokes speculation about whether the top quark might play a special role in the mechanism of electroweak symmetry breaking.

Top quarks can either be produced in pairs of top and antitop quarks via the strong interaction or singly in charged-current weak interactions. While the pairwise production led to its discovery in 1995, the second production mechanism was experimentally observed only about two years ago [5–7], again by the CDF and DØ collaborations. Once produced, top quarks almost exclusively decay via the weak interaction into a b quark and a charged W boson, leading to a categorisation of $t\bar{t}$ events as all-hadronic, dilepton, or lepton+jets events, according to the W bosons decay-mode.

Until last year, only the Tevatron collider provided interactions of particles exhibiting sufficient kinetic energy for the production of top quarks. However, with the first intentional proton-proton collisions at a centre-of-mass energy of 7 TeV on March 30$^{\mathrm{th}}$ 2010, the Large Hadron Collider (LHC) became the most powerful collider ever operated. Now, about sixteen years after the top quark was discovered, the LHC enables its re-discovery and permits scrutiny of its properties and interactions. The two general-purpose detectors ATLAS and CMS have been built to detect and analyse hard interactions in pp collisions provided by the LHC, which has been designed to unveil the mechanism of electroweak symmetry breaking and to search for physics beyond the Standard Model. The CMS apparatus is located near Cessy, France, in an underground cavern about 100 m below surface. Since the first recorded pp collision event, a data set corresponding to about 43.2 pb^{-1} has been acquired with the CMS detector, among which 36.1 pb^{-1} were considered usable for the analysis of top quarks. The ultimate aim of the analysis presented in this thesis was to establish a top quark signal in this early data set and to perform a first measurement of the $t\bar{t}$ production cross section in the muon+jets channel.

The expected $t\bar{t}$ production cross section is about nine orders of magnitude smaller than the total inelastic pp cross section. Moreover, the experimental signature of a high-energetic muon, missing transverse energy entailed by the emerging neutrino, and four jets

in a typical $t\bar{t}$ muon+jets event, is not unique. Several other Standard Model processes exhibit a similar experimental signature and could thus lead to erroneous classification as signal events. Therefore, Monte Carlo techniques have been used to generate and simulate $t\bar{t}$ signal and the expected background processes. Based on these samples of simulated events and driven by the requirements for a good signal-to-background ratio and high signal efficiency, an event selection has been developed which employs criteria on exactly one well-identified and isolated muon, the absence of additional lepton candidates, and at least four jets per event. A dedicated selection requirement on the amount of missing transverse energy has been omitted in favour of granting this observable another, more central role to achieve the aspired analysis objectives. Furthermore, information provided by b-tagging algorithms have not been used for the selection of events, leading to a so-called untagged analysis.

The simulated samples of signal and background events allowed for the estimation of acceptances and selection efficiencies, which have been of central importance in the search for top quarks and the measurement of the $t\bar{t}$ production cross section. In order to minimise the dependency on these simulation-based estimates, supplementary information provided by data-driven techniques on muon reconstruction, selection, and trigger efficiencies were used. For this purpose, the tag-and-probe method was employed in observed and simulated $Z \rightarrow \mu\mu$ events, in order to derive correction factors for the simulation-based efficiency estimates. Applying these procedures and selection criteria on at least four (exactly three) jets per events, about 220 (204) $t\bar{t}$ signal and approximately 146 (388) background events have been expected in a data set corresponding to an integrated luminosity of 36.1 pb^{-1}. Consequently, a signal-to-background ratio of $S/B = 1.5$ (0.3) and a pseudo-significance of $S/\sqrt{B} = 18.2$ (8.3) has been expected for candidate event samples with a requirement on at least four (exactly three) jets per event. The comparison of observed and expected event yields, however, showed deviations of up to 20% which have been ascribed to an underestimation of background contributions, as suggested by the comparison of kinematic distributions.

The analysis procedures employed in the search for top quarks and the measurement of the $t\bar{t}$ production cross section were based on a binned likelihood fit and thus closely followed the methods used for the observation of the top quark in 1995. Using this approach, the selection of discriminating observables has been required which facilitated the separation of signal and background processes. The missing transverse energy and M3 were chosen as discriminating observables, where the latter denotes the invariant mass of those three jets per event which exhibit the highest vectorial-summed transverse momentum. A simultaneous investigation of $\not\!\!E_{\mathrm{T}}$ and M3 as discriminating observables has thereby been permitted by the statistically orthogonal samples of candidate events, obtained by the applied selection criteria on exactly three or at least four jets per event, respectively. Besides the selection of kinematic observables, the application of the binned likelihood fit required appropriate models for the description of the observed $\not\!\!E_{\mathrm{T}}$ and M3 distributions. For this purpose, the simulated samples of $t\bar{t}$, single top quark, W+jets, and Z+jets production have been used to derive probability distributions for the discriminating observables. Since the simulation of QCD multijet background events has been considered particularly unreliable, a modified event selection was developed which aimed for the selection of a candidate sample highly-enriched in QCD multijet events. Application of these altered

selection criteria to observed pp collision data thus facilitated a data-driven emulation of kinematic distributions for QCD multijet events. Given the observed $\not\!\!E_{\mathrm{T}}$ and M3 distributions and the models for signal and background processes, a likelihood function was defined which incorporated the number of signal and background events as model parameters. The maximisation of this likelihood function with respect to the model parameters then allowed for the determination of signal and background contributions in the given data set.

The search for top quarks was accomplished by means of a hypotheses test, determining the probability for erroneously claiming observation of $t\bar{t}$ production based on a mere fluctuation of background contributions. Based on a hypothesis assuming signal and background contributions and an alternative hypothesis neglecting signal contributions, a likelihood ratio Q was defined which is deemed to provide the most sensitive observable for discriminating hypotheses. In order to determine the significance level of the $t\bar{t}$ search, an ensemble test based on the background-only assumption was performed. Comparison of the resulting Q value distribution with the observed value $\widehat{Q}_{\mathrm{obs}}$ in pp collision data corresponding to an integrated luminosity of $L = (36.1 \pm 4.0)\ \mathrm{pb}^{-1}$, led to a lower limit for the observed significance level of 6.13σ. Consequently, the discrepancy between the observed Q value and expectations based on the background-only assumption justify to claim observation of top quark pair production at the LHC.

The second objective of the analysis presented in this thesis was the measurement of the $t\bar{t}$ production cross section. For this purpose, the contribution of $t\bar{t}$ events in the given data set was extracted by means of the binned likelihood fit to observed $\not\!\!E_{\mathrm{T}}$ and M3 distributions. Moreover, to determine the statistical-plus-systematic uncertainties, a Neyman construction for central intervals was employed, using the maximum likelihood estimate for the signal parameter as test statistic. Accordingly, the top quark pair production cross section at a centre-of-mass energy of 7 TeV for an assumed top quark mass of 172.5 GeV/c^2 was determined to

$$\sigma_{t\bar{t}} = 169^{+42}_{-33}\,(\text{stat.+syst.}) \pm 19\,(\text{lumi.})\ \ \text{pb}, \tag{5.17}$$

which is in remarkably good agreement with theory predictions of $\sigma_{t\bar{t}}^{\text{theo.}} = 164.6^{+11.4}_{-15.7}$ pb, obtained from approximate NNLO calculations [8–10]. The purely statistical uncertainty of about $\pm 11\%$ on this cross section measurement was deduced from an ensemble test omitting systematic uncertainties. Therefore, the measurement of the $t\bar{t}$ production cross section is already systematically limited, with dominant contributions originating from uncertainties on the jet energy scale. Thus, in order to improve the accuracy of this determination, either the sources of systematic uncertainties have to be reduced or an alternative method has to be employed, e.g. a simultaneous measurement of $\sigma_{t\bar{t}}$ and the jet energy scale.

Furthermore, the presented result on the measurement of the $t\bar{t}$ production cross section in the muon+jets channel can be compared to the corresponding results obtained in the dilepton channel [14], the electron+jets channel [15], and to the combined measurement in the lepton+jets channel [15], where lepton refers to an electron or muon, respectively.

These three measurements yield

$$\sigma_{t\bar{t}}^{\text{dilepton}} = 194 \pm 76\,(\text{stat.+syst.}) \pm 21\,(\text{lumi.})\ \text{pb}, \tag{5.18}$$

$$\sigma_{t\bar{t}}^{e+\text{jets}} = 178^{+45}_{-37}\,(\text{stat.+syst.}) \pm 20\,(\text{lumi.})\ \text{pb}, \tag{5.19}$$

$$\sigma_{t\bar{t}}^{l+\text{jets}} = 172^{+39}_{-32}\,(\text{stat.+syst.}) \pm 19\,(\text{lumi.})\ \text{pb}. \tag{5.20}$$

While the result in the dilepton channel is based on a data set corresponding to 3.1 pb^{-1}, the measurements in the lepton+jets channels are based on the full data set. Due to a slightly more conservative estimation of jet energy scale uncertainties, the uncertainties on $\sigma_{t\bar{t}}$ in the lepton+jets channels are marginally larger compared to the result obtained from the analysis presented in this thesis. Moreover, the ATLAS collaboration recently published a result of $\sigma_{t\bar{t}}^{\text{ATLAS}} = 145 \pm 31\,(\text{stat.})\,^{+42}_{-27}\,(\text{syst.})$ pb [16] on the $t\bar{t}$ production cross section, based on a combination of measurements in the electron+jets, muon+jets, and dilepton channels in a data set corresponding $L = 2.9\ \text{pb}^{-1}$. In contrast to the previously given results, the quoted $\pm 1\sigma$ systematic uncertainties on this measurement additionally account for the $\pm 11\%$ uncertainty on the integrated luminosity. Within the given uncertainties, good agreement is observed for the results obtained in the various channels, the measurement provided by ATLAS, and the result obtained from the analysis presented in this thesis.

Less than one year of LHC operation at a centre-of-mass energy of $\sqrt{s} = 7$ TeV has already allowed for the re-discovery of the top quark and the first measurement of the $t\bar{t}$ production cross section. Pioneered by this observation, further investigations like the measurement of the top quark mass [17], or even the search for physics beyond the Standard Model [18], are conceivable. Consequently, this very first step on the top quark sector opens up promising perspectives for scrutinising the interactions and characteristics of this heaviest fermion in the Standard Model of elementary particle physics.

Appendix A

Additional Information on Systematic Samples

Table A.1: Summary of simulated $t\bar{t}$, W+jets, and Z+jets events with modified parameters for the investigation of systematic uncertainties. All samples have been generated using MADGRAPH interfaced to the PYTHIA, according to the MLM matching prescription and the D6T tune has been employed to account for the underlying event. The quoted numbers of simulated events correspond to the number of sucessfully analysed Monte Carlo events. More information about these samples can be found in [189].

Process	Systematic	Simulated Events
$t\bar{t}$	less ISR/FSR	1,221,664
	more ISR/FSR	1,394,010
	smaller renormalisation/factorisation scale	1,098,971
	larger renormalisation/factorisation scale	1,153,236
	smaller matching threshold	938,005
	larger matching threshold	1,036,492
	including pile-up	1,281,237
W+jets	smaller renormalisation/factorisation scale	5,242,219
	larger smaller renormalisation/factorisation scale	6,218,255
	smaller matching threshold	2,706,986
	larger matching threshold	10,370,368
	including pile-up	14,766,396
Z+jets	smaller renormalisation/factorisation scale	1,436,150
	larger smaller renormalisation/factorisation scale	1,329,028
	smaller matching threshold	1,662,884
	larger matching threshold	1,667,367

List of Figures

List of Tables

Bibliography

[1] F. Abe et al., "Observation of Top Quark Production in $p\bar{p}$ Collisions with the Collider Detector at Fermilab", Phys. Rev. Lett. 74, 2626–2631 (1995).

[2] S. Abachi et al., "Observation of the Top Quark", Phys. Rev. Lett. 74, 2632–2637 (1995).

[3] Tevatron Electroweak Working Group, "Combination of CDF and DØ Results on the Mass of the Top Quark using up to 5.6 fb^{-1} of Data", `arXiv:hep-ex/1007.3178` (2010).

[4] K. Nakamura et al., "Review of Particle Physics", J. Phys. G37, 075021 (2010).

[5] T. Aaltonen et al., "Observation of Electroweak Single Top Quark Production", Phys. Rev. Lett. 103, 092002 (2009).

[6] V. M. Abazov et al., "Observation of Single Top Quark Production", Phys. Rev. Lett. 103, 092001 (2009).

[7] T. Aaltonen et al., "Observation of Single Top Quark Production and Measurement of $|V_{tb}|$ with CDF", Phys. Rev. D82, 112005 (2010).

[8] S. Moch and P. Uwer, "Theoretical Status and Prospects for Top-Quark Pair Production at Hadron Colliders", Phys. Rev. D78, 034003 (2008).

[9] U. Langenfeld, S. Moch, and P. Uwer, "New Results for $t\bar{t}$ Production at Hadron Colliders", `arXiv:hep-ph/0907.2527` (2009).

[10] M. Aliev et al., "HATHOR — Hadronic Top and Heavy Quarks Cross Section Calculator", `arxiv:hep-ph/1007.1327` (2010).

[11] CMS Collaboration, "Measurement of CMS Luminosity", CMS Physics Analysis Summary EWK-10-004 (2010).

[12] CMS Outreach Group, "CMS Outreach Web Page." `http://cms.web.cern.ch`, (February 2011).

[13] J. Neyman and E. S. Pearson, "On the Problem of the Most Efficient Tests of Statistical Hypotheses", Phil. Trans. R. Soc. Lond. A231, 289–337 (1933).

[14] V. Khachatryan et al., "First Measurement of the Cross Section for Top-Quark Pair Production in Proton-Proton Collisions at $\sqrt{s} = 7$ TeV", Phys. Lett. B695, 424–443 (2011).

[15] CMS Collaboration, "Measurement of the Top-Quark Pair-Production Cross Section in the Lepton+Jets Channel without the Use of b-Tagging", CMS Physics Analysis Summary TOP-10-002 (in preparation) (2010).

[16] G. Aad et al., "Measurement of the Top Quark-Pair Production Cross Section with ATLAS in pp Collisions at $\sqrt{s} = 7$ TeV", `arXiv:hep-ex/1012.1792` (submitted to EPJC) (2010).

[17] CMS Collaboration, "First Measurement of the Top Quark Mass in the Dilepton Channel in pp Collisions at $\sqrt{s} = 7$ TeV", CMS Physics Analysis Summary TOP-10-006 (in preparation) (2010).

[18] CMS Collaboration, "Search for TeV Top Resonances into Jets Plus Muon", CMS Physics Analysis Summary EXO-09-008 (2009).

[19] S. L. Glashow, "Partial Symmetries of Weak Interactions", Nucl. Phys. 22, 579–588 (1961).

[20] A. Salam and J. C. Ward, "Electromagnetic and Weak Interactions", Phys. Lett. 13, 168–171 (1964).

[21] M. Gell-Mann, "A Schematic Model of Baryons and Mesons", Phys. Lett. 8, 214–215 (1964).

[22] S. Weinberg, "A Model of Leptons", Phys. Rev. Lett. 19, 1264–1266 (1967).

[23] S. L. Glashow, J. Iliopoulos, and L. Maiani, "Weak Interactions with Lepton-Hadron Symmetry", Phys. Rev. D2, 1285–1292 (1970).

[24] H. Georgi and S. L. Glashow, "Unified Weak and Electromagnetic Interactions without Neutral Currents", Phys. Rev. Lett. 28, 1494 (1972).

[25] G. 't Hooft, "Renormalizable Lagrangians for Massive Yang-Mills Fields", Nucl. Phys. B35, 167–188 (1971).

[26] G. 't Hooft and M. J. G. Veltman, "Regularisation and Renormalisation of Gauge Fields", Nucl. Phys. B44, 189–213 (1972).

[27] G. 't Hooft and M. J. G. Veltman, "Combinatorics of Gauge Fields", Nucl. Phys. B50, 318–353 (1972).

[28] D. J. Gross and F. Wilczek, "Asymptotically Free Gauge Theories. 1", Phys. Rev. D8, 3633–3652 (1973).

[29] D. J. Gross and F. Wilczek, "Ultraviolet Behaviour of Non-Abelian Gauge Theories", Phys. Rev. Lett. 30, 1343–1346 (1973).

[30] H. D. Politzer, "Reliable Perturbative Results for Strong Interactions?", Phys. Rev. Lett. 30, 1346–1349 (1973).

[31] H. D. Politzer, “Asymptotic Freedom: An Approach to Strong Interactions”, Phys. Rept. 14, 129–180 (1974).

[32] Y. Fukuda et al., “Evidence for Oscillation of Atmospheric Neutrinos”, Phys. Rev. Lett. 81, 1562–1567 (1998).

[33] S. Fukuda et al., “Solar ^{8}B and hep Neutrino Measurements from 1258 Days of Super-Kamiokande Data”, Phys. Rev. Lett. 86, 5651–5655 (2001).

[34] M. B. Smy, “Solar Neutrino Precision Measurements using all 1496 Days of Super-Kamiokande-I Data”, Prepared for 4th Workshop on Neutrino Oscillations and their Origin, Kanazawa, Japan (2003).

[35] Y. Ashie et al., “Evidence for an Oscillatory Signature in Atmospheric Neutrino Oscillation”, Phys. Rev. Lett. 93, 101801 (2004).

[36] Q. R. Ahmad et al., “Direct Evidence for Neutrino Flavor Transformation from Neutral Current Interactions in the Sudbury Neutrino Observatory”, Phys. Rev. Lett. 89, 011301 (2002).

[37] S. Khalil and E. Torrente-Lujan, “Neutrino Mass and Oscillation as Probes of Physics beyond the Standard Model”, J. Egyptian Math. Soc. 9, 91–141 (2001).

[38] P. Ramond, “Neutrinos: A Glimpse beyond the Standard Model”, Nucl. Phys. Proc. Suppl. 77, 3–9 (1999).

[39] O. W. Greenberg, “Spin and Unitary Spin Independence in a Paraquark Model of Baryons and Mesons”, Phys. Rev. Lett. 13, 598–602 (1964).

[40] M. Y. Han and Y. Nambu, “Three-Triplet Model with Double $SU(3)$ Symmetry”, Phys. Rev. 139, B1006–B1010 (1965).

[41] H. Fritzsch, M. Gell-Mann, and H. Leutwyler, “Advantages of the Colour Octet Gluon Picture”, Phys. Lett. B47, 365–368 (1973).

[42] A. Einstein, “Grundlage der Allgemeinen Relativitätstheorie”, Annalen Phys. 49, 769–822 (1916).

[43] A. Einstein, “Prinzipielles zur Allgemeinen Relativitätstheorie”, Annalen Phys. 55, 241 (1918).

[44] Tevatron Electroweak Working Group, “Updated Combination of CDF and DØ Results for the Mass of the W Boson”, FERMILAB-TM-2439-E (2009).

[45] S. Tomonaga, “On a Relativistically Invariant Formulation of the Quantum Theory of Wave Fields”, Prog. Theor. Phys. 1, 27–42 (1946).

[46] J. S. Schwinger, “Quantum Electrodynamics. I: A Covariant Formulation”, Phys. Rev. 74, 1439 (1948).

[47] J. S. Schwinger, “Quantum Electrodynamics. II: Vacuum Polarisation and Self-Energy”, Phys. Rev. 75, 651 (1948).

[48] J. S. Schwinger, “Quantum Electrodynamics. III: The Electromagnetic Properties of the Electron: Radiative Corrections to Scattering”, Phys. Rev. 76, 790–817 (1949).

[49] R. P. Feynman, “The Theory of Positrons”, Phys. Rev. 76, 749–759 (1949).

[50] R. P. Feynman, “Space-time Approach to Quantum Electrodynamics”, Phys. Rev. 76, 769–789 (1949).

[51] R. P. Feynman, “Mathematical Formulation of the Quantum Theory of Electromagnetic Interaction”, Phys. Rev. 80, 440–457 (1950).

[52] J. S. Schwinger, “Renormalisation Theory of Quantum Electrodynamics: An Individual View”, In *The Birth Of Particle Physics* (Cambridge University Press) 329–353 (1983).

[53] N. Cabibbo, “Unitary Symmetry and Leptonic Decays”, Phys. Rev. Lett. 10, 531–533 (1963).

[54] M. Kobayashi and T. Maskawa, “CP Violation in the Renormalizable Theory of Weak Interaction”, Prog. Theor. Phys. 49, 652–657 (1973).

[55] F. Englert and R. Brout, “Broken Symmetry and the Mass of Gauge Vector Mesons”, Phys. Rev. Lett. 13, 321–322 (1964).

[56] G. S. Guralnik, C. R. Hagen, and T. W. B. Kibble, “Global Conservation Laws and Massless Particles”, Phys. Rev. Lett. 13, 585–587 (1964).

[57] P. W. Higgs, “Broken Symmetries, Massless Particles, and Gauge Fields”, Phys. Lett. 12, 132–133 (1964).

[58] P. W. Higgs, “Broken Symmetries and the Masses of Gauge Bosons”, Phys. Rev. Lett. 13, 508–509 (1964).

[59] P. W. Higgs, “Spontaneous Symmetry Breakdown without Massless Bosons”, Phys. Rev. 145, 1156–1163 (1966).

[60] Y. Nambu and G. Jona-Lasinio, “Dynamical Model of Elementary Particles based on an Analogy with Superconductivity. I”, Phys. Rev. 122, 345–358 (1961).

[61] Y. Nambu and G. Jona-Lasinio, “Dynamical Model of Elementary Particles based on an Analogy with Superconductivity. II”, Phys. Rev. 124, 246–254 (1961).

[62] J. Goldstone, “Field Theories with Superconductor Solutions”, Nuovo Cim. 19, 154–164 (1961).

[63] J. Goldstone, A. Salam, and S. Weinberg, “Broken Symmetries”, Phys. Rev. 127, 965–970 (1962).

[64] W. Hamilton, “Report of the 4th Meeting of the British Association for the Advancement of Science”, London (1835).

[65] P. A. M. Dirac, “The Quantum Theory of the Electron. 2”, Proc. Roy. Soc. Lond. A118, 351 (1928).

[66] E. Noether, “Invarianten beliebiger Differentialausdrücke”, Nachr. Königl. Ges. Wiss. Göttingen 235–257 (1918).

[67] U. Nierste and F.-M. Stober, “Vorlesung zur Theoretischen Teilchenphysik I-III”, WS 2005/06, SS 2006 and WS 2006/07, Karlsruher Institut für Technologie.

[68] D. Chang, W.-F. Chang, and E. Ma, “Alternative Interpretation of the Tevatron Top Events”, Phys. Rev. D59, 091503 (1999).

[69] Z. Gunay Unalan, “First CDF Measurement of the Top Quark Charge using the Top Decay Products”, Nucl. Phys. Proc. Suppl. 177-178, 297–299 (2008).

[70] R. D. Peccei, S. Peris, and X. Zhang, “Non-Standard Couplings of the Top Quark and Precision Measurements of the Electroweak Theory”, Nucl. Phys. B349, 305–322 (1991).

[71] R. D. Peccei and X. Zhang, “Dynamical Symmetry Breaking and Universality Breakdown”, Nucl. Phys. B337, 269–283 (1990).

[72] J. R. Incandela et al., “Status and Prospects of Top Quark Physics”, Prog. Part. Nucl. Phys. 63, 239–292 (2009).

[73] Y. Grossman and I. Nachshon, “Hadronisation, Spin, and Lifetimes”, JHEP 07, 016 (2008).

[74] D. Wicke, “Properties of the Top Quark”, `arXiv:hep-ex/1005.2460` (2009).

[75] M. Gluck, J. F. Owens, and E. Reya, “Gluon Contribution to Hadronic J/ψ Production”, Phys. Rev. D17, 2324 (1978).

[76] L. M. Jones and H. W. Wyld, “On Hadronic Charm Production by Gluon Fusion”, Phys. Rev. D17, 1782 (1978).

[77] J. Babcock, D. W. Sivers, and S. Wolfram, “QCD Estimates for Heavy Particle Production”, Phys. Rev. D18, 162 (1978).

[78] H. M. Georgi et al., “Charmed Particles From Two-Gluon Annihilation in Proton Proton Collisions”, Ann. Phys. 114, 273 (1978).

[79] B. L. Combridge, “Associated Production of Heavy Flavoured States in Hadron Interactions - Some QCD Estimates. (Talk)”, Phys. Scripta 20, 5–9 (1979).

[80] K. Hagiwara and T. Yoshino, “Hadroproduction of Heavy Quark Flavors in QCD”, Phys. Lett. B80, 282 (1979).

[81] V. D. Barger and R. J. N. Phillips, "Collider Physics", Addison-Wesley, Frontiers in Physics 71, 592 (1987).

[82] A. D. Martin, W. J. Stirling, R. S. Thorne, and G. Watt, "Parton Distributions for the LHC", Eur. Phys. J. C63, 189–285 (2009).

[83] A. D. Martin, W. J. Stirling, R. S. Thorne, and G. Watt, "Uncertainties on α_s in Global PDF Analyses and Implications for Predicted Hadronic Cross Sections", Eur. Phys. J. C64, 653–680 (2009).

[84] P. M. Nadolsky et al., "Implications of CTEQ Global Analysis for Collider Observables", Phys. Rev. D78, 013004 (2008).

[85] P. Nason, S. Dawson, and R. K. Ellis, "The Total Cross-Section for the Production of Heavy Quarks in Hadronic Collisions", Nucl. Phys. B303, 607 (1988).

[86] W. Beenakker, H. Kuijf, W. L. van Neerven, and J. Smith, "QCD Corrections to Heavy Quark Production in $p\bar{p}$ Collisions", Phys. Rev. D40, 54–82 (1989).

[87] W. Bernreuther, A. Brandenburg, Z. G. Si, and P. Uwer, "Top Quark Spin Correlations at Hadron Colliders: Predictions at next-to-leading Order QCD", Phys. Rev. Lett. 87, 242002 (2001).

[88] W. Bernreuther, A. Brandenburg, Z. G. Si, and P. Uwer, "Top Quark Pair Production and Decay at Hadron Colliders", Nucl. Phys. B690, 81–137 (2004).

[89] M. Czakon and A. Mitov, "Inclusive Heavy Flavor Hadroproduction in NLO QCD: The Exact Analytic Result", Nucl. Phys. B824, 111–135 (2010).

[90] M. Cacciari et al., "Updated Predictions for the Total Production Cross Sections of Top and of Heavier Quark Pairs at the Tevatron and at the LHC", JHEP 09, 127 (2008).

[91] U. Langenfeld, S. Moch, and P. Uwer, "Measuring the Running Top-Quark Mass", Phys. Rev. D80, 054009 (2009).

[92] N. Kidonakis, "Higher-Order Corrections to Top-Antitop Pair and Single Top Quark Production", `arXiv:hep-ph/0909.0037` (2009).

[93] N. Kidonakis, "NNLL Resummation for QCD Cross Sections", `arXiv:hep-ph/1011.4866` (2010).

[94] N. Kidonakis and R. Vogt, "The Theoretical Top Quark Cross Section at the Tevatron and the LHC", Phys. Rev. D78, 074005 (2008).

[95] N. Kidonakis, "Single Top Quark Production Cross Section at Hadron Colliders", PoS DIS2010, 196, `arXiv:hep-ph/1005.3330` (2010).

[96] CMS Generator Tools Group, "CMS TWiki Page: Standard Model Cross Sections for CMS at 7 TeV."
https://twiki.cern.ch/twiki/bin/view/CMS/StandardModelCrossSections (internal), (February 2011).

[97] J. M. Campbell and R. K. Ellis, "MCFM for the Tevatron and the LHC", Nucl. Phys. Proc. Suppl. 205-206, 10–15 (2010).

[98] N. Kidonakis, "Two-loop Soft Anomalous Dimensions for Single Top Quark Associated Production with a W^- or H^-", arXiv:hep-ph/1005.4451.

[99] S. Frixione et al., "Single-Top Hadroproduction in Association with a W Boson", JHEP 07, 029 (2008).

[100] DØ Public Web Page, "Useful Diagrams of Top Signals and Backgrounds", http://www-d0.fnal.gov/Run2Physics/top/top_public_web_pages/top_feynman_diagrams.html (February 2011).

[101] K. Desler and D. A. Edwards, "Accelerator Physics of Colliders", Phys. Rev. D66, 010001 (2002).

[102] L. Evans et al., "LHC Machine", JINST S080001, 3 (2008).

[103] O. S. Brüning et al., "The LHC Design Report v.1: The LHC Main Ring", CERN, Geneva, CERN-2004-003-V-1 (2004).

[104] S. Myers and E. Picasso, "The Design, Construction and Commissioning of the CERN Large Electron Positron Collider", Contemp. Phys. 31, 387–403 (1990).

[105] J. Alcaraz et al., "A Combination of Preliminary Electroweak Measurements and Constraints on the Standard Model", arXiv:hep-ex/0612034 (2006).

[106] The LEP Electroweak Working Group and the SLD Electroweak and Heavy Flavour Groups, "Precision Electroweak Measurements on the Z^0 Resonance", Phys. Rept. 427, 257 (2006).

[107] B. Povh et al., "Teilchen und Kerne", Springer Verlag (2006).

[108] M. Benedikt et al., "The LHC Design Report v.3: The LHC Injector Chain", CERN, Geneva, CERN-2004-003-V-3 (2004).

[109] G. Arnison et al., "Experimental Observation of Isolated Large Transverse Energy Electrons with Associated Missing Energy at $\sqrt{s} = 540$ GeV", Phys. Lett. B122, 103–116 (1983).

[110] M. Banner et al., "Observation of Single Isolated Electrons of High Transverse Momentum in Events with Missing Transverse Energy at the CERN $p\bar{p}$ Collider", Phys. Lett. B122, 476–485 (1983).

[111] G. Arnison et al., "Experimental Observation of Lepton Pairs of Invariant Mass around 95 GeV/c^2 at the CERN SPS Collider", Phys. Lett. B126, 398–410 (1983).

[112] P. Bagnaia et al., "Evidence for $Z^0 \to e^+e^-$ at the CERN $p\bar{p}$ Collider", Phys. Lett. B129, 130–140 (1983).

[113] G. Aad et al., "The ATLAS Experiment at the LHC", JINST 3, S08003 (2008).

[114] CMS Collaboration, "Physics Technical Design Report, Volume I: Detector Performance and Software", CMS TDR, CERN, Geneva, CERN-LHCC-2006-001 (2006).

[115] S. Chatrchyan et al., "The CMS Experiment at the LHC", JINST 3, S08004 (2008).

[116] K. Aamodt et al., "The ALICE Experiment at the LHC", JINST 3, S08002 (2008).

[117] A. A. Alves et al., "The LHCb Detector at the LHC", JINST 3, S08005 (2008).

[118] O. Adriani et al., "The LHCf detector at the LHC", JINST 3, S08006 (2008).

[119] K. Osterberg, "The TOTEM Experiment at the LHC", JINST 3, S08007 (2008).

[120] CMS Collaboration, "CMS Physics Technical Design Report v.2: Addendum on High Density QCD with Heavy Ions", J. Phys. G34, 2307–2455 (2007).

[121] Carli, C. (ed.), "Proceedings of the 2010 Charmonix Workshop on LHC Performance", CERN, Geneva, CERN-ATS-2010-026 (2010).

[122] Brennan, G. (ed.), "Proceedings of the 2010 Evian Workshop on LHC Commissioning", CERN, Geneva, CERN-ATS-2010-028 (2010).

[123] CMS Collaboration, "CMS Luminosity — Public Results." `https://twiki.cern.ch/twiki/bin/view/CMSPublic/LumiPublicResults2010`, (February 2011).

[124] S. Chatrchyan et al., "Commissioning of the CMS Experiment and the Cosmic Run at Four Tesla", JINST 5, T03001 (2010).

[125] V. Khachatryan et al., "Transverse Momentum and Pseudorapidity Distributions of Charged Hadrons in pp Collisions at $\sqrt{s} = (0.9 \text{ and } 2.36)$ TeV", JHEP 02, 041 (2010).

[126] CMS Collaboration, "The CMS Tracker System Project: Technical Design Report", CMS TDR, CERN, Geneva, CERN-LHCC-98-06 (1997).

[127] CMS Collaboration, "The CMS Tracker: Addendum to the Technical Design Report", CMS TDR, CERN, Geneva, CERN-LHCC-2000-016 (2000).

[128] CMS Collaboration, "The CMS Electromagnetic Calorimeter Project: Technical Design Report", CMS TDR, CERN, Geneva, CERN-LHCC-97-33 (1997).

[129] CMS Collaboration, "Changes to CMS ECAL Electronics: Addendum to the Technical Design Report", CMS TDR, CERN, Geneva, CERN-LHCC-2002-027 (2002).

[130] CMS Collaboration, "The CMS Hadronic Calorimeter Project: Technical Design Report", CMS TDR, CERN, Geneva, CERN-LHCC-97-31 (1997).

[131] P. Adzic et al., "Energy Resolution of the Barrel of the CMS Electromagnetic Calorimeter", JINST 2, P04004 (2007).

[132] F. Ferri and P. Govoni, "The CMS Electromagnetic Calorimeter Pre-Calibration with Cosmic Rays and Test Beam Electrons", CMS-CR-2007-012 (2007).

[133] CMS Collaboration, "The CMS Muon Project: Technical Design Report", CMS TDR, CERN, Geneva, CERN-LHCC-97-32 (1997).

[134] CMS Collaboration, "CMS TriDAS Project: The Trigger System: Technical Design Report v.1", CMS TDR, CERN, Geneva, CERN-LHCC-2000-038 (1997).

[135] CMS Collaboration, "CMS Trigger and Data Acquisition Project: Technical Design Report", CMS TDR, CERN, Geneva, CERN-LHCC-2002-026 (2002).

[136] CMS Collaboration, "CMS Computing: Technical Design Report", CMS TDR, CERN, Geneva, CERN-LHCC-2005-023 (2005).

[137] WLCG Collaboration, "LHC Computing Grid: Technical Design Report", LCG TDR, CERN, Geneva, CERN-LHCC-2002-024 (2005).

[138] I. Antcheva et al., "ROOT: A C++ Framework for Petabyte Data Storage, Statistical Analysis and Visualisation", Comput. Phys. Commun. 180, 2499–2512 (2009).

[139] M. Dobbs and J. B. Hansen, "The HepMC C++ Monte Carlo Event Record for High Energy Physics", Comput. Phys. Commun. 134, 41–46 (2001).

[140] V. N. Gribov and L. N. Lipatov, "Deep Inelastic ep Scattering in Perturbation Theory", Sov. J. Nucl. Phys. 15, 438–450 (1972).

[141] G. Altarelli and G. Parisi, "Asymptotic Freedom in Parton Language", Nucl. Phys. B126, 298 (1977).

[142] Y. L. Dokshitzer, "Calculation of the Structure Functions for Deep Inelastic Scattering and e^+e^- Annihilation by Perturbation Theory in Quantum Chromodynamics", Sov. Phys. JETP 46, 641–653 (1977).

[143] S. Catani, F. Krauss, R. Kuhn, and B. R. Webber, "QCD Matrix Elements + Parton Showers", JHEP 11, 063 (2001).

[144] S. Mrenna and P. Richardson, "Matching Matrix Elements and Parton Showers with HERWIG and PYTHIA", JHEP 05, 040 (2004).

[145] M. L. Mangano, M. Moretti, and R. Pittau, "Multijet Matrix Elements and Shower Evolution in Hadronic Collisions: $Wb\bar{b} + n$ Jets as a Case Study", Nucl. Phys. B632, 343–362 (2002).

[146] S. Frixione and B. R. Webber, "Matching NLO QCD Computations and Parton Shower Simulations", JHEP 06, 029 (2002).

[147] B. Andersson, G. Gustafson, G. Ingelman, and T. Sjostrand, "Parton Fragmentation and String Dynamics", Phys. Rept. 97, 31–145 (1983).

[148] B. R. Webber, "A QCD Model for Jet Fragmentation Including Soft Gluon Interference", Nucl. Phys. B238, 492 (1984).

[149] D. Amati and G. Veneziano, "Preconfinement as a Property of Perturbative QCD", Phys. Lett. B83, 87 (1979).

[150] T. Sjostrand et al., "High Energy Physics Event Generation with PYTHIA 6.1", Comput. Phys. Commun. 135, 238–259 (2001).

[151] G. Corcella et al., "HERWIG 6: An Event Generator for Hadron Emission Reactions with Interfering Gluons (Including Supersymmetric Processes)", JHEP 01, 010 (2001).

[152] F. Maltoni and T. Stelzer, "MADEVENT: Automatic Event Generation with MADGRAPH", JHEP 02, 027 (2003).

[153] M. L. Mangano et al., "ALPGEN, a Generator for Hard Multiparton Processes in Hadronic Collisions", JHEP 07, 001 (2003).

[154] P. Richardson, "Spin Correlations in Monte Carlo Simulations", JHEP 11, 029 (2001).

[155] S. Agostinelli et al., "GEANT4: A Simulation Toolkit", Nucl. Instrum. Meth. A506, 250–303 (2003).

[156] D. Orbaker, "Fast Simulation of the CMS Detector", J. Phys. Conf. Ser. 219, 032053 (2010).

[157] T. Speer et al., "Track Reconstruction in the CMS Tracker", Nucl. Instrum. Meth. A559, 143–147 (2006).

[158] R. E. Kalman, "A New Approach to Linear Filtering and Prediction Problems", Transactions of the ASME. Series D: Journal of Basic Engineering 82, 35–45 (1960).

[159] R. Frühwirth, "Application of Kalman Filtering to Track and Vertex Fitting", Nucl. Instrum. Meth. A262, 444–450 (1987).

[160] B. Mangano, "CMS Track Reconstruction Performance", PoS VERTEX2008, 015 (2008).

[161] R. Fruhwirth, W. Waltenberger, and P. Vanlaer, "Adaptive Vertex Fitting", J. Phys. G34, N343 (2007).

[162] S. Baffioni et al., "Electron Reconstruction in CMS", Eur. Phys. J. C49, 1099–1116 (2007).

[163] R. Fruhwirth, "Track Fitting with Non-Gaussian Noise", Comput. Phys. Commun. 100, 1–16 (1997).

[164] W. Adam, R. Fruhwirth, A. Strandlie, and T. Todorov, "Reconstruction of Electrons with the Gaussian Sum Filter in the CMS Tracker at LHC", ECONF C0303241, TULT009 (2003).

[165] H. Bethe and W. Heitler, "On the Stopping of Fast Particles and on the Creation of Positive Electrons", Proc. Roy. Soc. Lond. A146, 83–112 (1934).

[166] R. Salerno, "Electron Reconstruction and Identification in CMS at LHC", Nucl. Phys. Proc. Suppl. 197, 230–232 (2009).

[167] CMS Collaboration, "Performance of Muon Identification in pp Collisions at $\sqrt{s} = 7$ TeV", CMS Physics Analysis Summary MUO-10-002 (2010).

[168] G. P. Salam and G. Soyez, "A Practical Seedless Infrared-Safe Cone Jet Algorithm", JHEP 05, 086 (2007).

[169] S. Catani, Y. L. Dokshitzer, M. H. Seymour, and B. R. Webber, "Longitudinally Invariant k_{T} Clustering Algorithms for Hadron Hadron Collisions", Nucl. Phys. B406, 187–224 (1993).

[170] Y. L. Dokshitzer, G. D. Leder, S. Moretti, and B. R. Webber, "Better Jet Clustering Algorithms", JHEP 08, 001 (1997).

[171] M. Wobisch and T. Wengler, "Hadronisation Corrections to Jet Cross Sections in Deep-Inelastic Scattering", `arXiv:hep-ph/9907280` (1998).

[172] M. Cacciari, G. P. Salam, and G. Soyez, "The Anti-k_{T} Jet Clustering Algorithm", JHEP 04, 063 (2008).

[173] CMS Collaboration, "Jet Performance in pp Collisions at $\sqrt{s} = 7$ TeV", CMS Physics Analysis Summary JME-10-003 (2010).

[174] CMS Collaboration, "Jet Plus Tracks Algorithm for Calorimeter Jet Energy Corrections in CMS", CMS Physics Analysis Summary JME-09-002 (2009).

[175] CMS Collaboration, "Particle-Flow Event Reconstruction in CMS and Performance for Jets, $\not\!\!E_{\mathrm{T}}$, and Taus", CMS Physics Analysis Summary PFT-09-001 (2009).

[176] CMS Collaboration, "Plans for Jet Energy Corrections at CMS", CMS Physics Analysis Summary JME-07-002 (2007).

[177] CMS Collaboration, "Offset Energy Correction for Jets", CMS Physics Analysis Summary JME-09-003 (2009).

[178] CMS Collaboration, "Determination of the Relative Jet Energy Scale at CMS from Dijet Balance", CMS Physics Analysis Summary JME-08-003 (2008).

[179] CMS Collaboration, "Commissioning of b-Jet Identification with pp Collisions at $\sqrt{s} = 7$ TeV", CMS Physics Analysis Summary BTV-10-001 (2010).

[180] CMS Collaboration, "$\not\!\!E_{\mathrm{T}}$ Performance in CMS", CMS Physics Analysis Summary JME-07-001 (2007).

[181] CMS Collaboration, "Track-Corrected Missing Transverse Energy in CMS", CMS Physics Analysis Summary JME-09-010 (2009).

[182] CMS Collaboration, "Missing Transverse Energy Performance in Minimum-Bias and Jet Events from Proton-Proton Collisions at $\sqrt{s} = 7$ TeV", CMS Physics Analysis Summary JME-10-004 (2010).

[183] J. M. Campbell, J. W. Huston, and W. J. Stirling, "Hard Interactions of Quarks and Gluons: A Primer for LHC Physics", Rept. Prog. Phys. 70, 89 (2007).

[184] CMS Data Quality Monitoring (DQM), "JSON file." `https://cms-service-dqm.web.cern.ch/cms-service-dqm/CAF/certification/Collisions10/7TeV/Reprocessing/Cert_136033-149442_7TeV_Nov4ReReco_Collisions10_JSON.txt` (internal), (February 2010).

[185] S. Van der Meer, "Calibration of the Effective Beam Height in the ISR", CERN, Geneva, CERN-ISR-PO-68-31 (1968).

[186] J. P. Chou et al., "Anomalous HB/HE Noise at Startup: Characteristics and Rejection Algorithms", CMS-IN-2010/006 (internal) (2010).

[187] R. Field, "Early LHC Underlying Event Data - Findings and Surprises", `arXiv:hep-ph/1010.3558` (2010).

[188] R. Gavin, Y. Li, F. Petriello, and S. Quackenbush, "FEWZ 2.0: A Code for Hadronic Z Production at next-to-next-to-leading Order", `arXiv:hep-ph/1011.3540` (2010).

[189] CMS Generator Tools Group, "CMS TWiki Page: Fall 2010 CMS Monte Carlo Production at 7 TeV." `https://twiki.cern.ch/twiki/bin/viewauth/CMS/ProductionFall2010` (internal), (February 2011).

[190] F. Blekman et al., "Selection of $t\bar{t}$ Candidates in the Lepton+Jets Channels", CMS-AN-2010/297 (internal) (2010).

[191] CMS Collaboration, "Jet Energy Corrections Determination at $\sqrt{s} = 7$ TeV", CMS Physics Analysis Summary JME-10-010 (2010).

[192] C. J. Clopper and E. S. Pearson, "The Use of Confidence or Fiducial Limits Illustrated in the Case of the Binominal", Biometrika 26, 404–313 (1934).

[193] J. Alcaraz et al., "Updated Measurements of the Inclusive W and Z Cross Sections at 7 TeV", CMS-AN-2010/264 (internal) (2010).

[194] Th. Müller, J. Ott, and J. Wagner-Kuhr, "theta — A Framework for Template-Based Modelling and Inference", CMS-IN-2010/017 (internal) (2010).

[195] F. James and M. Roos, "MINUIT: A System for Function Minimisation and Analysis of the Parameter Errors and Correlations", Comput. Phys. Commun. 10, 343–367 (1975).

[196] M. R. Whalley, D. Bourilkov, and R. C. Group, "The Les Houches Accord PDFs (LHAPDF) and LHAGLUE", arXiv:hep-ph/0508110 (2005).

Danksagung

Ohne die vielfältige Unterstützung von Personen im beruflichen und privaten Umfeld ist eine erfolgreiche Promotion undenkbar. Ich möchte mich daher ganz herzlich bei allen bedanken die mir geholfen, mich motiviert und an mein Durchhaltevermögen appelliert haben. Ebenso gilt ein großes Dankeschön denen, die viel Nachsicht und Geduld mit mir beweisen mussten, vor allem in der nervenaufreibenden Endspurt-Phase.

Zunächst möchte ich meinem Doktorvater Herrn Prof. Dr. Th. Müller danken. Als ich mich vor etwas mehr als 3 Jahren in Karlsruhe bewarb, wurde ich mit offenen Armen empfangen. Innerhalb der starken Karlsruher Top-Gruppe und dank seiner Rückendeckung, konnte ich ungehindert meinem Forscherdrang nachgehen. Ich denke, den Erfolg, den unsere Gruppe momentan in der CMS-Kollaboration genießt, spricht für sich selbst. Solch eine erfolgreiche Arbeit wäre ohne seine stete Unterstützung nicht möglich gewesen! Ein besonderer Dank geht auch an Prof. Dr. G. Quast für die Übernahme des Korreferats und seine unermüdliche Hilfsbereitschaft. Wann immer ein Problem ins Haus stand, seine Tür stand stets offen, auch wenn es mal wieder um CMS-Politik und Approval-Stress ging. Auch für Dummy-Fragen zu statistischen Themen hatte er immer ein offenes Ohr. Für diese ultimative Rundum-Betreuung kann ich mich gar nicht genug bedanken!

Ein weiteres Dankeschön geht an die Postdocs der Karlsruher Top-Gruppe. Insbesondere möchte ich hierbei Dr. Frank-Peter Schilling, Dr. Thorsten Chwalek, Dr. Jan Lück, Dr. Jeannine Wagner-Kuhr und Dr. Philipp Schieferdecker erwähnen, die mir auf die unterschiedlichste Art und Weise durch meine Promotion geholfen haben. Vielen Dank für die vielen konstruktiven Gespräche über physikalische und auch manchmal nicht ganz so physikalische Themen, das intensive Lesen meiner Dissertation und den Zuspruch für meine Arbeit, den ich von Euch erhalten habe. Vor allem für die unentwegte Diskussionsbereitschaft während meiner Prüfungsvorbereitung möchte ich mich ganz herzlich bei Euch bedanken.

Des Weiteren möchte ich den Mitgliedern der Karlsruher Top-Gruppe für eine angenehme und inspirierende Arbeitsatmosphäre danken. Insbesondere seien hier, neben den bereits genannten Postdocs, Manuel Renz, Jochen Ott, Thomas Peiffer und (leider mittlerweile zum HIT entlaufen) Dr. Julia Bauer erwähnt. Vielen Dank, dass Ihr mich so herzlich in Karlsruhe aufgenommen und durch konstruktive Kritik bei meiner Arbeit unterstützt habt. Auch für die kritische Durchsicht meiner Dissertation möchte ich mich bedanken. Unseren Diplomanden möchte ich zudem ein großes Lob und ein ganz liebes Danke aussprechen für das fleißige Basteln meines Doktorhuts.

Die Fertigstellung einer Dissertation hapert manchmal nicht an den Fähigkeiten des Doktoranden, sondern kann leicht durch unwillige Computer und Netzwerke zunichte gemacht werden. Jedoch gibt es am EKP eine Vielzahl an Administratoren die unermüdlich gegen diesen Umstand ankämpfen. Ich möchte mich daher bei Dr. Thomas Kuhr und seinem Admin-Team bedanken, denn ohne dieses hervorragend funktionierende Netzwerk

an helfenden Händen wären wir wohl völlig ausgeliefert. Darüber hinaus möchte ich Michael Prim danken, der auf der letzten Silvesterrakete ans EKP geflogen ist, um mir die rechtzeitige Fertigstellung meiner Dissertation zu ermöglichen. Vielen, vielen Dank Euch allen für Eure Arbeit im Admin-Team und die Hilfe, die Ihr jedem zukommen lasst, der an seinen Computerproblemen verzweifelt!

Vielmals bedanken möchte ich mich auch bei Frau B. Bräunling, die das EKP-Sekretariat fest im Griff hat und die gute Seele des Instituts ist. Von der Hilfe bei offiziellem Papierkram über benötigte Unterschriften bis hin zur Organisation der Weihnachtsfeier, Sie helfen einfach überall. Haben Sie vielen Dank für Ihre umfangreiche Unterstützung und die herzliche und angenehme Atmosphäre, die Sie im EKP verbreiten.

Ein Zeichen für die überall zu findende Hilfsbereitschaft sind die Türen, die nicht nur im wörtlichen Sinne im EKP stets offen stehen. Ich möchte hier keine Namen nennen, um zu vermeiden jemanden zu vergessen, aber ich möchte mich bei allen Kollegen am EKP bedanken für die wunderbare Zeit, die ich bislang in Karlsruhe verbringen durfte. Für die vielfältigsten physikalischen Diskussionen, vor allem kurz vor der Doktorprüfung, möchte ich Euch allen meinen Dank aussprechen. Darüber hinaus geht ein großes Dankeschön an „den 8. Stock" für die tatkräftige Unterstützung im Bereich Computing.

Für die Native-Speaker Durchsicht meiner Arbeit möchte ich Richard von der Heyde danken. Schon bei der Diplomarbeit hast du mir mit Rat und Tat zur Seite gestanden, vielen Dank, dass du auch bei meiner Doktorarbeit nicht das Weite gesucht hast.

Der Weg zur Promotion besteht nicht allein aus physikalischen Fragestellungen, denn ohne die nötige Rückendeckung im privaten Bereich würde man vermutlich nie das angestrebte Ziel erreichen. Für den seelischen und moralischen Beistand möchte ich meiner Familie, meinen Schwiegereltern und meinem Schwager danken, die stets an mich geglaubt haben und immer für mich da waren! Ohne Eure liebevolle Unterstützung hätte ich das alles nicht erreichen können. Das allergrößte Dankeschön gebührt meinen Mann Moritz. Vielen Dank, dass du immer an mich geglaubt hast, auch wenn ich es manchmal selbst nicht so ganz getan habe. Du hast mich aufgebaut, mir Wege aufgezeigt und mir gesagt, dass wir es gemeinsam schaffen können. Und du hast bis zum Ende Recht behalten, denn wir haben es gemeinsam geschafft. Ohne Dich wäre meine Promotion nicht möglich gewesen, ich danke Dir!